STUDIES OF STATIC AND DYNAMIC CRITICAL BEHAVIOR OF SIMPLE BINARY FLUIDS AND POLYMER MIXTURES USING X-RAY PHOTON CORRELATION SPECTROSCOPY

by

Teamour Sandibeck Nurushev

A dissertation submitted in partial fulfillment
of the requirements for the degree of
Doctor of Philosophy
(Physics)
in The University of Michigan
2000

Doctoral Committee:

Professor Steven B. Dierker, Chair
Professor Roy Clarke
Professor Joanna Mirecki-Millunchick
Professor Leonard Sander
Professor Gregory Tarle

I am dedicating this work to my loving wife Svetlana,
who has been next to me through all ups and downs of life.
She has never lost her belief in me and with her support
I have pulled through countless years of my studies
and now crossing the finish line.
I also dedicate this thesis to my father, who envisioned
me as a physicist and who hoped that I would continue
working on his remarkable contributions to
High Energy Spin Physics.
Dear Dad! There is not much left there to do after you!

ACKNOWLEDGMENTS

I would like to express my deepest gratitude to Steven Dierker, my advisor and a very knowledgeable person for supporting me financially and morally during my studies. I would like to thank him for all the opportunities given to me to participate in various scientific meetings, which greatly enhanced my vision of physics and gave me an understanding of the importance of the research that I was involved in. I treasure every conversation I had with Steve as a valuable lesson.

I owe a great deal to Eric Dufresne, who has shown me a new degree of openness and was always there to listen to me and answer my questions about every detail involved in the research. I appreciate his literature searches that helped introduce me to my new field of physics and that helped steer me in the right direction. I loved his company when we pulled miles of cables for our setup.

I would like to thank Meigan Aronson for letting me borrow some equipment from her lab when needed.

In addition, I would like to thank Ernest Williams, Tom Sanchez, and Harold Gibson for their expertise and help in electronics, and in designing and assembling the setup. The staff of the Physics Shop, with Ted Webster as their leader, deserve a warm thank you for machining the “last minute and due yesterday” orders extremely quickly and with high quality. It would not have been possible to perform some of these experiments without their help.

This work was partially supported by the Donors of the Petroleum Research Fund, administered by the American Chemical Society, under grant ACS-PRF#32105-AC7. The MHATT-CAT facility located at the APS was built with grants from NSF and DOE

as well as contributions from the University of Michigan, Bell Laboratories-Lucent Technologies, and Howard University. Its current operation is supported by DOE grant DE-FG02-99ER45743. The APS is supported by the U.S. Department of Energy, BES, Office of Energy Research under contract No. W-31-109-ENG-38.

TABLE OF CONTENTS

LIST OF TABLES

Table

LIST OF FIGURES

Figure

CHAPTER 1.

INTRODUCTION

For many years electromagnetic scattering had been used as an experimental probe in interdisciplinary sciences. Physicists and chemists have utilized light scattering and small-angle x-ray scattering to study the size and shape of macromolecules in solution as well as a whole range of materials including colloidal suspensions, glasses, and polymers. Meteorologists have used microwaves to observe the scattering by rain, snow, hail, and other objects in the atmosphere, while astrophysicists have been interested in the scattering of starlight by interplanetary and interstellar dust. The same basic scattering principles govern all such different phenomena[1].

The scattering of coherent waves by a random medium causes a modulation in the scattered beam, which appears in the far-field region as a speckle pattern. Exner[2,3] and Laue[4] first observed this effect over a hundred years ago on Fraunhoffer diffraction rings produced by visible light scattered from small particles. Speckle is a general feature of the scattering of coherent waves by spatial variations in the cross section of a medium. It can be seen in many experiments, such as in laser light reflected by a rough surface or scattered from equilibrium density or composition fluctuations in a fluid[1].

Photon correlation spectroscopy (PCS) is a well-developed technique, which uses coherent visible light to study the long wavelength hydrodynamics of fluids, including simple liquids, liquid mixtures, liquid crystals, polymers and colloids. It probes the

dynamics of a material by analyzing the temporal correlations among speckles formed from the scattering of coherent visible photons by a material.

X-ray photon correlation spectroscopy (XPCS) is a logical extension of visible PCS into the x-ray region. There is no fundamental barrier to performing PCS measurements with coherent x-rays, with wavelength of ~ 1Å, rather than with visible light. If one would have a sufficiently intense source of coherent x-rays, this would enable studies of the short length scale, slow dynamics of condensed matter systems. The ability of x-rays to easily penetrate materials would also permit studies of optically opaque materials such as metals.

XPCS experiments have only recently become practical. In the early days of synchrotron radiation, the first generation of synchrotron sources, such as the Stanford Synchrotron Radiation Laboratory (SSRL), were primarily operated for use in High Energy Experiments. Beam steering bending magnets are used to keep the electrons or positrons in orbit around a synchrotron. To a high energy physicist, the synchrotron radiation emitted by the charged particles as they are accelerated by the bending magnets is simply a nuisance, as it represents a source of energy loss. However, condensed matter researchers recognized it as a valuable source for x-ray experiments[5,6,7]. The energy of photons produced by bending magnets has a broad spectrum with a flux that is several orders of magnitude greater than that of laboratory x-ray sources. The success of early "parasitic" condensed matter experiments at 1st generation synchrotrons eventually led to the construction of a 2nd generation of synchrotrons, such as the National Synchrotron Light Source (NSLS), which were dedicated to producing synchrotron radiation exclusively for condensed matter experiments[8,9]. The 2nd generation synchrotrons still

Figure 1.1. Aerial view of the Advanced Photon Source (APS) at Argonne National Laboratory. The APS is a 3rd generation synchrotron source, dedicated to condensed matter experiments. The x-ray experiments in this Thesis were performed at the MHATT-CAT Sector 7 facilities at the APS.

produce radiation almost exclusively from bending magnets. In recent years, a 3rd generation of synchrotrons[9] has been built, including the Advanced Photon Source[10] (APS) at Argonne National Laboratory near Chicago, Illinois, shown in Figure 1.1.

The 3rd generation synchrotrons are also dedicated to condensed matter experiments, including structural biology. Most importantly, the accelerator "lattice", or orbit structure, of 3rd generation synchrotrons has been optimized for the use of so-called insertion devices[11,12], called undulators, shown in Figure 1.2. An insertion device is a periodic magnetic structure inserted into the straight section of an accelerator storage ring

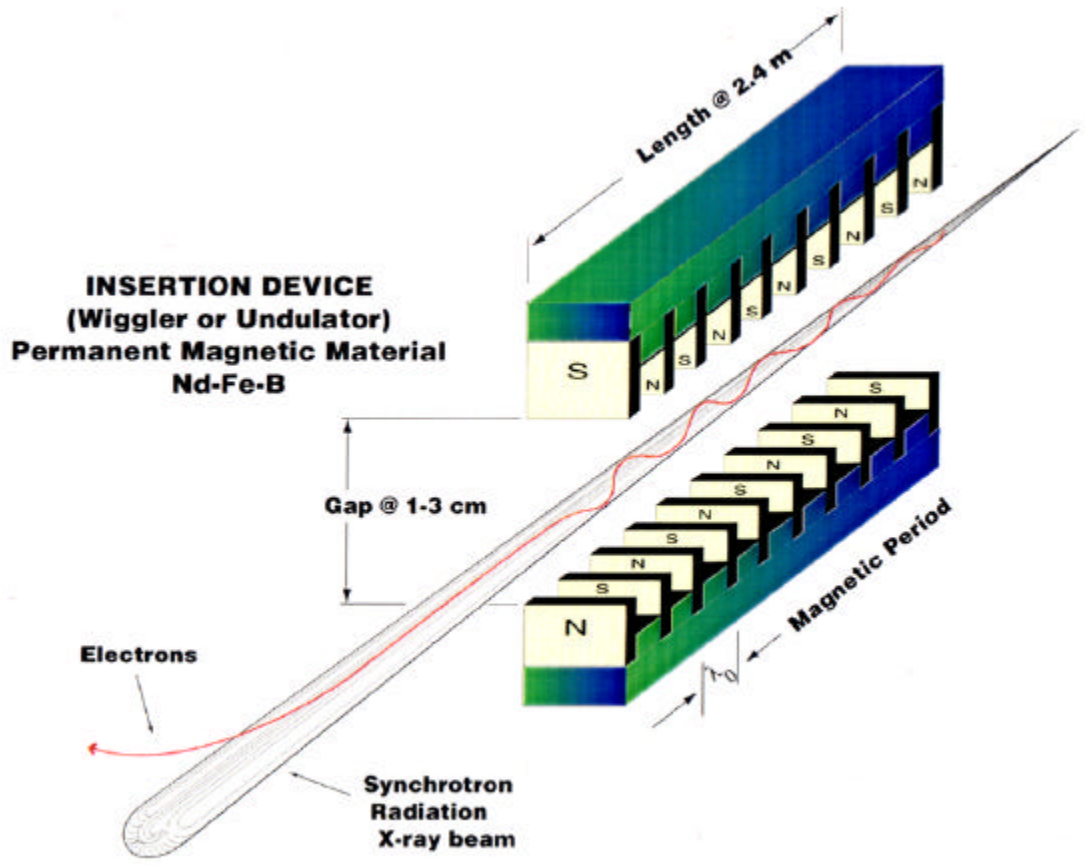

Figure 1.2. Schematic illustration of an undulator. Interference of the radiation from the different magnetic poles results in an intense, quasi-monochromatic, and highly collimated x-ray beam.

for the sole purpose of creating synchrotron radiation. On the simplest level, the radiation from a periodic magnetic structure with *N* poles can be thought of as the combined radiation from *N* bending magnets. In fact, the radiation from the different poles interferes with each other. This interference effect manifests itself in two ways. First, the radiation spectrum is sharply peaked at a fundamental wavelength and its harmonics, as shown in the top half of Figure 1.3. The fundamental wavelength is approximately given by the Lorentz contraction of the magnetic period (typically a few cm) as seen by the

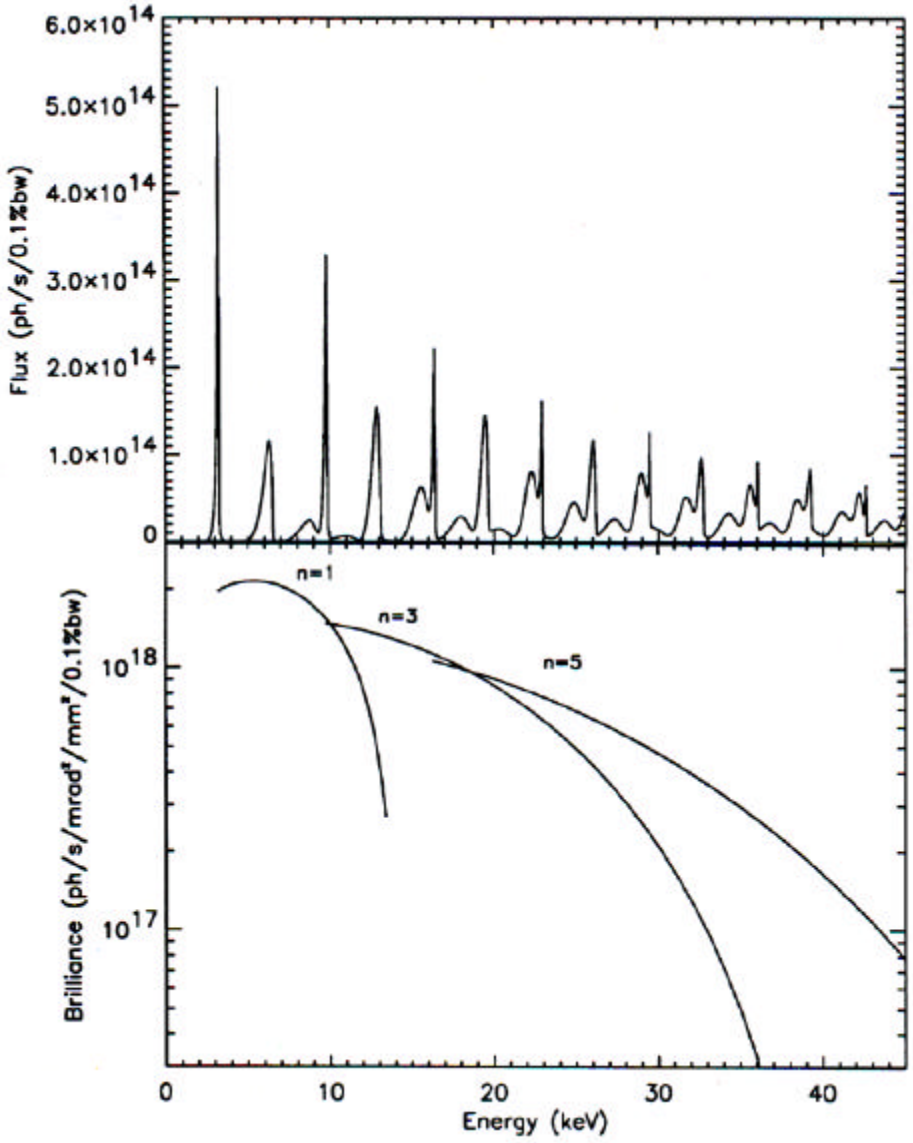

Figure 1.3. Top: Output spectrum of undulator A, used at the APS, showing harmonic frequency bunching. Bottom: Peak brilliance of the 1st, 3rd, and 5th harmonics versus energy as the undulator gap is tuned.

relativistic 7 GeV electrons. It is typically of the order of an Angstrom, for a fundamental energy of order 10 keV, but can be tuned, as shown in the bottom half of Figure 1.3, by varying the gap between the magnetic poles, which varies the strength of the magnetic field. Second, there is a spatial interference, which results in a highly collimated beam of

radiation from the undulator, as shown in Figure 1.2. Both of these effects make the radiation from an undulator intense, quasi-monochromatic, and highly collimated, similar to that from a visible laser, even though the mechanisms are quite different.

A 4th generation of x-ray sources is currently being planned[13] which operate on a very different principle, i.e., self-amplified spontaneous emission[14] (SASE). The first of these "Free Electron Lasers" (FELs), the Linac Coherent Light Source[15] (LCLS), is planned to be built within the next few years at the Stanford Linear Accelerator Center (SLAC) in order to both test the SASE effect as well as to conduct scientific experiments with its intense x-ray beams. XPCS experiments are among the first few experiments planned to be conducted at the LCLS[16].

The coherent x-ray flux available from x-ray sources ranging from conventional x-ray tubes to 4th generation FELs is shown in Figure 1.4. This figure shows the very dramatic rise in available coherent flux over the last several decades. With the current 3rd generation synchrotron sources, coherent x-ray beams suitable for XPCS measurements have fluxes ranging from a few times 10^9 ph/s to a few times 10^{11} ph/s. These levels of coherent flux are sufficient for XPCS experiments on relatively strongly scattering materials. The LCLS 4th generation FEL will produce 230 fsec pulses at a 120 Hz rate. The peak coherent flux during the pulses is expected be as high as 10^{23}-10^{25} ph/s and the time average coherent flux will be about 10^{13} ph/s to 10^{14} ph/s. The increased coherent fluxes from the LCLS will enable XPCS measurements of dynamics on shorter time scales, smaller length scales, and a wider variety of materials. With these current and future prospects, combined with continued enhancements in apparatus and technique, it is highly likely that XPCS will enjoy a wide range of applications and have a similarly large

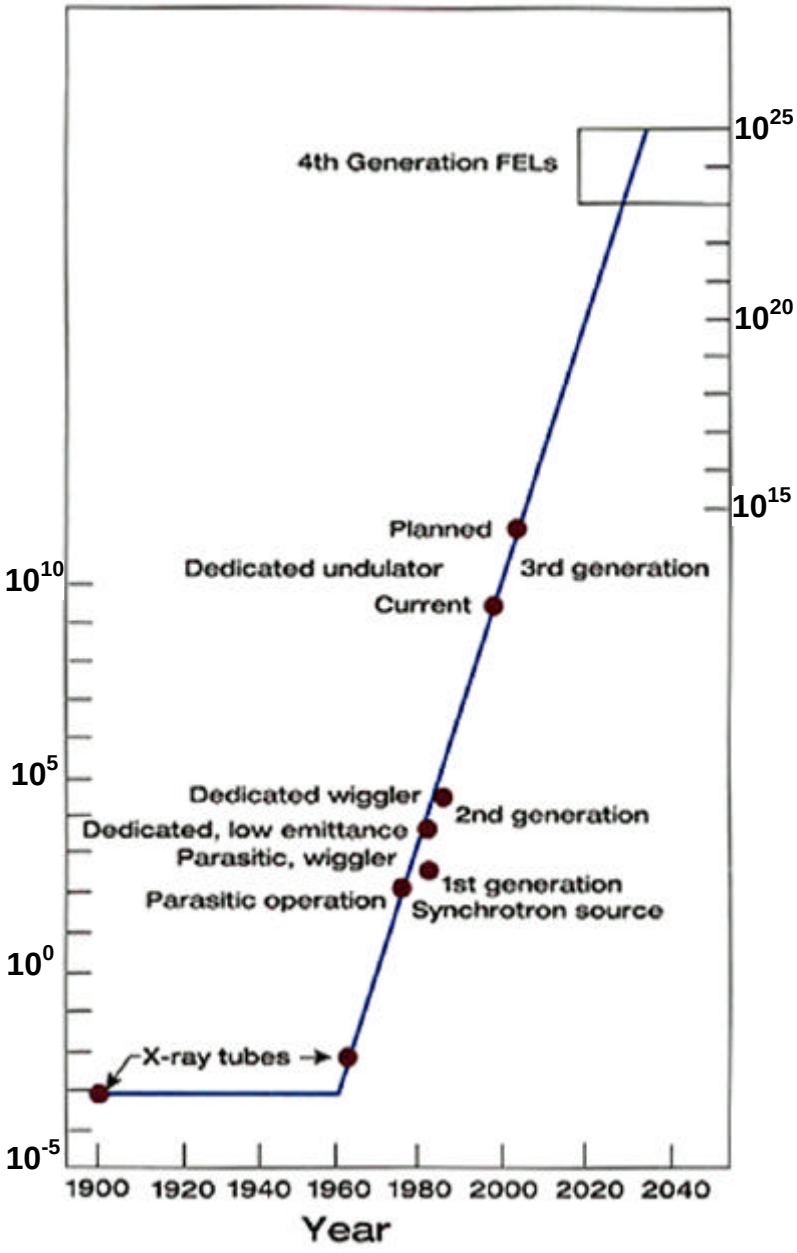

Figure 1.4. Evolution of coherent flux produced by various x-ray sources.

scientific impact as visible PCS has had.

The first unequivocal report of using XPCS to measure the dynamics of a material was made by Dierker, et. al.[17], in 1995. They used XPCS to measure the diffusion coefficient for Brownian motion of gold colloid particles, with a radius of 400 Å,

dispersed in the viscous liquid glycerol. The samples had a gold concentration of 1.3%, sufficiently high that they were completely opaque to visible light, and hence could not be studied with visible PCS. The work was done on the wiggler beam line X25 at the NSLS, with a coherent incident flux at 8 keV of only 4×10^7 ph/s. Despite this low coherent flux, the experiments were feasible due to two key innovations. First, it was recognized that the scattering from large length scale microstructures, such as the gold particles, is enhanced in the forward direction. This enhancement of the Small Angle X-ray Scattering (SAXS) is due to the coherent addition of the scattering from the large number of atoms in the microstructure, similar to the way in which Bragg peaks are enhanced in scattering from well-ordered crystals. In addition, the requirements on the degree of monochromaticity of the x-ray beam are relaxed at small scattering angles, as described in Chapter 4. As a result, a broader bandwidth, more intense x-ray beam could be used. Second, a CCD detector was used to collect the data, which resulted in a dramatic increase in collection efficiency. Since the colloid was isotropic, the dynamics only depended on the magnitude of transferred momentum q, and it was possible to average the autocorrelation function for all detector pixels in the same band of q.

Most of the subsequent XPCS measurements have taken advantage of both of these two innovations, i.e., studying samples with large length scale microstructure, and hence intense SAXS, and employing an area detector to gain the efficiencies of ensemble averaging. This includes XPCS studies of palladium[18,19], Sb_2O_5[20], and latex[21] colloids, polystyrene-polyisoprene block copolymer micelles within a polystyrene homopolymer matrix[22], anti-phase domains in metal alloys[23,24,25], and domain coarsening during phase separation in a sodium borosilicate glass[26]. An exception is the work by T. Thurn-

Albrecht, et. al. on palladium colloids[18]. That experiment was done at the European Synchrotron Radiation Facility (ESRF), a 3rd generation synchrotron, using the intense x-ray beam from an undulator. This, plus the strong scattering from the palladium spheres, enabled them to obtain good data with a conventional single-channel correlator rather than an area detector.

All of the previous XPCS studies have been done on aggregate systems of one form or another and thus benefited from a strong enhancement in SAXS. However, a large number of important materials do not have an aggregate microstructure. In this thesis, a primary goal was to explore the feasibility of conducting XPCS studies on non-aggregate systems, i.e., systems in which the fluctuating entities do not consist of large numbers of atoms permanently grouped together. A secondary goal was to study systems consisting of low-Z (Atomic Number) atoms, which scatter x-rays more weakly than large-Z atoms (scattering is proportional to Z^4). This would constitute an important test of the general applicability of XPCS to a wider variety of materials.

As a first test case, XPCS was used to study the equilibrium static and dynamic critical behavior of equilibrium concentration fluctuations in a simple binary mixture of small molecule, low-Z, fluids, i.e., hexane (C_6H_{14}) and nitrobenzene ($C_6H_5NO_2$). Binary mixtures of small molecular weight fluids have much faster fluctuations and scatter much more weakly than systems previously studied. These experiments were successful and the results showed that it is feasible to use XPCS to study the fast dynamics of even such weak scatterers as these low molecular weight hydrocarbon fluid mixtures.

A second series of experiments attempted to study the equilibrium static and dynamic critical behavior of equilibrium concentration fluctuations in homopolymer

mixtures of polystyrene and polybutadiene. These systems are of particular interest as there are a number of unanswered questions regarding the short-length scale dynamics of polymer systems. Soft condensed matter organic-based materials are often susceptible to various kinds of damage upon prolonged exposure to high energy radiation beams, such as electron, γ-ray, or x-ray beams. This is an important issue in XPCS studies of the dynamics of such materials. Often the effects of radiation damage are cumulative over time. This implies that there may be a maximum duration for an XPCS measurement at a particular position in a material. In the course of these experiments, we discovered that the SAXS from the polymer mixtures changed dramatically upon x-ray irradiation and that the changes scaled with radiation dose for widely varying dose rates. There appears to be a threshold dose, below which no significant effects of damage were observable in the SAXS pattern. By limiting the x-ray dose, we were successful in measuring the static critical behavior of the polymer mixtures. A crossover from mean-field to Ising critical behavior was observed. A limited set of measurements was also carried out on the critical dynamics of the polymer mixtures.

Last, but by no means least, before any of these experiments could be conducted, it was necessary to build the coherent SAXS setup with which to make the measurements. The x-ray experiments I am reporting on here were conducted at the insertion device beam line operated by the University of Michigan, Howard University and Lucent Technologies (Formerly AT&T Bell Laboratories) joint Collaborative Access Team (MHATT-CAT) at the APS. The MHATT-CAT facility was under construction when I began my thesis work and I participated in some aspects of its completion, including pulling and terminating miles of cables and helping with the installation of

some beamline components, such as the High Heat Load Monochromator. This was in addition to taking the primary role in the major task of building the coherent SAXS setup from scratch.

To conclude this Introduction, here is a brief outline of the rest of the thesis. Chapter 2 contains a general introduction to the technique of XPCS. Chapter 3 discusses the critical behavior of binary mixtures. Chapter 4 contains a detailed description of the Small Angle X-ray Scattering (SAXS) setup used in the experiments. Chapter 5 presents results on the studies of the simple binary liquid mixture hexane/nitrobenzene. Chapter 6 presents the results of a study of x-ray radiation damage effects seen in binary polymer mixtures of polystyrene and polybutadiene. Chapter 7 presents the results of studies of the static and dynamic critical behavior of the polystyrene/polybutadiene mixtures. Finally, Chapter 8 presents the conclusions of the thesis.

CHAPTER 2.
X-RAY PHOTON CORRELATION SPECTROSCOPY

Introduction

Photon Correlation Spectroscopy probes the dynamics of a material by analyzing the temporal correlations among photons scattered by the material. Although this statement seems entirely plausible, it leaves several questions unanswered. What is the precise relationship between the dynamics of a material and the temporal correlations among the scattered photons? What characteristics of the dynamics are revealed by PCS? What experimental factors are important in conducting a PCS experiment and what are their consequences? This chapter presents answers to these questions. After this introduction, it reviews the basic statistical concepts at the foundation of an understanding of the analysis of PCS data. It then discusses the application of these concepts to the statistics of photon detection events and intensity fluctuations. Next, a number of factors which affect the quality of PCS data are considered, including having a finite detector area, finite sample times, multiple sample times, noise sources and normalization schemes, and non-zero detector dead time. This is followed by a calculation of the autocorrelation function for Brownian motion as an example application of XPCS. Finally, the range of opportunities for scientific studies using XPCS is discussed.

Gopalsamudram Ramachandra of the Indian Institute of Science in Bangalore introduced the basic principle of PCS in 1943[27,28]. Ramachandra studied the random diffraction patterns, now called “speckle”, that formed when coherent light from a filtered mercury arc source was shone on pollen grains that were dusted onto a glass slide. In a remark attributed to his colleague Chandrasekhara Raman, Ramachandra noted that the speckle pattern would fluctuate in time if the grains were to move. Thus, for example, the Brownian motion of particles suspended in a liquid could be studied by analyzing the fluctuations in scattered coherent light. Raman subsequently observed by eye fluctuations in mercury arc light scattered by a thin film of milk[29]. Hariharah[30] has given a survey of the history of speckle patterns, which dates back to the 19th century.

This idea remained an almost forgotten curiosity until an intense source of coherent light – the laser – was invented in the early 1960s. PCS then progressed rapidly[31], and groups led by George Benedek at MIT and Herman Cummins at Columbia performed pioneering PCS measurements of Brownian motion of latex colloids[32], concentration fluctuations in a critical binary fluid mixture[33], and entropy fluctuations of a pure fluid near its gas-liquid critical point[34] and of a normal fluid[35]. Around this time Theodore Forrester[36] advanced an alternative explanation of PCS in terms of beating at the detector between different frequency components of the optical spectrum. The beating occurs because photon detectors respond to intensity, and hence are square law detectors of electromagnetic amplitude. Although expressed in different terms, Forrester’s theory is equivalent to Raman’s fluctuating speckle picture.

Since these early experiments, PCS using visible light has become an indispensable technique and found wide application in studies of the physics, chemistry,

and materials science of soft condensed matter systems[1]. However it has a number of important limitations. First, it can only be applied to optically transparent materials. Although the recently developed technique of Diffusing Wave Spectroscopy[37] can be used to study strongly multiply scattering materials, nevertheless it can only be applied to studies of materials for which the absorption length is small but still much larger than the wavelength of light and cannot be applied to truly opaque materials such as metallic solids. Secondly, since visible light couples primarily to the polarization fluctuations in a material, it cannot be used to study optically isotropic fluctuations, such as, to give just one example, bond orientational fluctuations in hexatic B liquid crystals[38]. In this latter case, the dynamics of bond orientational fluctuations in the hexatic phase have only been able to be studied with visible PCS in tilted hexatic phases, where the bond orientational order couples to the optically anisotropic molecular tilt field[39,40,41]. Finally, and most importantly, visible PCS can only probe long wavelength excitations, i.e., those having wave vectors less than about 4×10^{-3} $Å^{-1}$, due to the roughly 0.5 μm wavelength of visible light. So, researchers interested in probing dynamics on shorter length scales or in opaque systems are exploring the use of coherent x-rays produced by synchrotron sources in XPCS measurements. Although these x-ray sources are not intrinsically coherent, they can now be produced at such high intensities, as discussed in Chapter 1, that the filtering needed to produce a coherent beam leaves enough photons to perform useful dynamic scattering experiments.

Fluctuations of the intensity of scattered light can be caused by a number of reasons. Perhaps the most straightforward example is fluctuations caused by a fluctuating number of scattering centers in the scattering volume, which is the region in space

defined by the field of view of the detector, the dimensions of the incident beam and the sample dimensions. Scattering of a narrow beam of sunlight from dust particles floating in air is the most familiar example. The intensity detected by a detector, placed outside of the main beam, will fluctuate as particles move in and out of the scattering volume. Information on the motions of the particles can be obtained by analysis of these fluctuations. It is noteworthy that number density fluctuations do not require the incident light to be coherent, as the intensity fluctuations do not occur as a result of any interference effects. The amplitude of these "number density" fluctuations is of order one over the square root of the number of particles in the scattering volume. It can be an important effect in special circumstances, such as scattering from low density colloids[42]. However, it is usually insignificant in most materials, since, at typical liquid or solid densities, even a $(1\ \mu m)^3$ scattering volume contains of order 10^{10} molecules.

When a coherent source is used in a scattering experiment, fluctuations in the scattered radiation can also appear due to interference between the electromagnetic waves emanating from different scattering centers. For example, radiation transmitted through a small hole made in an opaque screen, when illuminated by coherent light, forms a familiar Fraunhoffer diffraction pattern in the far field. If a second hole is made, a more complicated, but still regular pattern of rings and fringes is formed. If more holes are punched in random positions, the pattern becomes increasingly random, tending towards a "speckle" pattern of randomly placed bright and dark areas of different intensities. An example of a speckle pattern is shown in Figure 2.1(b).

If the scattering centers are moving randomly, for example by diffusion, as in Brownian motion, or changing size, as in a medium with a fluctuating composition,

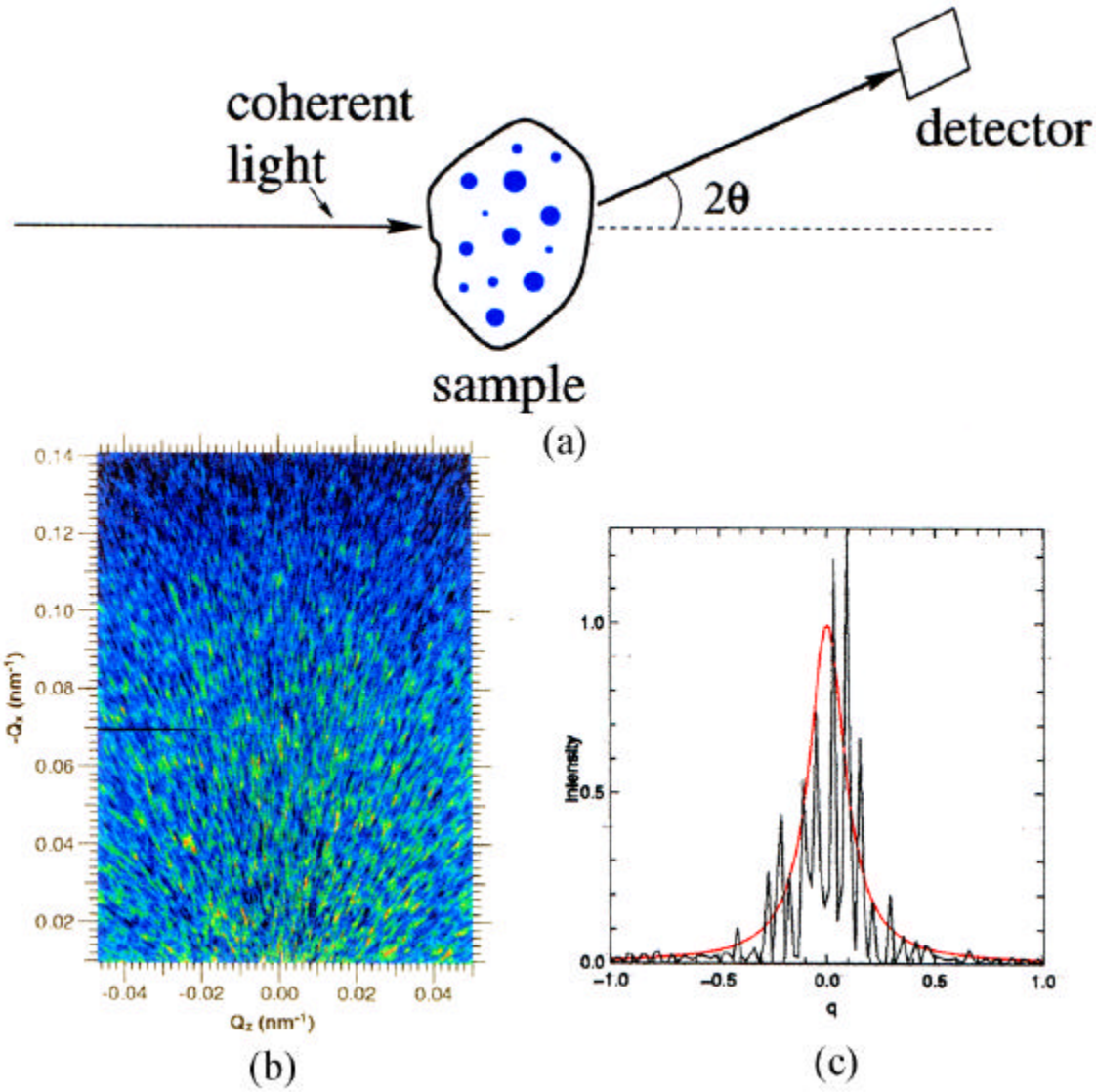

Figure 2.1. (a) Schematic of a detector measuring the coherent light scattered by a random sample. (b) A typical speckle pattern. In this example, the intensity is greatest at small scattering angles (near the bottom center). (c) One dimensional scans through a scattering peak illuminated with coherent light, and hence speckled (sharply modulated curve) and illuminated with incoherent light, and hence not speckled (smooth curve).

instead of being stationary, then at any instant we will see a particular speckle pattern in the far field. As the scattering centers change their positions or sizes at random, different

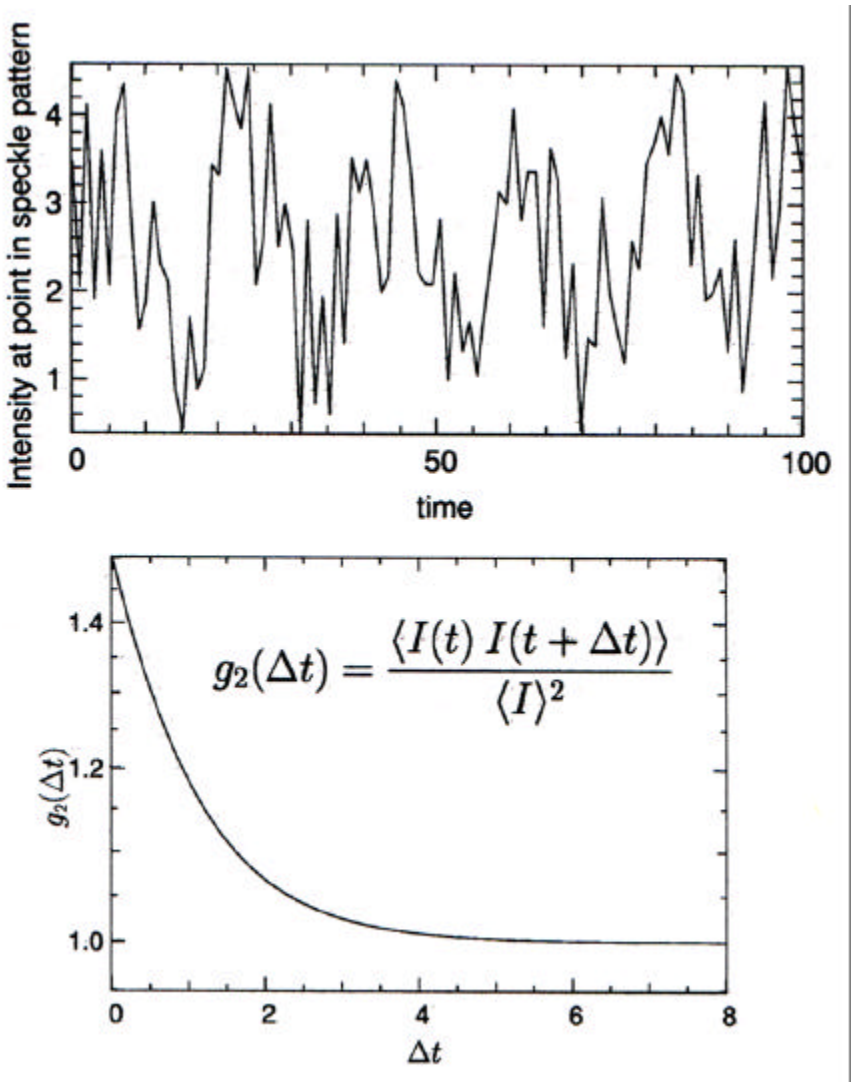

Figure 2.2. Top: Changes in arrangement of sample domains causes speckle pattern to fluctuate in time. Bottom: Time autocorrelation function of intensity gives information on equilibrium dynamics.

phase relations will form between fields scattered by different centers, and the speckle pattern will fluctuate in time. A small detector placed in the far field, as in Fig. 2.1(a), will register a fluctuating intensity whose time dependence contains information on the motion of the scatterers, as shown in the top of Fig. 2.2.

The basic idea of PCS is to detect a speckle at a given position in the far field, at a certain time t_0 and correlate it's detection with all consecutive detections of a speckle at the same spatial region after a specified delay time t. The time autocorrelation function of the fluctuating intensity, shown in the bottom of Fig. 2.2, is equivalent to the frequency Fourier transform of the usual dynamic structure factor, as shown later in this Chapter. The speckles can be a result of coherent beam scattering from any non-uniformity in the sample. In the case of critical dynamics of a binary mixture, it is a result of scattering from the concentration fluctuations in the mixture and the time autocorrelation function measures the relaxation time for concentration fluctuations at a particular wave vector to relax via diffusion. The critical behavior of binary mixtures is reviewed in Chapter 3.

If the scatterers are static, or sufficiently slowly varying, then a scan of a detector, whose acceptance is small compared to a speckle, through the speckle pattern will give a randomly varying intensity profile, as shown by the sharply modulated curve in Fig. 2.1(c). If the incident beam is perfectly coherent, then the contrast, or variation in intensity between maximum and minimum, will be 100% as the interference varies between completely constructive to completely destructive.

In a very real sense, a speckle pattern represents the magnitude of the *exact* spatial Fourier transform of the scattering density at a given instant in time[43]. This is quite different than the usual situation, in which the incident beam has only partial, or essentially no, coherence. In that case, the scattering profile will be smoothly varying, as shown by the smooth curve in Fig. 2.1(c), and reflects the magnitude of the Fourier transform of the scattering density spatial *autocorrelation* function, rather than of the

spatial variation in the scattering density itself. In effect, there is insufficient wave vector resolution to resolve the speckles and so the profile is determined by the ensemble averaged structure rather than any particular exact arrangement. This is consistent with the fact that the degree of coherence required to resolve the speckle pattern is proportional to the size of the scattering volume, as we shall now discuss.

Coherence of the x-ray beam is a necessary condition for detection of speckle. However perfect coherence is only attained with a perfectly monochromatic plane wave. Real sources of electromagnetic waves, which include synchrotrons, are only partially coherent. Two coherence lengths, transverse and longitudinal to the beam propagation direction, as shown in Figure 2.3, describe the coherence of a beam of radiation. The transverse coherence length, l_t, measures the "spatial" coherence perpendicular to the beam and is given by $l_t \sim R_s \lambda / 2d$, where R_s is the distance from the source, λ is the average wavelength of the radiation and d is the size of the source. As shown in Figure 2.3(a), this can be understood as the requirement that no two waves contributing to the radiation differ in phase by more than $\pi/2$ in the transverse direction. A transversely coherent portion of a beam can be selected by collimating the beam with a small pinhole whose size is given by l_t. The longitudinal coherence length, l_l, measures the "temporal" coherence parallel to the beam and is given by $l_l \sim \lambda(\lambda/\Delta\lambda)$, where $\Delta\lambda$ is the spread of wavelengths (bandwidth). As shown in Figure 2.3(b), this corresponds to the requirement that no two waves contributing to the radiation differ by more than $\pi/2$ in the longitudinal, or propagation, direction. l_l can be increased by monochromating the radiation to reduce $\Delta\lambda$.

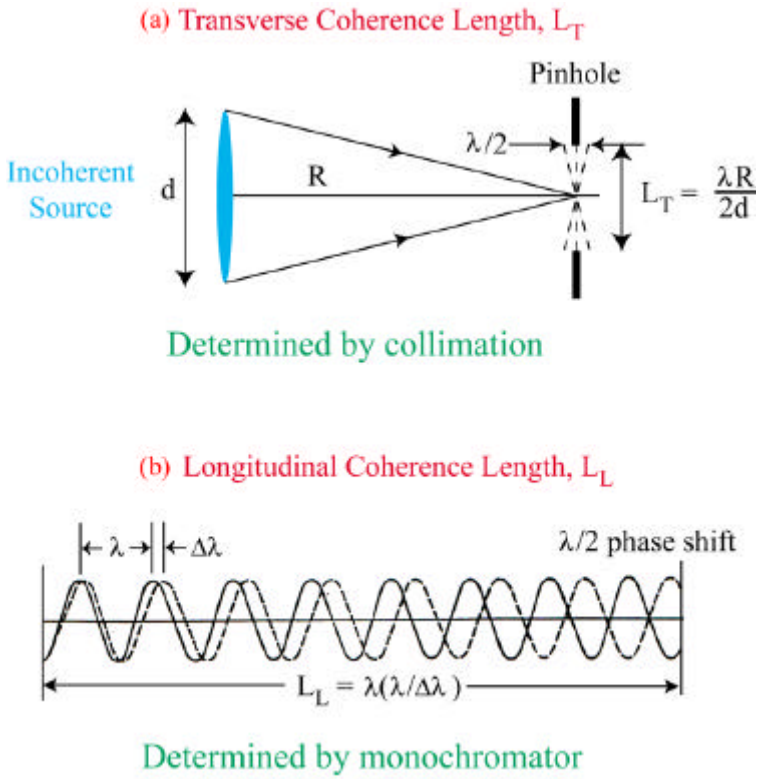

Figure 2.3. (a) The transverse coherence length is determined by how collimated a beam is. (b) The longitudinal coherence length is determined by how monochromatic a beam is.

A speckle pattern is observed if two conditions are met. First, the transverse coherence length must be greater than the *illuminated* transverse dimension of the sample, L_t, i.e., $l_t > L_t$. This requirement is straightforward and is automatically met by simply having a transversely coherent incident beam. Second, the maximum path length difference between radiation scattered from different parts of the sample must be smaller than l_l. This requirement is more complex as the maximum path length difference depends on the scattering angle, q, and the transverse and longitudinal dimensions of the sample, L_t and L_l. The maximum path length difference has two contributions, one from the transverse dimension of the sample, which is given by $L_t sinq$, and one from the

longitudinal dimension of the sample, which is given by $2L_l sin^2(q/2)$. The longitudinal coherence length must be larger than the larger of these two contributions. If these coherence criteria are met, there will be sufficient resolution to resolve the speckle pattern. Otherwise, the scattered radiation will consist of many uncorrelated independent speckle patterns and the amplitude of the intensity variations will be reduced and ultimately vanish.

Note that at small scattering angles the maximum path length, and hence the necessary longitudinal coherence length, can be much smaller than the sample dimensions. Since the longitudinal coherence length is inversely proportional to the x-ray bandwidth, this means that a significantly greater bandwidth of x-rays, with a proportionately greater flux, can be used in small angle coherent scattering experiments. As pointed out in Chapter 1, this fact has been taken advantage of in most XPCS experiments reported to date. The experiments on the hexane/nitrobenzene binary fluid mixture described in Chapter 5 also used this feature. However, as described in Chapters 6 and 7, the polystyrene/polybutadiene polymer mixture proved to be too sensitive to x-ray radiation damage to benefit from this approach. Consequently, a more monochromatic beam than was strictly necessary for the purpose of longitudinal coherence, with a correspondingly reduced flux, had to be used. This made the XPCS experiments on the polymer mixtures much more difficult.

Statistical concepts

The basic concepts of the statistics of stochastic processes necessary to understand the interpretation of PCS data are reviewed in this section. For more thorough

treatments of the relevant problems in statistics, many excellent books are available[44,45,46,47].

Photon counting is the process of recording the number of detected photons in regularly spaced time intervals. The number of photons, *n*, detected during a particular sampling time interval is called a sample. These samples are classic examples of random variables.

The random character of photon detection prevents an accurate prediction of the count *n* in a given sample interval. The most complete knowledge that can be obtained about *n* is a specification of all the probabilities P_n, for non-negative, integer values of *n*, where P_n is the probability to detect a certain *n*. P_n represents a fraction of a very large number of samples that yields the particular *n*. This idea of having a large number of samples leads to the statistical concept of an ensemble: a very large number of repetitions of one experiment. By making a size of this ensemble large enough it is in principle possible to define P_n to any desired accuracy. Obvious properties of the probabilities P_n are their non-negativity and the fact that they sum to 1.

A good example of a distribution of probabilities P_n is the well known Poisson distribution. It is a distribution with a single parameter m:

$$P_n = m^n \exp(-m)/n! \qquad \textbf{(2.1)}$$

For values of m less than 1, the P_n decrease monotonically with increasing *n*; for larger values there is a single peak. This peak moves towards larger *n* with increasing m.

While a probability distribution is the most complete stochastic description of a discrete random variable, it is often possible to get by with much less information. As an example we may just want to know the intensity of the detected light, that is, the average

number of photons detected. The desired statistical average or mean count value may be obtained from the probability distribution as

$$\langle n \rangle = \sum_n n P_n \,, \tag{2.2}$$

where the summation runs over all non-negative values of *n*. For the Poisson distribution we obtain a mean of

$$\langle n \rangle = \sum_n n m^n \exp(-m)/n! = m \exp(-m) \sum_n m^{n-1}/(n-1)! = m \,, \tag{2.3}$$

which is identical to the distribution parameter *m*.

The mean is just a particularly simple example of what is called a moment of a distribution. The average or mean is the first moment. Higher moments are expectations of higher powers of the random variable,

$$\langle n^k \rangle = \sum_n n^k P_n \,. \tag{2.4}$$

For discrete random variables, the alternative concept of factorial moments,

$$F_n^{(k)} = \langle n(n-1)(n-2)\ldots(n-k+1) \rangle = \sum_{n \geq k} n! P_n/(n-k)!, \tag{2.5}$$

will often be more useful. If *n* varies only over some finite range, say $n < m$, all factorial moments of order *m* and higher vanish.

For example, the Poisson distribution has a very simple expression for the factorial moments:

$$F_n^{(k)} = \langle n(n-1)(n-2)\ldots(n-k+1) \rangle = \langle n \rangle^k = m^k \,. \tag{2.6}$$

We shall use this expression later to connect moments of the underlying classical intensity distribution.

A few useful relations follow from factorial moments. From the second factorial moment

$$F_n^{(2)} = \langle n(n-1) \rangle = \langle n^2 \rangle - \langle n \rangle = m^2 \qquad \textbf{(2.7)}$$

we may quickly calculate the ordinary second moment of a Poisson distribution:

$$\langle n^2 \rangle = m^2 + m\,, \qquad \textbf{(2.8)}$$

or it's central second moment, the variance:

$$\mathrm{Var}(n) = s_n^2 = \langle n^2 \rangle - \langle n \rangle^2 = \left\langle \left(n - \langle n \rangle \right)^2 \right\rangle = m\,. \qquad \textbf{(2.9)}$$

The square root of the variance is a common measure of the width of a distribution, called its standard deviation, s_n.

Let's consider two random variables, say the photon counts n_1 and n_2 obtained in two different sample time intervals. For such a pair of random variables it is generally no longer sufficient to know their two individual probability distributions. Instead we must use the joint probability distribution, $P(n_1,n_2)$, which gives the probability that one experiment yields both count values, n_1 and n_2.

If n_1 and n_2 are measured in non-overlapping sample time intervals, the two counts will typically be independent from one another. This physical independence implies statistical independence, or the factorization of the joint probability distribution into the product of a distribution of n_1 that does not depend on n_2, and a distribution of n_2 that does not depend on n_1. As an immediate consequence, mixed moments may be reduced to simple moments such as

$$\langle n_1^k n_2^m \rangle = \langle n_1^k \rangle \langle n_2^m \rangle\,. \qquad \textbf{(2.10)}$$

For overlapping sample time intervals, on the other hand, we certainly expect statistical dependence between the counts n_1 and n_2. In this case, the joint probability distribution will not factorize and mixed moments may not be reduced as in Equation (2.10). If we consider n_2 to be fixed at a certain value, we obtain a conditional distribution, $P(n_1 \mid n_2)$, the probability of n_1 given n_2 or conditional moments such as

$$\left\langle n_1^k \,\middle|\, n_2 \right\rangle = \sum n_1^k P(n_1 \mid n_2). \tag{2.11}$$

If on the other hand we consider an average over n_2, we obtain the marginal distribution:

$$P(n_1) = \sum P(n_1, n_2)\,. \tag{2.12}$$

If marginal and conditional distributions are known, we can reconstruct the joint probability distribution from

$$P(n_1, n_2) = P(n_1 \mid n_2)P(n_2) = P(n_2 \mid n_1)P(n_1)\,. \tag{2.13}$$

Generalization to more than two random variables is straightforward.

If we look at moments of a joint distribution, statistical dependence typically shows up in the second central mixed moment known as the covariance:

$$\mathrm{Cov}(n_1, n_2) = \left\langle n_1 n_2 \right\rangle - \left\langle n_1 \right\rangle \left\langle n_2 \right\rangle. \tag{2.14}$$

If the covariance does not vanish, there must be statistical dependence between the two random variables n_1 and n_2. The converse is not true in general. Random variables may be statistically dependent and still possess zero covariance.

If the covariance is normalized by the variances of n_1 and n_2, we obtain the correlation coefficient:

$$\mathrm{Cov}(n_1, n_2) / \sqrt{\mathrm{Var}(n_1)\,\mathrm{Var}(n_2)}\,. \qquad \textbf{(2.15)}$$

Correlation coefficients are limited to the interval [-1,1] and vanish for independent random variables.

If we consider two time intervals to be adjacent time intervals, the sum

$$n = n_1 + n_2 \qquad \textbf{(2.16)}$$

would yield the number of photon detection events for the longer time interval obtained by joining the two original intervals. How can we calculate the distribution of the new count n from given distributions of n_1 and n_2? The most elegant solution to this problem involves the use of moment-generating functions[48].

Just as there are several varieties of moments, there are also different kinds of moment-generating functions, for example the one related to factorial moments, the factorial moment-generating function:

$$Q_f(s) = \left\langle s^n \right\rangle = \sum_n s^n P_n\,. \qquad \textbf{(2.17)}$$

This function indeed generates factorial moments by repetitive differentiation and setting $s = 1$:

$$d^k Q_f(s) \Big/ ds^k \,|_{s=1} = \left\langle n(n-1)\ldots(n-k+1)s^{n-k} \right\rangle = F_n^{(k)}\,, \qquad \textbf{(2.18)}$$

and sometimes this scheme provides a simpler route to the factorial moments than does the direct summation approach.

Since the factorial moment-generating function is defined as an expectation, there is no difficulty in relating $Q_f(s)$ to the distribution of initial random variables n_1 and n_2:

$$Q_f(s) = \left\langle s^n \right\rangle = \left\langle s^{n_1+n_2} \right\rangle = \sum_{n_1} \sum_{n_2} s^{n_1+n_2} P(n_1, n_2). \quad \textbf{(2.19)}$$

For statistically independent n_1 and n_2, this expectation factorizes into the two factorial moment-generating functions of these two random variables:

$$Q_f(s) = \left\langle s^{n_1} \right\rangle \left\langle s^{n_2} \right\rangle. \quad \textbf{(2.20)}$$

This scheme may be generalized to sums of more than two random variables. If all the summed variables are statistically independent of each other, the factorial moment-generating function of their sums equals the product of all their factorial moment-generating functions. If, as is often the case, the summed variables all follow an identical distribution, the product of their factorial moment-generating functions is merely a power of one variable's factorial moment-generating function.

Let us now return to our example, the Poisson distribution. Its factorial moment-generating function reads

$$Q_f(s) = \sum_n s^n P_n = \sum_n s^n m^n \exp(-m)/n! = \exp(ms)\exp(-m) = \exp[m(s-1)] \quad \textbf{(2.21)}$$

Adding two statistically independent Poisson variables n_1 and n_2 with distribution parameters m_1 and m_2, we obtain the factorial moment-generating function for the sum variable n:

$$Q_f(s) = \exp[m_1(s-1)]\exp[m_2(s-1)] = \exp[(m_1+m_2)(s-1)] \quad \textbf{(2.22)}$$

Comparison with Equation (2.21) shows that n is just another Poisson random variable with distribution parameter

$$m = m_1 + m_2 \,. \tag{2.23}$$

Generally, any sum of independent Poisson variables will result in another Poisson variable, a feature closely related to the fundamental importance of the Poisson distribution.

Having looked at a pair of adjacent photon counting samples we now proceed to a continuous train of such samples n_j. The integer index j refers to a particular sampling interval. The typical sampling arrangement is such that all sampling intervals are equally spaced, and the interval j immediately follows its predecessor $j - 1$.

Such an ordered sequence of random variables n_j is known as a stochastic process. A full specification of such a process requires the joint distribution of all the n_j. This specification may be greatly simplified by symmetries. Many stochastic processes possess a translational symmetry: the joint distribution of any n_j, n_k, … n_m does not depend on the particular value of the indices, as long as all their differences k-j, …, m-j remain constant. This important property defines a stationary stochastic process. Stationarity is typically a direct consequence of time invariance in a physical system.

For a stationary stochastic process there is only one single-point distribution, $P(n_j)$, independent of j. However, there are still many double-point distributions $P(n_j,n_{j+k})$, one for each positive value of k. Negative values of k do not require new joint distributions, because the obvious symmetry of joint distributions and stationarity lead to

$$P(n_j, n_{j-k}) = P(n_{j-k}, n_j) = P(n_j, n_{j+k}) \,. \tag{2.24}$$

In practice it is often difficult to determine joint distributions, and we restrict our attention to moments. The lowest-order two-point moment,

$$G_n(k) = \langle n_j n_{j+k} \rangle = \langle n_j n_{j-k} \rangle, \quad \textbf{(2.25)}$$

is known as the autocorrelation of the stochastic process. For this definition to be meaningful, the expectation on the right-hand side must not depend on *j*. This is satisfied for any stationary process. Since all of the processes studied in this thesis are stationary, non-stationary processes will not be considered further.

Autocorrelations are always bounded between $-\langle n_j^2 \rangle$ and $\langle n_j^2 \rangle$. They will attain their maximum $\langle n_j^2 \rangle$ at $k = 0$. If the n_j are never negative, as in photon counting, the autocorrelation must also be non-negative. For most stochastic processes, n_j and n_{j+k} approach statistical independence for large values of *k*. Consequently the autocorrelation will approach $\langle n_j \rangle^2$ for large values of *k*. This asymptotic value of the autocorrelation is often denoted as its baseline.

If the shape rather than the absolute magnitude of an autocorrelation is of interest, normalized autocorrelations are commonly used. Two possible definitions are

$$g_n(k) = \frac{[G_n(k) - \langle n_j \rangle^2]}{\langle n_j \rangle^2}, \quad \textbf{(2.26)}$$

and

$$c_n(k) = \frac{[G_n(k) - \langle n_j \rangle^2]}{\langle n_j^2 \rangle}, \quad \textbf{(2.27)}$$

where in both cases we subtracted the baseline and then divided by the square of the mean or the variance n_j, respectively.

The first definition is more common in photon counting. For $k = 0$, $g_n(k)$ equals the relative variance of n_j.

The definition of $c_n(k)$ parallels that of the correlation coefficient; it starts at 1 for $k = 0$ and is limited to values between –1 and +1. Just like the correlation coefficient, this normalized autocorrelation is a measure of similarity between two random variables, in this case of self-similarity of the stochastic process with a time-displacement version of itself.

Both normalized autocorrelations typically decay to zero for large values of k, corresponding to large temporal displacements or large delay times, τ, sometimes called lag times:

$$t = k\Delta t\,, \tag{2.28}$$

where Δt denotes the sampling time.

As an alternative to autocorrelations a stochastic process may also be characterized in frequency space. For any finite sequence of n_j, $j = 0, 1, \ldots, M\text{-}1$, we can define a discrete Fourier transform:

$$F_n^{(M)}(m) = \sum_{j=0}^{M-1} n_j \exp(-2p \cdot i \cdot j \cdot m/M)\,, \tag{2.29}$$

a Fourier representation equivalent to the original process. Taking the ensemble average of the absolute square of this Fourier transform, we obtain the discrete power spectrum:

$$P_n^{(M)}(m) = \left\langle \left| F_n^{(M)}(m) \right|^2 \right\rangle. \tag{2.30}$$

For infinite processes we use the same approach and consider the limit $M \to$. In this limit, our discrete frequency m is better replaced by a continuous frequency $f = m/(M\Delta t)$, that is, we consider the limit where both M and m go to infinity at fixed frequency f.

Unfortunately the power spectrum $P_n^{(M)}(m)$ typically diverges in this limit, being of order M (or even of order M^2 for some m, if n_j contains strictly periodic components with frequency m/M). Hence we introduce the concept of power spectral density:

$$S_n(f) = \lim_{M\to\infty}\left\langle (1/M)\left|F_n^{(M)}(M\Delta t\cdot f)\right|^2\right\rangle. \qquad \textbf{(2.31)}$$

This power spectral density is well defined for stationary random process, if we allow d-function components in $S_n(f)$ to represent finite periodic components in the process n_j.

In order to connect time and frequency space, consider the inverse discrete Fourier transform of the power spectral density before going to the limit $M \to$ for some k between 0 and M-1:

$$(1/M)\sum_{m=0}^{M-1}\left\langle (1/M)\left|F_n^{(M)}(m)\right|^2\right\rangle \exp(2p\cdot ikm/M)$$

$$= M^{-2}\sum_{m=0}^{M-1}\sum_{j=0}^{M-1}\sum_{l=0}^{M-1}\left\langle n_j n_l\right\rangle \exp[2p\cdot i(k-j+l)m/M]$$

$$= M^{-2}\sum_{j=0}^{M-1}\sum_{l=0}^{M-1}\left\langle n_j n_l\right\rangle Md_{k-j+l} = M^{-1}\sum_{j=k}^{M-1}\left\langle n_j n_{j-k}\right\rangle$$

$$= \left\langle n_j n_{j-k}\right\rangle (M-k)/M = G_n(k)(1-k/M). \qquad \textbf{(2.32)}$$

In the limit $M \to$ m by integration over $M\Delta t\mathrm{d}f$ and obtain the famous theorem of Wiener and Khintchine:

$$G_n(k) = \Delta t \int S_n(f) \exp(2p \cdot ik\Delta tf)\, \mathrm{d}f \,. \qquad \textbf{(2.33)}$$

For finite *M*, the triangular weight factor (1-*k*/*M*) in general may not be neglected. This feature is important for the correct evaluation of a digital Fourier transform.

Equation (2.33) may be inverted to yield

$$S_n(f) = \sum_k G_n(k) \exp(-2p \cdot ik\Delta tf) \qquad \textbf{(2.34)}$$

Most concepts introduced for discrete random variables are easily carried over to continuous variables. The probability distribution is replaced by a probability density $p_x(x)$, where $p_x(x)dx$ denotes the probability of obtaining a sample in the range $[x,x+dx]$. If $y = f(x)$ is a monotonic differentiable function, the probability density of y is most easily obtained by equalizing the two probabilities:

$$p_x(x)dx = p_y(y)|dy| \qquad \textbf{(2.35)}$$

with the implication that

$$p_y(y)|dx/dy| = p_x[f^{-1}(y)]/|f'[f^{-1}(y)]| \,. \qquad \textbf{(2.36)}$$

The calculation of moments (as well as other expectation values) requires integration over the probability density. As an example we introduce the moment-generating function

$$q_x(s) = \langle \exp(-sx) \rangle = \int \exp(-sx)\, p(x)dx \,, \qquad \textbf{(2.37)}$$

the Laplace transform of the probability density. Setting $s = iw$, we obtain the Fourier transform or characteristic function. Moments may be generated by differentiation:

$$\langle x^m \rangle = \int x^m p_x(x)dx$$

$$= \int (-1)^m [d^m xp(-sx)/ds^m]|_{s=0} p_x(x)dx = (-1)^m d^m q_x(s)/ds^m|_{s=0}. \quad \textbf{(2.38)}$$

Again, generating functions are most useful if we have to compute a sum of independent random variables such as

$$x = \sum_{j=1}^{N} x_j \ . \quad \textbf{(2.39)}$$

If we assume identical distributions with mean 0 and variance s^2/N for all the x_j, the generating function for x is obtained as

$$q_x(s) = \langle \exp(-sx) \rangle = \left\langle \exp(-s\sum_{j=1}^{N} x_j \right\rangle = \langle \exp(-sx_j) \rangle^N , \quad \textbf{(2.40)}$$

the N^{th} power of the generating function of the x_j. In order to pass to the limit of infinite N, we expand the exponential,

$$q_x(s) = \left[1 - s\langle x_j \rangle + s^2 \langle x_j^2 \rangle / 2! - \cdots\right]^N \approx \left[1 + s^2 s^{\,2}/2N\right]^N$$

$$\xrightarrow[N\to\infty]{} \exp(s^2 s^{\,2}/2) \quad \textbf{(2.41)}$$

and obtain a generating function for x that is independent of higher order moments or details of the probability density of the x_j. This remarkable behavior of sums of (reasonably well-behaved) independent random variables is known as the central limit theorem. Inverse Laplace transformation (or, rather, inverse Fourier transformation after setting s = iw) leads to the probability density

$$p_x(x) = \exp(-x^2/2s^{\,2})/(2ps^{\,2})^{1/2}, \quad \textbf{(2.42)}$$

the well known Gaussian or normal density.

Gaussian statistics is frequently encountered when considering x-ray scattering by physically independent particles. If the particles are illuminated by a coherent source and we detect scattered x-rays with a small detector in the far field, the electromagnetic field

amplitude at the detector is typically a sum over many single-particle contributions. Hence we can immediately predict Gaussian statistics for the amplitude at the detector. Electromagnetic amplitudes are commonly expressed in complex notation, and in fact we obtain independent Gaussian probability densities for the real and imaginary parts of the complex amplitude *u*:

$$p_u(u) = \exp(-|u|^2 / 2\sigma^2)/(2\pi\sigma^2). \quad \textbf{(2.43)}$$

Associated with any complex amplitude are intensity *I* and phase ϕ with

$$u = I^{1/2}\exp(i\phi). \quad \textbf{(2.44)}$$

This case constitutes an example for the transformation of multiple random variables, here the real and imaginary parts of *u* and our new *I* and ϕ. The scheme is a straightforward generalization of that already introduced for single variables. We merely have to replace the derivative by the Jacobian. Hence we need the derivatives

$$\partial\,\mathrm{Re}(u)/\partial I = \partial(I^{1/2}\cos\phi)/\partial I = I^{-1/2}\cos\phi/2 \quad \textbf{(2.45)}$$

$$\partial\,\mathrm{Im}(u)/\partial I = \partial(I^{1/2}\sin\phi)/\partial I = I^{-1/2}\sin\phi/2, \quad \textbf{(2.46)}$$

$$\partial\,\mathrm{Re}(u)/\partial\phi = \partial(I^{1/2}\cos\phi)/\partial\phi = -I^{1/2}\sin\phi, \quad \textbf{(2.47)}$$

$$\partial\,\mathrm{Im}(u)/\partial\phi = \partial(I^{1/2}\sin\phi)/\partial\phi = I^{1/2}\cos\phi, \quad \textbf{(2.48)}$$

which lead to a Jacobian $\cos^2\phi/2 + \sin^2\phi/2 = \frac{1}{2}$. The final joint probability density for intensity and phase reads

$$p(I,\phi) = \exp(-I/2\sigma^2)/(2\sigma^2\cdot 2\pi), \quad \textbf{(2.49)}$$

and factorizes into a negative exponential density for *I*,

$$p(I) = \exp(-I/2\sigma^2)/(2\sigma^2), \quad \textbf{(2.50)}$$

and a uniform density,

$$p(f) = 1/2p \ , \tag{2.51}$$

for the phase f over the interval [0, 2π]. This factorization implies statistical independence of phase and intensity.

A more general class of intensity distributions is generated if we consider a detector with a finite area, not necessarily small compared with one coherence area of the source at the detector plane. This rather common case is most easily modeled by assuming the detector looks at several, say α, independent speckles, that is, mutually incoherent patches of light. In this case we have to add several independent intensities with negative exponential probability densities:

$$I = \sum_{j=1}^{a} I_j \ . \tag{2.52}$$

The generating function for negative exponential I_j with expectations m is quickly computed as

$$\left\langle \exp(-sI_j) \right\rangle = \int_0^\infty \exp(-sI_j) \exp(-I_j/m)\, \mathrm{d}\, I_j/m = (1+ms)^{-1}. \tag{2.53}$$

Hence the generating function for the sum intensity reads

$$q(s) = \left\langle \exp(-sI) \right\rangle = (1+ms)^{-a} \ , \tag{2.54}$$

which corresponds to the probability density

$$p(I) = (I/m)^{a-1} \exp(-I/m)/[m\Gamma(a)] \, . \tag{2.55}$$

where $\Gamma(a)$ denotes the gamma function; for integer a it may be replaced with the factorial [$(a$+1)!]. The probability density in Equation (2.55) is known as the gamma distribution. It is closely related to the c^2 distribution, where $2a$ is known as the number of degrees of freedom.

Although we proved above that almost any sum of many independent random variables finally obeys the central limit theorem, apparently we now have found a counterexample. No matter how many intensities I_j we add, the resulting sum will always remain gamma-distributed. However, the solution to this dilemma is easily found: for large values of α it becomes increasingly difficult to tell a gamma density from Gaussian with identical mean αm and second moment $\alpha(\alpha+1)m^2$ or variance αm^2.

We keep in mind that gamma distributions are useful models for partially coherent light. For $\alpha = 1$ we obtain the limit of perfect spatial coherence, and negative exponential probability density for the intensity. With increasing α, we lose spatial coherence, finally approaching Gaussian intensity statistics.

Returning to the autocorrelation, we now express it as a function of a continuous time lag t:

$$G_u(t) = \langle u(t')u^*(t'+t)\rangle, \tag{2.56}$$

where we immediately consider the case of a complex stochastic process, of obvious relevance for complex electromagnetic amplitudes. The asterisk denotes complex conjugation.

The power spectral density $S(f)$ is defined as a limiting value of the finite-time continuous Fourier transform,

$$F_u^{(T)}(f) = \int_{-T/2}^{T/2} u(t')\exp(-2\pi i f t')\,dt', \tag{2.57}$$

$$S_u(f) = \lim_{T\to\infty} \left|F_u^{(T)}(f)\right|^2 / T, \tag{2.58}$$

where T is the duration of the observations. The Wiener-Khintchine relation now reads

$$G_u(t) = \int S_u(f) \exp(2p \text{ i } ft) \, \mathrm{d} f \, . \qquad \textbf{(2.59)}$$

We illustrate these concepts by two examples of particular relevance to the dynamics of condensed matter systems. Our first example involves a real periodic signal

$$x(t') = a + b \sin(\Omega t' + \Phi) \, , \qquad \textbf{(2.60)}$$

where Φ is random over the interval $[0, 2\pi]$ (but fixed for any particular realization of our stochastic process). This form is characteristic of an *undamped oscillatory* excitation. We easily compute an autocorrelation

$$G_x(t) = a^2 + (b^2 / 2) \cos(\Omega t) \, , \qquad \textbf{(2.61)}$$

which we see is also oscillatory; and a power spectral density

$$S_x(f) = a^2 d(f) + (b^2 / 2) d(f - \Omega / 2p) + (b^2 / 2) d(f + \Omega / 2p) \qquad \textbf{(2.62)}$$

which has delta functions at plus and minus the oscillation frequency.

Our second example is a simple model of an *overdamped* process, which is commonly referred to as a relaxation process. Again we assume a real process $x(t')$, but now given as a sum over randomly timed negative exponentials,

$$x(t') = m \sum_m \exp[-\Gamma(t' - t_m)] \Theta(t' - t_m) \, , \qquad \textbf{(2.63)}$$

where

$$\Theta(t') = 0 \text{ for t' } < 0, \qquad \textbf{(2.64)}$$

$$\Theta(t') = 1 \text{ for t'} \geq 0. \qquad \textbf{(2.65)}$$

The times t_m are assumed to be distributed uniformly and statistically independent with an average density of one per time T. Hence we obtain a mean

$$\langle x(t') \rangle = (m / T) \int_0^\infty \exp(-\Gamma t') \, \mathrm{d} t' = m / \Gamma T \qquad \textbf{(2.66)}$$

and a temporal autocorrelation

$$G_x(t) = (m/\Gamma T)^2 + (m/T)\int_0^\infty \exp[-\Gamma t' - \Gamma(t'+t)]\,\mathrm{d}t'$$

$$= (m/\Gamma T)^2 + (m^2/2\Gamma T)\exp(-\Gamma t)\,. \qquad \textbf{(2.67)}$$

We see that the autocorrelation of the overdamped relaxation process consists of an exponential decay, with a decay rate equal to the relaxation rate of the process. The power spectral density is

$$S_x(f) = (m/\Gamma T)^2 d(f) + (m^2/\Gamma T)2\Gamma/(\Gamma^2 + 4p^2 f^2)\,. \qquad \textbf{2.68)}$$

This is a lorentzian centered at zero frequency, with half width equal to the relaxation rate. In conventional condensed matter language, it is the central peak in the dynamic structure factor corresponding to an overdamped relaxation process. Exponential correlations corresponding to Lorentz-type spectra are particularly common in photon correlation measurements since many low frequency processes are overdamped, as discussed in the last section of this Chapter.

Photon statistics

After this review of the basic statistics, we are now in a position to describe its application to the statistics of photon detection. For simplicity we shall initially focus on an idealized single-photon, single channel detector with negligible afterpulses and dark count rate.

Even for illumination with x-rays of perfectly constant intensity, such an ideal detector would not give a regular train of detection pulses. Every individual photon detection event is essentially independent of all the others and we must expect completely

random pulse trains, that is, Poisson statistics for the number of photon detection pulses counted during some finite sample time interval Δt.

If I denotes intensity (expressed as the number of photons hitting the area of the detector in unit time) and q is the quantum efficiency of the detector, the mean number of detection pulses per sample time Δt is simply

$$\langle n \rangle = m = Iq\Delta t \,. \tag{2.69}$$

Next we consider a sequence of consecutive samples n_j, typically taken over immediately adjacent time intervals in order to obtain maximum efficiency. As was just discussed, this sequence constitutes a discrete stochastic process. However, for constant intensity I this process is rather trivial, being essentially a pure noise process.

More interesting is the case where the intensity I of the detected light is itself a stochastic process in time, thus making the n_j a doubly stochastic process. In order to separate both processes, it is useful to consider first only a single realization of the intensity process $I(t)$. This is equivalent to consideration of conditional photon counting distributions given $I(t)$. For any particular time interval j, we still obtain Poisson photon-counting statistics, owing to the factorization property of the Poisson distribution demonstrated in Equation (2.22). Now however, the mean is given by the time integral of the intensity over the sample time interval:

$$\left\langle n_j \,\middle|\, I(t) \right\rangle = m_j = \int_{(j-1)\Delta t}^{j\Delta t} qI(t)\,\mathrm{d}\,t \,. \tag{2.70}$$

We see that the intensity does not enter photon statistics directly but rather through what we may call time integrated intensity values m_j. The m_j constitute a

stochastic process on a discrete time grid with a continuous range of (positive) real values. For the rather common case of short integration times, where a sample time t_s is smaller than the time scale of typical intensity changes, the statistics of the m_j is practically identical to that of the intensities $I(j\Delta t)$, if we ignore the trivial constant prefactor qt_s.

In order to obtain ordinary single-interval photon statistics, we must average over intensity fluctuations and obtain

$$P(n) = \left\langle P(n \,|\, I(t)) \right\rangle = \left\langle m^n \exp(-m) \right\rangle / n! = \int_0^\infty m^n \exp(-m)\, p_m(m)\, \mathrm{d}\, m / n! \qquad \textbf{(2.71)}$$

for the distribution of photon counts, where we dropped the unnecessary time index j. The photon counts distribution equals the Poisson transform of the probability density over the time-integrated intensity. This relation is well known as the Mandel formula and may be derived from the quantum theory of light[49].

The expression for the factorial moments is even simpler:

$$F_n^{(k)} = \left\langle m^k \right\rangle . \qquad \textbf{(2.72)}$$

The factorial moments of the photon counts correspond directly to the ordinary moments (of the same order) over the time-integrated intensity m. For short integration times, these moments are proportional to the intensity moments (prefactor $q^k \Delta t^k$). This fact is often used to estimate intensity statistics from measured photon counting statistics. If we were to consider detector dead-time distortions it will complicate the simple relation between factorial photon count moments and intensity moments[50]. Also the possibilities of obtaining a full intensity distribution from the intensity moments are generally very limited[51].

In the context of photon correlation, our dominant interest lies in the temporal behavior of the sequence of photon detection counts n_j. For later reference we calculate mixed conditional moments of the n_j up to fourth order for given time-integrated intensities m_j. All these moments are easily derived from the known factorial moments of Poisson variables, using the fact that n_i and n_j are statistically independent, unless i and j are equal. We obtain[45]

$$\left\langle n_i \,\middle|\, m_i \right\rangle = m_i, \tag{2.73}$$

$$\left\langle n_i n_j \,\middle|\, m_i, m_j \right\rangle = m_i m_i + \delta_{ij} m_i, \tag{2.74}$$

$$\left\langle n_i n_j n_m \,\middle|\, m_i, m_j, m_m \right\rangle = m_i m_j m_m + \delta_{ij} m_i m_m + \delta_{im} m_i m_j + \delta_{jm} m_i m_j + \delta_{ij}\delta_{im} m_i, \tag{2.75}$$

$$\begin{aligned}\left\langle n_i n_j n_m np \,\middle|\, m_i, m_j, m_m, mp \right\rangle &= m_i m_j m_m m_p + \delta_{ij} m_i m_m m_p + \delta_{im} m_i m_j m_p \\ &+ \delta_{ip} m_i m_j m_m + \delta_{jm} m_i m_j m_p + \delta_{jp} m_i m_j m_m + \delta_{mp} m_i m_j m_m \\ &+ \delta_{ij}\delta_{im} m_i m_p + \delta_{ij}\delta_{ip} m_i m_m + \delta_{im}\delta_{ip} m_i m_j + \delta_{jm}\delta_{jp} m_i m_j \\ &+ \delta_{ij}\delta_{mp} m_i m_m + \delta_{im}\delta_{jp} m_i m_j + \delta_{ip}\delta_{jm} m_i m_j + \delta_{ij}\delta_{im}\delta_{ip} m_i.\end{aligned} \tag{2.76}$$

Note that all these relations will be slightly violated for nonideal detectors.

Equation (2.74) is of particular relevance to photon correlation. If we use subscripts $\langle\ldots\rangle_n$ to denote averages over photon statistics and $\langle\ldots\rangle_\mu$ to denote averages over (time-averaged) intensity statistics; we may rewrite this relation as

$$\left\langle n_j n_{j+k} \right\rangle_{n,m} = \left\langle \left\langle n_j n_{j+k} \,\middle|\, m_j m_{j+k} \right\rangle_n \right\rangle_m = \delta_{k0} \left\langle m_j \right\rangle_m + \left\langle m_j m_{j+k} \right\rangle_m. \tag{2.77}$$

The first term vanishes for non-zero k and we obtain the well-known equality of the temporal autocorrelation of photon counting data on the one hand and that of the classical (time-integrated) intensity of the other – in short, the equality of photon correlation and intensity correlation. This equality is the very basis of the photon correlation technique. Note that the equality is the sole consequence of photon counting statistics. It holds independently of the underlying intensity statistics.

Intensity Statistics

We have now established a connection between time-averaged intensities and photon counting statistics. Next we turn our attention towards intensity statistics obtained in typical PCS experiments. For this purpose, a purely classical treatment of electrodynamics is perfectly adequate.

We progress in four steps. First we derive the two-time distribution of light scattered by many independent scatterers. Next we discussed spatial averaging effects. Then we calculate the temporal correlation function for free Brownian particles. Finally we address the topic of multiple sample times.

The conceptually simplest possible x-ray scattering experiment uses a single, unpolarized x-ray beam to illuminate a number of scattering particles. The beam is well described by plane wave approximation:

$$\mathbf{E}(\mathbf{x},t) = (\mathbf{e}_x + \mathbf{e}_y)E_0(x,y)\exp(\mathrm{i}\,kz - \mathrm{i}\,wt), \qquad \textbf{(2.78)}$$

where we have oriented orthogonal coordinates $\boldsymbol{x} = (x,y,z)$ such that $\mathbf{e}_x$ and $\mathbf{e}_y$ are unit vectors in the direction of the electric field vectors, $\mathbf{e}_z$ is the unit vector in the direction of

beam propagation, k denotes the propagation vector equal to $2\pi/\lambda$, ω is the frequency, and t is the time. $\mathbf{k}$ and $k = |\mathbf{k}|$ are also known as the wave vector and wave number, respectively, of the x-ray photons.

The scattered x-rays are registered by a point detector in the far field, most commonly placed in the (z, y) plane at scattering angle q with respect to $\mathbf{e}_z$. Since we assume quasi-elastic x-ray scattering, the magnitude of the final wave vector is again given by k.

The scattering kinematics are simple. The scattering process involves an initial wave vector

$$\mathbf{k}_i = k\mathbf{e}_z \qquad \textbf{(2.79)}$$

and a final wave vector

$$\mathbf{k}_f = k\mathbf{e}_y \sin q + k\mathbf{e}_z \cos q \ . \qquad \textbf{(2.80)}$$

A quick geometric consideration yields their difference, the scattering vector, or momentum transfer, as

$$\mathbf{q} = \mathbf{k}_f - \mathbf{k}_i = k[\mathbf{e}_y \sin q - \mathbf{e}_z(1-\cos q)], \qquad \textbf{(2.81)}$$

with a magnitude

$$q = |\mathbf{q}| = k[\sin^2 q + (1-\cos q)^2]^{1/2} = 2k\sin(q/2), \qquad \textbf{(2.82)}$$

which may be varied between zero and 2k (corresponding to backscattering) by proper choice of the scattering angle q.

X-ray scattering by a single free electron corresponds to well known Thomson scattering[52]. The resulting electric field amplitude at distance R from an electron at position $\boldsymbol{x_j}$ is given by

$$\mathbf{E}(\mathbf{q},t) = \frac{[\mathbf{e}_x + \mathbf{e}_y \cos(q)]E_0(x_j, y_j)r_o \exp(\mathrm{i}\,\mathbf{q}\cdot\mathbf{x}_j - \mathrm{i}\,wt)}{R}, \qquad \textbf{(2.83)}$$

so that the intensity is

$$I(\mathbf{q},t) = I_o \frac{r_o^2}{R^2}\frac{[1+\cos^2(q)]}{2}. \qquad \textbf{(2.84)}$$

r_o is the Thomson cross section for a free electron,

$$r_o = \frac{e^2}{mc^2} = 2.82x10^{-13}cm. \qquad \textbf{(2.85)}$$

The small value for r_o is why x-ray scattering is considered to be a weak process. The angular factor, $[1+\cos^2(q)]/2$, is the so-called polarization factor. In fact, the x-ray beam from a synchrotron is very nearly purely linearly polarized (about 99% in the horizontal direction), and so it is common to scatter in the plane perpendicular to the plane of polarization, i.e., the vertical plane as in the discussion above, and hence avoid the reduction due to the polarization factor. We shall limit our following considerations to this case.

The scattered electric field amplitude for scattering of linearly polarized x-rays in the polarization plane from an atom, with an electron charge distribution characterized by charge density $r(\boldsymbol{x_j})$, is given by integrating the scattering over the volume of the charge distribution:

$$\mathbf{E}(\mathbf{q},t) = \frac{\mathbf{e}_x E_0(x_j, y_j)r_o \exp(-\mathrm{i}\,wt)}{R}\int r(\mathbf{x}_j)\exp(\mathrm{i}\,\mathbf{q}\cdot\mathbf{x}_j)dV, \qquad \textbf{(2.86)}$$

where the incident electric field amplitude is assumed to vary slowly on the scale of the electron charge distribution. The integral in Equation (2.86) is known as the atomic scattering factor, *f*,

$$f = \int r(\mathbf{x}_j) \exp(\mathrm{i}\mathbf{q} \cdot \mathbf{x}_j) dV . \qquad \textbf{(2.87)}$$

Because of the finite size of the atom, *f* has a weak *q* dependence, falling off at higher scattering angles. This angular dependence of *f* is referred to as the atomic form factor. At small scattering angles, the exponential term in the integral can be neglected and *f* approaches Z, the atomic charge of the atom. Scattering from the protons in the nucleus can be neglected due to to their much larger mass than the electrons.

The simple treatment of atomic scattering outlined above ignored the fact that electrons in atoms are not free but are bound to their nuclei, so that there are resonant frequencies for their motion corresponding to their electronic shells, or energy levels. These resonances may only be ignored if the x-ray energy is much larger than the transition energies of the electrons. It turns out that most atoms have transition energies within the ~ 5 to 20 keV energy range typically covered by x-rays; therefore, the resonances cannot be neglected. The resonances will, in general, affect both the magnitude and phase of the scattering amplitude from the atom. A quantum mechanical treatment[53,54,55] gives

$$f = f_o + \Delta f' + i\Delta f'', \qquad \textbf{(2.88)}$$

where f_o is the unmodified term given by Equation (2.87) and which approaches Z at small angles, and $\Delta f'$ and $\Delta f''$ are the real and imaginary parts of the so-called anomalous dispersion term. $\Delta f'$ and $\Delta f''$ are generally found to be insensitive to the

scattering angle, being chiefly dependent on the x-ray wavelength. They are relatively small even near atomic transition energies and can usually be considered small corrections to the scattering amplitude.

As a brief step aside, it is interesting to note that it is the anomalous dispersion terms that describe the macroscopic interaction of x-rays with matter. This can be described by the complex refractive index

$$n = 1 - d - ib \tag{2.89}$$

where d, the refractive index decrement, and b, the absorption index, are given by

$$d = K\Delta f', \quad b = K\Delta f'' \tag{2.90}$$

and

$$K = \frac{r_o l^2}{2p}\frac{N_A}{A} r_m \tag{2.91}$$

where N_A is Avagadro's number and A and r_m are the atomic weight and mass density of the material. δ and β are typically of order 10^{-6} and 10^{-9}, respectively. Note that the real part of the refractive index of materials is negative in the x-ray region.

Scattering by a single atom j in a material is then characterized by a scattering amplitude b_j (equal to $r_o f_{oj}$) and a phase determined by the scalar products of atomic position $\boldsymbol{x}_j$ and scattering vector $\boldsymbol{q}$:

$$\mathbf{E}_j(\mathbf{q},t) = \frac{\mathbf{e}_y E_0(x_j, y_j) b_j \exp(\mathrm{i}\mathbf{q}\cdot\mathbf{x}_j - \mathrm{i}wt)}{R}. \tag{2.92}$$

In this situation we may drop the vector character of the field as well as its explicit time dependence, and express the scattered electric field by its complex amplitude:

$$u_j(\mathbf{q},t) = \frac{E_0(x_j, y_j) b_j \exp(\mathrm{i}\,\mathbf{q}\cdot\mathbf{x}_j)}{R}. \qquad \textbf{(2.93)}$$

$E_0(x_j,y_j)$ is a weakly varying function of atomic position. The temporal behavior of the complex scattered electric field amplitude is clearly dominated by changes of the phase factor, and it is useful to absorb $E_0(x_j,y_j)$ into a new scattering amplitude:

$$a_j = \frac{E_0(x_j, y_j) b_j}{R}. \qquad \textbf{(2.94)}$$

This scattering amplitude a_j now contains the entire geometry of the experiment, including the particle position $\boldsymbol{x}_j$ within the beam, the illuminating electric field strength, and the distance to the detector.

The sum of the scattered amplitudes from all N atoms in the measurement volume is

$$u_f(\mathbf{q},t) = \sum_{j=1}^{N} a_j(\mathbf{x}_j) \exp(\mathrm{i}\,\mathbf{q}\cdot\mathbf{x}_j). \qquad \textbf{(2.95)}$$

Note the implicit time-dependence of this amplitude due to motion of the atoms, that is, the $\boldsymbol{x}_j$ are functions of time $\boldsymbol{x}_j(t)$. Our next task is the determination of the statistical properties of the amplitude $u_f(\mathbf{q},t)$ as a function of time. This task is greatly simplified by three common assumptions.

First, we assume the atomic positions $\boldsymbol{x}_j$ to be statistically independent. This is a good approximation in an ideal gas or a highly disordered liquid. However, real materials display spatial correlations over sufficiently short length scales and the statistical independence assumption fails on the atomic level. However, the scattering volume will typically still be well in excess of a material's spatial correlation lengths. Hence, we may

imagine the system subdivided into correlation volumes, where only interactions within such a volume are considered, but neglected between different correlation volumes. We can now formally replace the sum over particles by a sum over correlation volumes that can be assumed to be statistically independent. This is analogous to what we did when we calculated the scattering from the Z electrons in an atom.

Note that in this case, the scattered electric field amplitude scales like the number of atoms in the correlation volume, M, so that the scattered intensity scales like M^2, just as the intensity scattered by an atom scales like Z^2 instead of Z. If the atoms were completely uncorrelated, the scattered intensities would add rather than the amplitudes and the scattered intensity would only be proportional to M instead of M^2. This is why Bragg peaks in x-ray scattering from crystals are so strong. The scattering from correlated volumes falls off with increasing scattering angle, just as the scattering from atoms does. However, as correlated volumes are usually much larger than atoms, the fall off is much stronger than in the atomic case. The scattering is often confined to a small range of angles about the forward direction in a disordered system or about a Bragg peak in a periodic crystal lattice. This is a main reason why almost all XPCS experiments to date have been confined to SAXS studies, as pointed out in Chapter 1.

The simplest example of a correlated material is one composed of aggregate particles, such as a colloid. Another example is the spatially correlated concentration fluctuations in a binary system, which can be described by a correlation length, ξ, as discussed in Chapter 3. In the following, we will use the term particle as a generic term to describe a correlated volume in a material.

Second, we restrict our attention to time scales much smaller than the typical transit time of the particle through the beam. For these time scales we can neglect the time dependence of the single particle scattering amplitudes a_j.

Third, we consider reasonably large particle densities only. That is to say, we always assume the presence of N particles inside the scattering volume, V, where the mean particle separation, $(V/N)^{1/3}$ is much smaller than the beam diameter. This means that we will neglect number density fluctuations. Particularly for small particles, this assumption is easily satisfied even at rather small volume fractions. To give an example, 100 nm diameter particles at a volume fraction of 10^{-6} in a 100 μm diameter beam still leave us with 10^3 particles in the measurement volume.

We have just stated all the assumptions that are required to apply the central limit theorem, which predicts Gaussian statistics for our complex amplitude $u_f(\boldsymbol{q},t)$. However, we want to go beyond single-time intensity statistics now and consider the simultaneous distribution of the complex amplitude $u_f(\mathbf{q},t\ \ )$ at two times, say $t\ \ = 0$ and $t\ \ = t$. The generalization to even more times is then straightforward.

We introduce the four real components of our two complex amplitudes as

$$u_1 = \mathrm{Re}[u_f(\mathbf{q},0)] = \sum a_j \cos[\mathbf{q}\cdot\mathbf{x}_j(0)], \qquad \textbf{(2.96)}$$

$$u_2 = \mathrm{Im}[u_f(\mathbf{q},0)] = \sum a_j \sin[\mathbf{q}\cdot\mathbf{x}_j(0)], \qquad \textbf{(2.97)}$$

$$u_3 = \mathrm{Re}[u_f(\mathbf{q},0)] = \sum a_j \cos[\mathbf{q}\cdot\mathbf{x}_j(t)], \qquad \textbf{(2.98)}$$

$$u_4 = \mathrm{Im}[u_f(\mathbf{q},0)] = \sum a_j \sin[\mathbf{q}\cdot\mathbf{x}_j(t)], \qquad \textbf{(2.99)}$$

where all sums run over the particle index j. The associated variables in the characteristic function of $p(u_f(\mathbf{q},0), u_f(\mathbf{q},t))$ will be denoted as s_1, …, s_4 and we shall also use vector notations **u** and **s** for the sake of brevity. The desired characteristic function reads

$$\begin{aligned}
\left\langle \exp(-\mathbf{s}\cdot\mathbf{u})\right\rangle &= < \exp[-\sum_{j=1}^{N} a_j \{s_1 \cos[\mathbf{q}\cdot\mathbf{x}_j(0)] + s_2 \sin[\mathbf{q}\cdot\mathbf{x}_j(0)] \\
&\quad + s_3 \cos[\mathbf{q}\cdot\mathbf{x}_j(t)] + s_4 \sin[\mathbf{q}\cdot\mathbf{x}_j(t)]\}] > \\
&= < \exp[a_j \{s_1 \cos[\mathbf{q}\cdot\mathbf{x}_j(0)] + s_2 \sin[\mathbf{q}\cdot\mathbf{x}_j(0)] \\
&\quad + s_3 \cos[\mathbf{q}\cdot\mathbf{x}_j(t)] + s_4 \sin[\mathbf{q}\cdot\mathbf{x}_j(t)]\}] >^N \\
&\approx [1 + \left\langle a_j^2 \right\rangle \{s_1^2 \left\langle \cos^2[\mathbf{q}\cdot\mathbf{x}_j(0)]\right\rangle + s_2^2 \left\langle \sin^2[\mathbf{q}\cdot\mathbf{x}_j(0)]\right\rangle \\
&\quad + s_3^2 \left\langle \cos^2[\mathbf{q}\cdot\mathbf{x}_j(t)]\right\rangle + s_4^2 \left\langle \sin^2[\mathbf{q}\cdot\mathbf{x}_j(t)]\right\rangle \\
&\quad + s_1 s_3 \left\langle \cos[\mathbf{q}\cdot\mathbf{x}_j(0)]\cos[\mathbf{q}\cdot\mathbf{x}_j(t)]\right\rangle + s_2 s_4 \left\langle \sin[\mathbf{q}\cdot\mathbf{x}_j(0)]\sin[\mathbf{q}\cdot\mathbf{x}_j(t)]\right\rangle\}/2]^N \\
&= [1 + N\left\langle a_j^2 \right\rangle \{s_1^2 + s_2^2 + s_3^2 + s_4^2 + s_1 s_3 \left\langle \cos\left[\mathbf{q}\cdot\mathbf{x}_j(0) - \mathbf{q}\cdot\mathbf{x}_j(t)\right]\right\rangle \\
&\quad - s_2 s_4 \left\langle \cos\left[\mathbf{q}\cdot\mathbf{x}_j(0) + \mathbf{q}\cdot\mathbf{x}_j(t)\right]\right\rangle\}/4N]^N, \qquad \textbf{(2.100)}
\end{aligned}$$

where we have already omitted the terms which average to zero due to uniform distribution of phases over [0, 2p], such as $\mathbf{q}\cdot\mathbf{x}_j(0)$, as well as terms of higher order than a_j^2. For large N we substitute the limiting exponential and obtain

$$\begin{aligned}
\left\langle \exp(-\mathbf{s}\cdot\mathbf{u})\right\rangle &= \exp[N\left(\left\langle a_j^2 \right\rangle/4\right)\{s_1^2 + s_2^2 + s_3^2 + s_4^2 \\
&\quad + s_1 s_3 \left\langle \cos\left[\mathbf{q}\cdot\mathbf{x}_j(0) - \mathbf{q}\cdot\mathbf{x}_j(t)\right]\right\rangle - s_2 s_4 \left\langle \cos\left[\mathbf{q}\cdot\mathbf{x}_j(0) + \mathbf{q}\cdot\mathbf{x}_j(t)\right]\right\rangle\}], \qquad \textbf{(2.101)}
\end{aligned}$$

the characteristic function for a Gaussian in four dimensions with equal variances $N<a_j^2>/2$ in all dimensions and vanishing covariances except between u_1 and u_3 as well as between u_2 and u_4. Both covariances are identical but of opposite sign and may be

derived from the complex temporal autocorrelation

$$\begin{aligned} G_u(t) &= \left\langle u_f(0) u'_f(t)^* \right\rangle \\ &= N \left\langle a_j^2 \right\rangle \left\langle \exp\left(i\mathbf{q} \cdot [\mathbf{x}_j(0) - \mathbf{x}_j(t)]\right) \right\rangle \\ &= N \left\langle a_j^2 \right\rangle \left\langle \cos\left(\mathbf{q} \cdot [\mathbf{x}_j(0) - \mathbf{x}_j(t)]\right) \right\rangle. \end{aligned} \quad \textbf{(2.102)}$$

This derivation proves the fact that not only does our complex amplitude yield Gaussian statistics if we consider it at the single time: we also obtain joint Gaussian statistics for the two-time probability density, and the procedure just outlined could in fact be continued to prove all higher-order statistics to be Gaussian. This situation is generally denoted as a Gaussian process.

The common occurrence of Gaussian statistics for the complex amplitude at the detector in light or x-ray scattering experiments underlines the great practical importance of autocorrelation measurements. Not only is temporal autocorrelation the lowest-order time-independent moment, and hence simplest quantity to consider, but for Gaussian processes it is also *all there is to know*. Every multi-time higher-order moment may be decomposed into an expression involving just the temporal autocorrelation of Equation (2.102), also known as the amplitude or first-order correlation (abbreviated as $G_1(t)$).

As the most important example of this rule, we discuss the intensity or second-order correlation,

$$G_I(t) = \left\langle \left| u_f(0) \right|^2 \right\rangle \left\langle \left| u_f(t) \right|^2 \right\rangle, \quad \textbf{(2.103)}$$

a fourth-order moment in complex amplitude. Such a moment is obtained by summing over all possible distinct permutations of amplitudes involved. Non-zero expectations are obtained for pairs of amplitudes only, where exactly one member of the pair must be a

complex conjugate:

$$G_I(t) = \left\langle \left| u_f(0) \right|^2 \right\rangle \left\langle \left| u_f(t) \right|^2 \right\rangle + \left\langle u_f(0) u_f(t)^* \right\rangle \left\langle u_f(0)^* u_f(t) \right\rangle$$

$$= G_1(0)^2 + \left| G_1(t) \right|^2. \qquad \textbf{(2.104)}$$

This important relation is fundamental to the analysis of PCS data. It was first obtained by Siegert in the context of radar signal processing and is known as the Siegert relation. It provides a relation between amplitude correlation, Equation (2.102), and the intensity correlation function actually measured in photon correlation.

Effects of Finite Detector Size

Until now we have considered only the far-field complex amplitude or intensity for a single point. Now we will consider a generalization to a finite detector size. Although detectors could be used with sufficiently small apertures to closely approximate the point detector idealization, this would be extremely wasteful in terms of the total power detected. In practice, larger detector apertures are commonly employed and we must estimate the statistical consequences of spatial averaging.

In order to obtain an exact solution, we need to know the complex field or the intensity as a stochastic process in space as well as in time. Spatial integration over the detector aperture, possibly weighted with detector sensitivity, will then yield the true detector signal as a stochastic process in time.

Typical beam intensity profiles are reasonably close to a Gaussian bell shape. Let R be the $1/e^2$ beam radius, or the radius at which the intensity falls to $1/e^2$ of its maximum on the beam axis. For simplicity we also assume a Gaussian aperture with the same radius

R to characterize the imaging performed by the detection system. In this case our scattering particles act spatially like a random phase source with a 2D Gaussian intensity profile:

$$u_s(x,y) = u_0 \exp[-(x^2+y^2)/R^2]\exp[i\Theta(x,y)]. \qquad \textbf{(2.105)}$$

We choose *x* and *y* to denote coordinates perpendicular to the detection direction. The phase $\Theta(x,y)$ has negligible spatial correlation – an assumption equivalent to the large particle-number limit.

As the detector is located in the far field, we must now consider the spatial Fourier transform of our complex source amplitude[56], which is formally obtained as

$$u_f(q_x,q_y) = u_0 \iint \exp\left[\left(-x^2+y^2\right)/R^2 + i\Theta(x,y) - iq_x x - iq_y y\right]dxdy. \qquad \textbf{(2.106)}$$

We now proceed to calculate the spatial amplitude correlation in the far field:

$$\begin{aligned}
&\left\langle u_f(q_x,q_y)u_f{}^*(q_x+dq_x,q_y+dq_y)\right\rangle \\
&= u_0^2 \iint\iint \exp\left[-\left(x^2+y^2\right)/R^2 - i\,q_x x - iq_y y\right] \\
&\quad\times\exp\left[-\left(x'^2+y'^2\right)/R^2 - i(q_x+dq_x)x' + i\left(q_y+dq_y\right)y'\right] \\
&\quad\times\left\langle\exp[\,i\Theta(x,y) - i\Theta(x',y')]\right\rangle dx\,dy\,dx'\,dy' \\
&= u_0^2 \iint\iint \exp\left[-\left(x^2+y^2\right)/R^2 - \left(x'^2+y'^2\right)/R^2\right] \\
&\quad\times\exp[-i\,q_x x - iq_y y - i(q_x+dq_x)x' + i\left(q_y+dq_y\right)y'] \\
&\quad\times d(x-x')d(y-y')\,dx\,dy\,dx'\,dy' \\
&= u_0^2 \iint \exp[-\left(x^2+y^2\right)/R^2]\exp[-idq_x x - idq_y y]dxdy
\end{aligned}$$

$$= u_0^2 \left(pR^2/2\right) \exp[-R^2(dq_x^2 + dq_y^2)/8], \qquad \textbf{(2. 107)}$$

a Gaussian spatial correlation function with correlation length 4/*R* in wave vector units. For $dq_x = dq_y = 0$ this amplitude correlation equals the mean intensity,

$$\left\langle I_f \right\rangle = u_0^2 (pR^2/2). \qquad \textbf{(2. 108)}$$

Assuming cross-spectral purity, that is, the factorization of spatial and temporal correlations, we may generalize our spatial amplitude correlation to spatio-temporal correlation, commonly known as a cross-correlation function:

$$G_u(dq_x, dq_y, t) = \left\langle u_f(q_x, q_y, t) u_f^*(q_x + dq_x, q_y + dq_y, t + t) \right\rangle$$

$$= \left\langle I_f \right\rangle \exp[-R^2(dq_x^2 + dq_y^2)/8] c(t), \qquad \textbf{(2.109)}$$

where c(t) denotes the normalized temporal amplitude correlation

$$c(t) = G_u(t) / \left\langle I_f \right\rangle. \qquad \textbf{(2.110)}$$

The far-field complex amplitude is now modeled as a Gaussian process in space as well as in time, with Gaussian spatial correlation (in Gauss-Gauss speckles) and unspecified temporal correlation c(t).

The Siegert relation including spatial dependence reads

$$G_I(dq_x, dq_y, t) = G_u(0,0,0)^2 + \left| G_u(dq_x, dq_y, t \right|^2$$

$$= \left\langle I_f \right\rangle^2 \left\{ 1 + \exp\left[-R^2 \left(dq_x^2 + dq_y^2 \right) / 4 \right] \cdot \left| c(t) \right|^2 \right\}, \qquad \textbf{(2.111)}$$

and $G_I(dq_x, dq_y, t)$ is called the intensity or second-order cross-correlation function.

Now we can finally integrate dq_x and dq_y, over the finite-size detector aperture.

For simplicity, we assume Gaussian detector apertures. We replace the integrals over the aperture area by an integral over the whole plane with a Gaussian weight function of width equal to the detector radius,

$$\iint \exp\left[-\left(dq_x^2 + dq_y^2\right)/Q^2\right] \mathrm{d}dq_x \, \mathrm{d}dq_y \,, \tag{2.112}$$

and obtain after some algebra the temporal autocorrelation of the spatially averaged intensity or second-order correlation

$$G_2(t) = \langle I \rangle^2 \left\{1 + b\left|c(t)\right|^2\right\}, \tag{2.113}$$

with

$$\langle I \rangle = pQ^2 \langle I_f \rangle \,, \tag{2.114}$$

$$b = 1/\left(1 + R^2Q^2/2\right). \tag{2.115}$$

After normalization according to

$$g_2(t) = G_2(t)/\langle I \rangle^2 - 1 \,, \tag{2.116}$$

our generalized Siegert relation simplifies to

$$g_2(t) = b\left|c(t)\right|^2. \tag{2.117}$$

Here *b* denotes the zero lag-time limit of the normalized second order correlation and is hence known as the intensity intercept. β is 1 for a point detector and fully coherent incident beam, decreasing towards zero as the detector aperture increases. Large values for β are desirable in order to have larger $g_2(t)$ to measure. However, photon shot noise is greatest for a point detector, decreasing for larger detector apertures as the mean

detected count rate increases. Detailed calculations[57] of the signal to noise in a measurement of $g_2(t)$ as a function of β have been done, with the result that $\beta \sim 0.2$ is optimal if the incident beam is perfectly coherent. For XPCS experiments the x-ray beam is usually only partially coherent, and the intercept value is typically smaller, ranging between 0.03-0.09. It is also straightforward to calculate $G_2(t)$ for other geometries, such as hard apertures, but Equation (2.117) is not changed other than through the value of b.

Finite Sample Time and Multiple Sample Times

Next let's discuss the effects of a finite sample time and of making measurements with multiple sample times. It is not uncommon for a system to have multiple relaxation modes that require the availability of correlation data over a large range of lag times. On the other hand, little is gained by very narrow spacing of the various lag-time channels, that is, by the use of sample time very much shorter than the lag time. Hence the ideal correlator should provide something like a logarithmic spacing of lag times in order to cover a larger lag-time range with a reasonably small number of channels.

As we shall see later, the sampling time should always be increased in proportion to the delay time, in order to provide optimum signal to noise ratios. This increase in sample time, however, implies significant temporal averaging of the measured photon correlation function. We saw above that photon correlation functions really correspond to the temporal autocorrelation of the time-integrated intensities

$$m_j = \int_{(j-1)\Delta t}^{j\Delta t} q_e I(t)\mathrm{d}t, \qquad \textbf{(2.118)}$$

rather than the intensity $I(t)$ itself.

Consequently photon correlation functions must be written as

$$G_n(k) = \int_0^{\Delta t}\int_0^{\Delta t} G_2(k\Delta t + t - t')\mathrm{d}t\,\mathrm{d}t'$$

$$= \int_0^{\Delta t}\int_{-t'}^{\Delta t - t'} G_2(k\Delta t + t)\mathrm{d}t\,\mathrm{d}t'$$

$$= \int_{-\Delta t}^{\Delta t} G_2(k\Delta t + t)(\Delta t - |t|)\mathrm{d}t\,, \qquad \textbf{(2.119)}$$

where we have performed the integration over t . Only if $G_2(t)$ remains constant over lag-time changes of order Δt may we use the common simplification

$$G_n(k) \approx \Delta t^2 G_2(k\Delta t)\,. \qquad \textbf{(2.120)}$$

If the intensity correlation $G_2(t)$ changes on time-scales comparable with a sampling time Δt we must take the triangular averaging as given in Equation (2.119) into account. For normalized autocorrelations, the triangular averaging reads

$$g_n(k) = \int_{-\Delta t}^{\Delta t} g_2(k\Delta t + t')(\Delta t - |t|)\mathrm{d}t' / \Delta t^2\,, \qquad \textbf{(2.121)}$$

For an exponential intensity correlation

$$g_2(t) = b\,\exp(-2\Gamma t)\,, \qquad \textbf{(2.122)}$$

the introduction of the sampling time Δt results in normalized photon correlation function

$$g_n(k) = b\Delta t^{-2}\int_{-\Delta t}^{\Delta t}\exp(-2\Gamma k\Delta t - 2\Gamma t)(\Delta t - |t|)\mathrm{d}t$$

$$bf\,(2\Gamma\Delta t)\exp(-2\Gamma k\Delta t) = f\,(2\Gamma\Delta t)g_2(k\Delta t) \qquad \textbf{(2.123)}$$

with

$$f(x) = x^{-2}[2\cosh(x) - 2]. \qquad \textbf{(2.124)}$$

The correction factor $f(x)$ may be expanded for small values of x:

$$f(x) \approx 1 + x^2/12. \qquad \textbf{(2.125)}$$

With this approximation we may readily compute the absolute deviation between $g_2(k)$ and $g_2(k\Delta t)$ as

$$g_n(k) - g_2(k\Delta t) \approx [(2\Gamma\Delta t)^2/12]b\,\exp(-2\Gamma k\Delta t), \qquad \textbf{(2.126)}$$

which increases with Δt at small values of the sampling time until it reaches a maximum of

$$b/3e^2k^2 \approx 0.045b/k^2 \qquad \textbf{(2.127)}$$

at $\Delta t = 1/k\Gamma$. For larger sampling times Δt the absolute deviation decreases exponentially.

Obviously it is sufficient to keep k, the ratio of the delay time to sample time, large enough to reduce this triangular averaging error below any given limit. As an example, for $k = 8$ we obtain

$$\left|g_n(k) - g_2(k\Delta t)\right| < 0.0007b\,. \qquad \textbf{(2.128)}$$

This is already less than the typical statistical accuracy in photon correlation measurements.

In conclusion, triangular averaging due to finite sample time leads to a small increase in measured photon correlation data. This increase is a constant factor for a given sample time in the case of a single exponential normalized correlation. The factor

is very close to unity for sample times significantly less than the decay time (say by a factor of 10). For the more complicated case of multicomponent correlation functions and/or multiple sample-time data, triangular averaging errors may be kept negligibly small by restricting oneself to the use of lag times considerably larger than the sample time. A factor $k = t/\Delta t \geqslant 8$ typically suffices.

Noise Contributions and Normalization

One important property shared by all physical measurements is their finite accuracy. Such a finite accuracy is often very obvious by what appears to be random noise on measured photon correlation data. That is an immediate consequence of the random character of photon counting.

However, except for the limiting case of very small count rates, there also exist a significant amount of almost invisible noise on photon correlation functions. This type of noise is due to the very intensity fluctuations under investigation. In some literature this noise is referred to as “signal noise” [58]. Signal noise does not appear to be random from one lag time to another in $g_2(t)$ but instead manifests itself as more smoothly varying departures from the underlying autocorrelation function on time scales of the characteristic relaxation processes being studied. Essentially it is simply the error on the measured estimate of the relaxation time distribution function that results from a limited number of samples of the fluctuations. Hence, extending the measurement duration, i.e., increasing the number of fluctuations sampled, can reduce it.

Both types of noise, due to photon as well as classical intensity statistics, or signal noise, are considered here. Particular attention is given to efficient normalization schemes

and their possible benefits, particularly at larger delay times.

A real photon correlation experiment is restricted to some finite total measurement time $T_m = M\Delta t$, or finite number of samples M; Δt again denotes the sample time interval. The most common algorithm for real-time correlators yields a correlation estimator

$$G_{ne}(k) = (1/M)\sum_{j=1}^{M} n_j n_{j-k} \qquad \textbf{(2.129)}$$

at the lag time $t = k\Delta t$. The subscript "e" is used to denote estimators. Quite obviously, $G_{ne}(k)$ constitutes an unbiased estimator for the photon correlation function $G_n(k)$, that is,

$$\left\langle G_{ne}(k) \right\rangle = G_n(k) = \left\langle n_j n_{j-k} \right\rangle. \qquad \textbf{(2.130)}$$

However, no finite measurement will yield estimator data $G_{ne}(k)$ exactly equal to $G_n(k)$: there will always be some statistical error

$$d\,G_{ne}(k) = G_{ne}(k) - G_n(k). \qquad \textbf{(2.131)}$$

The general comments above on the noise sources are borne out by a detailed calculation of the covariance matrix of the errors. At low count rates, the photon noise contributions dominate and the covariance matrix of $dG_{ne}(k)$ is nearly diagonal. This noise behavior agrees with that of independent Poisson variables. In the opposite limit – at high-count rates – the covariance matrix of $dG_{ne}(k)$ is dominated by contributions due to the statistics of the time-integrated intensity m_j. The matrix then generally possesses non-negligible off-diagonal elements, that is, the noise on photon correlation measurements is typically correlated between different delay-time channels. Such correlations occur on the same time-scale as the decay of the desired correlation function[59]. Correlated noise is very

difficult to spot on a single measurement and may easily lead to overfitting during further evaluation.

Most applications of photon correlation spectroscopy do not require knowledge of the scale of $G_n(k)$. Hence normalized correlation estimators are commonly applied. Fortunately, such normalization even provides a reduction of (relative) estimator noise, owing to partial cancellation of count-rate fluctuation effects. The most efficient step to reduce the noise in our correlation estimator is subtraction of the baseline, that is, the limiting value of $G_{ne}(k)$ for large k.

Various schemes have been devised for baseline estimation. The most common ones are the use of "far point channels", measured correlation data at some large delay-time values, and “monitor channels”, special counters, which monitor the average, count rate.

While "far point normalization" may be useful in the presence of low-frequency disturbance, this scheme always introduces some arbitrariness as to the exact delay-time location of a good baseline estimator. Furthermore, single sample-time correlators typically provide less than satisfactory statistical accuracy for their "far point" baseline estimates.

More generally applicable is normalization with monitor channels. Most commercial correlators provide a count rate estimator

$$n_e = (1/M)\sum_{j=1}^{M} n_j\,, \qquad \textbf{(2.132)}$$

measured simultaneously with correlation data. The square of this estimator is commonly used to estimate the baseline – a procedure known to reduce the estimator variance[60].

Even more efficient is the use of a symmetrical baseline estimator

$$n_{e0}n_{ek} \qquad \textbf{(2.133)}$$

based upon individual monitor channels

$$n_{ek} = (1/M)\sum_{j=1}^{M} n_{j-k}. \qquad \textbf{(2.134)}$$

Such individual monitors are available on the new hardware correlators manufactured by ALV (Germany) and could easily be implemented in software correlators as well. The advantage of individual-channel symmetric normalization can be very considerable for multiple-sample-time correlators, where the total numbers of samples *M* may not be a very large number at large delay times[61].

Note that the use of a baseline calculated from "monitors" does not preclude subsequent "far point" normalization corrections. As a matter of fact, with a multiple-sample-time correlators it is probably an excellent idea to apply symmetric baseline subtraction as a first step, which removes a lot of noise and large delay (and sample) times, and only then to select a proper far-point location for further baseline correction. But one should always be aware of possible artifacts due to such subjective approach to "data correction".

To summarize, it is necessary to emphasize two facts associated with the estimation of photon correlation data by multiple sample time correlators, which are particularly important for large delay times. First, the sample time must be increased in proportion to the delay time. Second, baseline subtraction should always employ symmetric estimation schemes. Only if both of these conditions are satisfied will it be possible to achieve good accuracy of measured correlation data without the need for

excessive total duration of the measurement.

Detector Dead Time Effects

Real devices show only finite temporal resolution. In our study of the dynamics of hexane/nitrobenzene critical mixtures, we used a solid state PIN diode detector, commonly referred to by the name of its manufacturer, Amptek, and dead time effects were noticeable. A suitable dead-time model may formally describe this fact. Two simple models are often discussed in the literature.

First, detectors may be inactive for certain dead time t_d after every detected photon. Such a detector will approach a finite maximum count rate $1/t_d$ if the illuminating intensities rose to very high levels (theoretically at least; in practice this procedure may destroy the device). This behavior is known as a non-paralysable dead time characteristic.

Second, every photoelectron may initiate its dead-time period, regardless of whether it leads to an output pulse or not. Such a detector will be completely dead at very high light levels and hence known as paralysable.

Real detectors (including their pulse detection electronics) often fall between those two models, typically rather close to the non-paralysable side. A two-parameter mixed model may then be used, in which the model parameters are obtained from a measurement of detected mean count rates as a function of the illumination intensity[62].

There are two major dead-time effects on photon correlation measurements. The first leads to what can be called direct dead-time distortions. These distortions occur at delay times of the same order as the dead time t_d. Quite clearly, autocorrelation functions must vanish completely at delay times smaller than t_d, at least if we use a sample time Δt

much smaller than the dead time t_d. At delay times equal to t_d we find a steep rise in the correlation, and for larger delay times the direct dead-time distortions vanish quickly for paralysable systems, while there are weak structures which extend to several dead times if non-paralysable systems are used at high count rates[63].

In practice it is often difficult to observe such a pattern, because a very fast correlator (or a very slow detector) would be required to ensure dead times large compared with sample time. Detector dead times typically range between 5 and 100 ns. Hence most correlation measurements are performed with sample times t_s much larger than the dead time t_d. In this case, direct dead-time distortions show up as the reduction of the first autocorrelation channel at delay times equal to the sample time[63]. As a common countermeasure, many data evaluation programs simply ignore this data point, as we did in our measurements on the hexane/nitrobenzene critical mixture described in Chapter 5.

The second type of dead-time distortions extends to all delay times. However, that is noticeable at high-count rates only, since it is a consequence of the count rate non-linearities due to a detector (or even correlator input) dead times. Typical count rates for XPCS are well below the typical saturation limit of a few thousand counts per second for most x-ray detectors.

These dead-time distortions may be computed exactly for paralysable detectors and gamma intensity statistics[63]. Reasonable approximations are also available for the non-paralysable and mixed models[62]. As a rule of thumb, dead-time effects first lead to reduction of the intercept in measured correlation functions. Only at still higher count rates, say at about $0.1/t_d$, does the shape of the correlation functions start to be severely affected. Both artificial shifts of time constants and increased apparent polydispersity are

produced[62].

Autocorrelation Function for Brownian Motion

For the sake of generality, we have until now left the temporal correlation $c(t)$ completely unspecified. This temporal autocorrelation may however be easily calculated for the case of non-interacting scattering particles, all undergoing their individual Brownian motion. This is an adequate model for all suspensions at sufficient dilution.

Lets consider Brownian motion of colloidal particles driven by molecular collisions. The random character of this driving force results in a highly irregular particle motion. The velocity autocorrelation of the Brownian particles decays on a time-scale of the order

$$t_r = m / 6\pi\eta a = \rho a^2 / 9\eta \qquad \textbf{(2.135)}$$

known as the hydrodynamic relaxation time[64]. Here m denotes the mass, a the radius, and ρ the density of the particle; η is the viscosity of the solvent.

For typical colloids with $\rho \approx 10^3$ kg/m^3 and $a \approx 10^{-7}$ m in water with $\eta \approx 10^{-3}$ $kg/s\cdot m$ we obtain $t_r \approx 10^{-9}$ s =1 ns. This is much less than the typical time-scales accessed in photon correlation experiments. Hence we may expect particle displacements on our time-scale to be composed of many independent small displacements. Application of the central limit theorem then predicts Gaussian statistics for each particle's displacement $\delta\mathbf{x}_j$ with a second moment that increases linearly with time:

$$\left\langle \delta x_j^2 \right\rangle = 6Dt\,. \qquad \textbf{(2.136)}$$

The proportionality factor is six times the particle's diffusion coefficient, which is know as the Stokes-Einstein diffusion coefficient[65]:

$$D = k_B T / 6\pi\eta a, \tag{2.137}$$

where k_B denotes Boltzman's constant and T is the absolute temperature.

Treating the far field complex amplitude as a sum over N single-particle contributions, as we did in Equation (2.95), we obtain a first-order, or amplitude, correlation

$$G_1(t) = \left\langle \sum_{j=1}^{N} a_j \exp[i\mathbf{q}\cdot\mathbf{x}_j(t')] \sum_{m=1}^{N} a_m^* \exp[-i\mathbf{q}\cdot\mathbf{x}_m(t'-t)] \right\rangle$$

$$= \sum_{j=1}^{N}\sum_{m=1}^{N} \left\langle a_j a_m^* \right\rangle \left\langle \exp[i\mathbf{q}\cdot d\mathbf{x}_j(t)] \right\rangle = N \left\langle \left| a_j \right|^2 \right\rangle \exp(-q^2 Dt), \tag{2.138}$$

where we have used the different time-scales of the a_j and the phase factors to separate their expectations, and the statistical independence of x_j and y_j for j not equal to m to eliminate non-diagonal terms in the double sum. The final expectation over the phase factor is then recognized as the spatial Fourier transform of the particle displacement $\delta x_j(t)$ over time interval t, which yields an autocorrelation that is a Gaussian in $\boldsymbol{q}$ and a negative exponential in t.

The corresponding normalized first-order correlation reads

$$c(t) = \exp(-q^2 Dt). \tag{2.139}$$

The second-order correlation of the spatially integrated intensity is

$$G_2(t) = \left\langle I \right\rangle^2 [1 + b \exp(-2q^2 Dt)], \tag{2.140}$$

or, in normalized form,

$$g_2(t) = b \exp(-2q^2 Dt). \quad \textbf{(2.141)}$$

These intensity correlations may now be estimated by photon correlation. The analysis in terms of a negative exponential readily yields the diffusion coefficient and hence the product of the size of the colloidal particles and the solvent viscosity.

So far we have implicitly assumed identical colloidal particles. For particles of different sizes, known as a polydisperse system, we must average over the particle sizes. Note that the scattering amplitude factors a_j depend strongly on particle size and act as weights in the averaging procedure. The analysis of correlation data obtained on polydisperse samples typically requires an inverse Laplace transform of the first-order autocorrelation.

The occurrence of particle interactions and internal modes of motion (as in flexible macromolecules) results in a similarly broadened distribution of decay times as is characteristic for polydisperse sample. An extreme example is represented by colloidal systems approaching a glass transition, where decay times may be spread over many decades[66].

Scientific opportunities

XPCS measurements enable us to study the short length scale, slow dynamics of condensed matter systems. In principle, one can study excitations with fluctuation times, t, ranging from μsec to ~10^3 seconds and having wave vectors ranging from 10^{-3} Å^{-1} on the low end, which overlaps the upper range of visible PCS, all the way up to several Å^{-1}

on the upper end, corresponding to wavelengths comparable to interatomic spacing. The good penetration ability of x-rays allow for studies of truly opaque materials such as metals. Finally, since for the x-ray region the $\mathbf{A}\cdot\ \mathbf{p}$ term in the radiation-matter interaction Hamiltonian is negligible compared to the $\mathbf{A}^2$ term, where **A** is the vector potential and **p** is the electron momentum (charge scattering dominates polarization scattering), one can study optically isotropic excitations.

In this section, we briefy compare XPCS to previously available techniques for studying the dynamics of materials and enumerate some of the scientific opportunities[67] it makes possible. XPCS enables the study of dynamics in a unique range of energy and momenta not previously covered by any technique, as shown in Figure 2.4. The visible light scattering techniques of visible PCS, Brillouin, and Raman scattering cover a large range of excitation energies from 10^{-17} to 1 eV at small momenta. At larger momenta, neutron scattering, including neutron spin echo, as well as inelastic x-ray scattering (another technique rejuvenated by 3rd generation synchrotron sources) cover the relatively high energy region from micro-eV to a few eV for momenta ranging from 10^{-2} Å^{-1} to several Å^{-1}. However whereas there was previously a gap in a region of low energy and large momenta excitations, we now have the technique of XPCS.

As a general rule, excitations tend to have low frequencies when weak restoring forces govern them. In this case, their dynamics tends to be dominated by damping, i.e., they usually have a diffusive, rather than a propagating, character. The dispersion relation for a diffusive excitation is simply given by $t = \frac{1}{D \cdot q^2}$, where τ is the relaxation time, D is the diffusion coefficient, and q is the wave vector. Diffusive excitations with diffusion coefficients ranging from 10^{-4} cm^2/sec down to 10^{-19} cm^2/sec can be studied with XPCS,

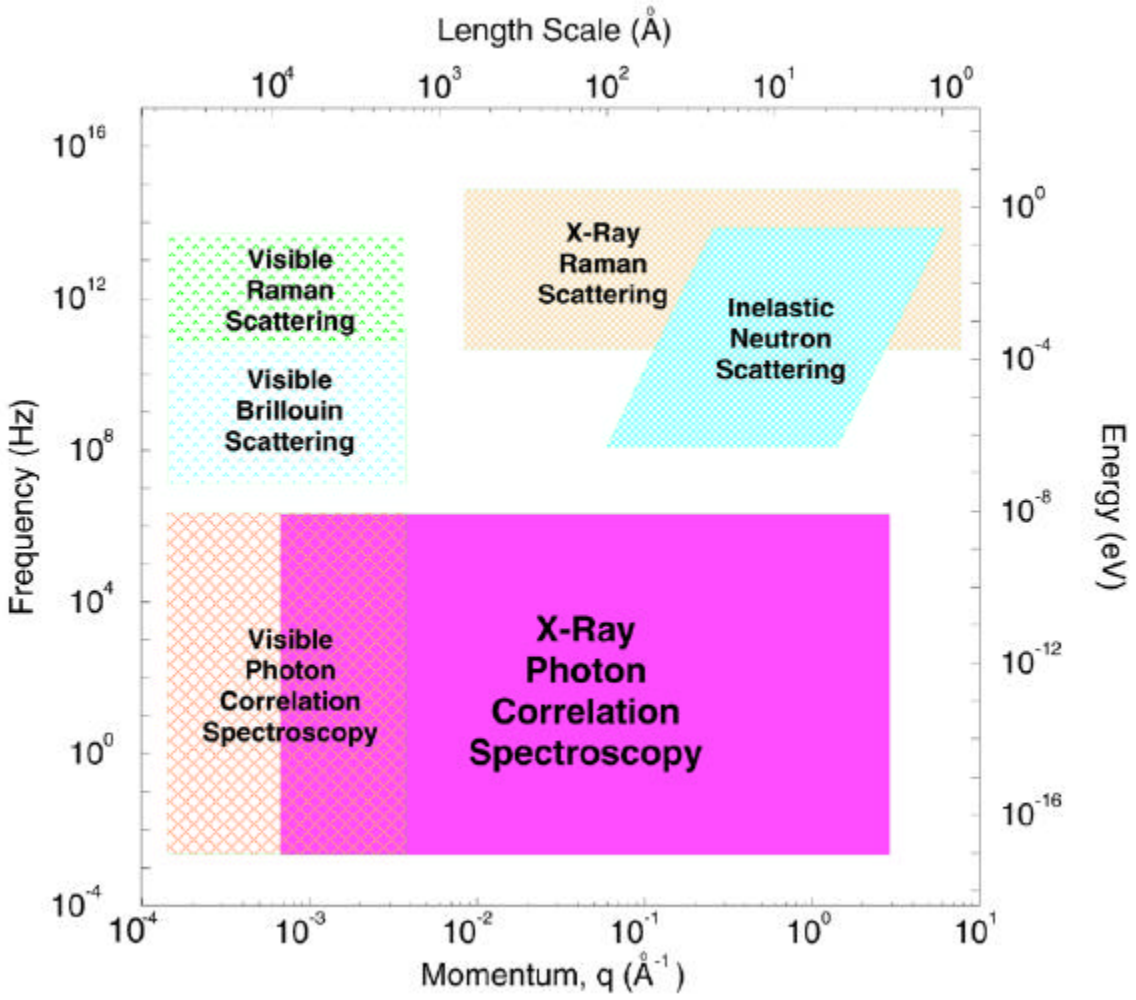

Figure 2.4. Regions of energy-momentum space accessible to various experimental techniques. XPCS provides a unique ability to study excitations in the previously inaccessible region of low energy and large momenta.

as shown in Figure 2.5. In addition to covering the range of diffusion coefficients typically covered by the visible PCS range, this also extends about 7 orders of magnitude lower than measurable with visible PCS. There are many systems for which this lower range of diffusion coefficients is the most interesting. The characteristic *q*-ω regime of diffusive excitations in solids, polymers, and complex fluids are also shown in Figure 2.5.

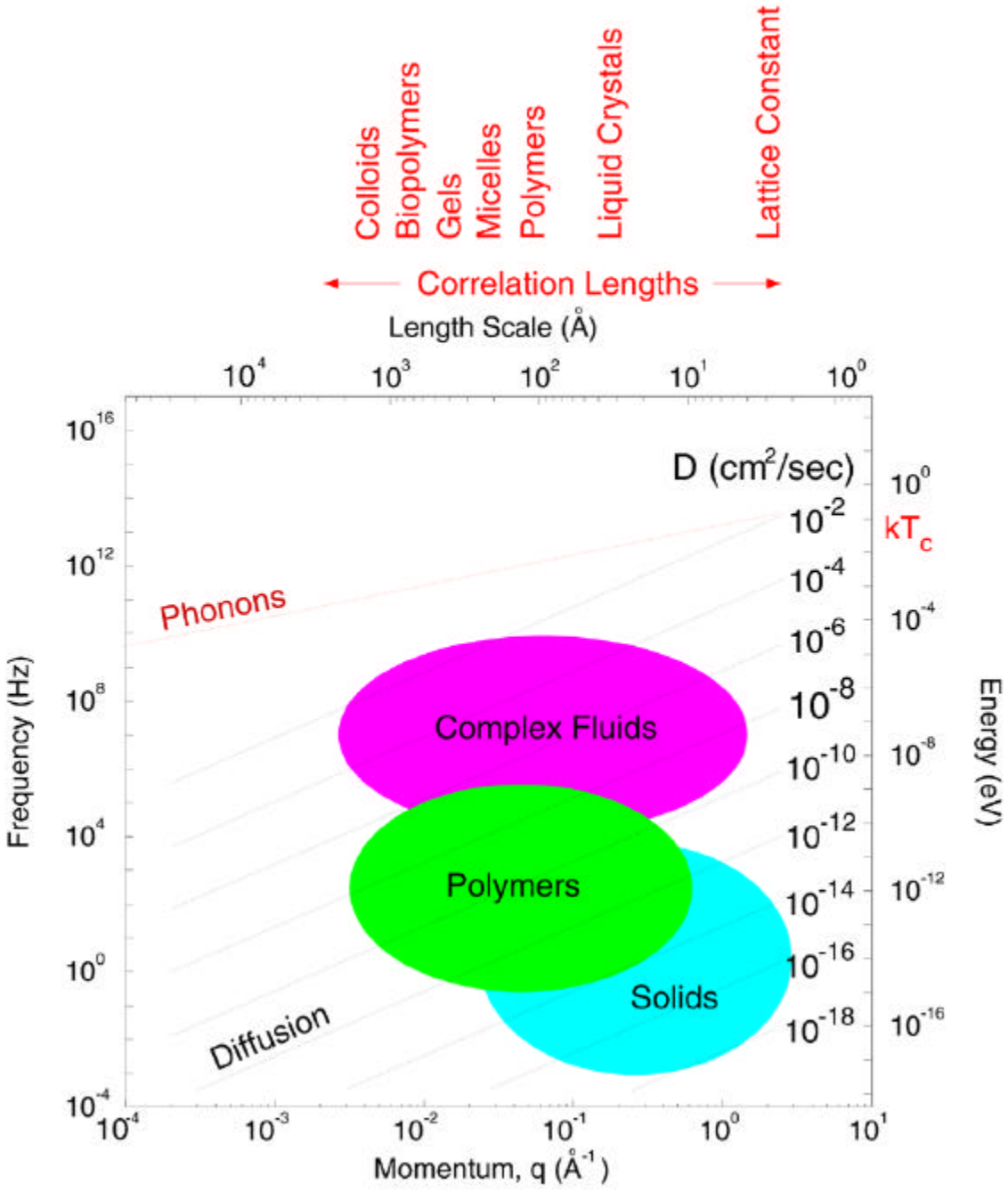

Figure 2.5. Diffusive excitations that can be studied with XPCS. The characteristic lengths of microstructures in various systems are also shown.

This regime has not been extensively studied previously due to the lack of adequate techniques for doing so.

It is an amazing fact that the collective dynamics of condensed matter systems, with of order 10^{23} constituent particles, can be characterized in the long wavelength limit in terms of just a few slow variables, such as, e.g., phonon modes or concentration fluctuations. This is understood from the theory of hydrodynamics to arise from the conserved quantities in the system. However, the fundamental assumptions of hydrodynamics break down on short length scales; i.e., materials are not really continua and are not in thermodynamic equilibrium at short length scales. This means that there is no longer a separation of time scales between the fast local modes and the slow modes originating from the conserved quantities and broken symmetries. It is this separation of time scales that allows the fast modes to be considered as providing an *effective medium* for the slow modes. There have been various theoretical attempts to extend the theory to these cases, including memory function formalism and mode coupling theory[68]. Typically, hydrodynamics breaks down on the characteristic length scale of microstructure in a material. The characteristic length scales of a number of materials are also shown in Figure 2.5. Their dynamics are expected to be especially interesting on these length scales.

A brief list of opportunities for scientific study using XPCS include:

a. Studies of the dynamic structure factor of liquids on length scale down to the interatomic spacing, including colloidal systems, moderate molecular weight simple liquids, liquid crystals, and polymers.
b. Studies of solid alloy phase transitions, including spinodal decomposition and nucleation and growth studies, and order-disorder transition.

c. Studies of the dynamics of moving domain walls in incommensurate systems, including ferroelectrics, charge density wave systems, magnets, and adsorbates on surfaces.

d. Studies of surface dynamics, including roughening and faceting transitions on single crystal surfaces, and pattern formation dynamics accompanying surface chemical reactions, including during in-situ crystal growth.

e. Studies of internal conformational dynamics of polymer molecules.

f. Studies of the dynamics of short range density fluctuations at the glass transition.

CHAPTER 3.
CRITICAL BEHAVIOR OF BINARY MIXTURES OF SIMPLE FLUIDS AND OF POLYMERS

The Structure and Dynamics of Polymer Chains

Polymers consist of chains of repeating organic molecular units, called monomers[69]. The number of repeat units N in one chain is called the degree of polymerization, and can be extremely large. For example, polystyrene can have $N > 10^5$. The synthesis of such long chains without error is quite difficult. Two of the most common errors of particular relevance to physical studies are polydispersity and branching. Most polymerization techniques produce polymers with a very broad distribution of N. It is possible to obtain relatively narrow distributions either by physical selection via precipitations, gel permeation, chromatography, etc., or through special methods of synthesis, such as anionic polymerization[70].

Many parasitic reactions can occur during polymerization which lead to chains which are not perfectly linear, but which contain branch points. For example, industrial polyethylene has many three-functional branch points. In some cases, polymers are intentionally synthesized with the geometry of “stars” or “combs”, as shown in Figure 3.1. In general, it is possible to obtain strictly linear chains if N is not too large, or it is

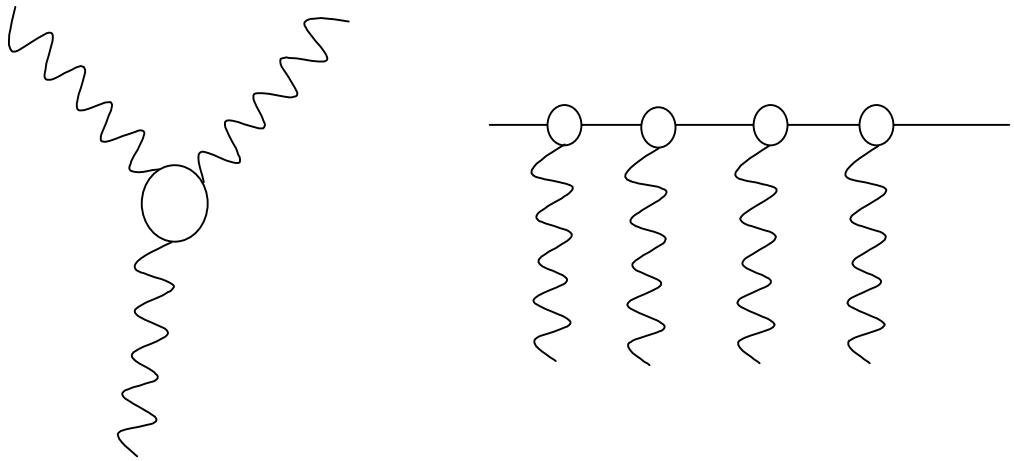

Figure 3.1. Common branched polymers structures.

possible to insert a controlled number of branch points. More often branching takes place statistically.

The flexibility of polymer chains can be understood either in a static or a dynamic sense. As an example, consider a simple carbon-carbon chain such as polyethylene. The angle q between successive C – C bonds is essentially fixed, but when we build up successive units with carbon atoms (n-3, n-2, n-1) fixed, and add carbon (n), we have one additional degree of freedom, i.e., the azimuthal angle j_n, as shown in Figure 3.2. There are three energy minima, corresponding to the three principal conformations, called trans and gauche. Trans corresponds to $j_n = 0°$ and has the lowest energy minimum. The two gauche conformations, which have $j_n = \pm 120°$, are degenerate and are $\Delta\varepsilon$ higher in energy than the gauche minimum. There is also an energy barrier ΔE between minima. Figure 3.3 shows a sketch of the energy between successive groups as a function of azimuthal angle.

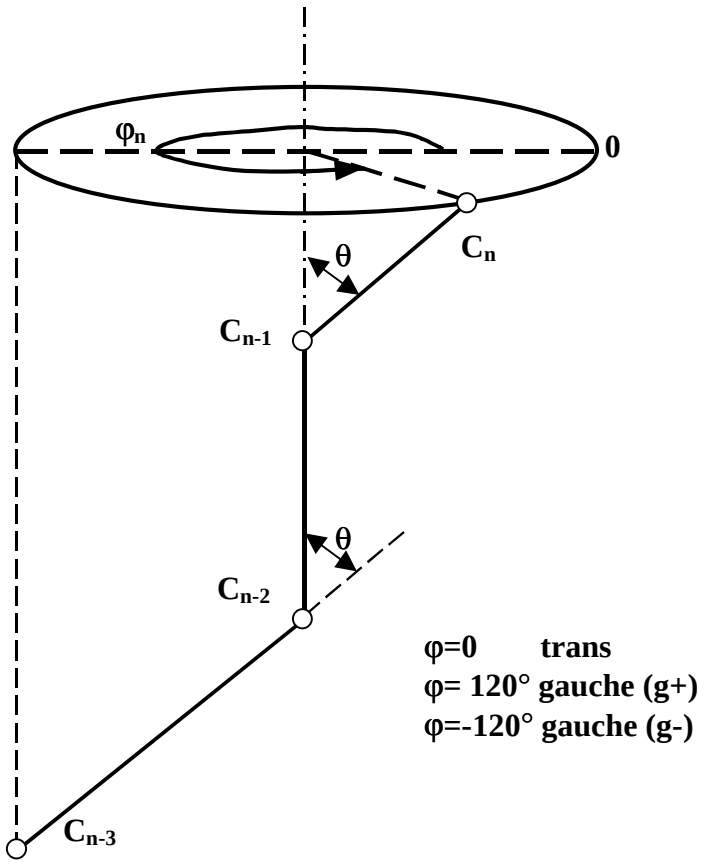

Figure 3.2. Orientational diagram for C – C link in a polymer chain. Trans and gauche principal conformations.

When $\Delta\varepsilon$ is smaller than the thermal energy k_bT, we say that the chain is statically flexible. This has striking consequences if we look not at one monomer but at the whole chain. Because the relative weight of gauche/trans conformations is of order unity, the chain is not fully stretched. It appears rather as a random gaussian coil. The case $\Delta\varepsilon < k_bT$ defines a limit of extreme flexibility. If we go to slightly higher values of $\Delta\varepsilon/k_bT$, there will be a definite preference for the trans state; locally the chain will be rigid. However, if we look at it on a scale that is large enough, it will again appear as a flexible coil.

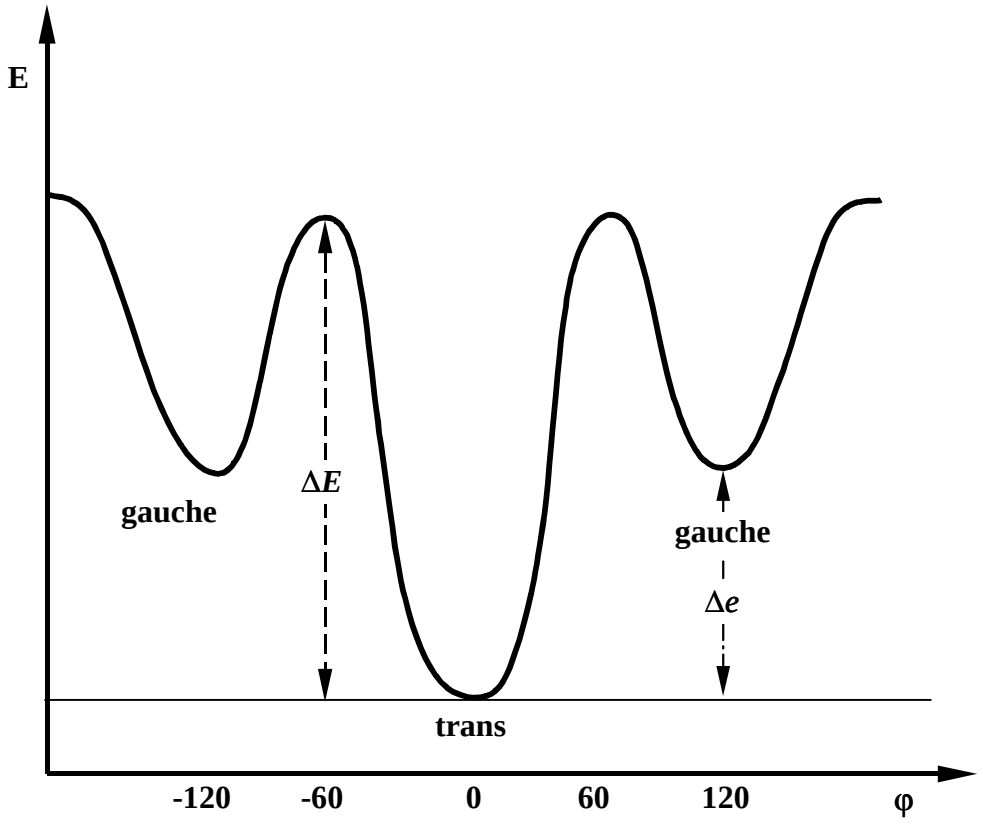

Figure 3.3. Energy between successive polymer groups as a function of conformational angle. ΔE is the barrier energy separating the minima, Δe is the energy difference between minima.

A useful measure of the size of a gaussian coil is the so-called radius of gyration, R_g. R_g is defined as the root mean square end-to-end distance of the chain. For gaussian coils, the radius of gyration is related to *a*, the statistical segment length, in the mean field approximation, via

$$R_g = a \cdot \sqrt{(N/6)}\,. \qquad \textbf{(3.1)}$$

The dynamic flexibility of a polymer chain is related to the time t_p required for a transition between trans and gauche states. This depends mainly on the height ΔE of the barrier separating them. If ΔE is not much larger than the thermal energy, the barrier is not important, and trans-gauche isomerization can take place in a typical time for a molecular vibration, i.e, $t_p \sim t_o \sim 10^{-11}$ sec. The chain is then said to be dynamically flexible. On the other hand, if the barrier ΔE is high, t_p becomes exponentially long: $t_p = t_0 \exp(\Delta E / k_b T)$. t_p is sometimes called the persistence time. The limit of very long time t_p leads to very rigid molecules. This is also characteristic of the so-called glass state.

The dynamics of the motion of a single polymer chain through a surrounding medium is very complex. It depends not only on the characteristics of the chain itself, but also on those of the surrounding medium. One especially important characteristic of the medium is the length scale on which the medium geometrically constrains the polymer, which is usually referred to as the "entanglement" length. On length scales shorter than the entanglement length, local vibrational motion of the individual polymer chain, including the hydrodynamic influence of the surrounding medium, will primarily determine the polymer motion. On length scales larger than the entanglement length, the polymer motion also depends on the nature and motion of the geometric constraints imposed by the surrounding medium. There are two main models for discussing polymer dynamics, which emphasize these different length scales. The Rouse model of dynamics applies on short length scales and the Reptation model applies on long length scales.

The classical Rouse[69,71] model is based on the notion of relaxation modes for one chain. Rouse described the chain as a succession of beads $\mathbf{r}_1 \ldots \mathbf{r}_n \ldots \mathbf{r}_{n+1}$ separated by

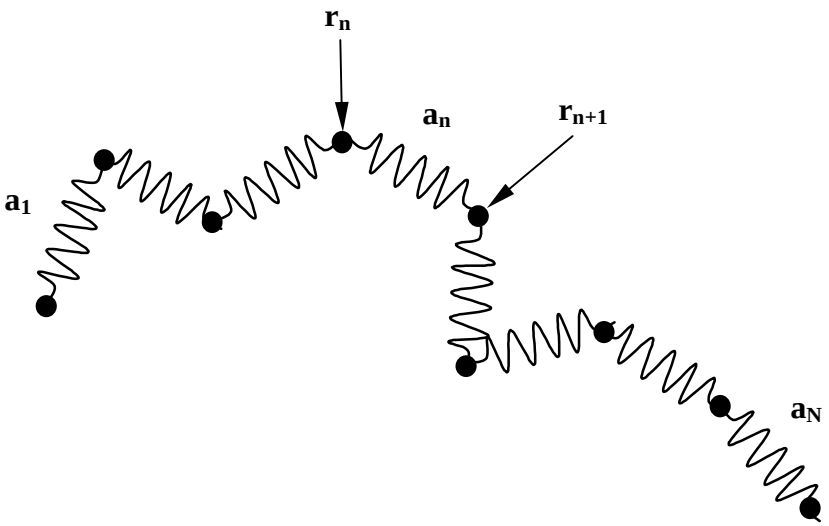

Figure 3.4. Illustration of the Rouse model of an elastic polymer chain. The $\mathbf{a_n}$ represent polymer subchains sufficiently long to obey Gaussian statistics. The $\mathbf{r_n}$ represent "beads", or connection points.

springs along vectors $\mathbf{a}_1 \ldots \mathbf{a}_N$, as shown in Figure 3.4. A spring can be thought of as a sequence, or subchain, of monomers, which is long enough to obey Gaussian statistics. The elastic energy for a subchain is then:

$$F_{n,n+1} = \frac{3k_bT}{2}\frac{(\mathbf{r}_{n+1}-\mathbf{r}_n)^2}{\left\langle(\mathbf{r}_{n+1}-\mathbf{r}_n)^3\right\rangle} = \frac{3k_bT}{2}\frac{\mathbf{a}_n^2}{a^3} \qquad \textbf{(3.2)}$$

where a is the average size of one subchain. The total elastic energy is the sum

$$F_{el} = \sum_0^{N-1} F_{n,n+1}\,. \qquad \textbf{(3.3)}$$

The model used by Rouse assumes "Phantom chains", i.e., chains are not prevented from crossing either themselves or other chains; entanglements are ignored.

The Rouse model also assumes that the response is local. Each bead experiences a force f_n from its two neighbors

$$f_n = -\frac{\partial F_{el}}{\partial \mathbf{r}_n} = \frac{3k_bT}{a^2}\left[(\mathbf{r}_{n+1} - \mathbf{r}_n) + (\mathbf{r}_{n-1} - \mathbf{r}_n)\right]. \quad \textbf{(3.4)}$$

It is then assumed that the velocity of bead ***n*** is a linear function of the forces applied to *n* and its neighbors

$$\frac{\partial \mathbf{r}_n}{\partial t} = \sum_m m_{nm} f_n \quad \textbf{(3.5)}$$

where m_{nm} is a mobility and is nonzero only for *n* close to *m* (locality of response). With a suitable redefinition of the subchains it is always possible to arrange that $m_{\mathrm{nm}} = 0$ for $n \neq m$, and to keep only one mobility constant $m_{\mathrm{nm}} = m$. This way the equation for the velocity of bead *n* reduces to

$$\frac{\partial \mathbf{r}_n}{\partial t} = m \cdot f_n \cong \frac{3k_bTm}{a^2}\frac{\partial^2 r}{\partial n^2} \quad \textbf{(3.6)}$$

This equation must be supplemented by boundary conditions at both ends of the chain:

$$\frac{\partial \mathbf{r}_n}{\partial n}|_0 = \frac{\partial \mathbf{r}_n}{\partial n}|_N = 0 \quad \textbf{(3.7)}$$

The motion of the beads can then be expressed in the form of eigenmodes

$$\mathbf{r}_{np}(t) = \cos\frac{ppn}{N}\exp(-t/t_p)\mathbf{á}_p \quad \textbf{(3.8)}$$

where *p* is a positive integer, and α_p is the mode amplitude. The relaxation time of mode *p* is

$$\frac{1}{t_p} = 3p^2\frac{Tm}{a^2}\left(\frac{p}{N}\right)^2. \quad \textbf{(3.9)}$$

If a Rouse chain is considered in a solvent, than its relaxation is considered through hydrodynamic diffusion, with associated friction. A Rouse chain may also be considered inserted into a matrix, or a network of polymer chains, where it moves through a random process of vacancy diffusion.

While the Rouse model is a good representation of the essential dynamics on short length scales, the reptation model[69] attempts to describe the motion of chains in a medium having a network of entanglements. The chain is not allowed to cross any of the entanglements, but it can move through them in a wormlike fashion. This process is called reptation. Reptation is similar to unraveling a knot. We begin by accumulating a stored length in one portion of the knot, and then we circulate it to different loops, up to the moment we have relaxed an essential constraint.

The Rouse model of a single, essentially unconstrained chain and the reptation model of a constrained chain in an entangled network of a polymer melt are well developed and have undergone continued refinements They form the basis for understanding the dynamics of polymer-solvent or polymer-polymer systems where the concentration of one constituent fluctuates. The resulting concentration fluctuations are particularly large near phase transitions.

Phase Transitions and Critical Phenomena

Phase transitions are common phenomena in a variety of different physical and chemical systems. The systems studied in this thesis are mixtures of two components that exhibit an order-disorder transition between a mixed, single phase state and a phase separated, two phase state. The phase state is governed by a balance between enthalpic (H

= U + PV where U, P, and V represent the energy, pressure, and volume, respectively) and entropic (S) factors that together constitute the system (Gibbs) free energy

$$G = H - TS\,, \tag{3.10}$$

Theoretical expressions for G are the starting point for predicting equilibrium phase behavior. Statistical models for the molecular configuration of a mixture that depend on molecular architecture, volume fraction, ϕ, degree of polymerization, N, and the energetics of the interaction between molecules, are the basis for formulating the mixture free energy.

Nearly 60 years ago Flory[72] and Huggins[73] independently estimated the change in the Gibbs free energy per segment, ΔG_m, associated with mixing random walk (Gaussian) polymer chains on an incompressible ($f_A + f_B = 1$) lattice,

$$\frac{\Delta G_m}{kT} = \frac{j_A}{N_A}\ln j_A + \frac{(1-j_A)}{N_B}\ln(1-j_A) + j_A(1-f_A)c\,, \tag{3.11}$$

where k is the Boltzman constant. The first two terms account for the combinatorial entropy of mixing, ΔS_m. Because mixing increases the system's randomness, it naturally increases ΔS_m and thereby decreases the free energy of mixing. Large chains can assume fewer mixed configurations than small chains so that ΔS_m decreases with increasing N. The third term represents the enthalpy of mixing, ΔH_m, and can either increase or decrease ΔG_m depending on the sign of χ.

χ is known as the Flory-Huggins segment-segment interaction parameter, and is given by

$$c = \frac{1}{kT}\left[e_{AB} - \frac{(e_{AA} + e_{BB})}{2}\right] \quad \textbf{(3.12)}$$

where ε_{ij} represents the contact energy between i and j segments. A negative value of χ results from a favorable energy of mixing, that is, A-B segment-segment contacts on average produce lower system energy than the average of A-A and B-B contacts. Certain types of specific A-B interactions, such as hydrogen bonding, can result in a negative χ paramter, and the system is always mixed. Positive values of χ occur when the net system energy increases upon forming A-B contact pairs from unmixed components. In this case, there may be a finite temperature phase transition.

Although the simple Flory-Huggins expression for ΔG_m is a mean-field theory that neglects spatial fluctuations in composition, it nonetheless predicts most of the observed phenomena of binary phase behavior. For $N = 1$ it reduces to regular solution theory, which is widely applied to low molecular weight solution thermodynamics[74] and which is a good (mean field) model for the hexane/nitrobenzene mixture studied in Chapter 5.

The phase behavior can be predicted from Equation (3.11) based on the standard criteria[74] for equilibrium, stability, and criticality evaluated at constant temperature and pressure:

Equilibrium: $$\frac{\partial \Delta G_m(j'_A)}{\partial j_A} = \frac{\partial \Delta G_m(j''_A)}{\partial j_A} \quad \textbf{(3.13)}$$

Stability: $$\frac{\partial^2 \Delta G_m}{\partial^2 j_A} = 0 \quad \textbf{(3.14)}$$

Criticality: $$\frac{\partial^3 \Delta G_m}{\partial^3 j_A} = 0 \quad \textbf{(3.15)}$$

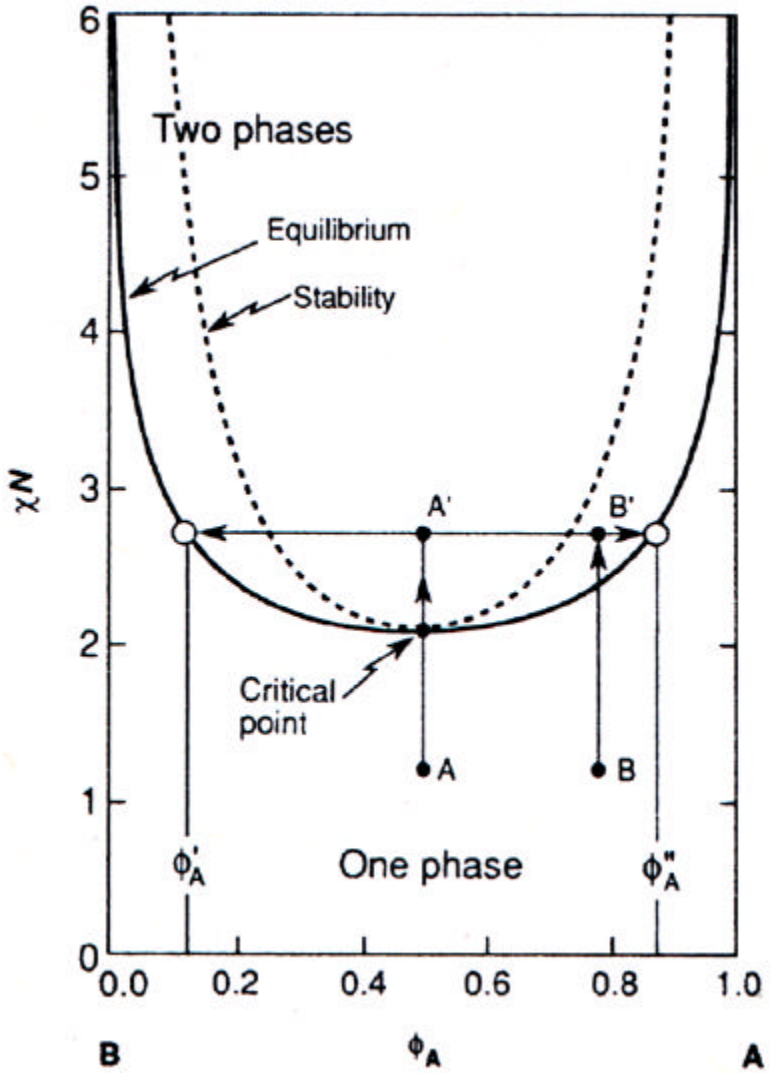

Figure 3.5. Theoretical mean field phase diagram for a symmetric ($N_A = N_B = N$) binary mixture of linear homopolymers.

where the superscripts f' and f'' refer to separate phases. Solving Equation (3.11) subject to these constraints yields the phase diagram shown in Figure 3.5 for the symmetric case $N_A = N_B = N$. The solid curve represents the solution of the equilibrium condition, Equation (3.13). For combinations of χN and ϕ lying inside this curve a mixture separates into two coexisting phases with compositions f'_A and f''_A, as shown in Figure 3.5. This is often signified by referring to the solid curve as the *coexistence* curve.

Between the solid and dashed curves a homogeneous mixture is thermodynamically metastable, while inside the dashed curve a mixture is thermodynamically unstable. The issues of metastability and stability are discussed further below. At the critical point, corresponding to a critical interaction parameter, c_c, and critical composition, f_c, the equilibrium and stability curves coincide and the transition is second order with divergent physical behavior. Combination of Equations (3.14) and (3.15) yields

$$f_c = \frac{N_A^{1/2}}{N_A^{1/2} + N_B^{1/2}} \qquad \textbf{(3.16)}$$

$$c_c = \frac{(N_A^{1/2} + N_B^{1/2})^2}{2N_A N_B} \quad . \qquad \textbf{(3.17)}$$

For a symmetric mixture $(\chi N)_c = 2$ and $f_c = 0.5$, as indicated in Figure 3.5. At other compositions, the transition is first order.

In the metastable region, phase separation occurs by a process of nucleation and growth. Classical nucleation theory[75] predicts that small droplets of a minority phase develop over time in a homogenous mixture that has been brought into the metastable region, e.g., from point B to point B' in Figure 3.5. Since the droplets have positive interfacial energy, droplet formation is a thermally activated process and is usually slow. Initially, droplet growth proceeds by diffusion of material from the supersaturated continuum. However, once the composition of the supernatant reaches equilibrium (f_A'' in Figure 3.5), further increases in droplet size occur by droplet coalescence or Ostwald ripening; the latter refers to the growth of large droplets through the "evaporation" of smaller ones.

In the metastable state, homogeneous mixtures must overcome a free energy barrier in order to nucleate a new phase. In the thermodynamically unstable state, there is

no such barrier, and mixtures phase separate spontaneously, e.g., from point A to A' in Figure 3.5. This process is known as spinodal decomposition[76]. It results in a disordered bicontinuous two-phase structure, in contrast to the droplet structure associated with the nucleation and growth mechanism. The initial size of the spinodal structure is controlled by the quench depth, $\chi_s - \chi$, where χ_s corresponds to the stability limit (dashed curve in Figure 3.5); deeper quenches produce finer structures. Almost immediately after the bicontinuous pattern begins to form, interfacial tension drives the system to reduce its surface area by increasing the size of the spinodal structure. In symmetric critical mixtures ($N_A = N_B = N$ and $\phi_c = 0.5$) coarsening does not disrupt the bicontinuous morphology, which evolves in a universal, scale invariant form.

The state of a binary mixture undergoing such an order-disorder transition can be described by the value of its order parameter, $y = (f - f_c)/f_c$, i.e., the normalized difference between the composition and the critical composition. Near the critical point, the system exhibits large fluctuations of the order parameter y, which give rise to intense scattering known as critical opalescence. These fluctuations have a certain characteristic length scale, known as the correlation length x, which increases as the phase transition is approached. For a mixture with the critical composition, x diverges at the critical point. Far from the critical point, in the single-phase region, the correlation length is typically comparable to the size of a mixture component. This value is often referred to as the bare correlation length, x_o.

The Fourier transform of the spatial autocorrelation function of the order parameter fluctuations is known as the Structure Factor. The structure factor for

concentration fluctuations can be derived[69,77,78] from Equation (3.11) and written in the form

$$S(q,T) \propto k_B \cdot T \cdot \Lambda \cdot G(q \cdot x), \quad \textbf{(3.18)}$$

where $G(x)$ is a scaling function, T is the temperature, L is the osmotic compressibility, q is the wave vector and x is the correlation length of the composition fluctuations. G(x) has the Ornstein-Zernicke form

$$G(x) = \left(1 + x^2\right)^{-1} \quad \textbf{(3.19)}$$

where $x = qx$. Since in all of the experiments reported in this thesis, $x < 3$, the Ornstein-Zernicke form provides a reliable approximation for G(x).

In general, the behavior of the characteristic quantities of a system in the vicinity of a critical point is described in terms of power laws[79,80], e.g. for L and x,

$$\Lambda = \Lambda_0 \cdot e^{-g} \quad \textbf{(3.20)}$$

$$x = x_0 \cdot e^{-n} \quad \textbf{(3.21)}$$

where γ and ν are critical exponents, L_0 and x_0 are prefactors giving the value of the susceptibility and correlation length far from the critical point, and e is the distance from the critical point. It is common to express ε in terms of some external control parameter, such as temperature. In the Flory-Huggins theory, $e = (c_c - c)/c_c$. Hence, the temperature dependence of c determines the nature of the scaling behavior.

There can be various contributions to c in organic liquid mixtures, including polymers. One of the most important contributions to the interaction energy between

nonpolar molecules are dispersive van der Waals interactions, which can be represented by[69]

$$e_{ij} = -\sum_{ij} \frac{3}{4} \frac{I_i I_j}{I_i + I_j} \frac{a_i a_j}{r_{ij}^6} \qquad \textbf{(3.22)}$$

where r_{ij} is the segment-segment (or molecule-molecule in a mixture of small molecule liquids) separation, and a and I are the segment polarizability and ionization potential, respectively. If there is no volume change ($DV_m = 0$) or preferential segment orientation upon mixing, Equations (3.12) and (3.22) can be rearranged to give

$$c = \frac{3}{16} \frac{I}{kT} \frac{z}{V^2} (a_A - a_B)^2 \qquad \textbf{(3.23)}$$

where a cubic lattice is assumed with $I_j = I_k = I$ (which is true within 10% for most hydrocarbons) and all but the z nearest neighbor contacts are neglected. Thus, van der Waals interactions give a positive χ, which can lead to a phase transition, as stated earlier.

For small molecule organic liquids such as the hexane/nitrobenzene mixtures presented in Chapter 5, van der Waals interactions are a good model for χ and so c has the weak temperature dependence of Equation (3.23). Near the critical point, c can be linearly expanded[77]

$$c(T) = c_c + c'(T - T_c) + \mathrm{O}(T - T_c)^2 \qquad \textbf{(3.24)}$$

and hence, neglecting terms of second order and higher,

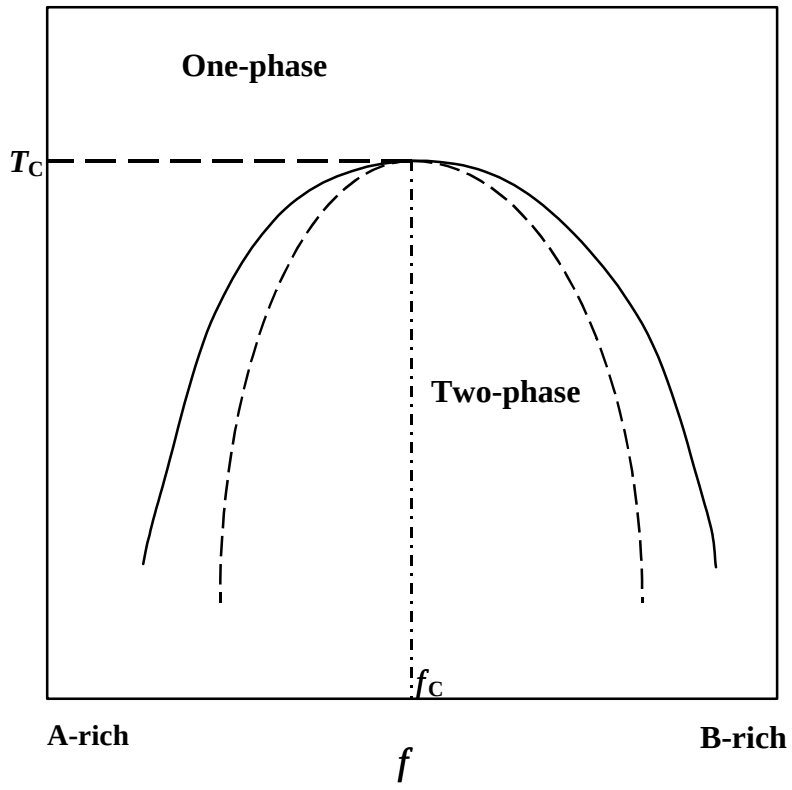

Figure 3.6. Typical temperature – composition phase diagram for a binary mixture having a UCST.

$$e = -\frac{c'}{c_c}(T - T_c) = \frac{c'T_c}{c_c}\frac{(T_c - T)}{T_c} = \frac{(T - T_c)}{T_c}, \qquad \textbf{(3.25)}$$

since, for χ given by Equation (3.23), $\chi' T_c/\chi_c = -1$. This is the usual form for the reduced temperature $t = (T\text{-}T_c)/T_c$. In this case, the homogeneous phase is the high temperature phase and the mixture phase separates upon cooling. There is an upper critical solution temperature (UCST), i.e., the coexistence curve is concave downward in a f vs T graph, as shown in Figure 3.6.

The situation is quite a bit more complicated in polymers, however. There are significant deviations from incompressibility and anisotropic monomer structures can

lead to nonrandom segment packing. These effects must be absorbed in c as excess entropy of mixing. In addition, Equation (3.11) represents a crude theory that neglects chain self-avoidance, self-contact, and intrachain and interchain segment correlations. These effects are usually included by empirically treating c in polymer mixtures as a phenomenological parameter of the form

$$c = \frac{a}{T} + b \tag{3.26}$$

where a and b represent empirical excess entropy and enthalpy coefficients for a particular composition. In general, a and b may depend on f, N, and molecular architecture. If a is positive and b is negative, decreasing temperature always increases χ and an UCST results. If a is negative and b positive, then a lower critical solution temperature (LCST) may result, i.e., the coexistence curve is concave upward on a f versus T graph, depending on the value of N and b. More complex forms for c can produce both UCST and LCST behavior, i.e., closed loop coexistence curves, with the two-phase region entered upon lowering the temperature but the one-phase region reentered upon lowering the temperature even further. UCST behavior, with positive a and negative b, is by far the most common and the rest of this discussion is restricted to that case. This is also the behavior displayed by the polystyrene/polybutadiene system studied in Chapters 6 and 7 as well as the hexane/nitrobenzene system studied in Chapter 5.

It is worth noting that since $c_c \sim 1/N$, c must be very small, especially for mixtures of large molecular weight polymers, in order for polymers to mix at all. In fact, van der Waals interactions by themselves are usually sufficient to prevent mixing, and

indeed most polymers are, in fact, incompatible. In most cases it is precisely the excess enthalpy contributions (b in Equation (3.23)) which contribute to lowering c sufficiently to allow mixing. In this case, c is small because there is a so-called compensation temperature[77,81,82] nearby where c vanishes. In this case, the assumption that c has a weak temperature dependence is invalid and it is common to use Equation (3.26) for χ directly in evaluating e. Then it is easy to show that

$$e \propto \frac{(T - T_c)}{T} \tag{3.27}$$

Note the term T in the denominator instead of T_c, as in Equation (3.25). Of course, Equations (3.25) and (3.27) are equivalent in the limit of $e \to 0$. However, Equation (3.27) can be a small but significant correction at larger reduced temperatures. We use Equation (3.27) in analyzing the data on polystyrene/polybutadiene mixtures presented in Chapter 7.

Several of the quantities relevant to critical phenomena are conveniently accessible experimentally. $S(q)$ can be determined from the rate of static small angle x-ray scattering, static light scattering or neutron scattering. The correlation length x can be derived from the angular dependence of the scattering intensity. The decay rate of fluctuations can be determined by photon correlation spectroscopy. For example, from Equation (3.18), in a SAXS experiment on a simple binary fluid mixture the measured scattering rate, $I(q,T)$, can be expressed as

$$I(q,T) = \frac{I_0 \cdot t^{-g}}{1 + q^2 \cdot x_0^2 \cdot t^{-2n}} + Bg(q), \tag{3.28}$$

where $Bg(q)$ is a q-dependent background term, with contributions from parasitic scattering of the beamline components and air, and the temperature independent

scattering from the individual mixture components. This expression is used to analyze the SAXS from binary fluids presented in chapter 5.

The values of the critical exponents γ and ν are predicted[83] in the framework of classical mean-field theory to be $\gamma = 1.0$ and $\nu = 1/2$, and in Ising theory to be $\gamma = 1.26$ and $\nu = 0.63$. The crossover between mean-field and Ising behavior is governed by the so-called Ginzburg criterion[84]. It states that mean-field theory ceases to be applicable when the fluctuations of the order parameter y become comparable with its average value. Then it can no longer be considered that a molecule in an A-B mixture "feels" an average interaction of A and B molecules. The crossover is not abrupt but is described by a crossover function.

In a mixture of low-molecular weight liquids, the system always behaves according to Ising theory, since the fluctuations in the system are always larger than the size of the constituent molecules. This is clearly demonstrated in Chapter 5 where the results of studies of the static critical behavior of a binary mixture of hexane and nitrobenzene are reported.

In the case of polymers, on the other hand, it is generally anticipated that mean-field theory is applicable[85]. For a binary mixture of symmetric polymers with the same N and R_g, where R_g is the radius of gyration from Equation (3.1), the Ginzburg criterion predicts that[86,87]

$$e_x \sim N^{-1}. \qquad \textbf{(3.29)}$$

For asymmetric polymer mixtures with different degrees of polymerization $N_A \neq N_B$ and segment lengths $a_A \neq a_B$ the appropriate Ginzburg criterion is[88]

$$e_x = C \cdot u_m^2 \frac{\left[N_A^{-1} \cdot f_A^{-3} + N_B^{-1} \cdot f_B^{-3}\right]^2}{\left[N_A^{-1} \cdot f_A^{-1} + N_B^{-1} \cdot f_B^{-1}\right] \cdot \left[R_{gA}^2 \cdot N_A^{-1} \cdot f_A^{-3} + R_{gB}^2 \cdot N_B^{-1} \cdot f_B^{-3}\right]^3}, \qquad \textbf{(3.30)}$$

where C = 0.29 is a system-independent constant and u_m is the geometric mean of the segment volume of each species, $u_{mi} = M_{Wi} / N_i \cdot r_i \cdot N_{av}$, where N_{av} is Avogadro's number. For the symmetric mixture this equation reduces to Equation (3.29).

For polymer chains, N is typically 10^2-10^4. So, R_g is large compared with the extent of a typical fluctuation, except for a narrow region in the vicinity of the critical point, where $x > R_g$. However, since the width of the non-classical region is related to R_g, it is possible to design polymeric systems of relatively low molecular number, which exhibit a transition between mean field and Ising behavior with varying temperature[88,89,90,91]. For example, the width of the critical region was reported to be less than 2 K in a polystyrene/polyvinylmethylether[89] mixture with $N \sim 10^3$ and about 30 K in a polyisoprene/poly(ethylene-propylene)[88] mixture with a much lower molecular weight.

We also found clear evidence for a mean-field to Ising crossover in the static critical behavior of a mixture of polystyrene and polybutadiene, which had molecular weights of 2000 and 1000, respectively, as reported in Chapter 7.

Decay Rate and Mode Coupling

As a system approaches the critical point and the fluctuations become larger it takes a longer time for them to relax back to equilibrium. This relaxation time, t, diverges at the critical point. This phenomenon is called critical slowing down[69]. The relaxation

rate Γ (inverse of the relaxation time *t)* of the order parameter fluctuations for a scattering vector *q* can be expressed as[92,93,94]

$$\Gamma(q) = \frac{\Omega(q)}{S(q)} \cdot q^2 , \qquad \textbf{(3.11)}$$

where *S(q)* is the static structure factor, which is identical to the susceptibility of the system, and Ω*(q)* is a microscopic dynamic Onsager kinetic coefficient, i.e., a transport coefficient. It can be thought of as a local diffusivity.

The detailed description of dynamics in the vicinity of a critical point is rather complicated and not completely understood. The description of the dynamics given in Equation (3.31), in terms of a susceptibility and a kinetic coefficient, is the result of essentially a linear theory. However, especially near the critical point, non-linear interactions between the fluctuations of the order parameter and the fluctuations of the momentum density can be important. The effects of these interactions are described by what is known as mode coupling theory. Mode coupling effects are particularly interesting in the case of polymer mixtures, where they are influenced by the microstructure of the polymers.

Leading order mode coupling contributions for Ω(*q*) have been calculated[95,98]:

$$\Omega(q) = \Omega_0(q) + k \cdot T \cdot \int d\mathbf{k} \cdot \hat{q} \cdot O(\mathbf{k}) \cdot \hat{q} \cdot S(q), \qquad \textbf{(3.32)}$$

where O(k) is the Oseen tensor with components $O_{ab}(\mathbf{k}) = \left(d_{ab} - \hat{k}_a \hat{k}_b\right) \Big/ 8p^3 h\, k^2$, $\hat{q} = \mathbf{q}/|q|$ is the unit vector in the direction of **q** and *h* is the viscosity. $\Omega_0(q)$ is the bare Onsager coefficient.

Kawasaki and Lo[96,97] derived an expression for the critical part of the decay rate of order parameter fluctuations which is appropriate to systems which are well described by a continuum approximation, i.e., which do not have any length scale other than the correlation length. They found

$$\frac{\Gamma_c}{q^3} = \frac{k \cdot T}{8 \cdot p \cdot h} \cdot (q \cdot x)^{-3} \cdot \left[1 + (q \cdot x)^2 + \left\{(q \cdot x^3) - (q \cdot x)^{-1}\right\} \cdot \tan^{-1}(q \cdot x)\right], \qquad \textbf{(3.33)}$$

where h is the viscosity and x the static correlation length. In the purely hydrodynamic region ($T >> T_c$, $qx < 1$) this equation simplifies to

$$\frac{\Gamma_c}{q^3} = \frac{k \cdot T}{8 \cdot p \cdot h} \cdot (q \cdot x)^{-1}, \qquad \textbf{(3.34)}$$

and thus

$$D = \frac{\Gamma_c}{q^2} \propto x^{-1}, \qquad \textbf{(3.35)}$$

where D is the diffusion coefficient.

In the critical non-diffusive region ($T >> T_c$, $qx > 1$), Equation (3.33) yields

$$\frac{\Gamma_c}{q^3} = const. \qquad \textbf{(3.36)}$$

We see that in the hydrodynamic region the relaxation of fluctuations proceeds via a diffusive process $\Gamma \propto q^2$, whereas closer to the critical point this behavior changes to $\Gamma \propto q^3$. The crossover between the two regimes can be quantified in terms of a dynamic scaling exponent $z(e)$:

$$\Gamma(T) \propto q^{z(e)}. \qquad \textbf{(3.37)}$$

Whether this crossover is accessible depends on the experimental technique, which determines the range of accessible values of q.

The situation is quite a bit more complicated in the case of polymer mixtures, due to the influence of the microstructure of the polymers on their transport coefficients. Binder[77] has shown that for a symmetric binary mixture,

$$\Omega_0(q) = 12\, l\, f(1-f) N_e N^{-2} (qa)^{-2} \left\{ 1 - \left[1 - \exp(-R_g^2 q^2)\right] \Big/ R_g^2 q^2 \right\}, \qquad \textbf{(3.38)}$$

where l is the segment based Onsager coefficient, and a is the segment length. For the case of polymer chains below their entanglement length, $N \le N_e$, N_e is replaced by N to obtain an expression for the bare Onsager coefficient that is appropriate for Rouse chains. For the case of chains above their entanglement length $N > N_e$, Equation (3.3) provides an expression for the bare transport coefficient that is based on the reptation mode[69].

Building on Binder's work, Fredrickson and Bates have derived an expression for the critical decay rate of polymer blends[98,99]. In terms of a dimensionless decay rate

$$\Gamma^* = \frac{6 \cdot p \cdot h \cdot x^3}{k \cdot T} \cdot \Gamma, \qquad \textbf{(3.39)}$$

where Γ is the experimentally measured decay rate, their result is, for $qR_g < 1$,

$$\Gamma^* = (q \cdot x)^2 \cdot (1 + q \cdot x)^2 \cdot \left[K(q \cdot x) + G \cdot R_g \cdot \frac{N^{3/2}}{N_e} \cdot \frac{1}{x} \right], \qquad \textbf{(3.40)}$$

where G is a constant and N_e is the average number of segments between entanglements. K is the Kawasaki scaling function:

$$K(x) = \frac{3}{4} \cdot \left[\frac{1}{x^2} + \left(\frac{1}{x} + \frac{1}{x^3} \right) \cdot \tan^{-1}(x) \right]. \qquad \textbf{(3.41)}$$

Equation (3.40) involves three characteristic length variables: R_g, x, q^{-1}, the respective ratios of which determine four possible dynamic regions when the condition that $qR_g < 1$ is met. R_g is an intrinsic property of the constituent molecules, q is a property of the measurement technique, and x reflects the thermodynamic conditions, i.e. the distance from the critical point.

These four regions can be classified as hydrodynamic and non-diffusive according to the value of the product qx, and as mode-coupled or mode-decoupled according to the value of $x / R_g\sqrt{N}$:

Region I. $qx << 1$ and $\xi < R_g N^{3/2}/N_e$, where the mode-coupling correction $K(x)$ is negligible and $\Gamma^*(q) \propto GN^{3/2}N_e^{-1}R_g q^2 x$

Region II $qx << 1$ and $\xi > R_g N^{3/2}/N_e$, where the mode-coupling correction dominates and $\Gamma^*(q) \propto q^2 x^2$

Region III. $qx >> 1$ and $qR_g << N_e/N^{3/2}$, where the mode-coupling correction dominates and $\Gamma^*(q) \propto (3\pi/8) q^3 x^3$

Region IV. $qx >> 1$ and $qR_g << N_e/N^{3/2}$, where the mode-coupling correction is again negligible and $\Gamma^*(q) \propto GN^{3/2}N_e^{-1}R_g q^4 x^3$

Since it is possible to determine the viscosity h, but the correlation length in not always available, we can use the relation $x \propto e^{-\nu}$ near the critical point, and conveniently introduce an experimentally measurable reduced decay rate as[100]

$$\Gamma_r = \Gamma^* / x^3 = \left[6 \cdot p \cdot h(T) \cdot \Gamma(T)\right] / k \cdot T \qquad \textbf{(3.42)}$$

Then for low molecular weight mixtures ($N \approx N_e$) the predictions for the four dynamic regions are:

Region I. $\Gamma_r(q) \propto q^2 e^{2\nu}$, with $qx << 1$ and $x << R_g N^{0.5}$,

Region II. $\Gamma_r(q) \propto q^2 e^{\nu}$, with $qx << 1$ and $x >> R_g N^{0.5}$,

Region III. $\Gamma_r(q) \propto q^3 e^{0}$, with $qx >> 1$ and $qR_g << N^{-0.5}$,

Region IV. $\Gamma_r(q) \propto q^4 e^{0}$, with $qx >> 1$ and $qR_g >> N^{-0.5}$.

Figure 3.7 presents a schematic of the various expected dynamical regimes for a binary polymer mixture at the critical composition for the case of unentangled polymer chains. The ordinate is the dimensionless correlation length and is therefore essentially inverse temperature, and represents the state of a system. The Ginzburg criterion is indicated by the horizontal line at $x = R_g$, although there will be a prefactor assocated with this crossover and the crossover is not sharp, but rather is a crossover function in this vicinity. The dashed horizontal line at $x/R_g = N^{0.5}$ indicates the crossover to mode-coupled dynamics, and again some numerical prefactor occurs here. For entangled systems $N^{1/2}$ should be replaced by $N^{3/2}/N_e$. The abscissa is the normalized inverse scattering vector, $1/qR_g$, reflecting the length scale of the fluctuations being probed in a particular experimental geometry. The diagonal line corresponds to $qx = 1$ and separates the hydrodynamic regimes (below the line) from the non-diffusive regimes (above the line). The region above this line corresponds to experiments where the behavior of a system is probed on length scales shorter than x but still larger than R_g.

The expression for $\Gamma(q)$ in region II (mode coupled, $qx << 1$) can be rewritten in the Kawasaki-Stokes form

$$\frac{\Gamma(q)}{q^2} = D_c = \frac{kT}{6\pi h x_d}, \qquad \textbf{(3.43)}$$

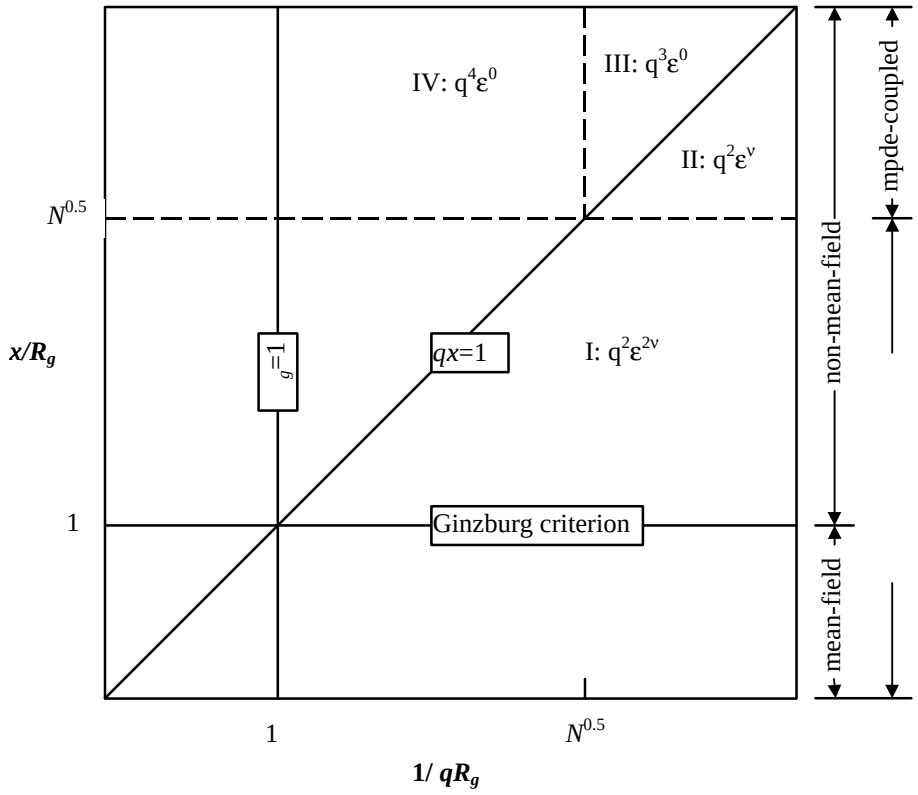

Figure 3.7. Schematic of dynamic behavior at the critical composition f_c. The ordinate is a normalized correlation length ξ/R_g and is essentially inverse temperature. The abscissa is a normalized inverse of the scattering vector $(q^{-1})/R_g$ and describes the geometry of an experiment. The individual regimes I-IV described are indicated as well as the Ginzburg criterion and the mode coupling crossover.

where x_d here is defined as the dynamic correlation length through this equation. It has been shown[96] that h is the macroscopic viscosity of the critical binary mixture in this case. Thus this equation can be used to determine the dynamic correlation length. The Kawasaki-Stokes relation is not generally valid for other dynamic regions.

The dynamic behavior in the regime $qR_g > 1$ is rather complicated in the general case of asymmetric homopolymer mixtures and special care has to be taken to obtain the bare Onsager coefficient for such systems[101]. The important predictions of the theory for the symmetric homopolymer mixtures relate to the scaling of the renormalized Onsager coefficient from Equation (3.31), $\Omega(q)$, which determines the dynamical response of the polymeric system to small perturbations from equilibrium. For the regime $qR_g >> 1$, in which we probe distances smaller than R_g, the second term in Equation (3.32) for $\Omega(q)$, is negligible and $\Omega_0(q)$ varies like $1/q^2$:

$$\Omega_0 = 12\, l\, f(1-f) N_e N^{-2} (qa)^{-2}. \qquad \textbf{(3.44)}$$

In this case the prediction for $\Gamma(q)$ is:

$$\Gamma(q) \sim (qa)^2\, N_e / N^2. \qquad \textbf{(3.45)}$$

Due to the limitations on q for visible PCS, experimental studies in the regime $qR_g > 1$ have been limited to a small number of studies of very large molecular weight mixtures. Since the tendency to phase separate increases with molecular weight, these mixtures also had to be diluted in solvent. Hence, it is fair to say that the regime $qR_g > 1$ is essentially unstudied. We also did not probe this regime in the experiments reported here. Hopefully this will be rectified by future XPCS studies.

CHAPTER 4.

EXPERIMENTAL SETUP

Introduction

It is hard to overemphasize the importance of having a high quality small angle x-ray scattering experimental (SAXS) setup for conducting static and dynamic measurements of binary mixtures. In this chapter, I discuss what necessary conditions should be satisfied in order to obtain high quality data and the system we implemented to meet them.

It is relatively easy to specify an ideal experimental setup but it is often hard to reach that ideal. Here I will try to specify some primary aspects of a desirable SAXS setup:

1. Background noise level: Ideally, one would want only the sample scattering to be present at the detector. In reality, the measured signal is always a mixture of useful signal from the sample and the background.
2. Temperature control: Typical experiments on critical behavior involve changing the temperature of a sample, often in steps as small as mK. One measure of the quality of a SAXS setup for use in critical behavior studies is how stable the temperature is and how conveniently the temperature can be changed and monitored. Ideally the

temperature of the sample should be controlled and displayed remotely, outside the experimental hutch

3. Accessible range of scattering wave vectors, *q*: The range of angle accessible to the detector must be sufficient to cover the *q* range of interest. This will depend on the sample, as some samples scatter more strongly, and so make measurements at high scattering angle, and thus *q*, feasible.
4. Available detectors: An ideal detector for XPCS measurements is an area detector in order to realize the benefits of ensemble averaging. The ideal area detector has a large format, i.e., number of pixels, to measure a large range of *q*'s simultaneously, small pixels matched in size to the speckles, very fast frame rate in order to measure fast dynamics, and good efficiency (100% quantum efficiency).
5. Convenience of operation: The ideal setup should be completely remotely controlled from outside of the experimental hutch. An ideal mode of operation would be placing your sample into the setup, closing the experimental hutch, turning the beam on, and taking all your data without ever turning the beam off. It takes at least several minutes to open the hutch doors, enter the hutch, make an adjustment, search the hutch, close the hutch doors and satisfy the interlocks. In addition to the obvious efficiency which avoiding this would provide, beamline optics also cool off after the beam is turned off, and it takes some time for the beam to stabilize after it has been turned back on.

The design of a typical SAXS setup begins with a few essential building blocks. First, you need your sample and the sample needs to be placed in a properly conditioned beam. The beam conditioning includes treatment for coherence and size, wavelength and bandpass, or monochromaticity. In general, all of these conditions are related to each

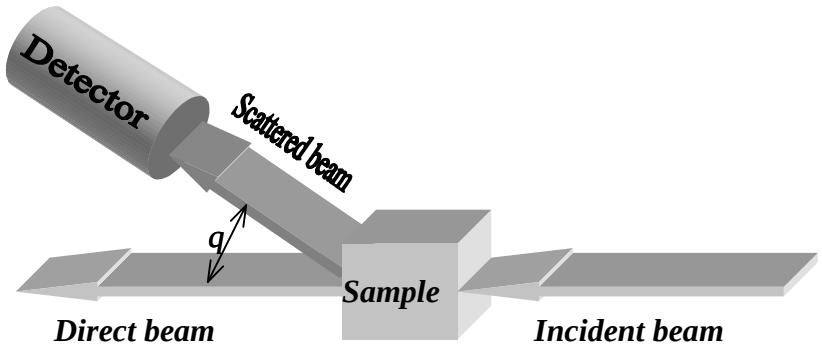

Figure 4.1. Block diagram of the typical experimental setup. Included in the diagram is the conditioned incident beam, sample under study, and scattered beam at the scattering angle q to the unscattered direct beam. Conditioning beamline components are omitted from this diagram.

other. After the sample is placed in the conditioned beam, we need to have a detector to measure the scattering from the sample. Figure 4.1 shows a schematic of a typical experimental setup, where all of the conditioning beamline components, such as apertures, filters and shutters, are not shown. The conditioned x-ray beam comes from the right, and illuminates the sample volume. The direct beam, partially attenuated by the sample transmission, passes through the sample without changing direction. Scattered x-rays, also partially attenuated by the sample transmission, are detected at various scattering angles, $\boldsymbol{q}$. The magnitude of the scattering wave vector, q, is related to the incident wavelength, l, and $\boldsymbol{q}$, by the usual kinematic condition, $q = (4p/l)\sin(\boldsymbol{q}/2)$, as shown in Equation (2.82).

As we proceed to a more detailed picture of the experimental setup, we should add the incident beam conditioning components, such that the conditioned x-ray beam satisfies the requirements on it's monochromaticity, size, energy and intensity.

The monochromaticity, or bandwidth, of the x-ray beam is typically controlled by a diffraction monochromator, or by grazing incidence angle mirror filters. The typical bandwidth of the x-ray beam, expressed as $\Delta E/E$, where E is the average incident beam energy, and ΔE is the spread in energy, after a diffraction monochromator is of the order of 0.01%. The typical bandwidth of the beam after a mirror filter is 2.5%.

The x-ray beam size is typically controlled by partially blocking it with absorbing blades, which are usually combined in pairs, with some controllable distance between the edges of the blades, thus forming slits. In order to obtain a beam limited in size in both the x and y directions, the slits are combined to form apertures, one being horizontal, the other being vertical. Normally in a beamline there is an initial limiting aperture, which cuts the size of the x-ray beam to limit the total beam power. This is often important for the normal operation of the monochromatizing components and other beamline optics. The requirements for the polishing of the edges of the aperture blades for this power-limiting aperture are not very strict. However, there should be proper cooling for those blades, since the total incident power of the undulator beam can be as much as 4 kW. For the secondary apertures located in experimental hutches and designed to satisfy coherence conditions, the edges are highly polished in order to minimize parasitic stray scattering.

Any nicely defined aperture placed in the beam will create a Fraunhoffer diffraction pattern, which can broaden the beam and contribute to the parasitic

background scattering. In order to minimize this effect, a slightly larger second aperture is placed in the beam following the coherent aperture, which blocks the tails of the diffraction pattern from the coherent aperture. Cleaned and conditioned in this way, the beam then illuminates the sample.

The sample is usually contained in a temperature-controlled sample oven. Strict temperature stability requirements usually require a more complicated, multishell design for the sample oven, as described later in this chapter.

A detector is placed downstream from the sample to detect the scattered intensity. Sometimes there is another aperture before the detector, called the detector aperture, which limits the solid angle accepted by the detector in order to obtain a particular q resolution or to measure a specific number of speckles (usually one).

A great deal of time and effort was spent in optimizing the coherent SAXS setup. In this chapter, I describe the resulting setup that we created. The following sections describe: the MHATT-CAT Sector 7 Insertion Device Beamline where these experiments were carried out; the in-hutch pink beam mirror filter and Ge monochromator which we assembled for these experiments; the small angle scattering setup used to produce a coherent x-ray beam to illuminate the sample and to measure the small angle x-ray scattering from the sample; the design of a sample oven that was used to control the temperature of the sample; sample preparation and characterization; x-ray detectors.

MHATT-CAT Sector 7 ID Beamline

The SAXS setup was developed and implemented on the Insertion Device beamline at Sector 7 of the Advanced Photon Source (APS) in Argonne National Lab

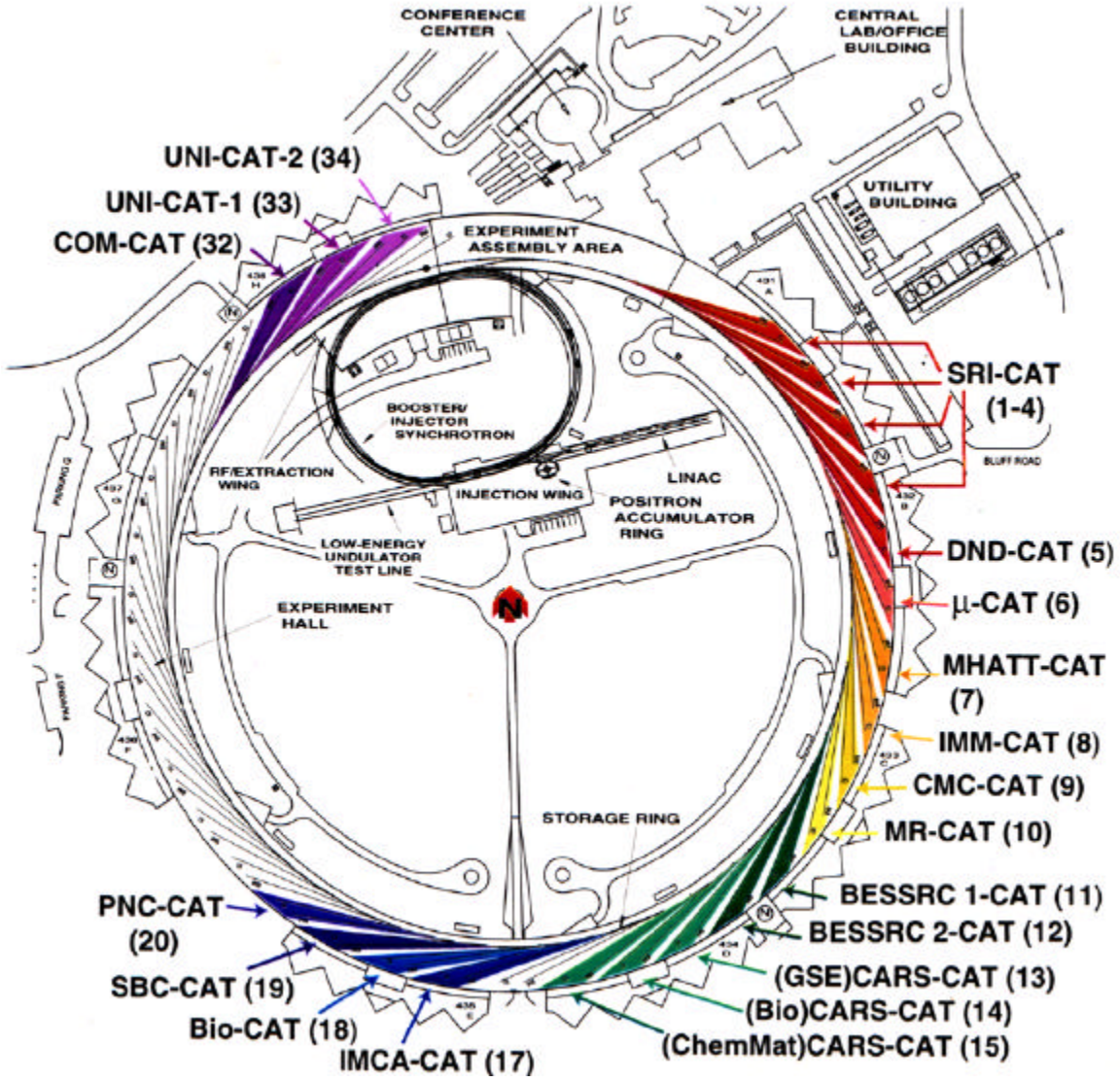

Figure 4.2. Plan view of the APS, showing the MHATT-CAT facilities at Sector 7.

(ANL), located at Argonne, Illinois, shown in Figure 4.2. The Sector 7 beamline facilities include an Insertion Device beamline and a Bending Magnet beamline and are jointly operated by the University of Michigan, Howard University and AT&T-Lucent Technologies (Formerly Bell Labs) Collaborative Access Team (MHATT-CAT). A schematic of the sector 7 facilities, including the principal experimental stations, is shown in Figure 4.3.

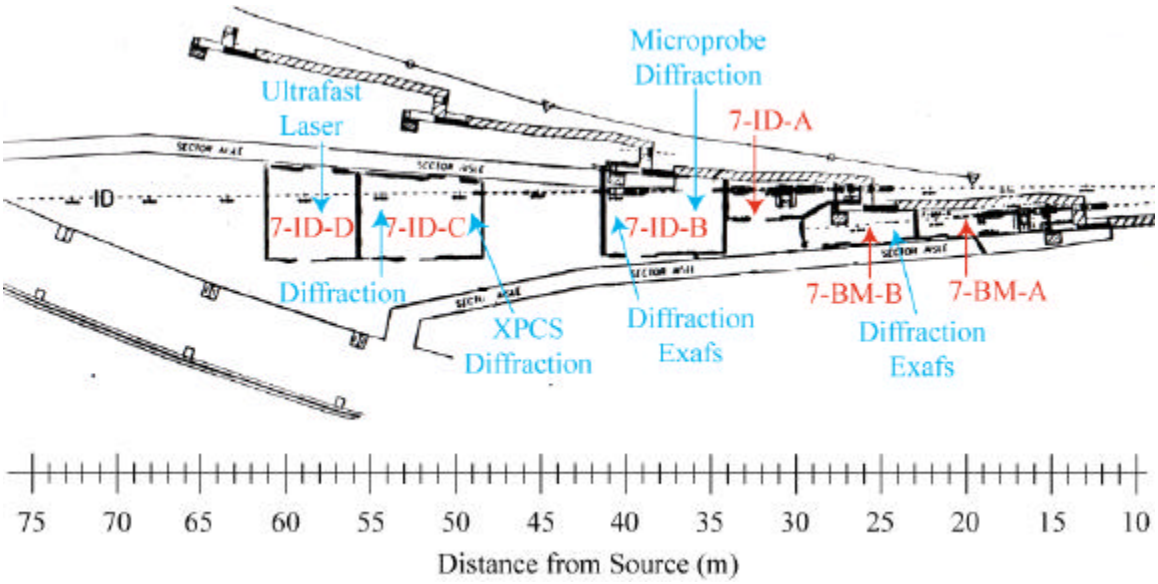

Figure 4.3. Plan view of MHATT-CAT beamlines showing the optical enclosures and experimental stations.

The APS undulator A[102,103,107] is used as a radiation source in the 7ID beamline. It is a 72 pole, 2.4 meter long insertion device located in the downstream half of the 7ID 5 meter straight section of the APS storage ring. The accelerator electron beam is stored at energy of 7.0 GeV, and for the purpose of flux calculations it is customary to normalize the beam current to its maximum of 100 mA. The output x-ray spectrum of the undulator consists of a series of harmonics, as shown in Figure 1.3. The energy of the first harmonic ranges from 3-13 keV, depending on the gap of the undulator. Our experiments were conducted with the gap set to a fundamental energy of either 9 or 11 keV. The x-ray source size corresponds to the particle beam size at the Insertion Device. It has a horizontal standard deviation of σ_x = 359 μm and a horizontal divergence of $\sigma_{x'}$ = 23 μrad. In the vertical, the size and divergence are σ_y = 21 μm and $\sigma_{x'}$ = 3.9 μrad, respectively. There is an additional contribution, σ_r, to the photon beam source size due

to diffraction effects, but this can be safely ignored for all types of insertion device and bending magnet sources at the APS. However, the contribution to the photon source divergence due to diffraction, $\sigma_{r'}$, is important for the insertion devices, especially in the vertical direction. For example, at 9.0 keV for undulator A, the calculated $\sigma_{r'} = (\lambda/2 \cdot L)^{1/2}$ is 5.4 μrad, where λ is the radiation wavelength and L is the length of the insertion device. This is greater than the electron beam vertical divergence, implying that the x-rays are quasi-diffraction limited in the vertical.

An x-ray beam generated by an undulator A is passed to the 7ID-A hutch through the APS front end (FE)[104]. The FE connects to the MHATT-CAT beamline through a commissioning window located in the 7ID-A radiation enclosure along with the other beamline components, as shown in Figure 4.4. The commissioning window reduces the total transmitted power by absorbing the low energy x-rays. It also protects the APS storage ring vacuum during the commissioning activities of the beamline. Currently there are plans to replace the commissioning window with a small aperture single Be window, which can withstand the full power of the white beam. This will provide a much cleaner beam, especially if a highly polished and etched IF-1 grade Be window is used. Motorized water-cooled white beam slits (WBS) by Oxford Instruments are next in the beamline, 27 m from the source. We usually set them to a nominal size of 100x100 μm^2, which limits the total x-ray power but is still much larger than the transverse coherence length. A filter unit follows the white beam slits. It is designed to introduce various attenuating filters in the beam to further reduce the beam intensity, or otherwise modify the beam intensity distribution.

Next in the beamline is a High Heat Load Monochromator (HHLM), which is a

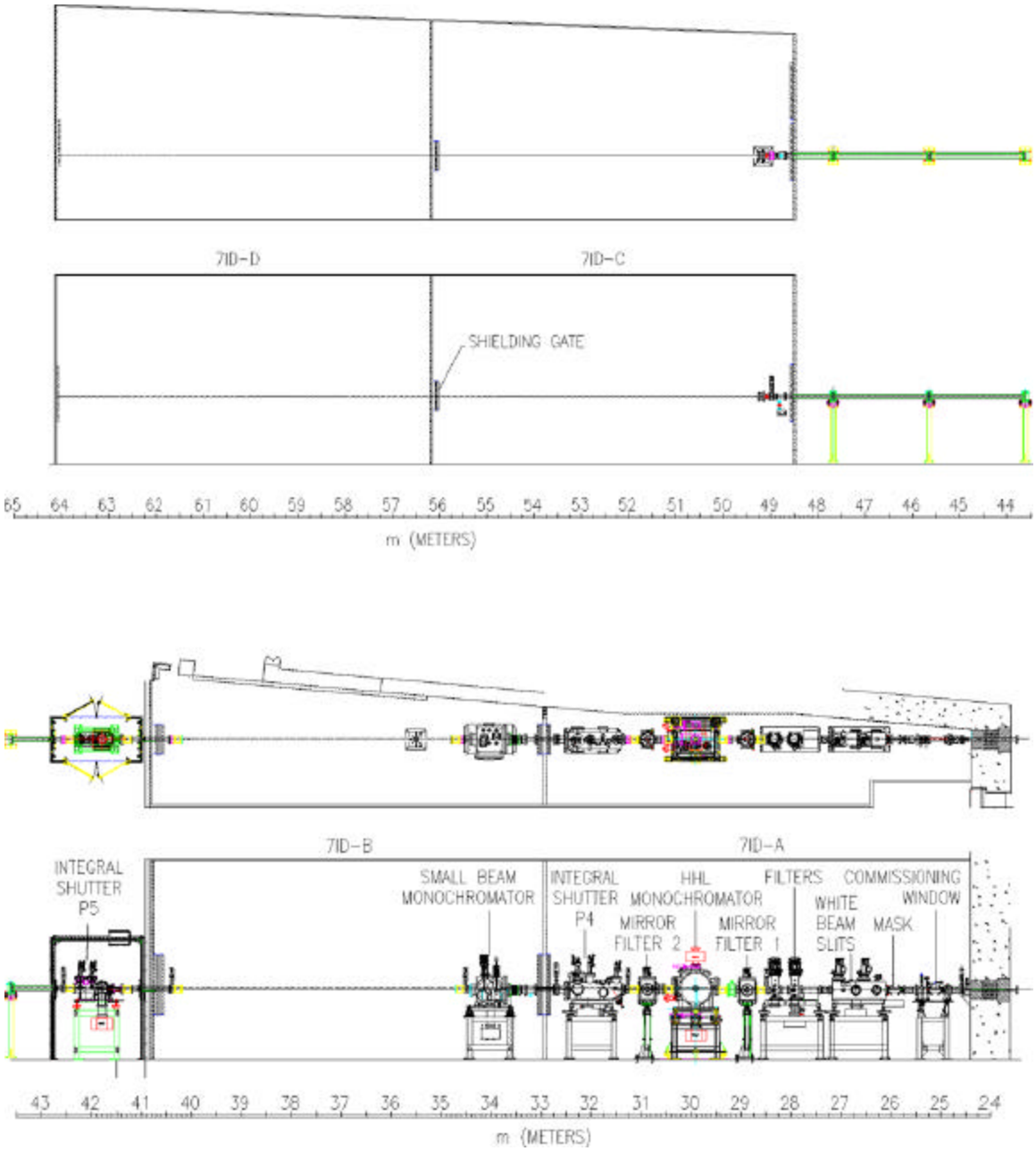

Figure 4.4. MHATT-CAT insertion device beamline. X-rays enters from lower right. Hutch 7ID-A is for beam conditioning components. Experimental hutches include 7ID-B, 7ID-C, and 7ID-D. Distances are measured from Undulator x-ray source.

constant offset (35 mm) double bounce design utilizing (111) Silicon crystals. The first silicon crystal is cooled with liquid nitrogen in order to handle the large heat load of the full undulator beam (maximum of 4 kW) and in order to take advantage of the fact that

the thermal expansion coefficient of Silicon goes through zero at about 120 K. Two 125 μm thick Be windows surround the HHLM during the initial commissioning phase. They will be removed in the near future.

As pointed out in chapter 2, the real part of the index of refraction of materials is less than 1 for x-rays. This means that x-rays incident on a surface at grazing angles undergo total external reflection up to a critical angle that depends on energy. This grazing incidence reflectivity is typically of order 50%, being less than unity due to the finite absorption of materials. Above the critical angle, the reflectivity falls off sharply with increasing incidence angle. The critical angle itself decreases with increasing x-ray energy. So, at fixed incidence angle, only x-rays having energies below some cut-off energy will be strongly reflected. Grazing incidence x-ray reflection from a mirror then acts as a low-pass filter of the x-ray spectrum. Since the x-ray spectrum output by an undulator consists of a quasi-harmonic fundamental and its harmonics, applying a low-pass filter to it results in a so-called “pink” beam consisting of only the fundamental, with a bandwidth of 2.5%. A typical example of the x-ray spectrum before and after reflecting the x-rays from 2 mirrors at grazing incidence is shown in Figure 4.5. Note the log scale for the flux on the y-axis.

Such a pink beam mirror filter (PBMF) is very effective at isolating the fundamental with very little harmonic contamination. It allows use of the entire fundamental of the undulator spectrum in order to maximize the available flux for, e.g., coherent SAXS experiments. It is critical to have maximum flux for some XPCS experiments with weakly scattering samples, such as the critical dynamics measurements on the hexane/nitrobenzene binary mixture that are presented in Chapter 5.

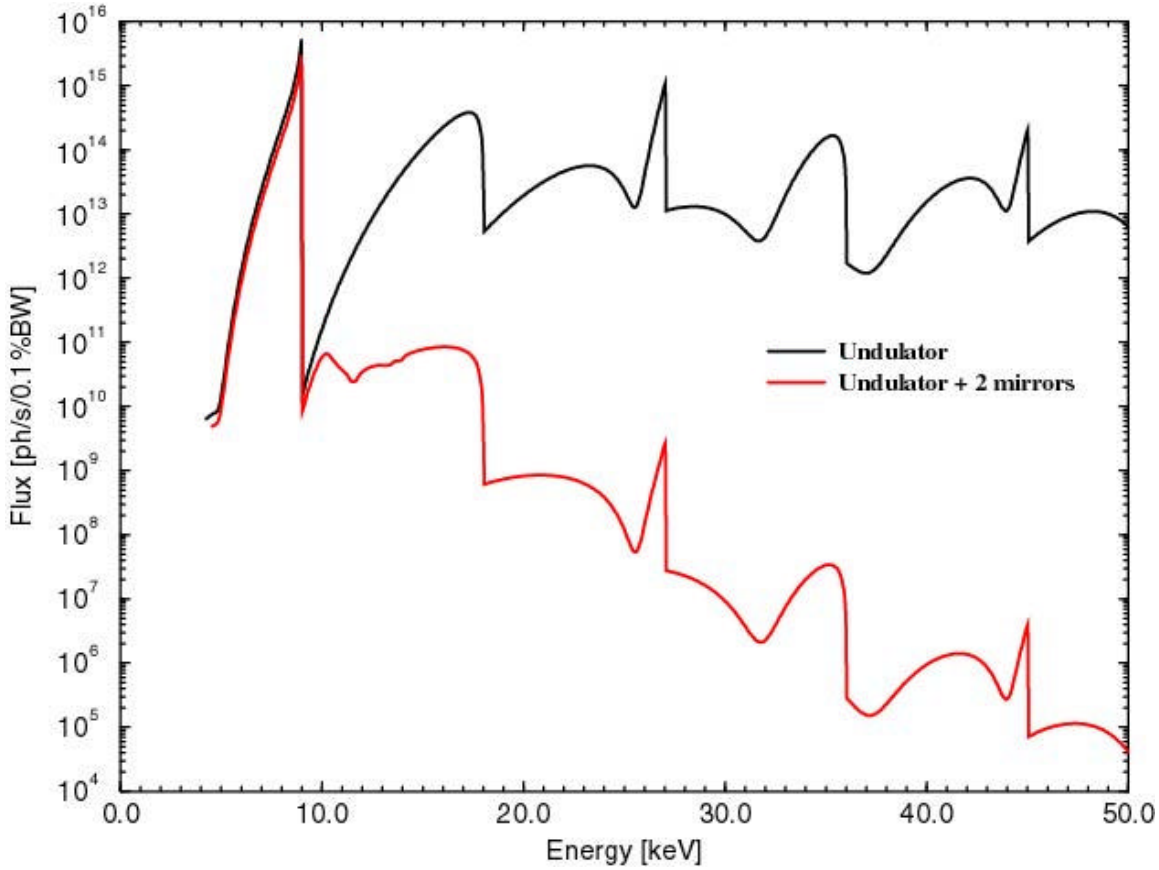

Figure 4.5. Typical Undulator A spectrum with the fundamental energy set at 9 keV in a 100x100 μm^2 aperture located 30 m downstream from the undulator (black). Red line represents the Undulator A flux after the double bounce pink beam mirror filter. Note the log scale for the flux on the y-axis.

In the 7ID beamline, a PBMF is implemented with two Silicon mirrors having Pt and Rh stripes and contained in separate UHV mirror tanks on the upstream and downstream side of the HHLM. The x-ray beam can be reflected from either the Pt stripes or the Rh stripes. The reflectivity of Pt and Rh cut off at different energies. Providing stripes of both materials allows optimization of the reflectivity and harmonic reduction depending on the working energy. The x-ray beam reflected from the first mirror passes through the HHLM without hitting the HHLM Silicon crystals, and then

reflects off of the second mirror in the downstream mirror tank. The vertical offset of the resulting pink beam is also 35 mm, identical to that of the monochromatic beam produced by the HHLM. This has the advantage that either a pink or a mono beam can be passed down the beamline to the experimental hutches along the same axis. Unfortunately, the PBMF was only just recently installed and was not available during the time the work described in this thesis was being carried out. Hence, a temporary PBMF was fabricated which was operated in the downstream experimental hutch. It is described later in this chapter.

The final beamline component in 7ID-A is a beam dump known as a 'P5'. This unit can work either in a white beam mode, passing the white beam through, or in a monochromatic mode, where the white beam is blocked and the passed beam is 35 mm higher than white beam. Monochromatic mode is used to pass through either a monochromatic beam produced by the HHLM or a pink beam produced by the PBMF (when it is commissioned).

In the 7ID-B hutch there are two more 125 μm thick Be windows surrounding a Small Beam Monochromator (SBM). The SBM was designed for microfocusing experiments. During our experiments, the SBM was operated in a pass-through mode.

The number of unpolished Be windows in the beamline is responsible for introducing a large and irregular spatial variation in the intensity of the x-ray beam, as shown in Figure 4.6. This beam structure is actually a speckle pattern due to the wave front distortion and angular spread of the x-rays transmitted by the Be windows, and is caused by their surface roughness[105]. In effect, this wave front distortion reduces the coherence of the x-ray beam considerably. The net effect is a serious reduction in

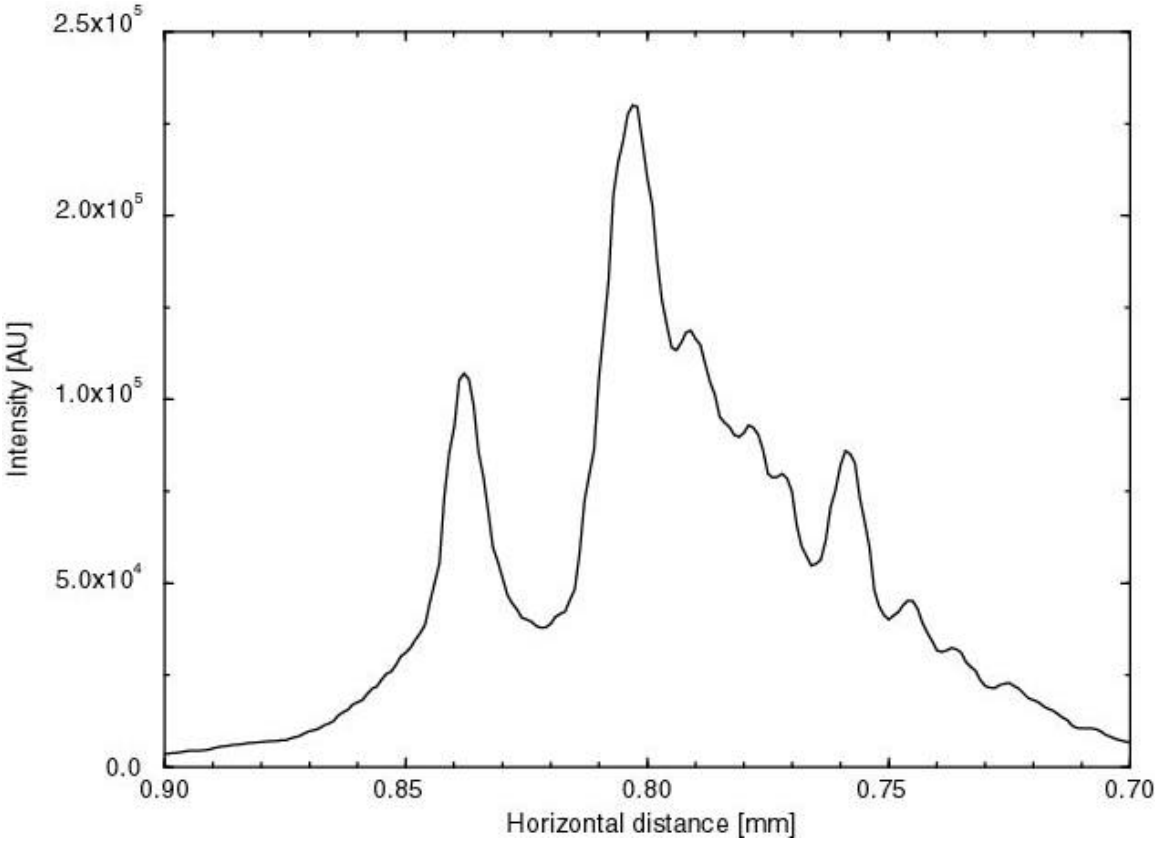

Figure 4.6. Typical horizontal scan of (5 μm)^2 aperture in the x-ray beam with white beam slits nominally set to 100 μm x 100 μm. Beam structure due to wave front distortion appears as multiple sharp peaks on top of normal bell shaped profile.

coherent flux of about a factor of 10. That is, the beam area with which we were able to get good diffraction patterns was only about 10 % of what it should have been based on the transverse coherence lengths calculated from the known source dimensions. Hopefully, this effect will be eliminated in the near future, when the Be windows introduced to the beamline for the commissioning period are removed, and the commissioning window is replaced either with a differential pumping station or with a single polished Be window. Polishing is proven to reduce wave front distortion and parasitic scattering[106] since it minimizes the surface roughness.

In-Hutch Pink Beam Mirror Filter and Ge Monochromator

As mentioned earlier, the beamline PBMF did not exist during the course of this thesis. In addition, the monochromatic x-ray beam produced by the HHLM proved to be too unstable in both position and intensity, during the period of the work described here, for most of these measurements. Hence, it was necessary for us to design and build both an in-hutch PBMF for producing a pink beam as well as an in-hutch Monochromator for producing a monochromatic beam with both good positional as well as intensity stability. Both of these were located in experimental hutch, 7ID-B, in which the experiments described in this thesis were conducted. Hutch 7ID-B was used for these experiments because that was the only one of the three downstream hutches (7ID-B, C, and D) which was commissioned during most of the period of the work described in this thesis. Now that hutch 7ID-C has been commissioned, the coherent SAXS setup is being relocated to that hutch, as shown in Figure 4.3. This section describes the design, construction, and performance of the in-hutch PBMF and monochromator that we built. The effort to implement these was substantial, but crucial to the ability to carry out these experiments.

Much of the complexity of the beamline components described in 7ID-A is due to the requirement that they be able to handle the high heat load of the full undulator beam. However, the SAXS experiments make use of only a small fraction of the entire beam. The coherent measurements use a beam of about $(10\ \mu m)^2$ and the incoherent SAXS measurements use a beam of $(100\ \mu m)^2$, which is still only about 1 % of the full beam. Hence, the power levels incident on the optics were never more than about 1 W and no active cooling of the optics was necessary, as shown below by an estimate of the heating of the optic with the greatest heat load. This greatly simplified the design of the in-hutch

components.

As stated above, the WBS were usually set to about $(100\ \mu m)^2$ in order to limit the heat load on the in-hutch components. However due to finite size and divergence of the source, the x-ray beam spreads out after the so-set WBS to about 260 μm x 110 μm (H x V) by the time it reaches the entrance to 7ID-B. In addition, it is sometimes necessary to open up the WBS in order to center and calibrate them. Hence, as a further power limiting aperture, the white beam passes through a fixed 1mm thick 200 μm diameter Tantalum mask placed on a motorized 2D stage at the entrance to 7ID-B. This mask is mounted on a thick copper heat sink, which is itself mounted inside of a double-sided conflat (CF) flange, as shown in Figure 4.7, and enclosed in vacuum. This mask limits the power in the beam incident on the first mirror and allows us to safely tune the WBS and/or mirrors without risk of overheating and introducing permanent damage to the first mirror surface. With these apertures in the beam we have not seen any noticeable beam intensity change due to the first mirror warming up. However, with the WBS aperture size increased to 400 μm, we have observed that the first mirror surface noticeably distorts and that the reflected beam changes direction during its warm up period, which is of order half an hour.

The Tantalum mask also helps with positioning the mirrors so as to reflect the center of the white beam, which results in a minimum bandwidth and reduced harmonic contamination. The bandwidth of the undulator increases[107] as one goes off-axis, particularly in the vertical direction, so it is important to align on the center of the beam. We measured this effect in hutch ID-B, 35 m downstream from the undulator. The results are shown in Figure 4.8. The peak energy and bandwidth of the radiation decrease and

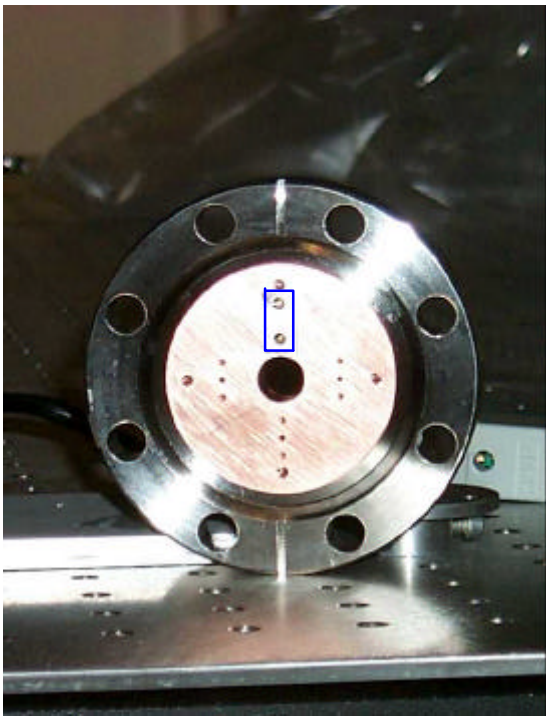

Figure 4.7. A heat reducing Ta pinhole is mounted on top of a copper block, which is mounted in a standard CF flange. The center of the copper block has a through hole for initial x-ray tuning

increase, respectively, as one goes further off-axis in the x-ray beam. The properties change more quickly in the vertical, consistent with its tighter collimation. The FWHM of the x-ray intensity, not shown in Figure 4.8, is 2.2 and 1.0 mm in the horizontal and vertical directions, respectively. We see that misalignment of the acceptance aperture of the optics on the beam by as little as half a mm can increase the x-ray bandwidth a factor of 2, resulting in a 50% shorter longitudinal coherence length. We found that measurement of the undulator bandwidth was the most reliable method of determining that the optics were properly aligned on the x-ray beam, especially given the large distortion of the x-ray intensity profile by the Be windows, as shown in Figure 4.6.

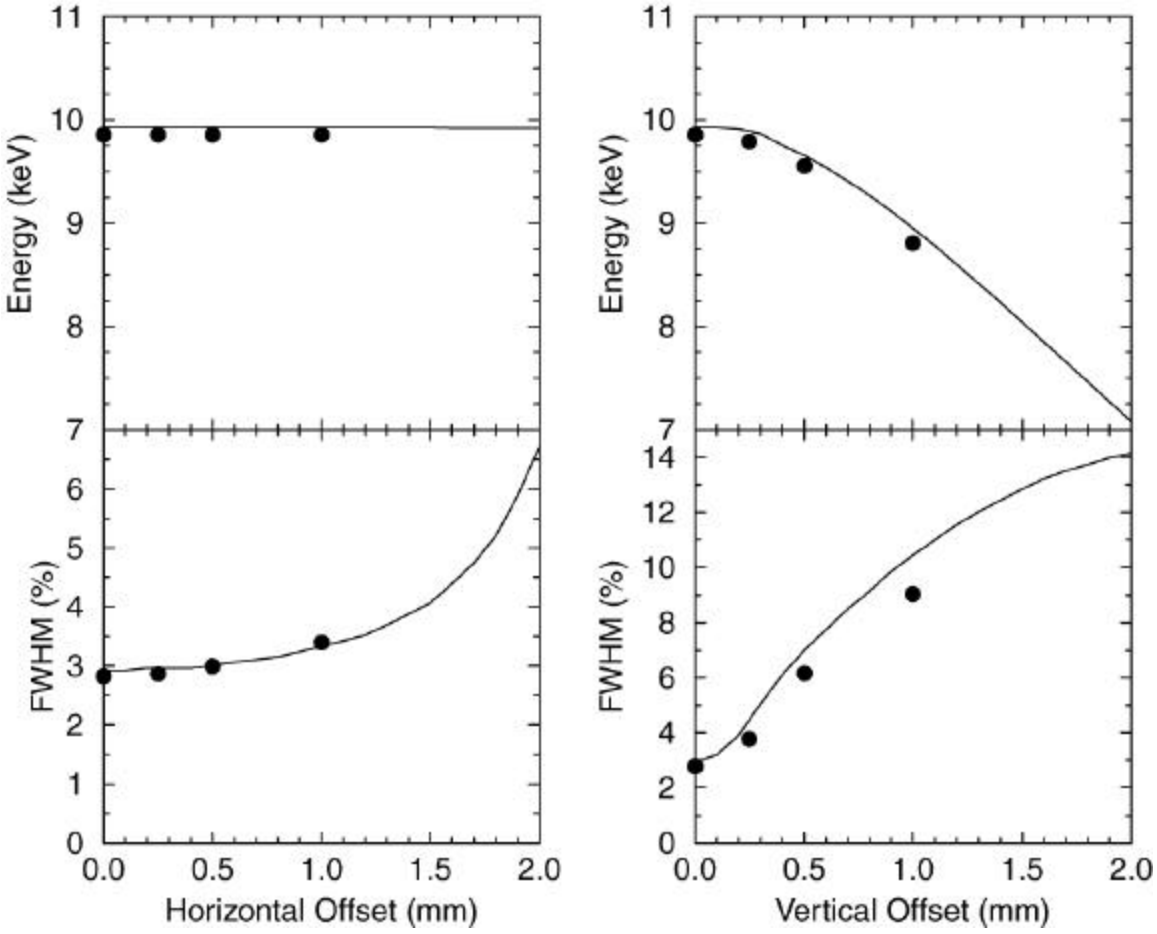

Figure 4.8. Measured (circles) and simulated (lines) peak energy and FWHM of the undulator fundamental as a function of horizontal and vertical offsets from the x-ray beam center. The undulator was set to a gap of 21.223 mm for a nominal x-ray fundamental energy of 9.85 keV. Measurements were made with a Ge monochromator after the x-ray beam underwent transmission through 3 mil Al, 70 mil Be, 498 μm C, and a double Pt mirror reflection at an angle of 7.85 mrad.

Pink beam is produced in the 7ID-B hutch by bouncing the collimated white x-ray beam in the horizontal plane off a pair of Pt/Rh coated silicon mirrors. Both mirrors were mounted in UHV housings at a separation of 1 m and kept in a relatively high vacuum of ~10^{-8} Torr. For the experiments described in this thesis, the in-hutch PBMF was operated at an x-ray energy of 9 keV. We used the Pt coated part of the mirror because its

reflectivity cut-off extends to higher energy than that of Rh. After bouncing off the second mirror the pink beam leaves the high vacuum and enters the air through a 5 mil Be window.

Optimum operation of the mirrors includes tuning the reflection angle so as to place the mirror cut-off energy just above the fundamental of the undulator spectrum. Positioning the mirrors at 7.85 mrad in our case allowed us to reach 2.55 % bandwidth with the fundamental set at 9 keV and with an average pink beam energy of 8.73 keV. The total reflectivity of a pair of Pt and Rh coated Si mirrors is 61 % and 54 %, respectively. A coherent pink beam flux as high as high as $4x10^{10}$ ph/s/(5 μm)^2 was available to illuminate the sample.

For an optimized SAXS setup it is crucial for the mirrors to preserve the brightness of the source and to tolerate the incident power load. To preserve the brilliance, the mirror slope errors must be smaller that the angular source size as viewed from the optics, placed ~35 m from the source. The Si flats used for the mirrors were purchased from General Optics[108] with the figure errors below 0.4 μrad rms and the roughness after coating below 1.8 Å. The mirrors do not reduce the horizontal brightness, since the horizontal source size is about 12 μrad (as viewed at the mirror positions, 35 m downstream from the undulator), but they may reduce the vertical brightness somewhat since the vertical source size is 0.7 μrad.

Numerical simulations of the power on the first mirror show that for the working range of energies the greatest power density is 145 W/mm, which occurs at the lowest energy of ~ 5.5 keV. If we limit the WBS aperture to 100x100 μm^2 then the maximum power on the mirror will be 1.45 W and the minimum 0.6 W. If we assume that all power

is absorbed at the surface of the mirror, then one can show that the maximum temperature difference between the bulk and the beam footprint will be:

$$\Delta T = \frac{P}{p \cdot a \cdot k} \ln\left(\frac{4a}{b}\right)$$

where P is the incident power, b = 0.1 mm is the vertical beam size, a = 12.7 mm is the horizontal beam footprint, and k = 0.131 W/mm/K is the thermal conductivity of the Si substrate[109]. Thus the temperature rise will range from 0.5° to 1.22° C. Since this is a small difference, no additional cooling is required.

These mirrors were mounted on a motorized optical table that we custom built, which simplified the tuning. The in-hutch mirror filter on the first optical table is shown in Figure 4.9. The SAXS setup was mounted on a second, identical, motorized optical table just downstream of the one holding the in-hutch PBMF. These optical tables have a surface area of 6′x4′, are motorized in six degrees of freedom, including x, y, z, and rotations about each of these axes. Here x is in the 6′ direction, which is usually the direction of the x-ray beam, y is in the 4′ direction, and z is vertical. Rotations about x, y, and z are referred to as roll, pitch, and yaw. The linear travel in x, y, and z are each 6″, and the angular travel in roll, pitch, and yaw are 4^o, 6^o, and 4^o, respectively. The linear and angular resolutions and repeatability are better than 0.1 μm and 0.1 μrad, respectively. The tables can support loads of up to about 3000 lbs, i.e., about 1350 kg. These tables work extremely well and proved to be invaluable in carrying out the experiments described in this thesis.

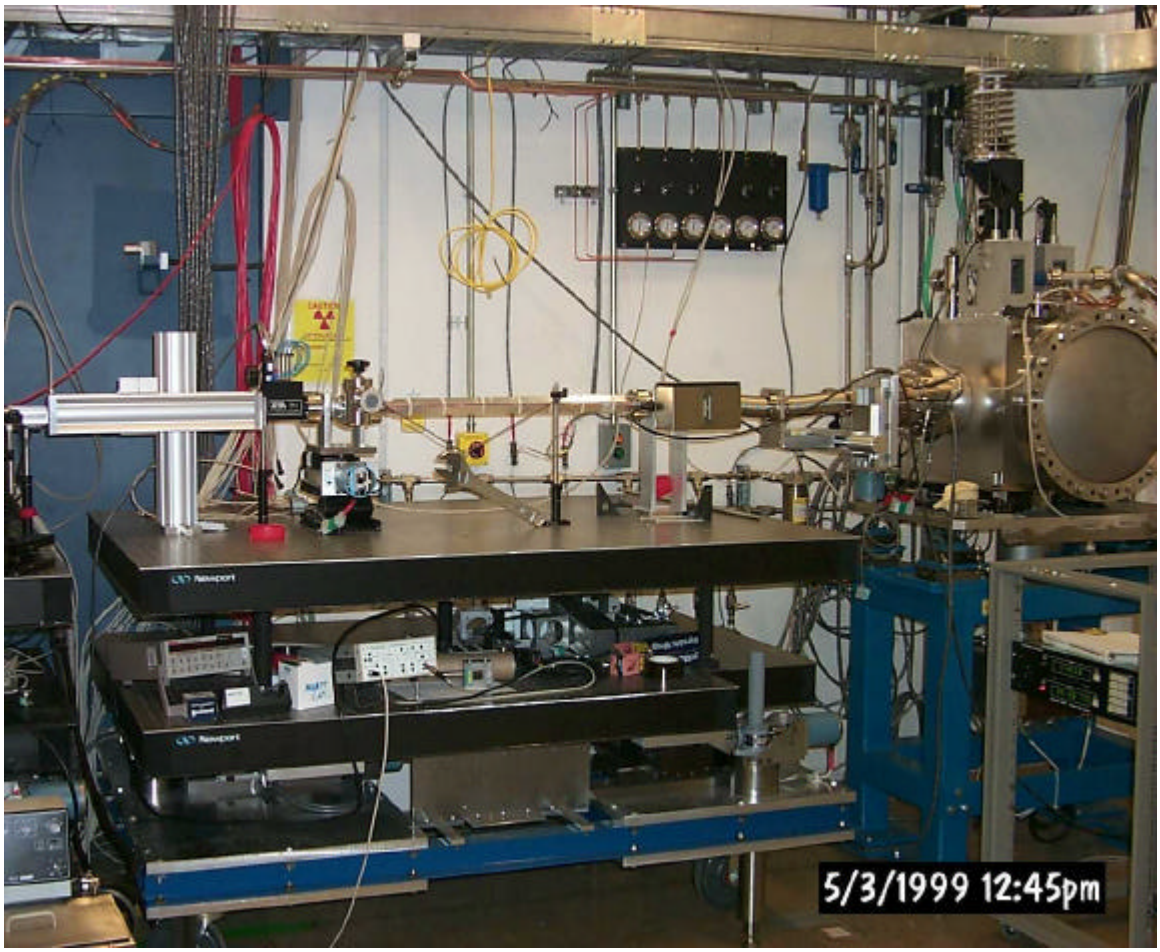

Figure 4.9. First motorized optical table with the double bounce mirror setup.

Most of the static scattering experiments may be conducted with the pink beam, which allows higher incident intensities. However, for some XPCS experiments, especially at higher q where the path length difference of the scattered x-rays increases, it may be necessary to have better longitudinal coherence. In addition, in order to have statistically good data, one has to expose the sample to the x-ray beam for periods at least comparable with the sample relaxation time if an area detector is used for the data acquisition, or much longer if a single channel detector is used. Some samples are susceptible to x-ray radiation damage, as proved to be the case for the polymer mixtures

studied in this thesis. In this case, a monochromatic beam can be used to either provide greater longitudinal coherence or to minimize radiation damage.

For measurements with a monochromatic x-ray beam, we used two different arrangements. For the measurements of the static structure factor of the binary mixture hexane/nitrobenzene, described in chapter 5, we used the HHLM in 7ID-A to produce the monochromatic beam. In those measurements, the HHLM was set to diffract x-rays at 11 keV. In this arrangement, a collimation slit and 1m flight path were placed on the first optical table instead of the Ta mask and the mirror filter. The available monochromatic flux with this arrangement was 7.7×10^{10} ph/s/(100 μm)^2/100 mA.

For the XPCS measurements on the polystyrene/polybutadiene polymer mixtures, described in Chapter 7, a combination of a single Pt coated silicon mirror and a single Ge 111 crystal was used to produce a monochromatic beam instead of the HHL Monochromator. The setup was similar to the double bounce mirror setup, except that the second mirror was moved out of the beam and the Ge crystal was added further downstream. The addition of a flexible 10 long stainless steel bellow and a special vacuum chamber to hold the Ge crystal allowed us to keep the setup in the same high vacuum as the double bounce mirror setup. The special chamber to hold the Ge crystal was made out of the modified 3-3/8 CF half nipple specifically designed to allow high diffraction angles. This vacuum chamber with the Ge crystal mounted inside was held on the Θ circle of a Huber 2Θ goniometer to allow for precise angle tuning.

This arrangement produced a much more stable beam, both in position and in intensity, than the HHLM. In addition, reflection from the first mirror suppressed the higher harmonics of the beam, the odd ones of which are reflected with good efficiency

by a 111 crystal. The bandwidth of the 111 reflection of Ge is about 3.0×10^{-4}, twice that of 111 Si, which is 1.5×10^{-4}. This compensated for the roughly 50 % reflectivity of the first mirror, such that the mirror plus Ge setup produced about equal flux to that of the HHL Si monochromator.

We used the following procedure to tune up the coherent setup. Tuning of the WBS, the white beam mask and the first mirror is similar to that for the pink beam setup. With those components in place, and the first mirror tuned to an angle of 0.45°, we had an x-ray beam horizontally deflected by a 2Θ of 0.9° relative to the direction of the original white beam. Then the Ge crystal was brought into the beam, and positioned such that the surface was roughly parallel to the singly reflected pink beam. Then the Ge crystal was rotated to $\Theta = 12.175°$, which corresponds to the 9 keV Bragg peak. Here, $\Theta = \sin^{-1}(\lambda/2d)$, where $2d = 6.532$ Å is the Ge 111 spacing, and $\lambda = 1.378$ Å, is the wavelength corresponding to the 9 keV beam. Next, the Θ circle of the Huber was scanned to maximize the intensity of the diffracted beam. Finally, the Θ circle was scanned around the maximum of the diffracted intensity, this time with one 25 μm thick copper foil to find the copper edge. Knowing the angle corresponding to the copper edge gave us a very precise calibration of the energy as a function of the Θ circle angle. After this calibration, we know what the energy of the maximum in the diffracted intensity is. Typically, with the undulator fundamental set at 9 keV, the peak intensity is at 8.961 keV. In addition to the energy calibration, this procedure also allowed us to precisely measure the bandwidth of the undulator fundamental after reflection by the first mirror, $\Delta E/E$, which served as an indication of the proper alignment of the setup on the center of the white beam, as shown in Figure 4.8. Being on the center of the white beam means

having the highest possible intensity available for the experiments, while maintaining the lowest possible bandwidth, as discussed earlier.

After being diffracted by the Ge crystal, the monochromatic x-ray beam, with a bandwidth of 0.03 %, goes into the air through a 5 mil thick Be window. The typical flux with Ge resolution after the coherent slits nominally set to $(50\ \mu m)^2$ is 2×10^{10} ph/s, or 3×10^{8} ph/s when measured with $(5\ \mu m)^2$ coherent slits.

The next component after the Ge vacuum chamber was a New Mexico Laser Products fast photon shutter. This device allows shuttering the x-ray beam on and off with rise and fall times of order 100 μs. This shutter is controlled by the CCD detector software, or can be manually opened during the initial setup by supplying 5 V DC on its controller input.

Continuing downstream, the next component is a remotely controlled XIA filter unit. It has four movable blades, which can introduce different combination of filters in the x-ray beam. The first three blades carry one, two and four 25 μm thick copper foils, respectively, allowing for attenuation of the x-ray beam by combinations of from 0 to 7 copper foils. The fourth movable blade contained lead tape to allow for completely stopping the x-ray beam. Very often we needed to take a dark frame exposure with the CCD, and completely stopping the beam with the lead filter is a convenient alternative to disabling the beam with, e.g., the front-end white beam shutter. Moving the lead filter in and out of the beam is much faster and it allows maintaining a constant heat load on the first mirror. The XIA filter unit is combined with a short piece of Newport X-95 structural component, to form an intermediate vacuum flight path. This flight path is

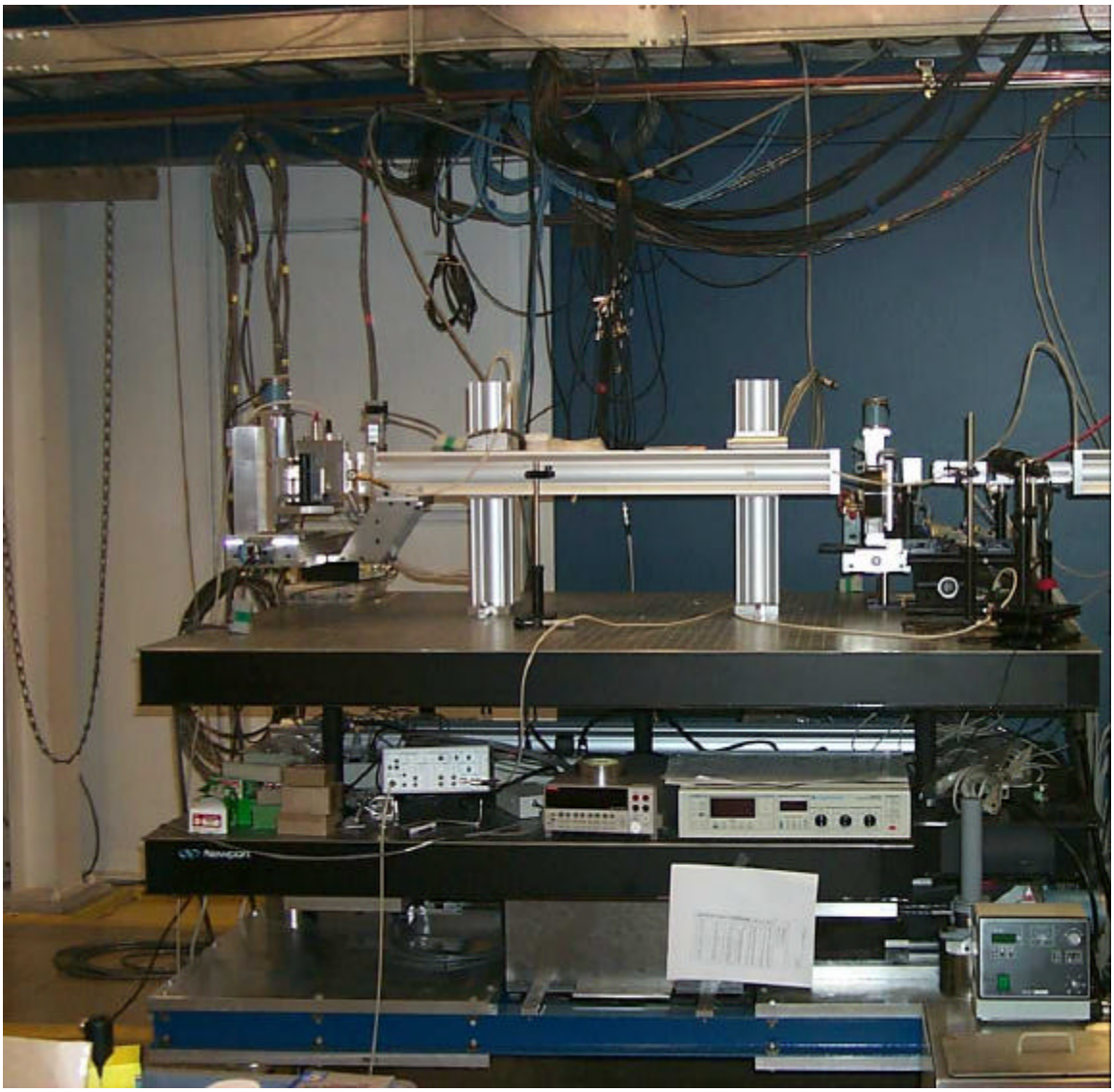

Figure 4.10. Second motorized optical table with apertures, sample oven and detector stage.

necessary to fill the air gap between the equipment set on the first and second optical tables.

Small Angle X-Ray Scattering Setup

Mounted on the second optical table, as shown in Figure 4.10, were coherence

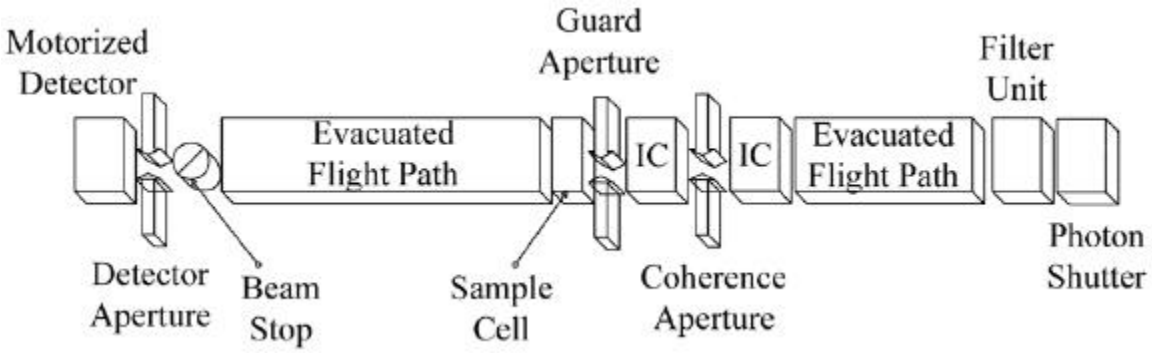

Figure 4.11. Schematic of the SAXS setup. The x-ray beam is incoming from the right. IC stands for ion chamber.

and guard apertures, which were separated by 20 cm of air. Two ion chambers, one just before the coherence aperture where the beam was typically $(100\ \mu m)^2$ and one just after it where the beam was typically $(5\ \mu m)^2$, were used to monitor the incident flux. It was important to monitor both of these as they did not always track each other perfectly due to motion of the fine structure in the beam shown in Figure 4.6. The sample oven, mounted on motorized stages which allowed it to be positioned in the two directions transverse to the beam direction, is located right after the guard aperture. Next after the sample oven is an X-95 vacuum flight path, which can be easily replaced by a different length X-95 to accommodate different requirements for sample-detector distance, i.e., q range. The detector flight path and the intermediate flight path are pumped down together, and can keep a vacuum of $\sim 10^{-5}$ Torr. A schematic of this arrangement is shown in Figure 4.11.

The motorized coherence, guard and detector apertures, which we custom built, deserve detailed explanation. They are miniature apertures with replaceable edges that can be translated by DC servomotors. We originally made the aperture blades from 400 μm thick GaAs (100) wafers. GaAs is known to cleave well in this direction with

perfectly flat edges. This material worked well near 11.0 keV for the static measurements with the HHLM beam on the hexane/nitrobenzene binary fluid mixtures because 11 keV is above the Ga K edge. The x-ray transmission through 400 μm of GaAs is 8.3×10^{-11} at 11 keV. All of the other measurements, however, used at least one mirror to reflect the beam and so were conducted at 9 keV since 11 keV is above the reflectivity cut-off for reasonable reflection angles. The x-ray transmission through 400 μm of GaAs is only 3.0×10^{-5} at 9 keV. Since we needed to detect signals of order 1 ph/s in the tails of an incident beam of order 10^{10} ph/sec, this was much too high a transmission. Hence, for subsequent experiments we replaced the GaAs blades with 1 mm thick Ta. Transmission of 1 mm thick Ta is less than 10^{-70} for all of the x-ray energies used in these experiments. By polishing the edges of the Ta blades to a sub-micron finish we found these blades to have negligible scattering from edge roughness.

A total of three motorized apertures were built and used as the coherence, guard and detector slit assemblies. A VME OMS-58 controller module remotely controlled them. Transition modules built by ANL were used to break the I/O of the OMS-58 into individual channels. They were mounted in the back plane of the VME crate. Initially the servomotors were driven with the power supplied to them by the OMS-58 boards, without transition modules. However, due to the insufficient power supplied by the board itself, and power loss in the long cables, the motions of the motors were not very repeatable. When we switched to the ANL built transition modules with external power supplies, the motors performed very reliably, with the blade positions being reproducible to about 0.1 μm.

The coherence aperture was used to collimate the incident pink or monochromatic beam to the desired size. The horizontal, l_x, and vertical, l_y, coherence lengths at 9 keV and 37 m downstream from the undulator source are 4 μm and 68 μm, respectively. So, for the dynamic experiments we operated with a 5x10 μm^2 (HxV) coherence aperture. An asymmetric opening was used to obtain higher flux. Increasing the vertical coherence aperture size from 5 μm to 10 μm only reduced the speckle size from 11 μm to 9 μm at the detector plane located a distance of 0.7 m from the sample, which was within the resolution of the detector. This is because the actual illuminated spot on the sample was already broadened with the 5 μm beam due to diffraction, and this diffraction broadening was less significant with a 10 μm beam. Maximum speckle size obtainable with our experimental conditions was 11.5 μm, corresponding to a coherence opening of 6 μm.

The sharp edges of the coherence aperture unavoidably diffracted some x-rays at low angles, providing a source of parasitic background that interfered with measuring the SAXS signal from weakly scattering samples. A guard aperture was placed 20 cm downstream from the coherence aperture and just before the sample, with the primary goal of blocking this diffracted beam. The sample was 6 cm downstream of the guard aperture.

A third motorized aperture was used in front of the detector to select a given *q* resolution or number of speckles. It was possible to mount the aperture either in front of the Amptek detector or in front of the CCD camera.

The detectors were mounted on a motorized detector stage that allowed them to be positioned horizontally or vertically to within better than 1 μm. It also allowed scanning of single channel (point) detectors across the scattered beam. We used ion

chambers we custom built, an Amptek XR100CR series detector, and an in-house built CCD detector. Ion chambers were used for high flux measurements, such as alignment of the coherence and guard apertures. The Amptek detector, with it's close to unity quantum efficiency, was used for precise measurements involving lower fluxes, or with high fluxes attenuated with copper filters. Some dynamic measurements with binary fluid mixture were performed with the Amptek detector connected to a Brookhaven Instruments BI-2030 128 channel hardware correlator.

In order to be able to measure the very weak scattering from the materials studied in this thesis, in close proximity to the very intense incident beam transmitted through the sample, special care had to be taken in creating the SAXS setup. Minimizing the background was one of the primary goals. This was achieved by enclosing as much of the beam as practical in vacuum flight paths, thus minimizing the possible losses and parasitic scattering due to air.

Figure 4.12 shows a typical parasitic background scan made by moving the Amptek XR-100CR detector, with the detector aperture in front of it, in the detector plane at 45° to the horizontal. Since the various apertures were mounted in such a way that the slit edges were either horizontal or vertical, most of the parasitic diffraction and scattering from them occurred in these directions. Purely horizontal and vertical scans confirmed the fact that 45° scans produced the lowest background scattering. Thus we most often scanned the detector at 45° to the horizontal.

This plot was created by overlaying the results of multiple scans with different detector aperture sizes, corrected for incident beam intensity changes and normalized to a common detector aperture size. Opening up the detector aperture allowed more precise

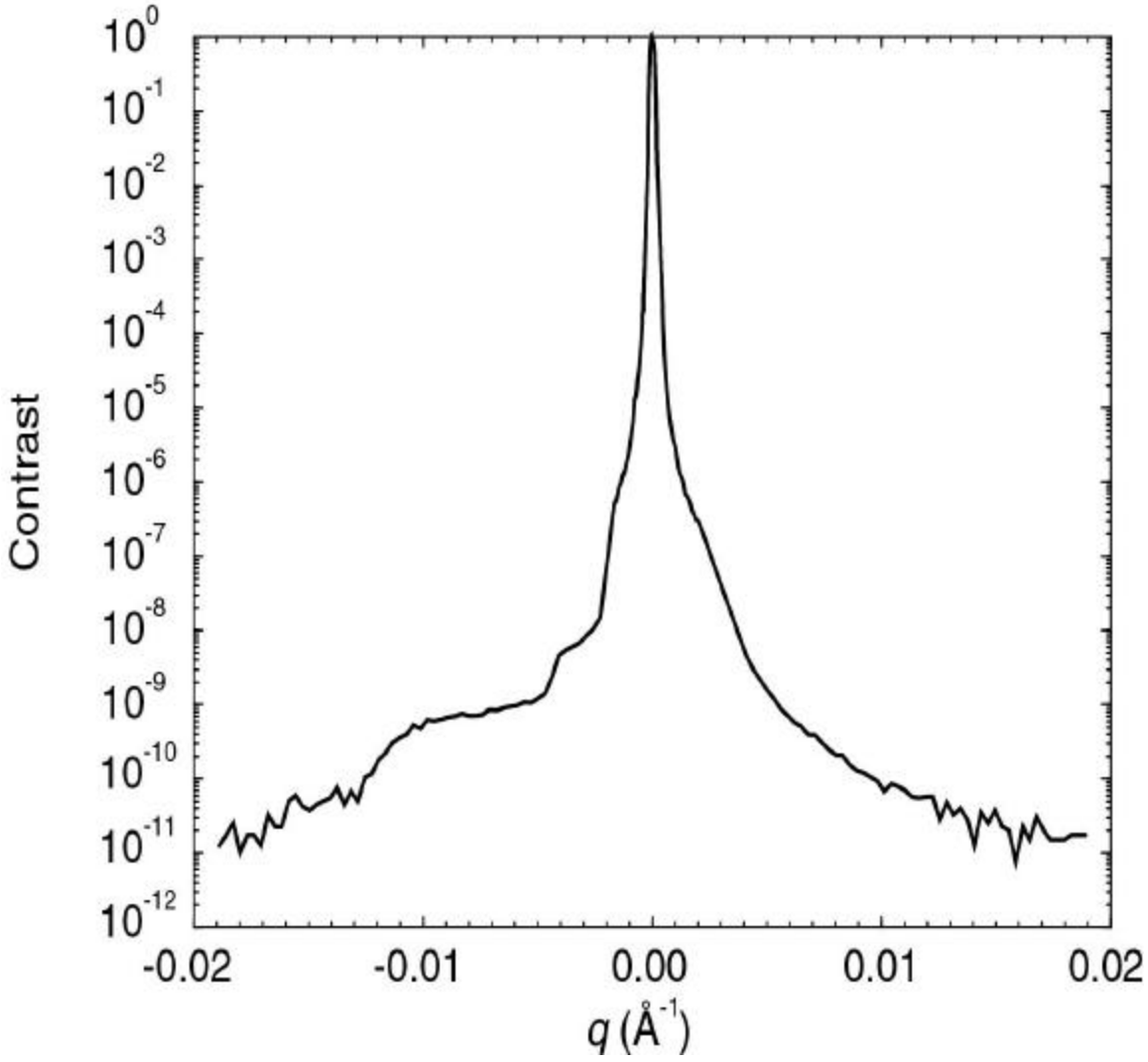

Figure 4.12. Typical parasitic background scan for the SAXS setup, showing excellent contrast.

measurements at higher *q*, where the background is weaker. By this technique, we could measure the stray x-ray rejection, or *contrast*, of the SAXS setup over 11 orders of magnitude.

The measurements summarized in Figure 4.12 were made with the arrangement used to measure the static scattering from the binary fluids reported in Chapter 5. The HHLM was used and the x-ray energy was 11 keV. A $(100\ \mu m)^2$ collimation aperture and

1 m flight path were placed on the first optical table in place of the Ta mask and mirror filter. The "coherence" aperture and guard aperture were set to $(100\ \mu m)^2$ and $(150\ \mu m)^2$, respectively, and the slit material was GaAs instead of Ta. A 2.5 m evacuated flight path was used between the sample and the detector stage in those experiments and for the contrast measurements shown in Figure 4.12. Of course, the sample was absent for the contrast measurements.

The coherence aperture and the source size at the undulator determine the transverse input resolution Δk_i. We approximate the source size by the electron beam rms sizes at the undulator, with σ_x = 359 μm in the horizontal and σ_y = 21 μm in the vertical directions[110,103,111]. The FWHM angle subtended by the source at the nominal sample position is then $\alpha_x = \sigma_x/35m = 10.3\ \mu rad$, while $\alpha_y = 0.6\ \mu rad$. The opening angle of the slit as viewed from the source is $100mm/35m = 2.9mrad$. Adding the two angles in quadrature gives the input resolution in the horizontal and vertical directions, $\Delta k_{ix} = 2 \cdot \frac{2 \cdot p}{l} \cdot \sqrt{(10.3mrad)^2 + (2.9mrad)^2} = 1.2 \cdot 10^{-4}$ Å^{-1} and $\Delta k_{iy} = 3.4 \cdot 10^{-5}$ Å^{-1}, where Dk_i has been expressed as the full width half maximum (FWHM) of the resolution function. The FWHM of the very narrow central peak in Figure 4.12 is 2.2×10^{-4} Å^{-1}, which is approximately consistent with the input resolution.

Stray parasitic scattering from the upstream beamline components is largely rejected by the $(100\ \mu m)^2$ collimation and coherence apertures separated by 1.1 m. Their transverse input wave vector acceptance is $Dk = \frac{2 \cdot p}{l}$ 100 μm/1.1m = 5.1×10^{-4} Å^{-1}. Similarly, the guard aperture blocks scattering from the coherence aperture beyond

approximately $Dk = \frac{2 \cdot p}{l}$ 150 μm/0.2m = 4.3 x 10^{-3} $Å^{-1}$. The effects of both of these sets of aperture can be seen in Figure 4.12 as fall-offs in the contrast.

The left-right asymmetry of the background in Figure 4.12 is most likely due to the motorized aperture design, where the blades corresponding to a single axis are longitudinally offset by ~10 mm. Because of this the body angle increases while the detector is being scanned in one direction and decreases while the detector is scanned in the opposite direction. The effect is that the acceptance aperture of the slits increases on one side and decreases on the other. Subsequent to the measurements shown in Figure 4.12, the blades were redesigned so that they are more nearly co-planar. At the same time, the GaAs was replaced with polished Ta.

As shown by the measurements in Figure 4.12, the SAXS setup had sufficiently good contrast so as to be able to measure sample scattering rates of order 1 ph/s within a few times 10^{-3} $Å^{-1}$ of a main beam of order 10^{10} ph/s. This same performance was achieved for the other SAXS configurations used in the dynamic measurements on the binary fluid mixture as well as the static and dynamic measurements on the polymer samples.

There was an unavoidable small air gap between the last Be window of the final flight path and detectors mounted on the motorized detector stage. Scattering from this air path created a very large background because although it was short in length it subtended a large solid angle as viewed by the detectors. The effects of this air scattering were minimized by using an interchangeable Ta or stainless steel wire as a beam stop. This motorized beam stop was placed inside of the last vacuum flight path just before the 5 mil thick Be exit window. Placing the beam stop before the window played a dual role: it not

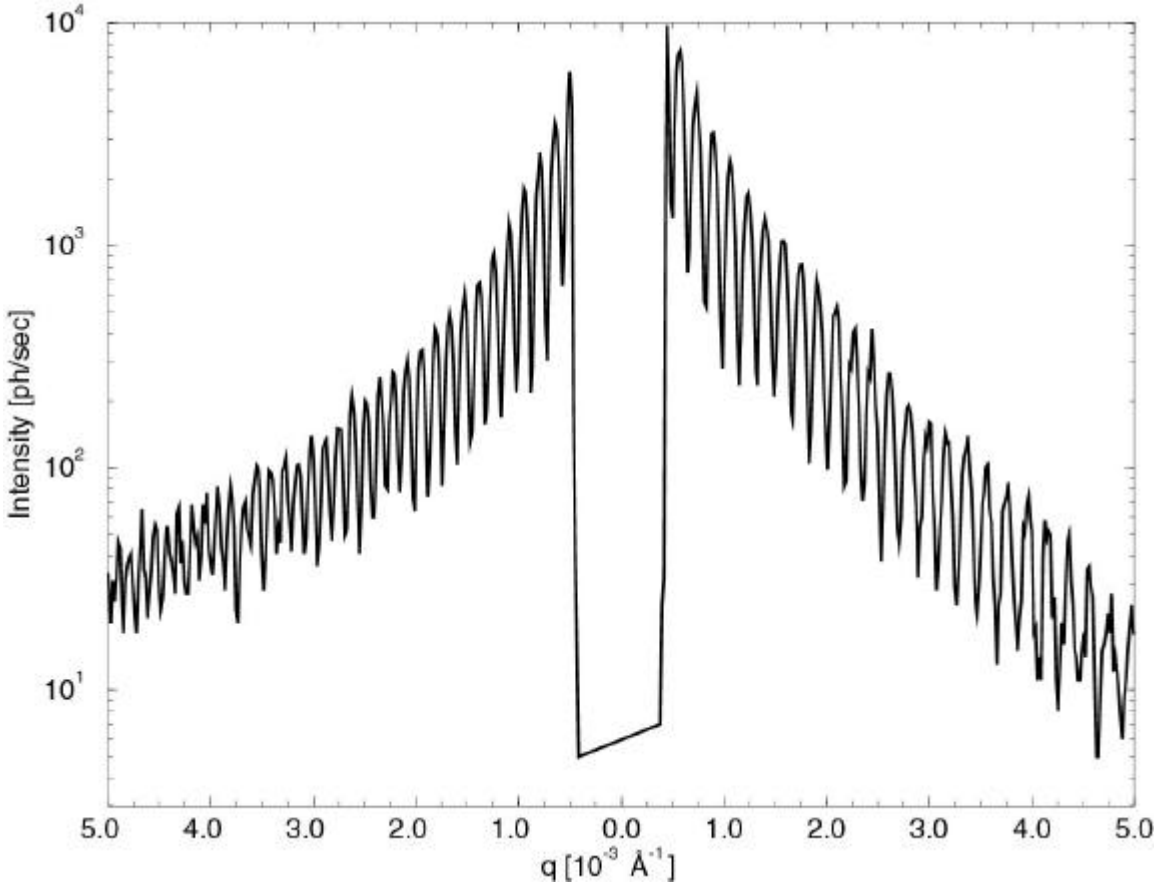

Figure 4.13. Typical Fraunhoffer diffraction pattern from the rectangular (5 μm)^2 coherence aperture, as seen in the detector plane 1.27 m downstream. Scanned with the Amptek detector, with a (5 μm)^2 detector aperture in front of it.

only minimized an otherwise significant amount of air scattering but also effectively prevented parasitic scattering from the exit Be window by preventing the direct beam from illuminating it. The scattered photon flux, being many orders of magnitude smaller than the flux of the main beam, does not cause significant parasitic scattering contributions to the background. This in-vacuum beam stop was constructed after the contrast measurement shown in Figure 4.12 was made. Thus, subsequent measurements were made with even better contrast.

Figure 4.13 shows the wings of a typical Fraunhoffer diffraction pattern measured from the $(5\ \mu m)^2$ rectangular coherence aperture in the far field. It was measured by scanning the Amptek detector with a $(5\ \mu m)^2$ detector aperture in front of it vertically through the x-ray beam. The sharp dip in intensity in the middle of the scan is due to the wire beam stop. Diffraction fringes with very good contrast are visible in the left and right portions of the figure. Vertical scans usually provided better quality diffraction patterns for high-q regions than horizontal scans. This effect is due to the vertical rms source size being smaller than the horizontal rms source size, thus the vertical coherence length is much larger than the horizontal coherence length.

Sample Oven

The importance of temperature stability of the sample for measurements of critical dynamics cannot be overstated. At temperatures close to the critical point, the scattering amplitude and correlation length vary dramatically with small changes in temperature. Good temperature stability also helps to minimize the risk of crossing T_c. If segregation occurs, it may be necessary to warm up the sample to allow remixing of components, a time consuming process.

Initial SAXS experiments on the hexane/nitrobenzene binary fluid mixture conducted at beamline X25 at NSLS and 7ID at APS confirmed the importance of having very good temperature stability. In these initial experiments, we only used a water bath oven controlled by an external Lauda water bath controller. The sample cell used was a 10 mm thick Aluminum cylinder, sealed with two 2-mil Kapton™ windows, which were held by two Aluminum caps. This cell was mounted on an Aluminum block, which was

temperature controlled by the closed loop Lauda external bath temperature controller. The sample temperature was measured with a precision YSI thermistor and was usually stable to within 20 mK during a scan but this was not always the case. The sample position was controlled by X-Y motorized translation stages. The sample could be moved out of the x-ray beam and into a HeNe laser beam in order to monitor the turbidity of the sample as an extra indication of the approach to the critical point. The laser beam was directed through the sample via a set of mirrors and lenses, and projected onto a screen. The image of the beam on the screen was viewed by a video camera.

Although this sample cell and oven were acceptable for rough static measurements, we ran into several problems when we attempted to measure the dynamic correlation function with the single channel correlator. Chief among these was scattering rate fluctuations due to instability of the sample temperature. Thus we had to dedicate some effort to modifying the existing simple sample oven and sample cell design into something more appropriate for dynamic critical behavior studies.

As a model for the new sample oven we used an existing sample oven used for earlier laser light scattering studies. The general idea was to have three isolating temperature shells. The outer shell would serve as an ambient temperature shield. The intermediate shell is a water bath shell with the temperature controlled by a Lauda external water bath temperature controller. The primary goal of this shell is to provide a controllable and stable temperature background for the innermost shell. The third and innermost shell serves as a sample holder and as a fully controllable temperature shell over a wide range of temperatures, variable from 10^{o} to 100^{o} C above the background

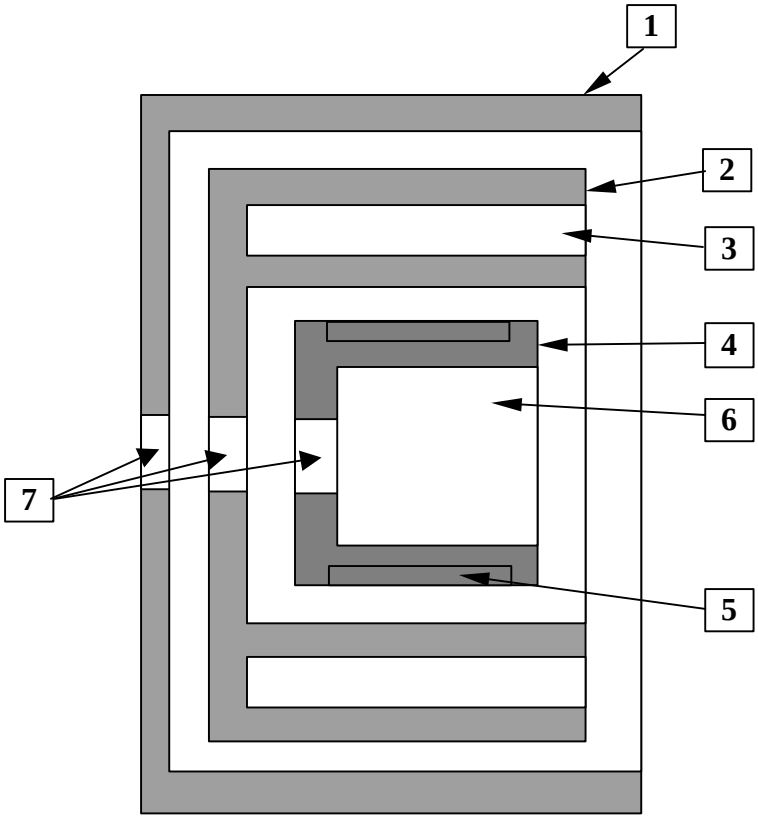

Figure 4.14. Schematic cross section of the sample oven. Thermally insulating spacers and covers for the shells are not shown for clarity. Item labels: 1. Outer shell; 2. Water bath shell; 3. Water filled space; 4. Inner shell; 5. Heater on the inner shell; 6. Space for sample cell; 7. Through holes for x-ray beam.

water bath temperature. A Lakeshore DRC-91CA temperature controller powering an electrical resistance heater regulated the temperature of this final shell.

The final implementation of this concept was as follows. The oven as a whole is a combination of concentric aluminum cylinders with air gaps between them, thermally insulated from each other by plastic spacers, and held together by plastic screws, with the x-ray beam being parallel to the axes, as shown in Figure 4.14.

The outer shell is an aluminum “pan” with a removable cover. Some mounting holes are provided on it for attaching the oven to motorized stages used to position it.

A water bath shell, which is a hollow cylinder with a cover sealed with two o-rings, is mounted inside the outer shell. Two water feedthroughs, made of ¼" diameter copper tubing water, are attached to the water bath shell with epoxy and feed freely through the corresponding holes in the outer shell. A tape electrical heater and a YSI thermistor are glued inside of the aluminum body of the water bath shell to provide control over the background temperature. However, the temperature control provided by the Lauda external water bath as a circulating water supply proved sufficient, and we did not find it necessary to use this capability.

The cylindrical inner shell was mounted inside the water bath shell in the same manner, using plastic screws and spacers for thermal insulation. A 65 Ω tape electrical heater glued on the cylindrical surface and two YSI thermistors provided temperature control. 30 kΩ and 100 kΩ thermistors were mounted in the inner shell aluminum body. They were located very close to the tape heater to provide faster thermal feedback. Thermistors with two different resistances were used in order to access a wider range of sample temperatures. A Lakeshore DRC-91CA temperature controller controlled the temperature of the inner shell. One of the thermistor outputs was connected to the Lakeshore controller to provide feedback for the heater. A four-wire resistance measurement scheme was used wherever possible.

A sample cell was mounted inside of the inner shell. It has a “coin stack” design, consisting of three “coins” stacked together. All three coins have an approximately 8 mm diameter hole in the center. The inner coin holds the sample and has two o-ring groves, one on each side, to seal the 5 mil thick Be windows. Two outer coins serve as window holders. When completely assembled, the sample cell provides for a 3 mm sample

thickness along the x-ray beam. This roughly corresponds to 1 absorption length for most organic materials at 9 keV, such as the fluid and polymer samples used in these experiments. The whole assembly tightly fits in the inner shell. We also used thermal compound to ensure good thermal contact between the sample cell and the inner shell.

The sample oven has a through hole, 0.9″ down from the sample window, that allows for bypassing the sample cell with the x-ray beam altogether. This proved to be a useful feature for alignment purposes when it was necessary to prevent x-ray radiation damage to the sample. It also allowed us to easily measure the x-ray transmission of the sample cell.

Two YSI thermistors of 30 kΩ and 100 kΩ were fed through the middle coin very close to the 8 mm diameter central hole to read the sample temperature. Again, two different thermistors were provided to cover a wider temperature range with maximum possible precision, even though only one was used at a time. A Keithley 2000 DMM was used to read out the sample temperature using a 4-wire resistance measurement scheme. Both the Keithley 2000 and the Lakeshore DRC-91CA were located on the middle shelf of the motorized optical table inside of the radiation enclosure. We wanted the temperature controlling equipment to be as close to the sample as possible to minimize the noise associated with long cables, so we placed the equipment on the second shelf of the motorized table, such that the top breadboard would provide some protection from radiation damage. The Keithley 2000 and Lakeshore DRC-91CA were connected to a PC located outside the hutch via a National Instruments GPIB extender box. Sample temperature was constantly monitored with custom written LabVIEW virtual instrument

software and the temperature was changed remotely by changing the set point of the Lakeshore temperature controller over the GPIB bus.

Overall, the low mass of the sample cell and good temperature control allowed us to keep the temperature stable to better than 1 mK and the response time to temperature changes was very fast. When properly tuned, the Lakeshore temperature controller showed ~ 5 minutes settling time for various size temperature steps, ΔT.

Sample Preparation

The hexane/nitrobenzene mixtures were prepared by weighing into a vial both components with a precision scale. After mixing, the sample was transferred into a preheated sample cell with a warm pipette. At room temperature, the two components mix easily and the vapor pressure is low, so the mixture composition was not changed during weighing in air. Finding the temperature where the mixture became milky provided a visual indication of the critical point.

The polystyrene/polybutadiene (PS/PB) polymer samples were mixed under air by weighing the components directly into the sample cell. Mixing the sample under dry Nitrogen atmosphere did not show any difference in the sample characteristics, so to simplify the sample preparation procedure we did most of the mixing in air. The sample cell was first cleaned in acetone in an ultrasonic cleaner, then let dry completely under a chemical fume hood. Then the cell was partially assembled, such that it only had one Be window. Then the cell was weighed on a precision electronic scale and the scale was zeroed.

The next step was to fill the sample volume. Usually we aimed to fill approximately half of the cell volume in order to let any trapped air flow up and keep the sample at the bottom. If less than a third of the sample volume was filled, then there was not enough sample to use a fresh spot for each x-ray measurement. When we tried to fill more than half of the volume, then the trapped air would form a bubble that would stay in the middle, thus pushing the useful sample to the sides. This proved to be inconvenient, so we usually filled half of the sample volume. Since the total cell volume was approximately 150 ml, we needed to have 60-70 mg of polymers weighed in. We would start by weighing in the PS powder with a micro-spatula until the desired weight was reached. Then a proper weight of the PB was added, until the desired total weight was achieved. The accuracy of the sample composition was limited by the minimum amounts of the polymers that could be deposited into the sample cell, but in all cases was within 0.5 % of the desired sample composition.

After weighing in the proper amounts of both polymers, the sample cell was sealed with the second Be window and window cover, and then placed in a laboratory oven to anneal at about 80° C for a few days. The temperature was monitored with the thermistor and a DVM. The sample cell was rotated and flipped every couple of hours to allow for better sample mixing. This method of sample preparation proved to be effective; it always produced samples of the desired composition and samples mixed at different times yielded the same properties.

A few tests were conducted to verify the temperature stability and thermal time constants of the sample. When we lowered the sample temperature towards the critical point, no temperature undershoot was noticed. That is very important for measurements

close to the critical temperature. We allowed the sample to thermally stabilize at a given temperature typically for 15-20 minutes. This was sufficient time to equilibrate the sample temperature, since the scattering did not change when measured after 15 minutes. We also checked for thermal reversibility in the sample by raising and lowering the temperature of the sample, while still keeping it above the phase transition point, and measuring the static scattering rate after letting the sample thermally stabilize for ~15 minutes at a given temperature. The scattering structure factors after such a cycle were exactly the same, provided that they were measured at the same temperature.

Detectors for SAXS

Various types of detectors are used in SAXS experiments and they can be classified in two basic types. The first type is relatively insensitive, slow, integrating detectors with wide dynamic range that can detect extremely large x-ray fluxes without damage. A typical representative of this type is the common ion chamber. The second type, commonly referred to as photon counting detectors, usually cannot tolerate large fluxes but have high detection efficiency. Pin diodes, photomultiplier tubes, and semiconductor area detectors are all examples of photon counting detectors.

These two types are loosely defined, because with some effort one type of a detector can perform as another type. For example, one can use a photon counting detector to estimate the total flux even for large fluxes, provided there is enough attenuation to keep detector response linear, and provided that the attenuation factors are well known. However, it is usually hard, if possible at all, to make an integrating detector perform as a photon counting detector.

An integrating detector such as an ion chamber is best used for monitoring large fluxes. It is often important to know how the x-ray flux incident on the sample changed with time. This is especially important information for measurements done with a coherent beam, where the x-ray beam is collimated to a few microns in size. This is due to the large variations in intensity as a function of position in the beam, typical sizes of which are comparable with the coherent aperture size. This means that there can be dramatic changes in the incident flux even with the smallest motions, of order 1 μm, of the beam. By accurately measuring the incident flux during an experiment one can make corrections to some kinds of static data, such as static structure factor measurements. However, it is much more difficult to use this information to correct dynamic data, such as correlation function measurements.

There are some known disadvantages associated with ion chambers. While they do not directly affect the properties of the incident beam, they do have to be filled with an ionizing gas, which is often simply air. The presence of the gas in the beam path provides extra parasitic scattering and absorption. Ideally, to lower the background scattering, the whole setup should be contained in vacuum. This way one can really eliminate the air scattering, plus the scattering and phase shifts from the number of windows in the beam path. Of course, ion chambers would not be usable then. As a compromise, He can be used instead of air. He scatters less but also ionizes less readily, so He filled ion chambers are less sensitive.

All single photon x-ray detectors operate through the absorption of x-ray photons, with an energy that is typically of order 10 keV. This is significantly larger than k_bT,

which is about 25 meV at room temperature, and allows single x-ray photons to be detected with moderate effort.

The response of photocathodes used in conventional photomultiplier tubes to x-ray photons is not very large, as they are mostly transparent to the x-rays. Instead, a scintillating material is used to convert each x-ray photon to many visible photons. These then impinge on the photocathode of a conventional photomultiplier and are detected as a large current pulse. A standard commercial version of such a device is a Bicron detector, and we used this in some of our early experiments. One drawback of Bicron detectors, however, is that their dark current is somewhat high, typically being of order 10's of counts/second.

Recently, semiconductor detectors have also been demonstrated to be efficient single photon x-ray detectors, and have become commercially available. Ultra-low dark current avalanche photodiodes are suitable devices, combining excellent noise performance with large quantum efficiency. We used such a detector made by Amptek, which has a dark current of about 0.5 counts/second and a quantum efficiency of 90 %, as shown in Figure 4.15. A fast Canberra 2025 amplifier amplified the output of the Amptek. It had a linear dependence on incident flux up to about 15,000 counts/second.

In contrast to Bicron detectors, the Amptek has a much smaller light-sensitive area, typically much less than 1 mm^2. Although this may be a problem in some applications, it is more than large enough for an XPCS experiment, since a single speckle occupies a typical area of only about $(10\ \mu m)^2$.

XPCS experiments can benefit greatly from the use of area detectors, such as Charge Couple Devices (CCDs). For example, in a single channel detector PCS

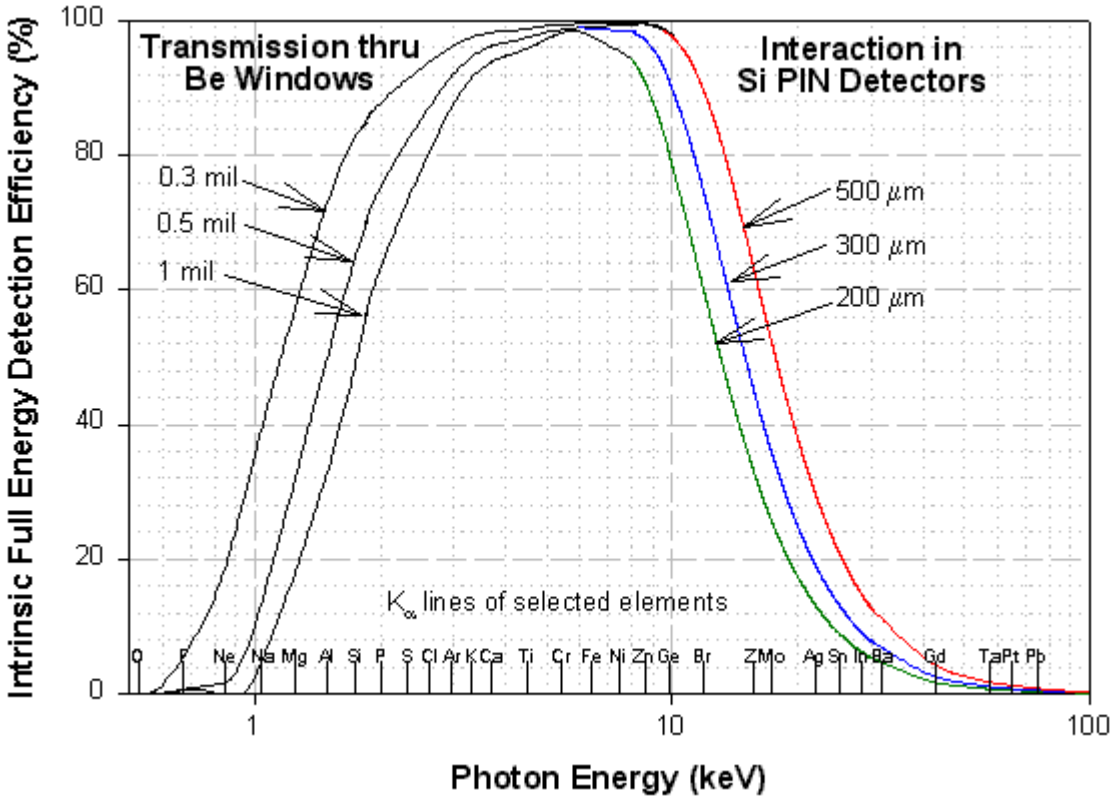

Figure 4.15. Detection efficiency for the Amptek XR-100CR detector. Figure shows the effects of transmission through the detector Be window, and interaction in the silicon detector. The low energy portion of the curves is dominated by the thickness of the Beryllium window, while the high energy portion is dominated by the thickness of the active depth of the Si detector.

experiment, a measurement over 10^4 characteristic decay times is required in order to attain a statistical uncertainty of 1% in the deduced intensity fluctuation relaxation time, as discussed in Chapter 2. The use of a single channel detector is impractical with systems exhibiting very slow dynamics, where the extent of the experiment becomes too long. For example, an average APS electron beam fill pattern is every 12 hours. During that time the incident x-ray beam intensity decays about 50% along with the electron beam current in the storage ring, and if the experiment length is comparable to or

exceeding the 12 hours, then complicated corrections for beam intensity would be required. Another time limiting factor is related to the radiation damage to the sample. As will be shown in Chapter 6, the polymer samples studied here have a limited lifetime in the x-ray beam, and only during that limited period can the sample be used for temperature dependent dynamic measurements

The great advantage of using a CCD area detector is the possibility of conducting ensemble averages over the pixels located in the same band of q. This is possible if the sample scatters x-rays isotropically, i.e., the scattering depends only on the magnitude of the wave vector and not on its direction. Since different speckles are statistically independent, the pixel averaging enhances the statistical accuracy and the total duration of the experiment can be reduced by a factor equal to the number of coherence areas sampled. The use of ensemble averaging with an area detector as opposed to conventional time averaging with a single channel detector becomes especially important when studying weakly scattering samples.

The time scale of dynamics that can be probed with a CCD camera is limited on the low end by the read out frame rate, typically to time scales of a few 10's of milliseconds. Saturation of a given pixel, i.e., the dynamic range of the CCD chip, usually dictates the higher limit. The quantum efficiency of a CCD detector is also sometimes an issue. When used in direct x-ray detection mode, a CCD chip usually has a quantum efficiency of only about 10% due to the relatively large x-ray penetration depth (~ 130 microns at 10 keV) in Silicon compared to the depth of the charge collection potential wells (typically of order 10 microns). Special purpose CCD chips can be fabricated on high resistivity silicon substrates, resulting in so-called 'deep depletion' CCDs, with

potential wells extending ~ 50 microns into the substrate and quantum efficiencies of 30-40%. One drawback of deep depletion CCDs, however, is that they usually have slower readout rates due to the high RC time constants caused by their high resistivity, limiting the rate at which the clock voltages can be changed.

In XPCS measurements, it is often more important to have a high quantum efficiency than a fast readout speed. In the work reported here, conventional CCDs were used for x-ray detection. In future work, it would be beneficial to use a deep depletion CCD detector with its higher quantum efficiency. For example for binary polymer mixtures near the critical temperature typical relaxation times are of the order of seconds to hundreds of seconds, so reading out a CCD chip at a rate of a few frames per second would be sufficient to probe the decay time.

Hardware correlators for analyzing multichannel data are not commercially available. This means that one has to use a software correlator to analyze the data obtained with a CCD camera. With increasingly fast computers it is even becoming possible to calculate the correlation functions in real time, especially if a multitau, or multiple delay time, scheme is used. This will be a great advantage in the future. For the experiments reported here, several Gbytes of data were typically collected for each correlation function measurement and then analyzed after the experiment. The immediate feedback of real-time analysis will be invaluable in directing future experiments.

CHAPTER 5.
RESULTS FOR HEXANE/NITROBENZENE CRITICAL BINARY MIXTURE

Introduction

This chapter presents the results of experiments[112] on a critical mixture of the binary fluids hexane (C_6H_{14}) and nitrobenzene ($C_6H_5NO_2$). Binary mixtures of small molecular weight fluids with their inherently weak scattering and fast fluctuations (μs to ms range) represent an important test of the general applicability of XPCS to a wide variety of materials. Despite the fact that simple binary fluid mixtures have been studied extensively with light and neutron scattering techniques[113,114], only one SAXS experiment has been reported previously on a binary fluid mixture[115]. In that work, only the relative *q*-dependence of the SAXS intensity was measured. This chapter reports the first measurements of the absolute scattering intensity from composition fluctuations and of their dynamics.

To prepare the mixture we used reagent grade hexane and nitrobenzene as purchased from Aldrich Chemical. The properties of the component fluids are shown in Table 5.1. The coexistence curve[113] of binary mixtures of hexane and nitrobenzene is

	Hexane	Nitrobenzene
Chemical Formula	C_6H_{14}	$C_6H_5NO_2$
Mass Density, r_m [g/cm^3]	0.659	1.196
Molar mass	86.18	123.11
Z	50	64
Molecular Volume, v_o [nm^3]	0.217	0.171
Electron Density, r_e [nm^{-3}]	230	374.5
X-ray Penetration Depth at 11 keV, δ [cm]	1.14	0.387

Table 5.1. Physical constants for hexane and nitrobenzene.

shown in Figure 5.1. Samples were prepared at a critical composition[113] of 41.6 mole % of nitrobenzene by using the procedure described in Chapter 4.

The measured x-ray transmission through 2 Kapton™ windows and the sample mixture was 0.34. After correcting the results for the 0.969 transmission of the 2 Kapton™ windows we found that the sample thickness of 10 mm corresponded to 1.05 x-ray absorption lengths. We calculated the mixture penetration depth by weighing each component's mass absorption coefficient $(r \cdot d)^{-1}$ with its weight fraction and then multiplying the total mass absorption coefficient by the actual sample density of $r_m = 0.852 g/cm^3$. The resulting penetration depth of 6.7 mm was in reasonable agreement with that of 9.5 mm deduced from the x-ray transmission measurements.

The relatively high x-ray contrast of hexane and nitrobenzene, due to their large electron density difference (see Table 5.1), makes this mixture a good choice for XPCS

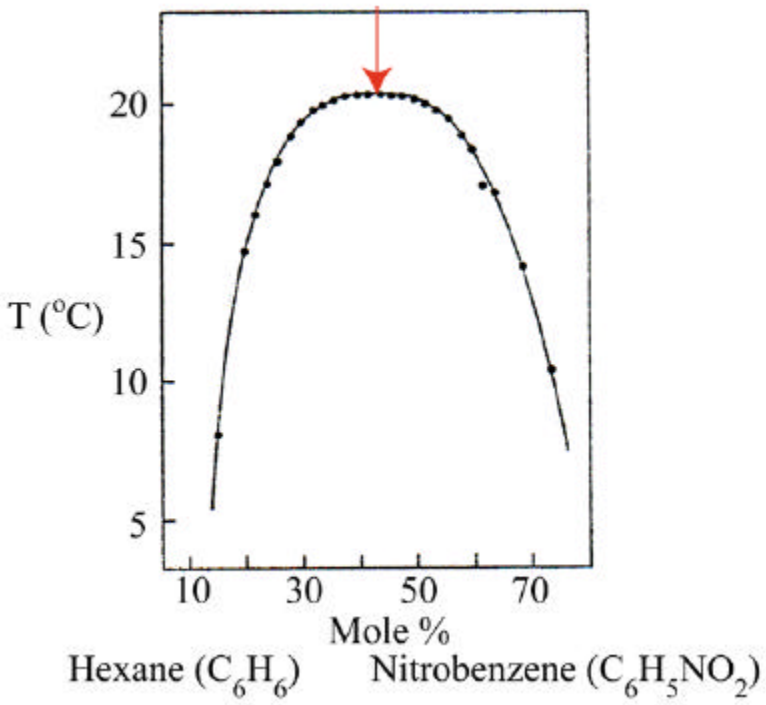

Figure 5.1. Coexistence curve[113] for hexane/nitrobenzene mixtures. The arrow shows an approach to the critical point, with T_c = 20.3° C and a critical composition of 41.6 mole % of Nitrobenzene.

studies. Scattering rates of 100 to 1000 ph/s/speckle were measured with an incident coherent flux of 3.6×10^{10} ph/s/(5 μm)^2 in a pink beam and the sample temperature within 0.06° K of the critical point.

The experiment was performed in two steps: first we measured the static scattering structure factor with our SAXS setup, and then we performed XPCS measurements with the slightly modified SAXS setup. The SAXS setup has been described in general in Chapter 4. In this chapter, we summarize the important parameters of the experimental setup and give a few additional details that were specific to these measurements.

Static Measurements

As described in Chapter 4, the static scattering was measured with collimation, coherence, guard, and detector apertures of $(100\ \mu m)^2$, $(100\ \mu m)^2$, $(150\ \mu m)^2$, and $(600\ \mu m)^2$, respectively. The distances between collimation and coherence apertures, coherence and guard apertures, guard aperture and sample, and sample and detector aperture were 1.1 m, 0.2 m, 0.06 m, and 2.95 m, respectively. The detector resolution was thus $\Delta q = (2\pi/\lambda)x600\ \mu m/2.95\ m = 1.13x10^{-3}\ Å^{-1}$. A flux of $7.7x10^{11}$ ph/s/(100 mA) of 11.0 keV x-rays monochromated by the Si(111) HHLM was incident on the sample.

Figure 5.2 shows the temperature dependence of the static scattering rate, i.e., the structure factor, for a sample at the critical composition. The data has been normalized to a standard beam current of 100 mA. Such a normalization was justified because the relatively large coherence aperture of $(100\ \mu m)^2$ averaged over the spatial structure in the beam (see Figure 4.6) due to the Be windows in the beamline and so the beam monitor scaled well with the beam current. As expected, the scattering rate increases when the temperature is lowered towards T_c.

As discussed in Chapter 3, we can write the expression for the scattering rate, $I(q,T)$, as

$$I(q,T) = \frac{I_0 \cdot t^{-g}}{1 + q^2 \cdot x_0^2 \cdot t^{-2n}} + Bg(q), \qquad \textbf{(5.1)}$$

where *Bg(q)* is the background, with contributions from parasitic scattering of the beamline components and air and the temperature independent molecular scattering from the individual mixture components. Izumi[115] chose to model the background as a weighted average of the measured scattering from each individual component in the

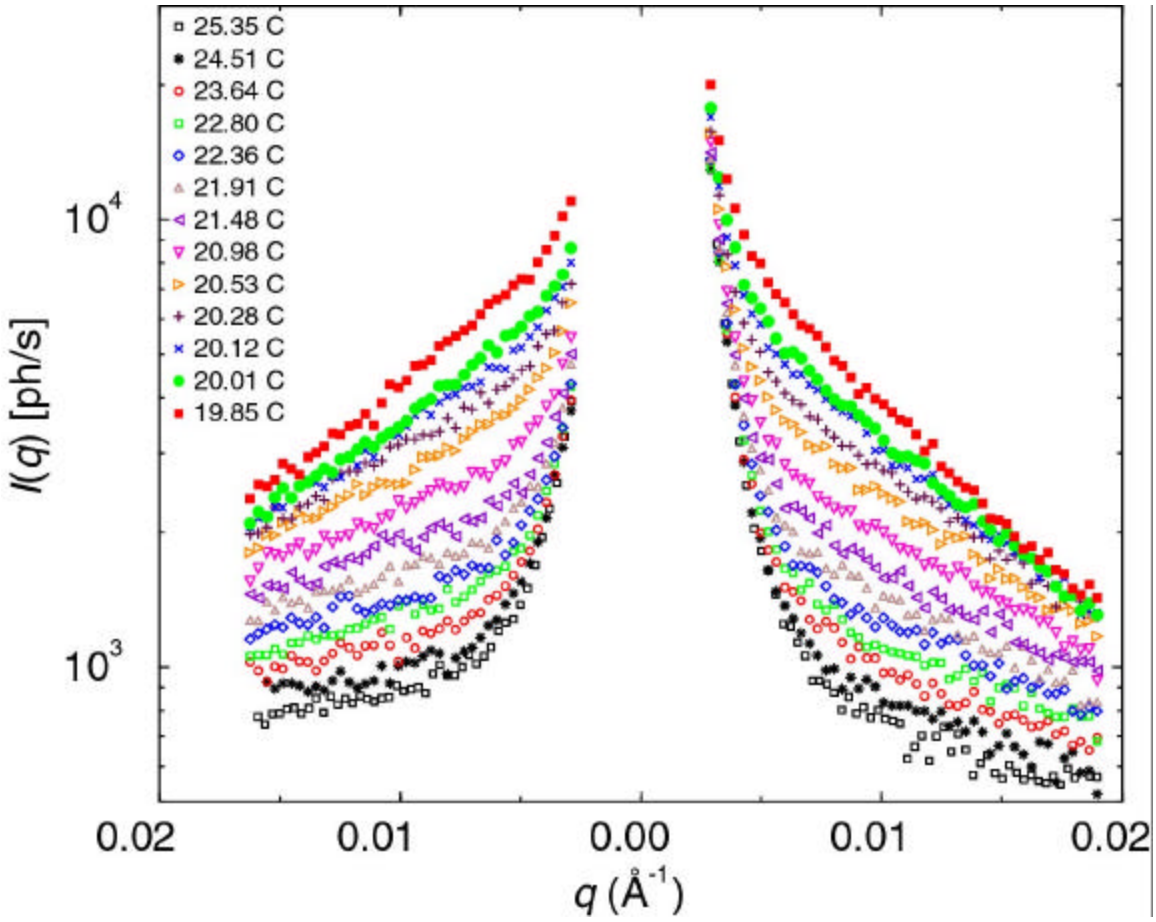

Figure 5.2. Static scattering rate as a function of wave vector *q*, which increases upon approaching the critical temperature.

sample cell. However, this neglects contributions from other sources of parasitic scattering, such as slit edges and air in the x-ray beam path.

We chose to use another approach to model the measured structure factor, first introduced by Damay, et. al.[114]. We use the scan measured at the temperature T_{max} farthest from the critical point, where the critical scattering is weak, as an approximation of the background and fit the difference

$$I(q,T) - I(q,T_{\max}) = I_0 \cdot \left(\frac{t^{-g}}{1 + q^2 \cdot x_0^2 \cdot t^{-2 \cdot n}} - \frac{t_{\max}^{-g}}{1 + q^2 \cdot x_0^2 \cdot t_{\max}^{-2 \cdot n}} \right) \qquad \textbf{(5.2)}$$

for all data with $T < T_{\max}$. Again, the second term in Equation (5.2) is small. This approach works well when *Bg(q)* is temperature independent, which is quite reasonable in this experiment. The fit parameters I_0, T_C, and ξ_0 were optimized by minimizing χ^2 of the whole data set simultaneously, while ν and γ were fixed at their Ising values of ν = 0.635 and γ = 1.23. If ν and γ were included in the fit parameters they did converge to these values and χ^2 did not improve significantly. Therefore, ν and γ were fixed to reduce the number of degrees of freedom in the fits. *Bg(q)* was then derived from the $T_{\max}$ data by subtracting the small critical scattering contribution.

In our experiments, T_{max} was 25.35° C and this scan was subtracted from all other data scans. We assumed that the error bars on each scan followed the Poisson distribution. The error bars for the left-hand side of Equation (5.2) were obtained by adding the error bars from each individual scan in quadrature. All data sets were fit simultaneously to the convolution of Equation (5.2) with the detector resolution Δq.

As an indication of the quality of the fits, Figure 5.3 shows the measured data and fits for two extreme temperatures of 20.01° and 25.35°. The fits are quite good. The subtraction of the scattering component from the fit function provides a good consistency test of the selected approach to the data fitting. The dashed and dotted lines in Figure 5.3 represent the so-calculated *Bg(q)* for the two data sets and provide an indication of the variability of the estimated background; they are identical within the noise. Figure 5.3 also shows another estimate of the background as the crossed curve. It was obtained by adding the measured background without the cell in the beam and the scattering from two

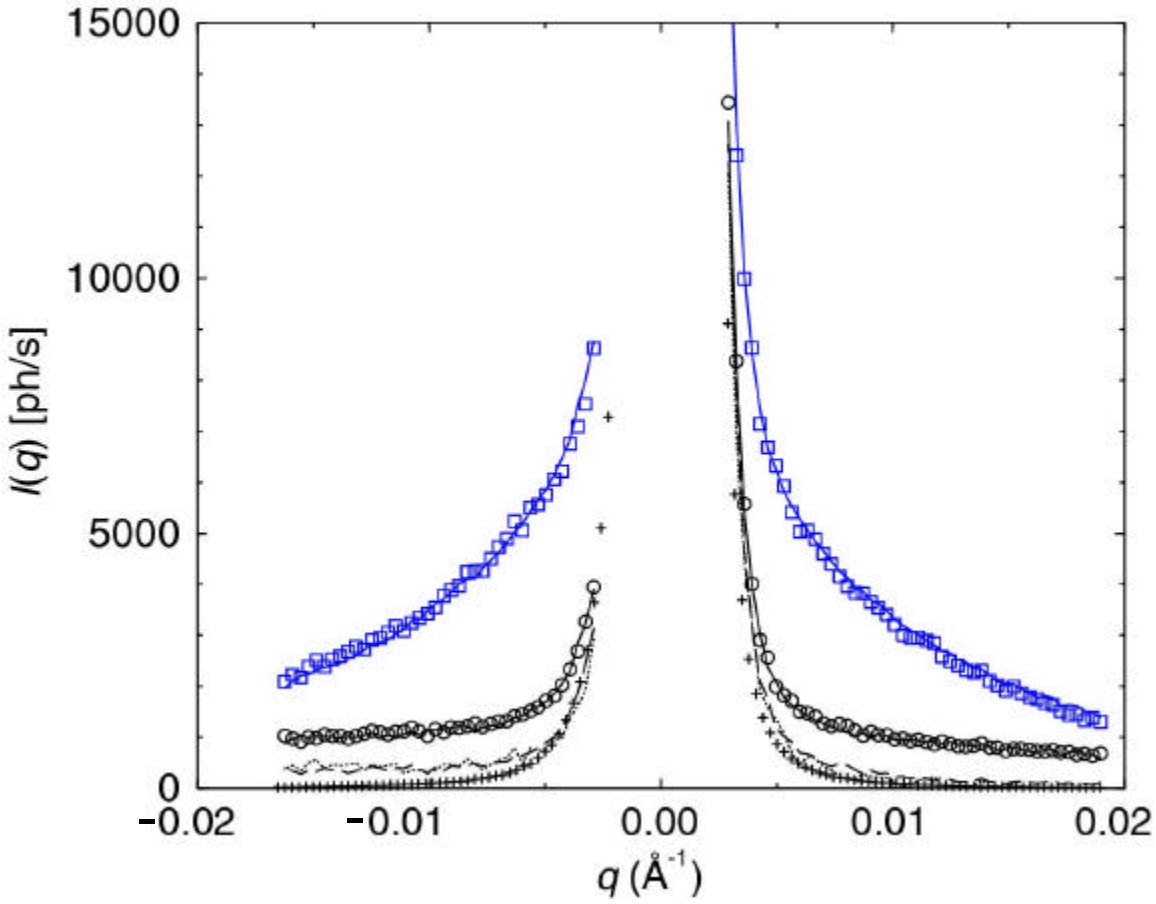

Figure 5.3. Sample fits. Circles and squares represent data measured at 20.01° C and 25.35° C, respectively. Solid lines are fits with T_c = 19.12° C, I_o = 4.86 ph/sec, and x_0 = 2.48 Å. Also shown is the estimated background (crosses) and maximum background variability (dashed and dotted lines), as explained in the text.

Kapton™ windows, and then scaling the sum with the measured sample transmission. It is clear that the background scattering deduced from the fitting is higher than the scaled scattering from the beamline optics and Kapton™ windows. The additional background most likely arises from the molecular scattering of the sample.

We found that if we exclude the data set taken at the temperature closest to T_c, T_{min} = 19.85° C then the χ^2 of the fits improves by 30 %. If this data set is included in the

fits then the fit parameters would not converge to reasonable values and the deduced background for positive wave vectors became negative. This probably indicates that we transiently crossed over into the two-phase region while cooling and the sample had not yet re-equilibrated. Hence, this data set was excluded from the fits.

The final results for the three fit parameters derived from data sets taken at temperatures between 20.01° and 25.35°, were T_c = 19.12° C, x_0 = 2.48 Å, and I_o = 4.86 ph/s/100 mA with χ^2 = 1.83. Previous light scattering experiments[113] with hexane/nitrobenzene critical binary mixtures determined that the bare correlation length x_0 = 3.54 Å, which is in reasonable agreement with our result.

The measured scattering rate, I_o, depends on experimental conditions such as incident flux, detector aperture, sample volume, etc. It is useful to express the scattering rate in terms of the absolute volume specific differential cross section, $d\sigma_v/d\Omega$, which depends only on the intrinsic sample properties and not on any specific experimental factors. $d\sigma_v/d\Omega$ is related to the measured scattering rate by the formula

$$\frac{ds_V}{d\Omega} = \frac{I(q,T) - Bg(q)}{e \cdot V \cdot I_i \cdot e^{-\Delta z/d} \cdot \Delta\Omega} = \frac{I(q,T) - Bg(q)}{e \cdot \Delta z \cdot F \cdot e^{-\Delta z/d} \cdot \Delta\Omega}, \qquad \textbf{(5.3)}$$

where I_i is the incident x-ray intensity, $F = I_i \cdot A = 7.7 \cdot 10^{10}\, ph/s$ is the total flux in the illuminated area A, $V = A \cdot \Delta z$ is the illuminated volume, Δz = 1.0 cm is the sample thickness, $e^{-\Delta z/d} = 0.34$ is the measured sample cell transmission, $e = 0.82$ is the detector quantum efficiency, and $\Delta\Omega = (600mm/2.95m)^2 = 4.13 \cdot 10^{-8}$ sr. is the detector solid angle. Using the fit results for I_o, we arrive at the volume specific absolute differential cross section for concentration fluctuations in a critical mixture of hexane and nitrobenzene:

$$\frac{ds_V}{d\Omega} = \frac{5.47 \cdot 10^{-3} cm^{-1} \cdot t^{-g}}{1 + q^2 \cdot x_0^2 \cdot t^{-2n}} . \qquad \textbf{(5.4)}$$

Our result for $d\sigma_v/d\Omega$ is the first report of an absolute cross section for x-ray scattering from concentration fluctuations in a binary mixture. Knowledge of $d\sigma_v/d\Omega$ is especially important for XPCS experiments as it allows one to predict whether an XPCS experiment on a given materials is likely to be successful or not. The ability to conduct XPCS experiments on any given materials is highly constrained by the limited coherent x-ray flux available. Hence, it is quite useful to have a way of predicting whether a sample will scatter sufficiently strongly for an XPCS study to likely be successful.

Using the following approach we can deduce an expression for the absolute cross section for x-ray scattering from concentration fluctuations in a binary mixture and compare it to our result for the mixture hexane/nitrobenzene. Extending the results from Chapter 2 to the case of composition fluctuations in a binary mixture, we can express the flux scattered into solid angle $\Delta\Omega$ from composition fluctuations in a binary mixture by

$$F = \frac{F_o}{A_i} \cdot r_e^2 \cdot V \cdot \Delta r_e^2 \cdot kT \cdot b \cdot \Delta\Omega \qquad \textbf{(5.5)}$$

where F_0 is the incident flux, A_i is the incident beam area, r_e = 2.8 x 10^{-13} cm is the classical electron radius, V is the scattering volume, Δr_e is the difference in electron density of the two components, k is the Boltzman constant, T is the absolute temperature, and b is the osmotic compressibility of the mixture. The solid angle corresponding to a single speckle is $\Delta\Omega = l^2/A_i$. Writing $V = A_i d$, where d is the penetration depth, we have

$$F = \frac{F_o}{A_i} \cdot r_e^2 \cdot d \cdot \Delta r_e^2 \cdot kT \cdot b \cdot l^2 \qquad \textbf{(5.6)}$$

Thus, it is clear that the flux per speckle is independent of the area of the incident beam, since F_0/A_i is just the incident intensity, which is fixed. Hence, the incident beam size can be dictated by other considerations, such as requiring good transverse coherence or small intensity in the wings of the aperture diffraction pattern. Note that this would not be the case if an area detector were used to simultaneously collect multiple speckles in a fixed solid angle. In that case, the total detected signal would increase with increased incident flux. It was necessary to use a single channel detector to measure a single speckle at a time in this experiment since available area detectors are too slow to measure the fast dynamics of this mixture.

If we ignore interactions then the osmotic compressibility can be approximated as that of an ideal gas mixture, which is detemined purely by entropic considerations and has a value of

$$b_o = c \cdot (1-c) \cdot \frac{< v_0 >}{k \cdot T} \qquad \textbf{(5.7)}$$

where c is the concentration in mole fraction of one of the components and $<v_0>$ is an average molecular volume. For real mixtures, there can be a departure from this ideal gas result. In particular, near a critical point, the compressibility diverges as t^{-g}. We make the rough approximation that the compressibility of a critical binary mixture is given by a bare compressibility equal to that of an ideal gas, enhanced by the critical factor, i.e., $b = b_o t^{-g}$. This is likely to be a good order of magnitude estimate.

As an aside, we note that Equation (5.6) for F also gives the flux per speckle for scattering from density fluctuations in a single component system if Δr_e is replaced by r_e, the electron density of the material, and the osmotic compressibility, b, is replaced by the

isothermal compressibility, k_T, of the material. For solids, k_T is of order $\langle v_0 \rangle / E_0$, where E_0 is a typical binding energy of order a few electron volts, i.e., $E_0 \sim 10^2\ kT$. For liquids, E_0 is of order one to a few times kT. Thus, b is very similar for liquids and solids whereas k_T is similar to b for liquids, but perhaps two orders of magnitude smaller for solids.

Returning to composition fluctuations in a binary system, by substituting Equation (5.7) in Equation (5.6) we obtain

$$F = F_o \cdot r_e^2 \cdot d \cdot \Delta r_e^2 \cdot c(1-c) < v_o > \cdot \Delta\Omega \qquad \textbf{(5.8)}$$

Finally, expressing this as an absolute volume specific differential cross section we have

$$\frac{ds_V}{d\Omega} \approx r_e^2 \cdot \Delta r_e^2 \cdot c \cdot (1-c) \cdot < v_o > \cdot t^{-g} \cdot G(q \cdot x) \approx C^* \cdot t^{-g} \cdot G(q \cdot x), \qquad \textbf{(5.9)}$$

where $G(x) = (1 + x^2)^{-1}$ is the Ornstein-Zernicke function. In the case of a critical binary mixture of hexane and nitrobenzene, using the values from Table 5.1, we have Δr_e = 144 e/nm^3, c = 0.416 is the mole fraction of nitrobenzene in the critical mixture, and $\langle v_0 \rangle$ = 0.194 nm^3 is the average molecular volume.

The prediction of this simple theory for the hexane/nitrobenzene critical mixture is thus

$$\frac{ds_V}{d\Omega} = \frac{7.66 \cdot 10^{-2}\, cm^{-1} \cdot t^{-g}}{1 + q^2 \cdot x_0^2 \cdot t^{-2n}}. \qquad \textbf{(5.10)}$$

This is 14 times greater than our measured value for the absolute differential cross section. The difference is likely to be due to our simplified assumption for the osmotic compressibility, although Equation (5.9) does provide a good order of magnitude estimate, as expected. Furthermore, it is reasonable that the measured value should be lower than our estimate based on an ideal gas since interactions in the single phase region

will tend to keep the components mixed, hence suppressing fluctuations, i.e., lowering the compressibility.

Equation (5.8) for the scattering rate does provide some useful guidelines regarding what sample characteristics will optimize the scattering rate from a binary mixture. A large electron density difference, low average electron density (for large x-ray penetration depth, δ, and hence scattering volume), and large molecular volume all contribute to an increased scattering rate. Hexane/nitrobenzene is quite favorable for these first two characteristics but its molecular volume is quite low. Polymer molecules on the other hand, with their large molecular volume, should have enhanced scattering. Organic polymers also have a low average electron density. Unfortunately, polymer molecules that readily mix in binary mixtures tend to be very chemically similar, which usually implies very small electron density differences. Hence, their large molecular volumes are offset to an extent by their small electron density differences. We will come back to this point when the results for the polymer mixture polystyrene/polybutadiene are presented in Chapter 7.

In order to determine the feasibility of XPCS measurements on this sample, the absolute differential cross section can be used to estimate the expected scattering rate per speckle under coherent illumination. Even though the size of a coherent beam is much smaller than was used for the SAXS measurements, using a pink beam rather than a monochromatic beam can increase the flux. The solid lines in Figure 5.4 show the predicted count rate per speckle for scattering from hexane/nitrobenzene at temperatures of 0.01 K, 0.1 K, and 1.0 K away from T_c, for an incident coherent pink beam of 1.9 x 10^{10} ph/s/(5 μm)^2 and a speckle size of (67 μm)^2.

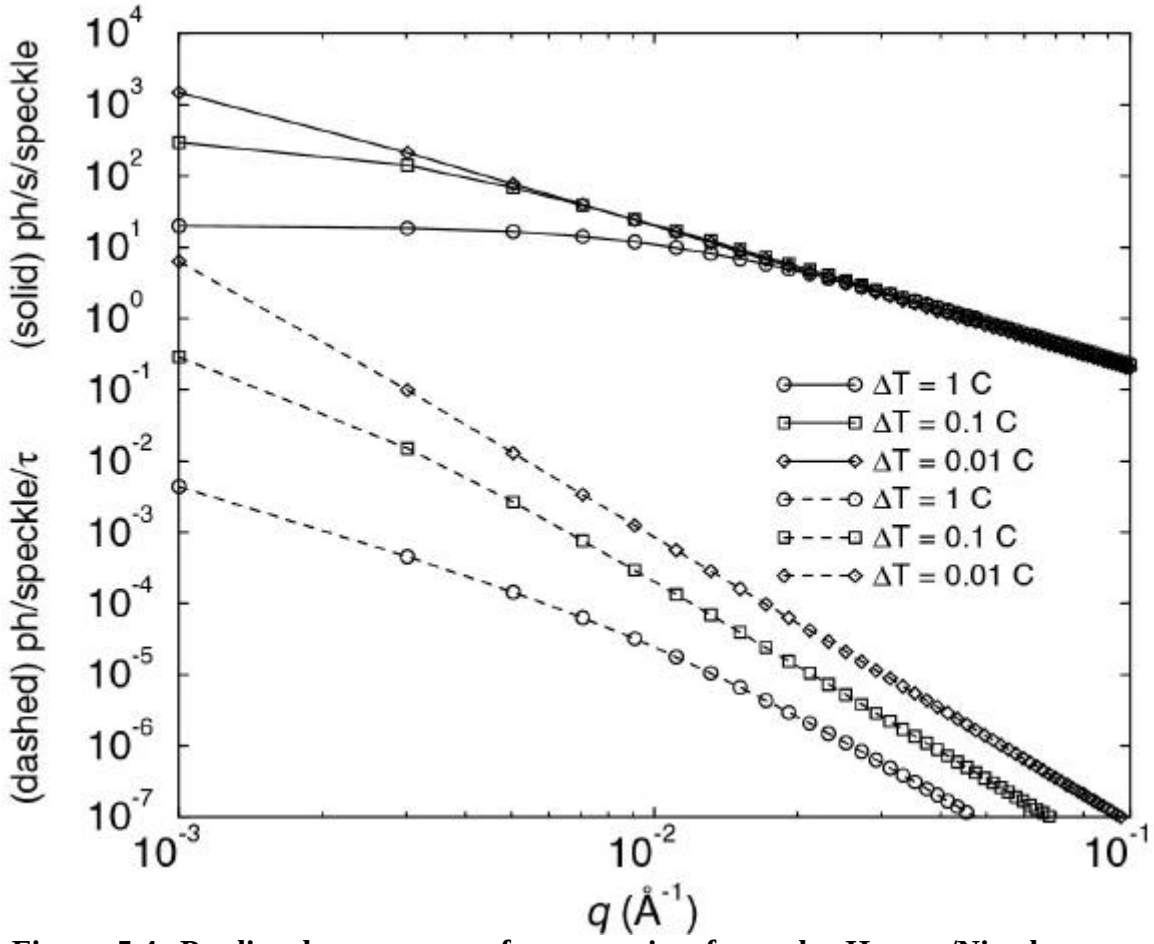

Figure 5.4. Predicted count rates for scattering from the Hexane/Nitrobenzene sample under coherent conditions. Solid lines represent the number of photons per second per speckle, while dashed lines represent the number of photons per speckle per correlation time.

The predicted count rate in Figure 5.4 ranges from about 10 to 1000 ph/s/speckle for $\boldsymbol{q} < 10^{-2}$ Å^{-1}, which sounds promising for an XPCS experiment. However, the real figure of merit for an XPCS experiment is the count rate per speckle per *correlation time*, not the count rate per *second*. We can estimate the correlation time with the Stokes-Einstein relation (see Equations (2.137) and (2.140))

$$t = \frac{6 \cdot p \cdot h \cdot x}{k_B \cdot T \cdot q^2} = 4.67 \cdot 10^{-10} \cdot \frac{h \cdot x}{q^2}, \qquad \textbf{(5.11)}$$

where h = 0.0053 P is the shear viscosity of the hexane/nitrobenzene mixture[113]. For a temperature of 0.1° K away from T_c and a q = 0.004 Å^{-1}, the correlation time is 61 μs. The dashed lines in Figure 5.4 represent the predicted count rate per speckle per correlation time, which, for $\boldsymbol{q} < 10^{-2}$ Å^{-1}, ranges from about 10^{-4} to 1 ph/speckle/τ. While challenging, these low rates and fast relaxation times are not out of the range of what are measurable with a standard single channel hardware correlator.

Dynamic Measurements

For the XPCS measurements the sample was illuminated with a pink beam rather than a monochromatic beam in order to have the highest possible coherent flux. The undulator fundamental was set to 9.0 keV and the in-hutch PBMF was used as described in Chapter 4. The resulting pink beam had an average energy of 8.73 keV and the coherent flux incident on the sample was 3.6 x 10^{10} ph/s/(5 μm)^2, about a factor of 2 more than was assumed in constructing Figure 5.4. Assuming a Lorentzian energy spectrum for the undulator fundamental, the longitudinal coherence length[44] is l_l = 0.318 $l/(DE/E)$ = 17.7 Å, where the measured bandwidth of the undulator fundamental, ΔE/E = 2.55 %, has been used.

As discussed in Chapter 2, the finite longitudinal coherence length limits our scattering angles to be less than 2q, such that the largest optical path difference in the sample, $D2q + tq^2/2$ is less than l_l, where D = 5 μm is the beam size, t = 3mm is the sample thickness, and $q << 1$. For these conditions, the quadratic term can be neglected and the limiting angle θ is about $l_l/(2D)$, or 0.18 mrad. Expressing this angle as a limiting

wave vector yields a q of $4\pi\theta/\lambda$, or 1.6 x 10^{-3} $Å^{-1}$. For measurements made with wave vectors above this value the speckle pattern contrast will be reduced. Although a monochromatic beam would provide for larger longitudinal coherence, thus allowing access to higher limiting wave vectors, it does not provide sufficient flux for this experiment.

For the dynamic scattering measurements, the coherence and guard apertures were set to $(5\ \mu m)^2$ and $(15\ \mu m)^2$, respectively, and the distances between coherence and guard apertures, guard aperture and sample, and sample and detector aperture were 0.2 m, 0.06 m, and 1.24 m, respectively. Thus, the beam size on the sample, which defines the speckle size in the detector plane, is larger than 5 μm due to diffraction. The beam size on the sample is given by $D_s = \sqrt{D^2 + l^2 \cdot R_c^2 / D^2}$, where R_c = 0.26 m is the coherence aperture to sample distance, and D = 5 μm is the beam size at the position of the coherence aperture. This gives D_s = 8.8 μm. The speckle size in the detector plane is then $l \cdot R_d / D_s = 20mm$, where R_d = 1.24 m is the sample to detector distance. It was possible to measure the correlation function on the hexane/nitrobenzene binary mixture with the detector aperture set to $(20\ \mu m)^2$. However, we found that the signal to noise ratio was noticeably improved by further opening the detector aperture, as discussed below. A Brookhaven Instruments BI-2030 hardware correlator was used to measure the dynamic correlation functions.

Figure 5.5 shows the temperature dependence of the scattering rate for the hexane/nitrobenzene mixture measured under coherent conditions. The data is normalized to a constant incident coherent flux of $3.6 \cdot 10^{10}\ ph/s/(5mm)^2$. As previously noted, this

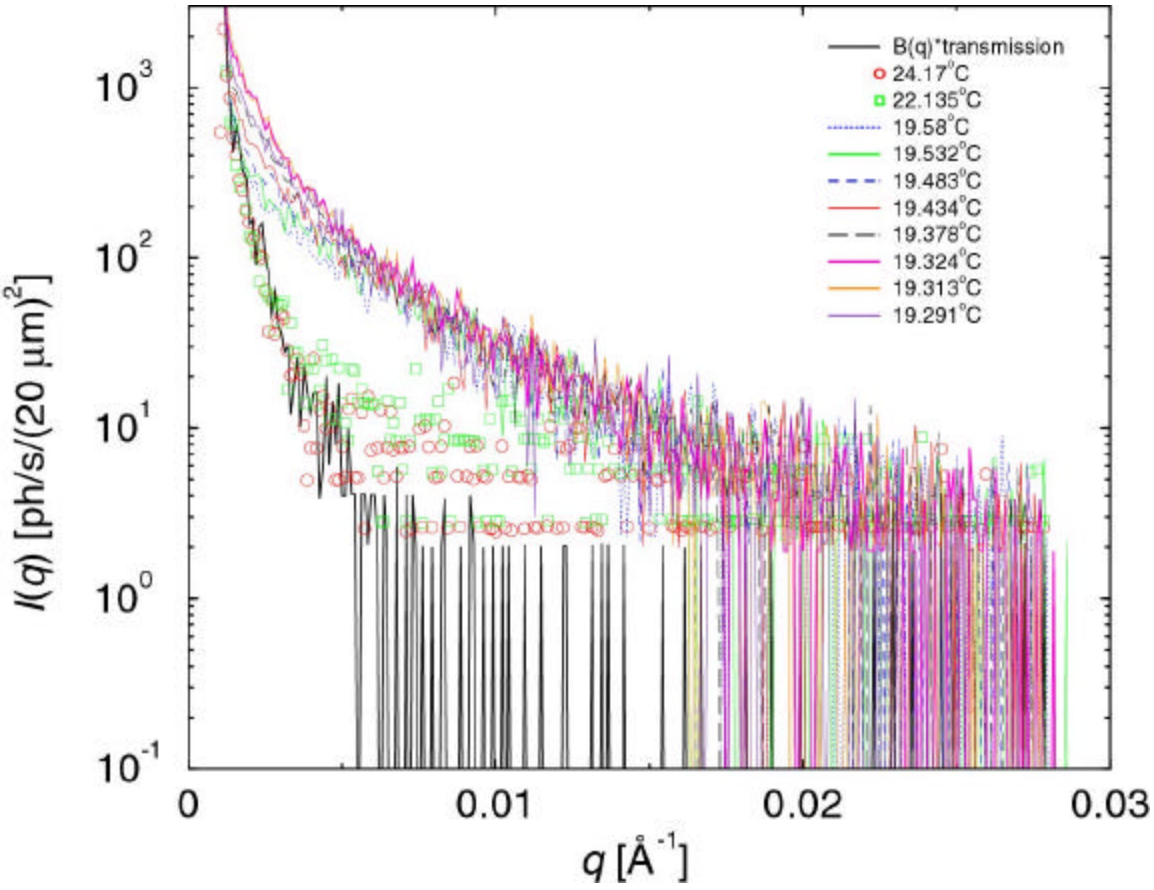

Figure 5.5. Measured scattering intensity per speckle per second under coherent conditions. Zero photon counts are off the logarithmic scale and are being cut. Also shown is the background scaled for the sample transmission. As expected, the sample shows critical opalescence as the sample temperature approaches T_c.

incident pink beam flux is 1.87 times greater than the estimate used in constructing Figure 5.4. However, in these measurements we also used the new sample cell, described in Chapter 4, which provided better temperature regulation but a sample thickness of only 3 mm rather than the 10 mm provided by the sample cell used in the static measurements. The estimates in Figure 5.4 are thus approximately applicable to these measurements. Indeed, we see that the measured scattering rates per speckle are in good agreement with expectations. The background, measured with an empty cell and scaled for the sample

transmission of 0.295, is also shown in Figure 5.5. For all data, the background is smaller than the sample scattering for $q > 0.005$ Å^{-1}. Closer to the main beam, the background becomes a larger fraction of the total scattering rate.

The scattering increases with decreasing sample temperature, consistent with critical opalescence. The scattering is a maximum at 19.313° C, decreasing at 19.291° C. From this we concluded that T_c is between these two temperatures and estimate it to be ~19.30° C. This gives us a slightly higher T_c than the one determined from the static measurements made under incoherent conditions, where we had estimated $T_c \sim 19.12°$ C. This is most likely due to the improved sample cell and oven design, where the sample temperature is now measured much closer to the sample, thus eliminating some temperature bias. Since T_c is below room temperature, it is possible that with the old sample cell, the actual sample temperature was slightly higher than measured, due to a possible thermal gradient induced by the warmer ambient surroundings.

Figure 5.6 shows the dynamic correlation function of the scattering intensity versus the delay time of the correlator at $q = 0.00156$ Å^{-1}, and $T = 19.363°$ C. The detector aperture was set to $(58\ \mu m)^2$ in order to optimize the signal to noise ratio of the correlation function, as further discussed below. The correlator sampling time was set to 25 μs, and the collection times were on the order of 30 to 60 minutes. Since the scattering rate decreases at higher q, we used longer collection times to improve the statistics. Table 5.2 lists the collection times for different wave vectors. The data for the first delay time is compromised by the detector dead time, as discussed in Chapter 2, so it was removed form Figure 5.6 and was not used in fitting. As discussed in Chapter 2, the correlation function can be fit to

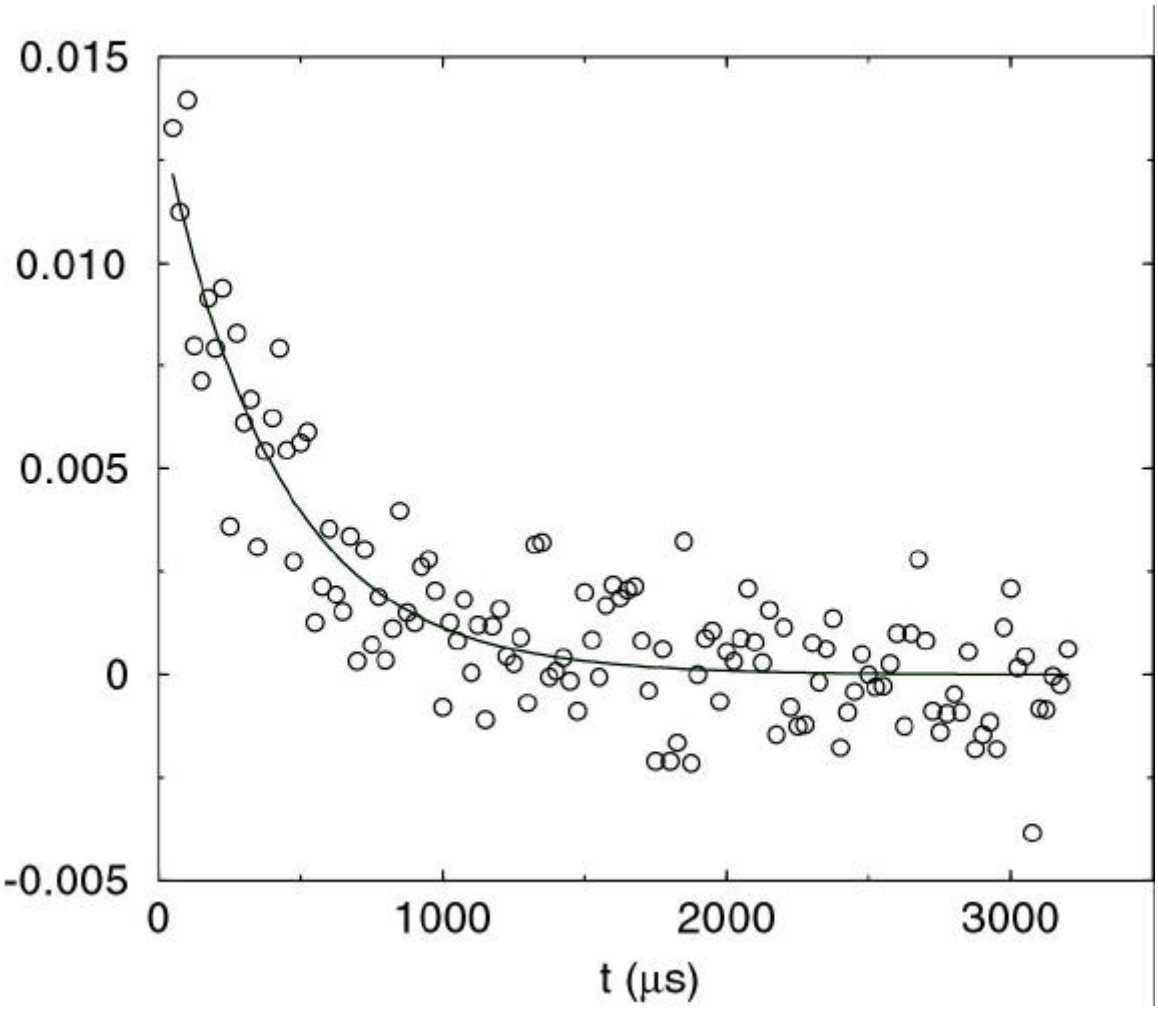

Figure 5.6. Typical dynamic correlation function for the critical binary mixture of hexane and nitrobenzene. Circles represent the measured data, and solid line is a single exponential fit to the data.

$$g_2(t) - 1 = \frac{< I(q,t) \cdot I(q,0) >}{< I >^2} - 1 = b \cdot e^{-2t/t} \,. \qquad \textbf{(5.12)}$$

A fit gave β = 0.0137 for the contrast and τ = 805 μs for the relaxation time of composition fluctuations in the mixture at this wave vector.

Figure 5.7 shows the contrast, β, and signal to noise ratio, SNR, as a function of detector aperture size. The SNR is defined as the ratio of the intercept of the signal at

q [Å^{-1}]	$\langle I \rangle$ [ph/s]	Collection time [s]	τ [μs]	b [%]	b/s	$Bg(q)/I(q)$ [%]
0.00120	12852	1195	2135.	0.274	5.6	-
0.00156	4567	1079	804.7	1.37	11.3	0.56
0.00209	2339	1990	379.6	1.57	8.2	0.24
0.00209	2031	2164	366.1	1.19	5.5	0.24
0.00261	1475	3822	252.0	1.93	6.8	0.16
0.00261	1509	5144	283.5	1.07	6.05	0.16

Table 5.2. Correlation function fit parameters at T = 19.363° C for the hexane/ nitrobenzene mixture. b is the contrast, and s is the standard deviation, thus b/s is the S/N ratio of our measurement. The ratio of background over total intensity is also shown.

zero delay divided by the rms noise at long time delay. The results shown in Figure 5.7 are representative of the dependence on detector size, but the vertical scale is somewhat sensitive to the amount of parasitic scattering collected. The parasitic scattering collected depends upon wave vector, among other things, and generally increases with decreasing wave vector. With a detector aperture of $(20\ \mu m)^2$, we measured a contrast as high as 8 %, although we typically opened the detector aperture to improve the SNR of g_2.

A simple model[26], along the lines of that discussed in Chapter 2, for the dependence of the contrast on detector aperture due to spatial averaging of the speckles is given by

$$b = \frac{b_o}{1 + A/A_s} \qquad \textbf{(5.13)}$$

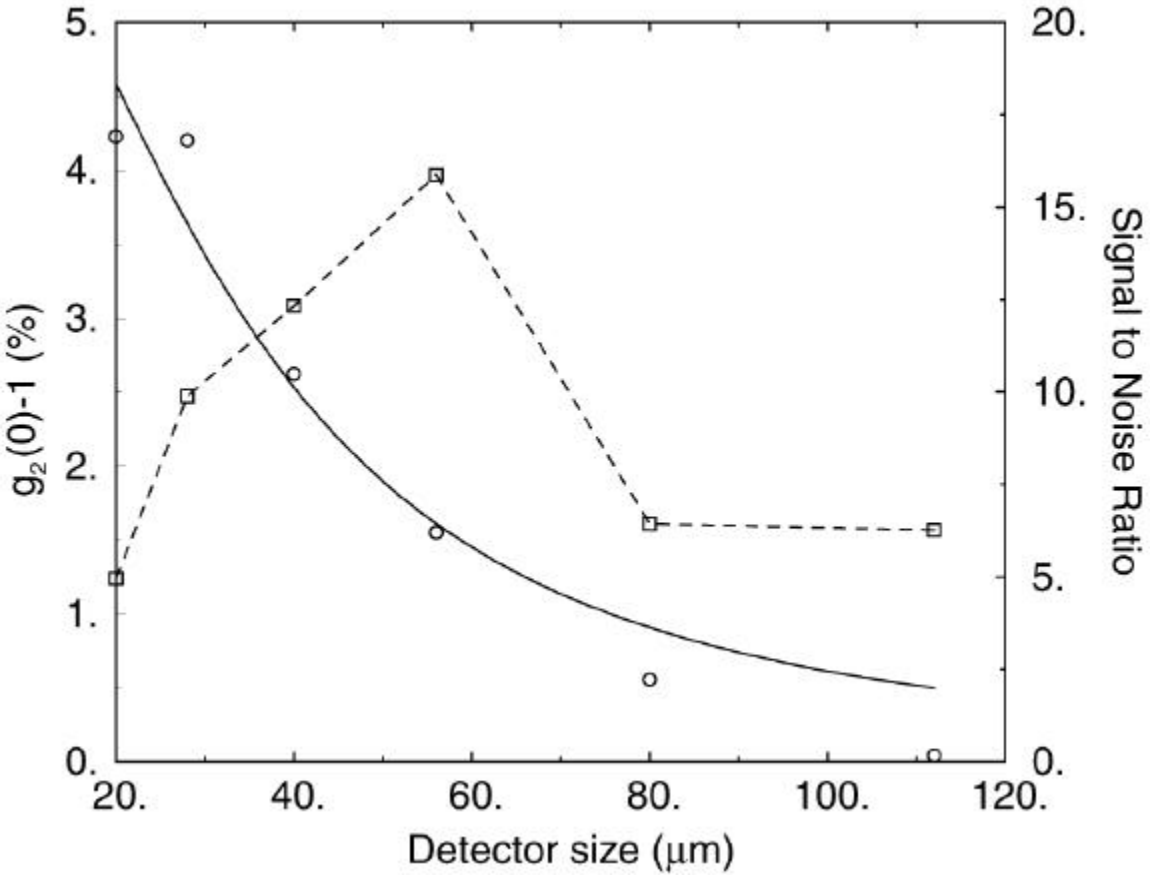

Figure 5.7. Contrast versus detector aperture size (left axis, circles). The solid line is a fit as discussed in the text. The signal to noise ratio versus the detector aperture is also shown (right axis, squares). The dashed line is a guide to the eye.

where b_o is the contrast in the limit of zero detector size, i.e., no spatial averaging, A is the detector area, and A_s is the speckle area. A fit of this equation to the contrast measurements is shown in Figure 5.7 as the solid line. The deduced speckle size is (33 μm)^2 and b_o is 6.3 %. The deduced speckle size is somewhat larger than the (20 μm)^2 we estimated based on our aperture size. However, the data with detector sizes greater than (25 μm)^2 were collected with sample times of 25 μs whereas data with detector sizes less than (25 μm)^2 were collected with sample times of 50 μs due to their lower SNR. Thus, there may be some additional reduction in b in Figure 5.7 due to time averaging of the

350 μs relaxations for smaller detector apertures which is not present for larger apertures. Nevertheless, this simple model of spatial averaging explains the data quite well.

The dependence of SNR shown in Figure 5.7 is also easily understood. For small detector apertures, the increasing photon noise reduces the SNR since the measurements were all for the same total time duration. At larger detector apertures, spatial averaging of the speckles reduces the SNR. We find a maximum in the SNR for a detector aperture which is 2 to 3 times the speckle size, as expected based on experience with visible light PCS and the discussion in Chapter 2.

Table 5.2 shows the fit parameters for several wave vectors at the same fixed temperature of 19.363^{o} C, which is about 63 mK above T_c. For two wave vectors, the data was measured twice. The correlation time was overall quite reproducible given that the data collection was reproduced several hours after it was first taken.

The repeatability of the correlation times deduced from data taken several hours apart, during which interval the sample was continuously exposed to the x-ray beam shows that the sample was not affected by x-rays. As noted in Chapter 1, this tolerance to exposure to a high intensity x-ray beam is remarkable among soft condensed matter, organic systems, which are generally much more susceptible to radiation induced charging or damage effects. In this case, we speculate that the small hexane and nitrobenzene molecules are resistant to chemical alteration due to irradiation and the low viscosity of the mixture and concomitant high diffusion coefficient contributes to alleviating the effects of any radiation damage that does occur. Unfortunately, the polymer samples studied in this thesis did not prove as robust under irradiation. The effects of radiation damage on those materials are presented in Chapter 6.

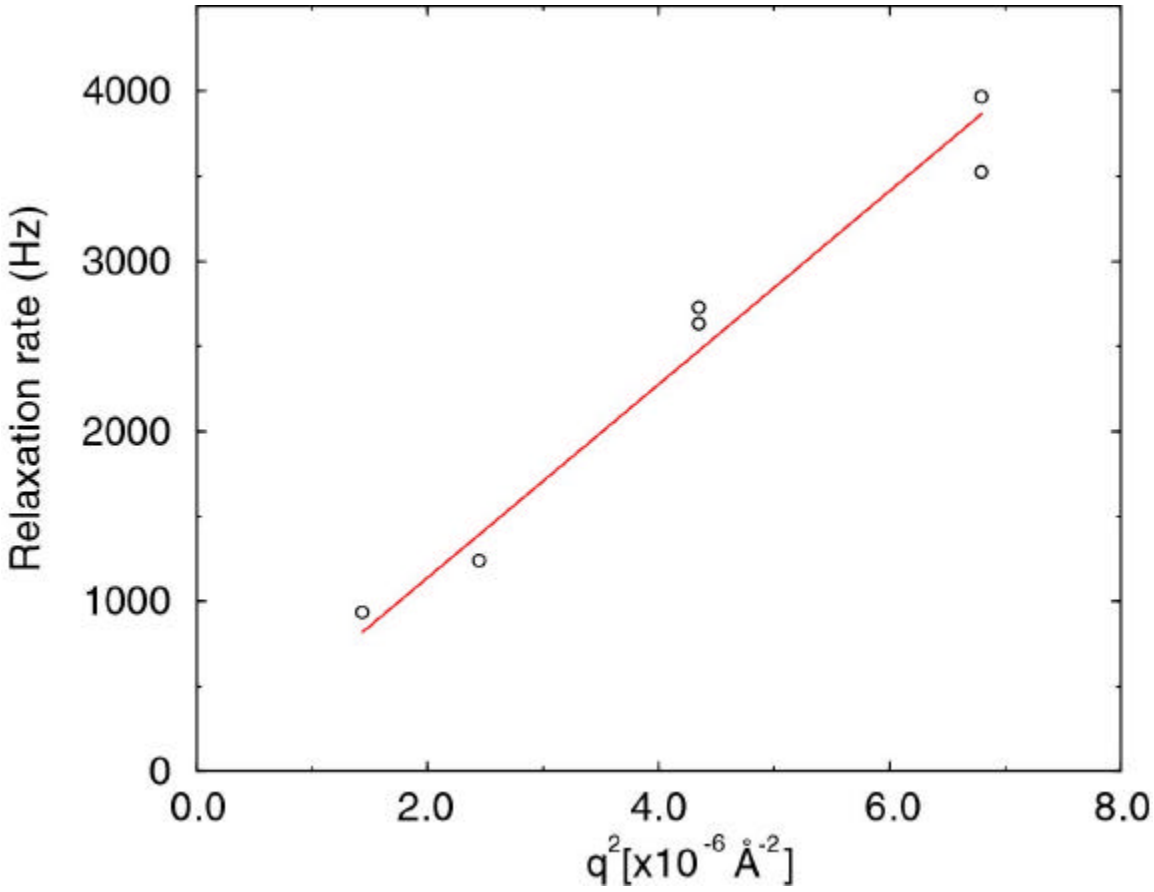

Figure 5.8. Relaxation rate, or inverse of relaxation time, vs. q^2. Circles represent the data points, while the solid line is the best fit to the data.

Figure 5.8 shows the relaxation rate versus the square of the wave vector for the critical mixture at T = 19.363° C. As one can notice from the data in Table 5.2, the correlation time for the smallest wave vector is much larger than expected. In addition, the signal to noise ratio of the correlation function is small at this wave vector and the intercept of g_2 at zero delay time is much smaller than expected. For data taken at wave vectors so close to the main beam, we believe that the stray parasitic background Bg(q) reduces the contrast and signal to noise of g_2. Furthermore, we believe that the scattered field from the sample is heterodyning with the main beam, which acts as a reference

signal. When such phenomena occur, it is well known that the measured contrast and signal to noise ratio of the correlation function is reduced, and the correlation time is twice as long as in a homodyne measurement. Hence, in Figure 5.8, we divided the correlation time derived from the data measured at the smallest wave vector by a factor of 2. The solid line in Figure 5.8 is a fit to $1/t = D \cdot q^2$ with a diffusion constant $D = 5.68 \cdot 10^8$ Å^2/s. The data shows nice agreement with the fit, which is an indication of simple diffusive relaxation for the range of wave vectors in this experiment.

From our SAXS measurements we estimated the bare correlation length x_0 = 2.46Å, from which we can calculate the correlation length at the temperature corresponding to the data in Figure 5.8 as $x = x_0 \cdot t^{-0.635} = 524$ Å. From the Stokes-Einstein relation (Equation 5.11) the diffusion constant is $D = k_B \cdot T/6 \cdot p \cdot h \cdot x$. Using the known viscosity of the mixture, this relation results in an estimate for D of 7.71x10^8 Å^2/s, which is in a good agreement with the diffusion coefficient derived from the fit to the slope of data in Figure 5.8.

Conclusion

In summary, we performed a SAXS study of the binary mixture hexane/nitrobenzene near its critical point. We extracted the critical component of the measured scattering rate from the data by fitting the data to a scaling form. The resulting critical exponents are consistent with previous light scattering measurements. We determined the absolute x-ray scattering cross section for scattering from composition fluctuations in the mixture and compared it to an approximate theoretical expression.

This approach allowed us to describe useful guidelines for determining good candidate materials for XPCS studies.

With a pink beam we were able to measure a scattering rate of several hundred ph/s/speckle under coherent conditions. We performed an XPCS measurement on the mixture at a fixed temperature of about 63 mK above the critical point. Although this mixture is composed of low molecular weight hydrocarbons, it scatters x-rays relatively well due to it's large x-ray contrast and x-ray penetration depth, although the scattering is still very weak on the scale of x-ray scattering from ordered materials such as crystals or even from disordered materials with an aggregate microstructure. Using a hardware correlator, we were able to measure the first XPCS dynamic correlation function from equilibrium fluctuations in a simple binary fluid. Although rather fast (250 μs), we were able to measure the correlation functions with sufficient signal to noise within an hour of collection time. This XPCS measurement would not have been possible without the large coherent flux provided by a 3rd generation synchrotron source like the APS. The diffusion constant deduced from the XPCS measurements is consistent with an estimate from light scattering measurements.

These measurements demonstrate the feasibility of using XPCS to study the dynamics of samples that scatter x-rays weakly, such as these low molecular weight hydrocarbon fluid mixtures. This further demonstrates the general applicability of XPCS to a wide variety of materials. We found no detectable signs of radiation damage in these mixtures even under the high intensity of a pink undulator beam at a 3rd generation synchrotron source such as the APS. With further improvements in technique, it should be possible to extend such measurements on this and other fluid mixtures into a new

range of wave vectors previously inaccessible. Such studies would be of interest in further testing the breakdown of hydrodynamics at short length scales beyond the Kawasaki-Ohta approximation. Studies of binary fluids in confined geometries should also benefit from this technique.

CHAPTER 6.
X-RAY RADIATION DAMAGE EFFECTS IN POLYSTYRENE / POLYBUTADIENE POLYMER MIXTURES

Introduction

During preliminary measurements of the critical dynamics of the low molecular weight binary polymer mixture polystyrene/polybutadiene with a coherent "pink" x-ray beam, we noticed that the scattering rate increased with exposure time. This could not be explained by the normal beam intensity change due to the decay of the current in the APS storage ring, and brought into question the stability of the sample in the x-ray beam. Obviously, it is important to know that the sample composition and properties have not changed during the duration of a measurement. Hence, we decided to explore the stability of this polymer mixture under the intense x-ray exposure produced by a third generation synchrotron source.

There have been a number of studies of the effects of high energy irradiation on polymeric materials over the past few decades[116]. The effects of radiation in space on polymer materials is now of considerable importance due to the increasing use of communications satellites and space stations.

A few types of radiation are typically considered in the literature on studies of radiation damage to polymers. They may be classified into photon and particle radiation.

Gamma radiation is utilized for fundamental studies and for low-dose rate irradiation with deep penetration. Radioactive isotopes, particularly Co^{60}, produced by neutron irradiation of naturally occurring Co^{59} in a nuclear reactor, and Cs^{137}, which is a fission product of U^{235}, are the main sources of gamma radiation. X-rays of lower energy are produced by electron bombardment of suitable metal targets with electron beams or by synchrotron sources. Photon radiation has a large penetration depth compared to that of particle radiation.

Electron irradiation is normally obtained from electron accelerators to give beams with energies in MeV-GeV range. The corresponding penetration depths are then a few mm. Much lower energy electron beams are used in electron microscopy and in electron beam lithography. These lower energy electron beams are used to study thin polymer films since a large proportion of the energy is deposited in a μm thick top layer. Such low energy electron beams are also used in computer controlled circuit pattern transfer to a resist film.

Nuclear reactors are another source of high radiation fluxes. This comprises mainly neutrons and gamma rays, and heavy ions. The neutrons largely produce protons in hydrocarbon polymers by “knock-on” reactions, so that the radiation chemistry of neutrons is similar to that of proton beams, which may also be produced by accelerators.

Alpha particles cause intense ionization and excitation due to their large mass, and consequently produce substantial surface effects. Heavy ions may be produced in charged particle accelerators.

Several books are available that cover the high-energy irradiation of polymeric materials[117,118,119,120,121,122]. However, all these books and other studies cover high energy

irradiation, where the energies involved are much greater than the electron binding energy of any electron to an atomic nucleus. Low energy radiation effects on polymers have also been intensively studied in industry. Resistance of polymeric materials to ultraviolet light is a very important subject in everyday life. However, there is relatively little literature on the effects of intermediate energy radiation, especially those produced by x-rays in the energy region of interest around a few to a few tens of keV.

There are only a very limited number of studies to date that cover the energy region accessible to synchrotron radiation. These studies are primarily concerned with the change of physical properties of thin solid polymer films upon irradiation. This is of particular interest to the industrial use of polymers as photoresist in micro-manufacturing[123]. Techniques such as x-ray photoelectron spectroscopy (XPS) and mass spectrometry have been used to determine the products of polymer decay under x-ray irradiation. These are interesting techniques, which can provide information on the detailed damage mechanism. However, such studies are out of the scope of this work. We are primarily interested in developing an empirical understanding of the change in dynamic scattering from polymer samples and the overall resistance of the samples to synchrotron radiation.

Resistance of polymer samples to the damaging effects of x-rays is an important issue with the use of high intensity x-ray sources, especially in the case of measurements of the dynamics of polymers with relatively large relaxation times, where the sample must be exposed to the x-ray beam for thousands of seconds. If during the measurement the sample properties change due to radiation damage, then the measurements may be affected by this change. Often the effects of radiation damage are cumulative over time.

This implies that there may be a maximum duration for an XPCS measurement at a particular sample spot. Very little information from previous studies of the effects of x-ray radiation on organic materials exists in a form that can be directly used to determine this maximum duration for an XPCS experiment. In this chapter, I describe such results for a polymer mixture of polystyrene and polybutadiene. Since this study is primarily concerned with the effects of x-ray radiation on polymers, I will henceforth omit discussion of the effects of other types of radiation.

Radiation Chemistry

For high energy x-ray radiation, with $E > 4$ MeV, the primary mechanism of energy absorption is by pair production. For low energy x-rays, with $E < 0.2$ MeV, energy absorption occurs by Compton scattering and the photoelectric effect. In the photoelectric effect, all the energy of the photon is transferred to an electron ejected from the valence shell, whereas in Compton scattering there is also a scattered photon of lower energy than the incident one. Thus, the radiation chemistry of photons occurs mainly through interactions of the excited atom and secondary electrons with the polymer molecules. The interactions of secondary electrons with valence electrons in the polymer cause excitations and ionization, which result in chemical reactions.

The absorption of the radiation depends only on the electron density of the medium. Mass density is a reasonable first approximation to the electron density. More accurately and conveniently, the average value of Z/A for the atoms, where Z is the atomic number and A is the atomic mass, can be used to calculate the relative dose.

Energy absorption has been traditionally expressed as a dose rate in rads, where 1 rad = 10^{-2} J/kg. The SI unit is the gray (Gy), where 1 Gy = 1 J/kg, so 1 Gy = 100 rads. Radiation chemical yields are conventionally expressed in G values for the number of molecules changed or formed for each 100 eV of energy absorbed. The chemical reactions that result from irradiation of polymers consume only a small fraction of the absorbed energy, and the rest is mainly dissipated in the form of heat. For example 0.1 MGy of energy absorbed in a thermally insulated volume of water will produce a temperature rise of 24° C, and about twice that in polymers, whose heat capacity is typically about half that of water. Of course, this rise depends on the thermal conductivity of the sample and on the effectiveness of any surrounding heat sink. In practice, the resulting temperature rise will usually be substantially smaller.

Absorption of radiation by polymer produces excitation and ionization and these excited and ionized species are the initial chemical reactants. The ejected electron must lose energy until it reaches thermal energy. Recombination with a parent cation radical may then occur and is more likely in materials with low dielectric constant. The resultant excited molecule may undergo homolytic or heterolytic bond scission. Alternatively, the parent cation radical may undergo spontaneous decomposition, or ion – molecule reactions. The initially ejected electron may be stabilized by interaction with polar groups, as a solvated species or as an anion radical. The radiation chemistry of polymers is therefore the chemistry of neutral, cation and anion radicals, cations and anions, and excited species.

The reactions of free radicals include (1) abstractions of H atoms, with preference for tertiary H, and of halogen atoms, (2) addition to double bonds, which are very

efficient scavengers for radicals, (3) decompositions to give small molecule products, such as CO_2, and (4) chain scission and cross-linking of molecules.

When main chain bond scission occurs in polymer molecules in the solid state to form two free radicals, the limited mobility of the resultant chain fragments mitigates against permanent scission. This concept is supported by the increased yields of scission in amorphous compared with crystalline polymers. Similarly, the scission yields are increased above the glass transition, T_g, and melting, T_m, temperatures. There is also evidence from NMR studies of the changes in tacticity in poly(methyl methacrylate) that racemization occurs at a higher rate than permanent scission of the main chain, consistent with initial main-chain bond scission, rotation of the newly formed chain-end radical, and geminate recombination.

Although the absorption of radiation energy is dependent only on the electron density of the material and therefore occurs spatially at random on a molecular scale, the subsequent chemical changes are not random. Some chemical bonds and groups are particularly sensitive to radiation-induced reactions. They include COOH, C-Hal, $-SO_2-$, NH_2, and C=C. Spatial specificity of chemical reaction may result from intramolecular or intermolecular migration of energy or of reactive species – free radicals or ions. Enhanced radiation sensitivity may be designed into polymer molecules by incorporation of radiation sensitive groups, and this is an important aspect of research in radiation lithography.

Compared to the aforementioned chemical bonds and groups, aromatic groups have long been known to give significant radiation resistance to organic molecules. There was early work on the hydrogen yields from cyclohexane ($G(H) = 5$) and benzene ($G(H)$

= 0.04) in the liquid phase, and of their mixtures, which showed a pronounced protective effect.

A substantial intramolecular protective effect by phenyl groups in polymers is shown by the low *G* values for H_2 and cross-linking in polystyrene (substituent phenyl) and in polyacrylene sulfones (backbone phenyl), as well as many other aromatic polymers. The relative radiation resistance of different aromatic groups in polymers has not been extensively studied, but appears to be similar, except that biphenyl provides increased protection. Studies on various poly(amino acids) indicate that the phenol group is particularly radiation resistant.

The combination of radiation-sensitive and radiation-resistant groups is interesting. Halogen substitution of the phenyl group in polystyrene results in high radiation sensitivity with inter-molecular cross-linking.

The molecular changes in polymers resulting from radiation-induced chemical reactions may be classified as:

1. Chain cross-linking, causing an increase in molecular weight. The continued cross-linking of molecules results in the formation of a macroscopic network and the polymer is no longer completely soluble, the soluble fraction decreasing with radiation dose.
2. Chain scission, causing decrease in molecular weight. Many material properties of polymers are strongly dependent on molecular weight, and are substantially changed by chain scission. Strength – tensile and flexural – decreases, and rate of dissolution in solvent increases.

3. Small molecule products, resulting from bond scission followed by abstraction or combination reactions, can give valuable information on the mechanism of the radiation degradation. Gaseous products, such as CO_2, may be trapped in the polymer, and this can lead to subsequent crazing and cracking due to accumulated local stresses. Contamination of the environment, e.g. by HCl liberated from poly(vinyl Chloride), can be a significant problem in electronic devices).
4. Structural changes in the polymer, which will accompany the formation of small molecule products from the polymer, or may be produced by other reaction, can cause significant changes to the material properties. Development of color, e.g. in polyacrylonitrile by ladder formation, and in poly(vinyl chloride) through conjugated unsaturation, is a common form of degradation.

The changes in molecular weight may be used to determine yields of scission and cross-linking. Average molecular weights may be obtained by viscometry, osmometry, light scattering, gel permeation chromatography and sedimentation equilibrium. Equations have been derived which relate scission yield, *G(S)*, and cross-linking rate, *G(X)*, to changes in molecular number, M_N, molecular weight, M_W and monomer Z, M_Z. Cross-linking produces branched molecules and the relative hydrodynamic volume (per mass unit) decreases compared with linear molecules. Therefore, molecular weights derived from viscometry and gel permeation chromatography will be subject to error.

The equations relating M_N and M_W to radiation dose which are most frequently used apply to all initial molecular weight distributions for M_N, but only to the most probable distribution ($M_W/M_N = 2$) for M_W. However, equations have been derived for other initial distributions, especially for representation by the Shultz-Zimm distribution.

Unfortunately these equations deal with large M_W and M_N polymers and not the small M_W and M_N polymers used in this study.

There is more information on scission and cross-linking available in the complete molecular weight distribution than in average molecular weights. Equations suitable for simulation of molecular weight distributions for any initial distribution and chosen values of *G(S)* and *G(X)* have been developed and demonstrated for high energy irradiation. A few other ways to determine G(S) and G(X) are available, such as NMR, stress relaxation measurements on elastomers, measurements of swelling of the irradiated polymer, soluble fraction measurements, etc., however, this is beyond the scope of this study. An interesting fact is that when the measurements for *G(X)* obtained by NMR for radiation cross-linked polybutadienes are compared with swelling, solubility and mechanical property methods, much larger values result from the NMR measurements. This has been attributed to clustering of cross-links. Clustering of cross-links can be explained by a kinetic chain reaction occurring through the C=C double bonds. Cross-linking by the conventional vulcanization process with sulfur has been shown by NMR to proceed through the allylic hydrogen atoms. Thus, the mechanism of cross-linking is different in the two methods.

The morphology affects the rates of different chemical reactions. As mentioned above, there is a well-established evidence that *G* values are usually greater in amorphous than crystalline regions, especially for cross-linking, which may not occur in crystalline regions, and greater in rubbery than glassy polymers.

Temperature also affects the rates of chemical reactions, which increase with temperature due to the greater proportion of molecules that have energies in excess of the

activation energy, and this will also apply to radiation-induced secondary reactions in polymers. All chemical reactions are in principle reversible and this applies equally to polymerization. Therefore, formation of active sites, particularly free radicals by chain scission, which are identical to propagating radicals, can lead to depropagation. The probability of depropagation will increase with temperature and can have an important role in the radiation degradation of polymers with low activation energy for propagation. For example, poly(alpha-methyl styrene) and poly(methyl methacrylate) show increasing amounts of monomer formation during irradiation above 150° and 200° C, respectively.

The main effects of dose rate are thought to be due to an increase in temperature of the polymer and depletion of oxygen (for irradiation in air) at high dose rates. It seems unlikely that direct effects of dose rate should occur for electron, gamma and high energy x-ray irradiation, due to the low spatial density of the ionizations and excitations. The effect of dose rate in the x-ray energy range of interest in this work is shown in the experimental part of this chapter.

The mechanisms of radiation effects on polymers are frequently investigated by studies of low molecular weight model compounds. Analysis of the chemical reactions is then much easier than with high molecular weight polymers. Thus, *N*-acetyl amino acids can be studied as model compounds for poly(amino acids) and hence for proteins. However, the chemical changes observed in low molecular weight compounds can be quite misleading as models for polymers. Difficulties include the high concentration of end groups, e.g. COOH in *N*-acetyl amino acids, which can dominate the radiation chemistry of the models. Low molecular weight compounds are usually crystalline in the solid state and reactions such as cross-linking may be inhibited or severely retarded.

Cross-linking of low molecular weight polymers (oligomers) is effectively a type of polymerization. Since it is low molecular weight polymers that are used in our binary mixture under study, we think that polymerization or cross-linking of polybutadiene is mainly responsible for the changes we observed in x-ray scattering rates. The effects of radiation on blends depend on the degree of compatibility and the extent of intermolecular interaction (physically and chemically) between the different types of homopolymers. Compatibility is influenced by the molecular weight of the homopolymers, with the components generally becoming less compatible with increasing molecular weight. Hence, compatibility may be reduced by a radiation-induced increase in molecular weight due to cross-linking.

There are a great number of parameters involved in determining how the properties of polymers are changed by radiation. Relationships between chemical structure and radiation sensitivity are modified by the morphology of the polymer and irradiation conditions. We have conducted our study under the same conditions used for our static SAXS and dynamic XPCS measurements except when we used a larger incident beam in order to subject the sample to a much higher x-ray flux. The goals of our study were limited to determining the time span during which our polymer samples could be exposed to x-rays under coherent conditions before any significant change in x-ray scattering rates occur.

Time Resolved Small Angle X-Ray Scattering

The undulator energy was set to 9.0 keV, a pink beam was created with the in-hutch PBMF and the SAXS setup was used, as described in Chapter 4. The sample was

illuminated with two different size x-ray beams, $(50\ \mu m)^2$ or $(5\ \mu m)^2$, with fluxes of $5x10^{12}$ ph/s and $4x10^{10}$ ph/s, respectively, to check for any dependence on beam size. A set of 1 mil thick copper foil filters was used as attenuators to vary the incident flux for each beam size in order to check for any dependence on dose rate. The remotely controlled XIA filter unit, described in Chapter 4, was used to provide up to two orders of magnitude attenuation of the x-ray beam. The sample was confined in the aluminum "coin-stack" cell design described in Chapter 4, having an 8-mm inner diameter and 3 mm thick volume for the sample, with entrance and exit windows made of 5-mil thick IF-1 grade Be. The sample cell was placed in the 3-stage sample oven and the temperature stability of the sample was within 1-mK of the set point over long periods of time.

The sample consisted of 65 % by weight of M_w = 2000 polystyrene mixed with M_w = 1000 polybutadiene. This mixture has an upper critical solution temperature of ~33.6° C, as discussed in Chapter 7. The data was taken at several different sample temperatures ranging from 80^o C down to 25^o C, which is below the critical temperature for this sample. Further details on the sample properties and preparation are given in Chapter 4.

Data was collected with a custom built direct detection CCD detector using a Kodak KAF-0400 front illuminated CCD chip with a 512x768 array of 9-μm square pixels. Time resolved SAXS patterns from the mixture were measured. Structure factors were extracted from the data at different times during irradiation. The time dependence during irradiation of the scattering intensity at several individual *q*'s uniformly covering the range from $4x10^{-3}$ $Å^{-1}$ to $4.5x10^{-2}$ $Å^{-1}$ was also extracted. The measurements were

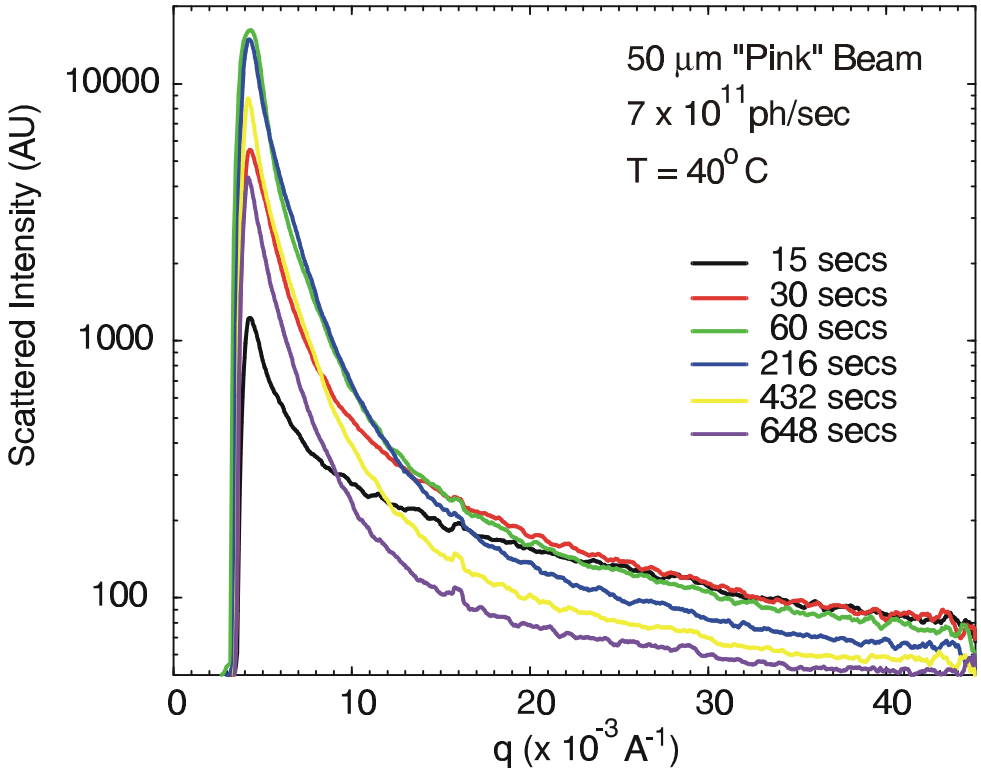

Figure 6.1. Time dependence of SAXS from the polystyrene/polybutadiene mixture.

repeated for different incident x-ray intensities, each on a fresh sample spot, by inserting a variable number of 1 mil thick copper foils into the beam with the XIA filter unit.

Figure 6.1 shows the time dependence of the measured SAXS scattering rate when the sample was illuminated by an attenuated $(50\ \mu m)^2$ pink beam at a sample temperature of 40^o C. At the earliest times, the SAXS is time invariant and is due to scattering from composition fluctuations in this critical mixture. This temperature dependent critical scattering is described in detail in Chapter 7. An initial 'quiescent' period is followed by a strong increase in scattering at wave vectors below ~ 0.025 $Å^{-1}$, while the intensity at higher wave vectors stays approximately constant. Finally, the late time behavior is characterized by a uniform reduction in scattering.

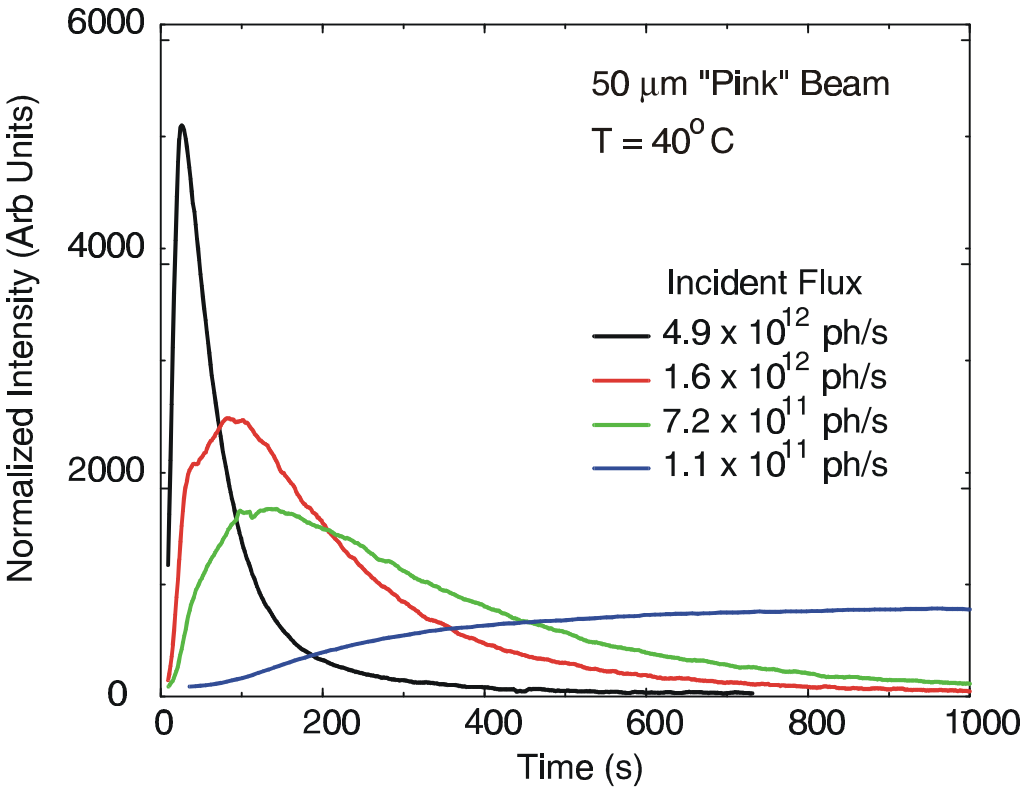

Figure 6.2. Time dependence of the scattering from the mixture at q = 6.5 x 10^{-3} Å^{-1} and a temperature of 40° C for various incident x-ray fluxes.

In Figure 6.2, the time dependence of the scattering rate at a wave vector of q = 6.5 x 10^{-3} Å^{-1} and a sample temperature of 40° C is shown for various incident fluxes obtained from a (50 μm)^2 pink beam by the use of attenuators. Again, we see three phases to the time dependence: a very early time-independent phase followed by an intermediate phase with a strong rise in scattering and a late phase with a strong decrease in scattering.

The large variation in times for the three phases in Figure 6.2 for different incident fluxes, with lower fluxes taking longer times to develop, suggests that the sample damage may be a function of accumulated dose. This relation is shown to be

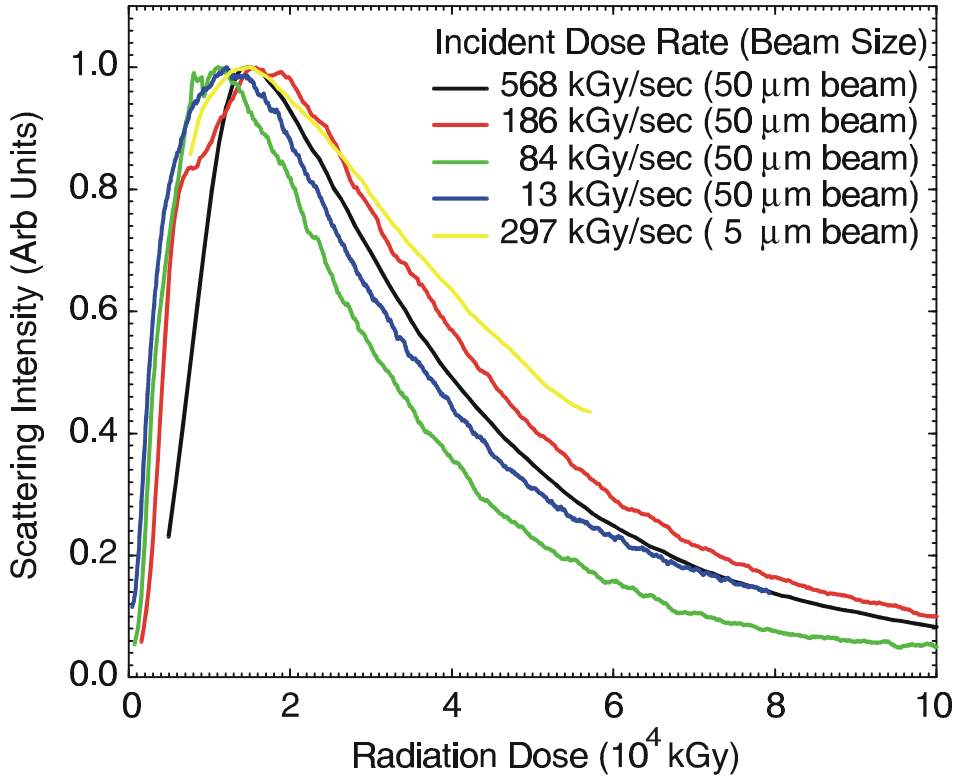

Figure 6.3. Scaling of the SAXS at q = 6.5 x 10^{-3} $Å^{-1}$ with accumulated dose for various incident dose rates.

obeyed remarkably well in Figure 6.3, where the scattering intensity is normalized to 1 at its maximum and plotted versus radiation dose, expressed in kGy. Also included in Figure 6.3 is the change of scattering intensity caused by an unattenuated (5 μm)^2 beam. When calculating the radiation dose due to the (5 μm)^2 beam we assumed that the beam size on the sample was broadened by Fraunhoffer diffraction to (9 μm)^2. All the data in Figure 6.3 follow a very similar curve even though the dose rate varies by a factor of 43 and the incident beam size varies from (5 μm)^2 to (50 μm)^2.

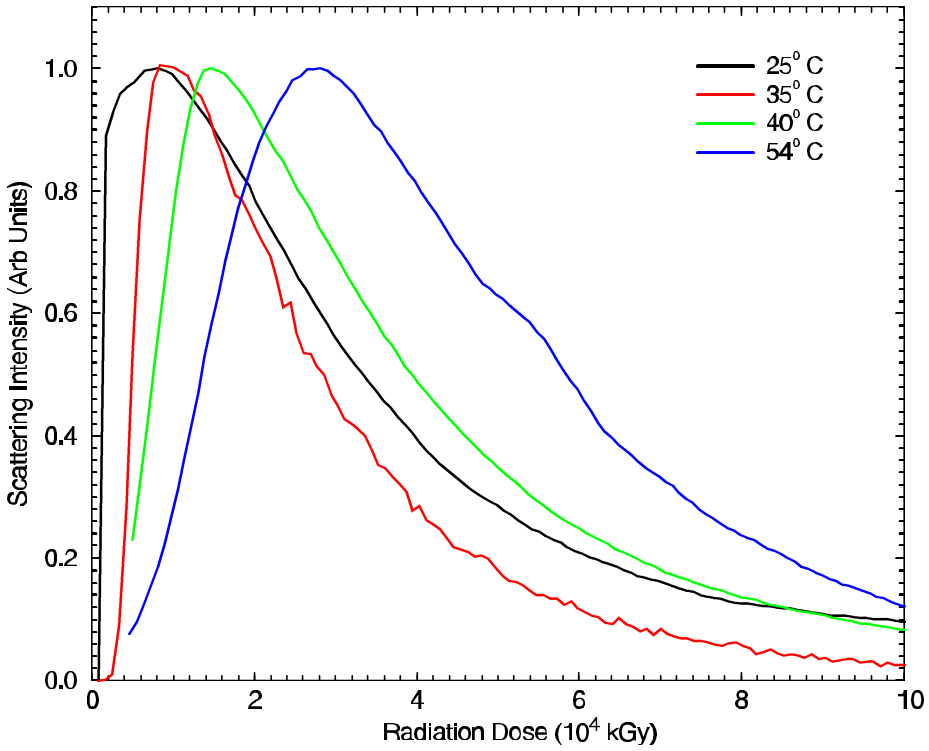

Figure 6.4. Effect of sample temperature on normalized SAXS versus dose at q = 6.5 x 10^{-3} $Å^{-1}$. Dose rate was 580 kGy/sec in a (50 μm)^2 beam.

Figure 6.4 shows the scattering intensity as a function of dose for temperatures from 25° C to 54° C, with similar incident fluxes corresponding to a dose rate of 580 kGy/sec on the sample and with (50 μm)^2 beam size. Even though we can see the same trend with three distinct time dependent phases, the peak of the scattering intensity occurs at a higher dose for higher sample temperature. We believe that this effect is due to the change in viscosity. At higher temperatures, the viscosity of the sample is substantially lower, which allows defects to diffuse out of the illuminated volume more quickly and slows the rate of increase in the accumulated defect density. A lower viscosity also promotes self-healing of the damage, as discussed in the section on radiation chemistry.

We believe the initial increase in scattering at small wave vectors is due to the x-

ray radiation induced formation of increasingly larger cross-linked molecules. The eventual diminution of the scattering at late times is thought to be due to the growth in size of the cross-linked molecules, with their scattering moving to lower *q*, together with a reduction in scattering from composition fluctuations as the damaged material grows to fill the scattering volume being probed. This uniformly reduces the scattering at late times. A secondary cause for the increase might be due to radiation induced phase separation. As the molecules increase in size, their interaction will increase and they will tend to phase separate at a higher temperature. This would give intensity versus time that would mimic that observed during a temperature quench. However, the fact that we see similar behavior even at temperatures for which the sample is already phase separated argues against this being a very significant component of the time dependence of the intensity.

This explanation is supported by the available data on the cross-linking, *G(X)*, and scission, *G(S)*, yields for polystyrene and polybutadiene upon high-energy irradiation[116]. Polystyrene is relatively resistant to the effects of the irradiation due to the "protective" effect of the aromatic groups. It does undergo cross-linking as the dominant process[124,125] with *G(X)* being in the range of 0.019 to 0.051, depending on the method of determination. Elastomers such as cis-1,4-polyisoprene (Natural Rubber), polybutadiene, polybutadiene-styrene (SBR) and polychloroprene have large amounts of unsaturation in the polymer backbone and all undergo cross-linking upon irradiation[126]. High-energy irradiation by electron or γ-ray data shows *G(X)* of 5.3 for polybutadiene (cis-1,4)[127], and *G(X)* of ~10 for polybutadiene (90% vinyl 1,2)[128] measured in vacuum. It is interesting to note the effect of styrene present in the SBR, where *G(X)* varies from 2.9 for SBR with

16% styrene to 0.3 for SBR with 85% styrene[129]. We believe that these data are valid for the lower energy x-rays of interest here and explains the behavior of the measured SAXS structure factor.

An additional visual observation further supports our interpretation in terms of cross-linking. When the sample cells were disassembled after the experiment, we observed polymerized formations extending across the thickness of the sample at the places where the x-ray beam traversed. Under a microscope we observed the formations to have rectangular cross sections with two distinct sizes corresponding to the $(5\ \mu m)^2$ and $(50\ \mu m)^2$ beams used in the experiment. For the polystyrene/polybutadiene mixture at room temperature these formations appeared as small "posts", with colors varying from light to dark brown, embedded in the white, creamy texture of the surrounding unperturbed mixture. These formations appeared to be more solid-like than the surrounding viscous mixture, consistent with expectations for cross-linked material. We also exposed a pure polybutadiene sample to the x-rays and observed the development of very similar post-like formations immersed in the surrounding undamaged liquid polybutadiene (polybutadiene with M_w = 1000 is liquid at room temperature). Thus, our results agree well with the high *G(X)* reported for polybutadiene and are consistent with the view that cross-linking of polybutadiene is the dominant x-ray damage mechanism in these polymer mixtures.

Conclusions

The results of these studies show that x-ray radiation induced damage to this polymer mixture depends on accumulated dose and can result in dramatic changes in the

polymer structure on relatively short time scales. Analyses of the data indicate that the first phase of irradiation, during which the structure and scattering are essentially unaffected, lasts up to about 2000 kGy. This damage threshold can be used to estimate the approximate maximum duration of an XPCS experiment on this material for different incident coherent x-ray intensities. A pink beam with an intensity of 4×10^{10} ph/s/$(5\ \mu m)^2$ results in a deposited dose of 180 kGy/s. At this dose rate, the damage threshold dose would be reached in only 10 seconds. With a Ge resolution x-ray beam, the dose rate is lowered by about a factor of 100 to 1.8 kGy/s and the time to damage threshold increases to ~1000 seconds. In these mixtures, the relaxation time for concentration fluctuations can be as long as several 10s of seconds. Thus, Ge resolution coherent beams are necessary. In addition, although the minimum measurement duration can be of the order of the slowest relaxation time, this is only possible when ensemble averaging techniques utilizing a multichannel detector, such as a CCD array, are employed to determine the autocorrelation function. Hence, a single channel detector, which requires a measurement duration of the order of thousands of decay times, is completely inadequate. Measurements of the temperature and wave vector dependence of the static and dynamic critical behavior of this mixture with SAXS and XPCS are presented in Chapter 7.

The damage threshold reported here for the polystyrene/polybutadiene mixture will surely vary for different materials, depending on their chemistry and viscosity. For example, in the experiments reported in Chapter 5 on the binary fluid mixture hexane/nitrobenzene, no radiation damage effects were observed even for much larger doses than the maximum dose the polystyrene/polybutadiene sample was exposed to. This is most likely due to the combination of the small aromatic molecules being more

resistant to damage and the mixture having very low viscosity, so any defects that are produced diffuse out of the scattering volume in much less that 1 second and also self-heal more efficiently. The correlation between the effect of high energy radiation reported in the literature and the effect of synchrotron x-rays on the polymers studied here suggests that it may be possible to select mixture components for future studies based on their known resistance to high-energy radiation damage. For example, one may consider aromatic group polymers, since they are naturally more resistant to radiation.

Finally, these results have implications for future experiments[16] at a 4th generation x-ray source, where the average coherent flux is expected to be much greater. For example, at the planned LCLS, the average coherent flux will be about 265 times greater than for the APS. However, this is spread out over a transversely coherent beam with an area of about (100 μm)^2. Thus, somewhat surprisingly, samples would be exposed to a similar dose rate as was the case in our experiments. This bodes well for future XPCS experiments, since the large increase in coherent flux will enable study of much faster fluctuations than are feasible with existing coherent fluxes.

CHAPTER 7.
STATICS AND DYNAMICS OF POLYSTYRENE / POLYBUTADIENE CRITICAL MIXTURES

Introduction

This chapter presents the results of experiments on binary mixtures of the low molecular weight homopolymers, polystyrene and polybutadiene. Mixtures of polystyrene and polybutadiene have been relatively well studied by a variety of techniques, including studies of the phase diagram[130,131,132,133,134,135], static critical behavior using neutron[136,137,138] and (incoherent) x-ray scattering[139,140], and dynamic critical behavior using light scattering[141,142]. Where similar results on the static behavior have been reported previously, the results reported here are in general agreement and often more precise. This chapter also reports the results of the first measurements of the dynamics using coherent x-rays. Unfortunately, the mixtures proved to be rather easily damaged by x-ray irradiation, as discussed in Chapter 6. Consequently, the measurements of dynamics reported here are somewhat limited. Nonetheless, they do demonstrate the ability to measure the dynamics of polymer mixtures via XPCS. With further improvements in technique applied to these mixtures, as well as selection of other polymer mixtures which are more robust to x-ray irradiation, a more comprehensive study should be entirely feasible.

	Polystyrene	Polybutadiene
Monomer Chemical Formula	$-(C_8H_8)-_n$	$-(C_4H_6)-_n$
Monomer Structure	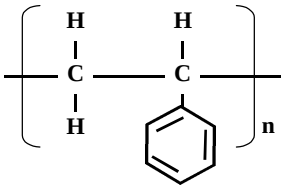	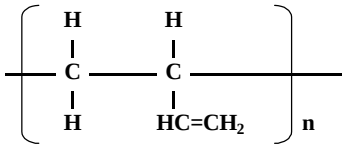
Density, ρ_m [g/cm^3]	0.97	0.90
Monomer Molar Mass	104.15	54.09
Monomer Z	104	54
Monomer Molecular Volume, v_o [nm^3]	0.178	0.0996
Electron Density, r_e [e/nm^{-3}]	584	542
Penetration Depth at 9 keV, δ [cm]	0.396	0.442
Polymer Molecular Weight, M_W	2046	1051
Degree of Polymerization	~ 20	~ 19
Polydispersity, M_W/M_N	1.04	1.07

Table 7.1. Physical constants for polystyrene and polybutadiene.

To prepare the polymer binary mixture samples we used polystyrene (PS) and polybutadiene (PB) as purchased from Polysciences[143]. The properties of the component homopolymers are shown in Table 7.1.

Samples were prepared at a range of compositions by using the procedure described in Chapter 4. The phase diagram of the samples was checked by measuring the

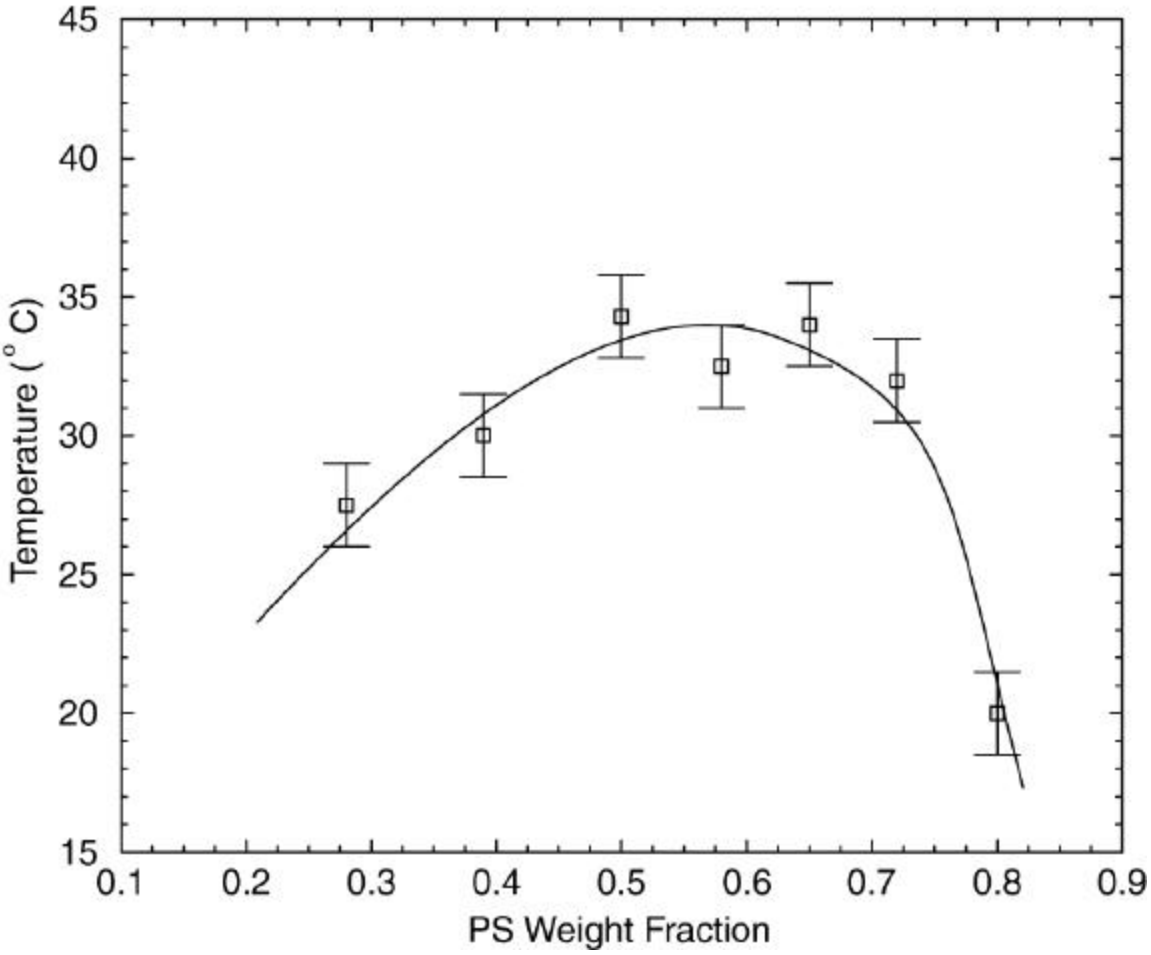

Figure 7.1. Coexistence curve for polystyrene/polybutadiene polymer mixtures as determined from cloud point measurements made using laser light. The critical point is roughly $T_c \sim 35^o$ C and f_c = 55 % polystyrene (weight fraction). Solid line is a guide to the eye.

cloud points using laser light. For those measurements, we used round #1 microscope glass cover slips in the sample cell instead of Be windows. Cloud points were obtained by two methods: visually observing the temperature at which the sample first appeared milky and by using a photodiode to detect a decrease in the sample transmission. The results of the measurements are shown in Figure 7.1. There is a relatively large uncertainty in the determination of the coexistence curve via clould point measurements,

as reflected in the error bars in Figure 7.1, due to the somewhat arbitrary choice of what amount of reduction in transmission to associate with the transition. There is also a certain amount of sample heating due to laser power absorbed by the sample, although our estimates and visual observations indicate that this temperature rise is not more than about 0.5^{o} C. Nevertheless, the cloud point measurements provide a good rough determination of the coexistence curve, indicating that $T_c \sim 35^{o}$ C and $f_c \sim 55$ % PS (weight fraction). Much more precise determinations of T_c by static x-ray scattering for several compositions, reported later in this Chapter, generally confirmed the results shown in Figure 7.1.

Our results for the coexistence curve agree well with literature values for similar molecular weight mixtures. For example, Rostami and Walsh[132] reported values of $T_c = 28.4^{o}$ C and $f_c = 0.5$ for a mixture of PS with $M_w = 1500$ and PB with $M_w = 960$. Atkin, et. al.[131], reported $T_c = 43^{o}$ C and $f_c = 0.7$ for a mixture of PS with $M_w = 1400$ and PB with $M_w = 2600$. Our results for our mixtures, consisting of PS with $M_w = 2046$ and PB with $M_w = 1051$, are about midway between the other results, as expected. It is interesting to note that the effect of deuteration on one or the other of the components has also been studied. Deuteration of PS has been shown[134] to have negligible effect on the coexistence curve of PS/PB mixtures. Deuteration of PB, on the other hand, has been shown[131,133] to increase T_c by about 15^{o} C.

Because polybutadiene proved to be quite susceptible to x-ray radiation damage, it was necessary to use a monochromatic, rather than a pink, beam in the x-ray measurements of both the statics as well as the dynamics. Thus, the in-hutch combination of a single bounce mirror followed by a Ge monochromator, as described in Chapter 4,

was used to monochromate the x-ray beam. This resulted in about 100 times less incident x-ray flux than in the hexane/nitrobenzene experiments described in Chapter 5. To partially compensate for the loss in signal strength, we used a CCD area detector to measure the static x-ray scattering from the sample. We were also able to use the CCD detector in XPCS measurements of the dynamics of concentration fluctuations in the mixtures, since the relaxations are quite slow due to the relatively high viscosity of the polymers. However, the quantum efficiency of the CCD was only about 14% versus 82% for the Amptek detector used in the measurements on the hexane/nitrobenzene mixtures.

Static Measurements

As described in Chapter 4, the static scattering was measured with collimation, coherence and guard apertures of $(200\ \mu m)^2$, $(50\ \mu m)^2$ and $(60\ \mu m)^2$, respectively. The distances between the collimation and coherence apertures, coherence and guard apertures, guard aperture and sample, and sample and detector were 1.1 m, 0.2 m, 0.06 m, and 0.30 m. The sample to detector distance was kept small in these measurements in order to access a wider range of scattering wave vectors, q. The KAF-0400 CCD pixel format was 768x512 $(9\ \mu m)^2$ pixels and the zero wave vector position was offset to the corner of the CCD to give a maximum accessible q range. As a result, the static measurements extended up to wave vectors of $q = 0.123$ Å^{-1} and had a resolution of 1.363×10^{-4} Å^{-1}/pixel. A flux of 2.1×10^{10} ph/sec/(100 mA) of 9.0 keV x-rays in the $(50\ \mu m)^2$ beam monochromated by the Ge monochromator was incident on the sample. Static data were collected in 10 second exposures of the CCD and the static structure factor was extracted by circular averaging over all pixels with the same q. The measured sample

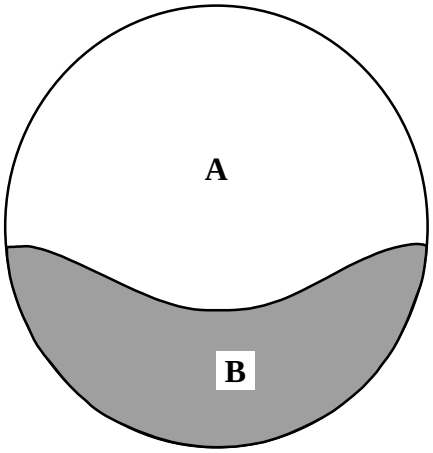

Figure 7.2. Typical sample fill pattern, or sample "map", taken with attenuated x-ray beam. Region A denotes the empty sample cell volume, while Region B is filled with PS/PB mixture. Bowing of the sample mixture on the sides is due to wetting of the cell walls.

scattering intensity was corrected for the background by subtracting the background multiplied by the measured sample transmission (typically 40%) and plotted as a function of *q*.

As a precaution against overexposing a given area on the sample, each x-ray measurement was made on a fresh spot on the sample. In order to know the accessible range of sample positions beforehand, each sample was "mapped" with a low intensity x-ray beam to find the useful sample boundaries. A typical sample map is shown in Figure 7.2. This figure is a cross section of the cylindrical sample cell volume that was intentionally left about half empty, as described in Chapter 4. The top portion of the volume, denoted as **A,** is empty and the bottom portion, denoted as **B,** is filled with the sample. Both the background scattering and the sample scattering were measured for

each temperature. The background scattering was measured with the x-ray beam passing through the empty portion of the sample cell and hence only passing through the two enclosing Be windows. To measure the sample scattering we moved to a new sample spot for each temperature. The distance between each illuminated sample spot used in the measurements was at least 400 μm (much larger than the x-ray beam size) and all of them were in a known good portion of the sample.

An example of the temperature dependence of the static x-ray scattering from composition fluctuations in a PS/PB mixture with f_{PS} = 50 % is shown in Figure 7.3. The x-ray scattering intensity was measured for a number of temperatures ranging from 85° C down to the phase transition temperature. We see that the scattering intensity rises as the temperature is lowered toward the critical point. Throughout most of the *q*-range, the background parasitic scattering is at least a factor of two less than the scattering from the sample. However, at high temperature the scattering below about q = 0.02 $Å^{-1}$ is dominated by parasitic stray scattering from the main beam. As the sample temperature nears the critical temperature, scattering from the sample dominates the background for all q.

The measured x-ray scattering rate was converted to an absolute volume specific differential cross-section, $d\sigma_v/d\Omega$, according to Equation (5.3) and that is what is plotted in Figure 7.3. The data were then fit to the Ornstein-Zernicke form for the critical scattering, as given by Equation 5.1 and as discussed in Chapter 3. Using the fit results, we arrive at the volume specific absolute differential cross section for x-ray scattering from concentration fluctuations in this mixture of polystyrene/polybutadiene:

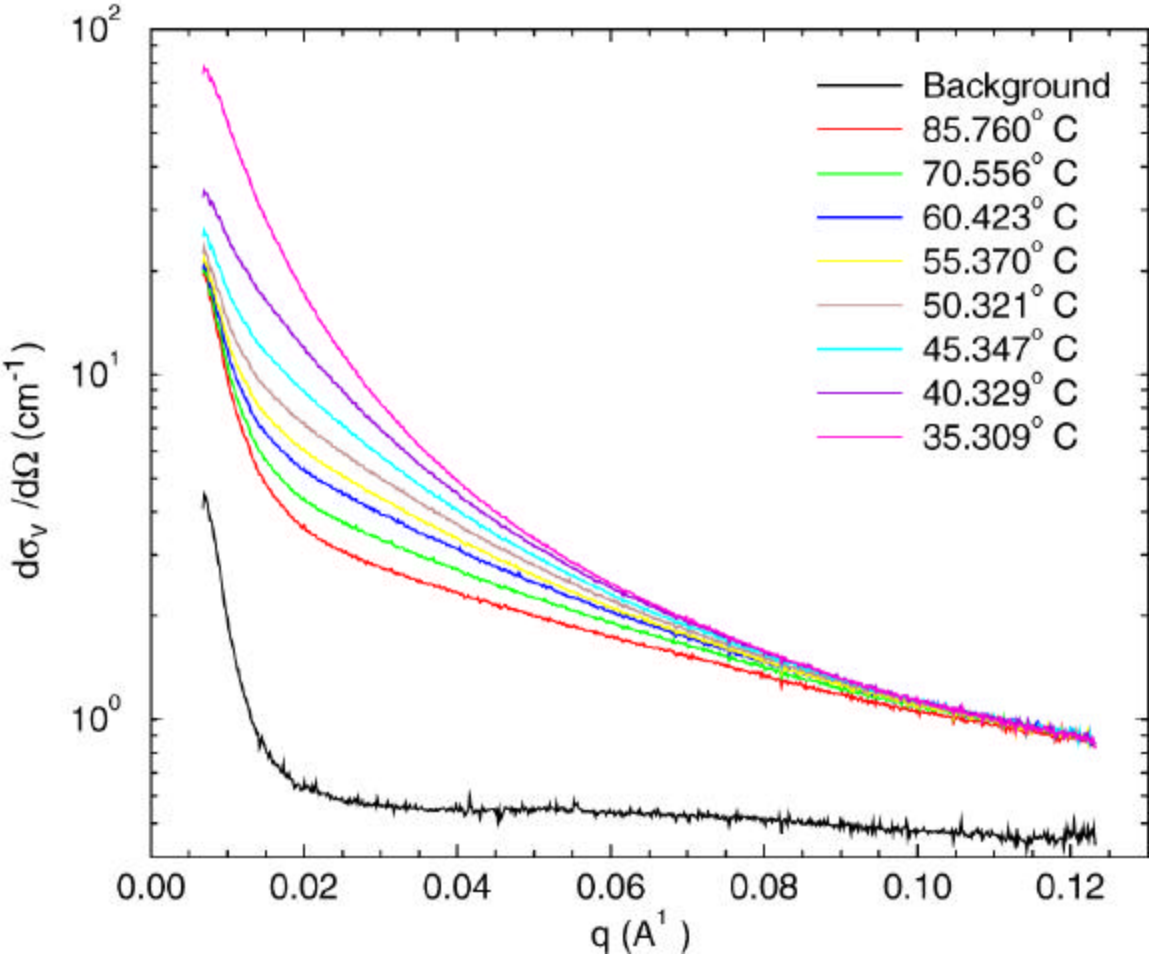

Figure 7.3. Absolute volume specific differential cross section for x-ray scattering from composition fluctuations in a f_{PS} = 50 % by weight mixture of polystyrene and polybutadiene. The cross section increases as the temperature is lowered toward the critical temperature.

$$\frac{ds_V}{d\Omega} = \frac{0.635\ cm^{-1} \cdot t^{-g}}{1 + q^2 \cdot x_0^2 \cdot t^{-2n}}. \qquad \textbf{(7.1)}$$

The rest of the fit results are discussed in detail later in this chapter.

Our results in Equation (7.1) indicate that the cross section in PS/PB is about two orders of magnitude larger than in hexane/nitrobenzene (5.47 x 10^{-3} cm^{-1} from Equation (5.4)). On the surface, this result is somewhat surprising. As shown in Table 7.1, there is

only about an 8 % difference in the electron density of PS and PB, much less than the 63 % difference in the electron density of hexane and nitrobenzene. The x-ray penetration depth, which determines the sample scattering volume, is about 4.2 mm in PS/PB, which is 37 % less than in hexane/nitrobenzene.

In an attempt to understand the origin of the strong scattering, we applied the same simplified theory for the cross section to this system as was done in the case of the hexane/nitrobenzene mixtures in Chapter 5. That is, we approximate the osmotic compressibility as that of an ideal gas and use Equation (5.9) to calculate $d\sigma_v/d\Omega$. The homopolymers are quite symmetric, each having a degree of polymerization of about 20, although their monomer molecular volumes differ by almost a factor of 2. Inspecting Equation (5.9), we see that the factors mentioned above which reduce $d\sigma_v/d\Omega$ are counteracted to some extent by the increased average molecular volume, $\langle v_o \rangle$, of the polymer molecules. We calculate an approximate value for $\langle v_o \rangle$ by taking the average of the degree of polymerization times the monomer volume for each homopolymer. This simple theory then predicts

$$\frac{ds_V}{d\Omega} = \frac{9.06 \cdot 10^{-2}\, cm^{-1} \cdot t^{-g}}{1 + q^2 \cdot x_0^2 \cdot t^{-2n}} . \qquad \textbf{(7.2)}$$

which has an amplitude which is almost identical to that predicted for hexane/nitrobenzene (7.66×10^{-2} from Equation (5.10)). However, recall that the measured cross section for hexane/nitrobenzene was about 14 times smaller than the prediction. Here, we find that the measured cross section is about 7 times larger than the prediction. Together, these are consistent with the measured cross section for PS/PB being about 100 times larger than that measured for hexane/nitrobenzene.

It is important to keep in mind that there are uncertainties in the various correction

factors used in converting measured scattering rates to absolute cross sections. For example, the calibration of the quantum efficiency of the CCD, the calculation of the efficiency of ion chambers, etc, altogether may result in an uncertainty in $d\sigma_v/d\Omega$ of up to perhaps a factor 3 to 5. In addition, the theory for the absolute cross section used in this thesis is certainly oversimplified and could be improved upon. One possibility for future investigation would be to use the Flory-Huggins theory to calculate the osmotic compressibility. Despite the shortcomings of the current approach, it does succeed at giving an order of magnitude estimate of the absolute cross section.

In order to investigate the scaling behavior of the amplitude and the correlation length near the phase transition, mixtures having three different compositions were studied in detail. The static scattering was fit to determine the amplitude and correlation length as a function of temperature. The results for PS/PB compositions of f_{PS} = 0.50, 0.557, and 0.65 are shown in Figures 7.4, 7.5, and 7.6, respectively. The results are plotted as a function of reduced temperature, defined as $(T - T_c)/T$, as discussed in Chapter 3. We see that for all compositions studied, the amplitude and correlation length obey power law scaling quite well. The values of T_c estimated from the scaling plots are 35.50^o C, 36.05^o C, and 33.60^o C, respectively. These T_c values are quite consistent with the rougher values shown in Figure 7.1 as determined by cloud points measurements.

As expected, the data show a crossover from mean field behavior far from the transition to Ising behavior near the transition. All three figures show lines as guides to the eye with slopes expected for Ising (γ = 1.26, ν = 0.63) and mean-field (γ = 1.0, ν = 0.5) critical behavior. The sample nearest the critical composition is the one with f_{PS} = 0.557, which has the highest T_c. For this sample, the crossover from mean field to Ising

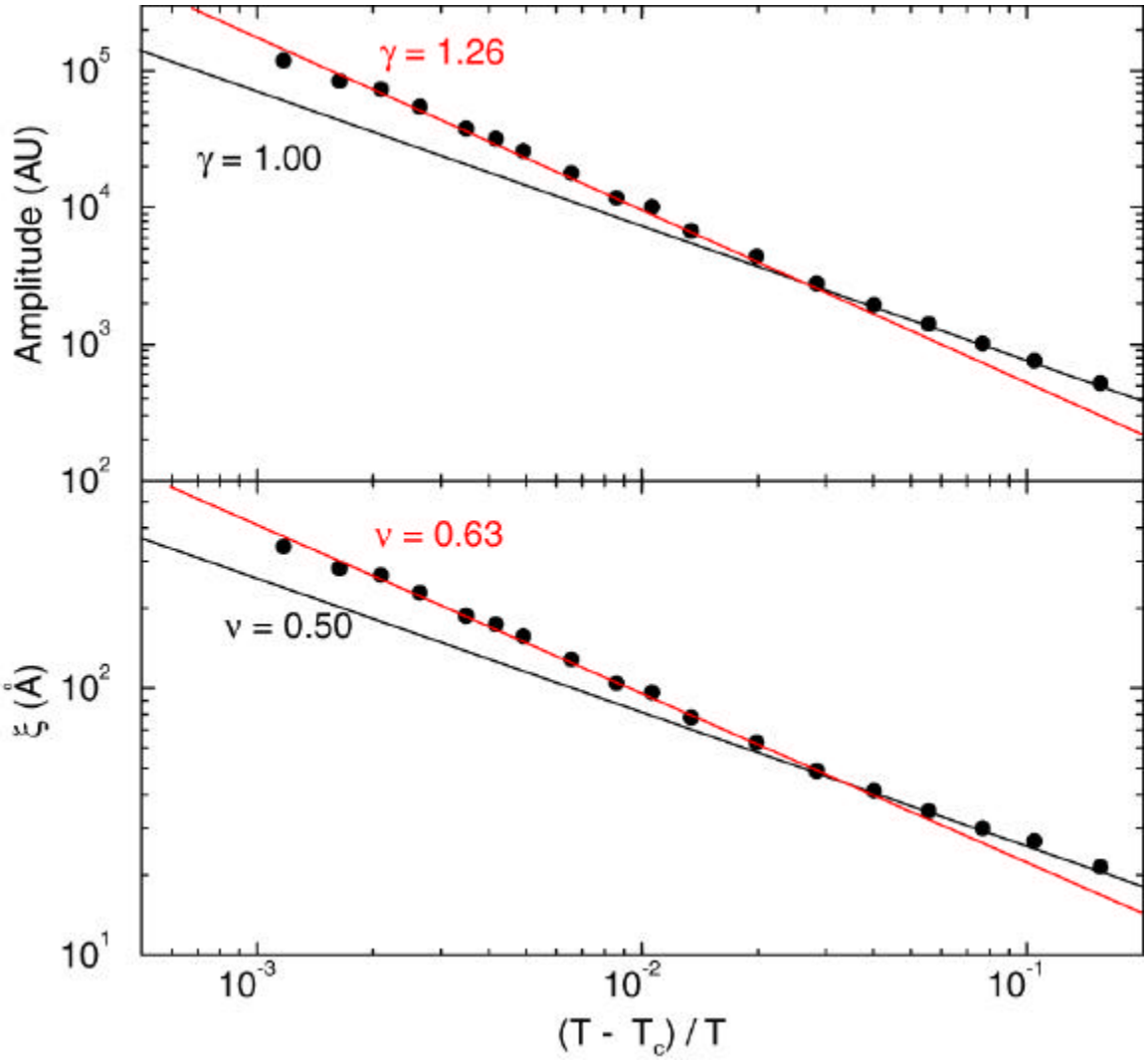

Figure 7.4. Scaling of the amplitude and correlation length as a function of reduced temperature for a f_{PS} = 0.50 PS/PB mixture. T_c = 35.50° C.

behavior occurs at a reduced temperature of e_x ~ 0.03. As discussed in Chapter 3, for a symmetric polymer mixture such as this, the Ginzburg criterion is expected to be given by Equation (3.29) as $e_x \sim N^{-1}$. For this mixture with N = 20, we thus expect the crossover to occur at e_x ~ 0.05, which is in good agreement with our observations.

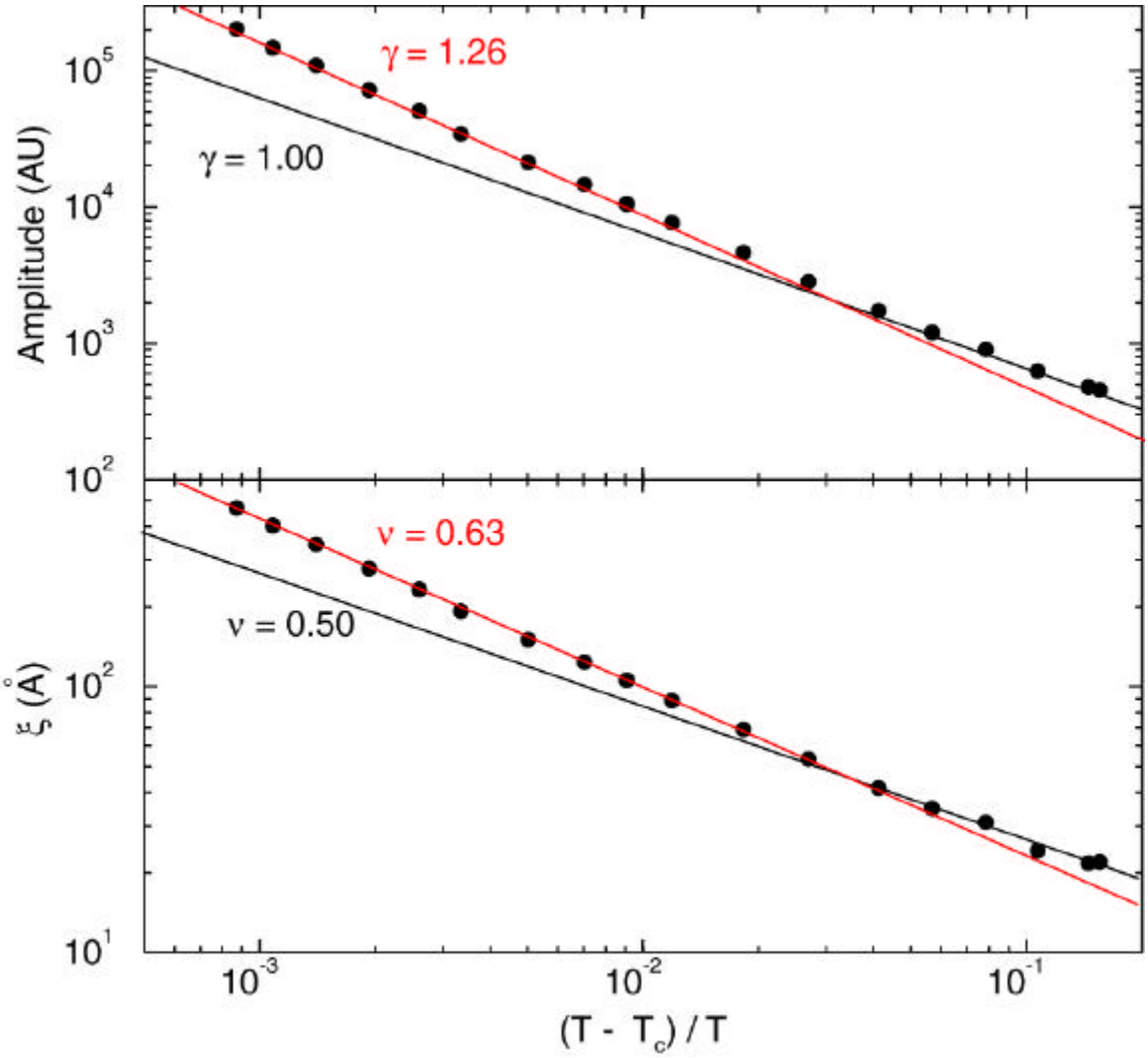

Figure 7.5. Scaling of the amplitude and correlation length as a function of reduced temperature for a f_{PS} = 0.557 PS/PB mixture. T_c = 36.05° C.

Dynamic Measurements

For the XPCS measurements, the coherence aperture was set to 5 μm x 10 μm (H x V). A flux of 6.6 x 10^8 ph/sec/(100 mA) of 9.0 keV x-rays monochromated by the Ge Monochromator was incident on the sample. The guard aperature was set to (25 μm)^2. The sample to detector distance was increased to 0.70 m in order to match the pixel size to that of a speckle. Under these conditions, the scattering from the sample was only

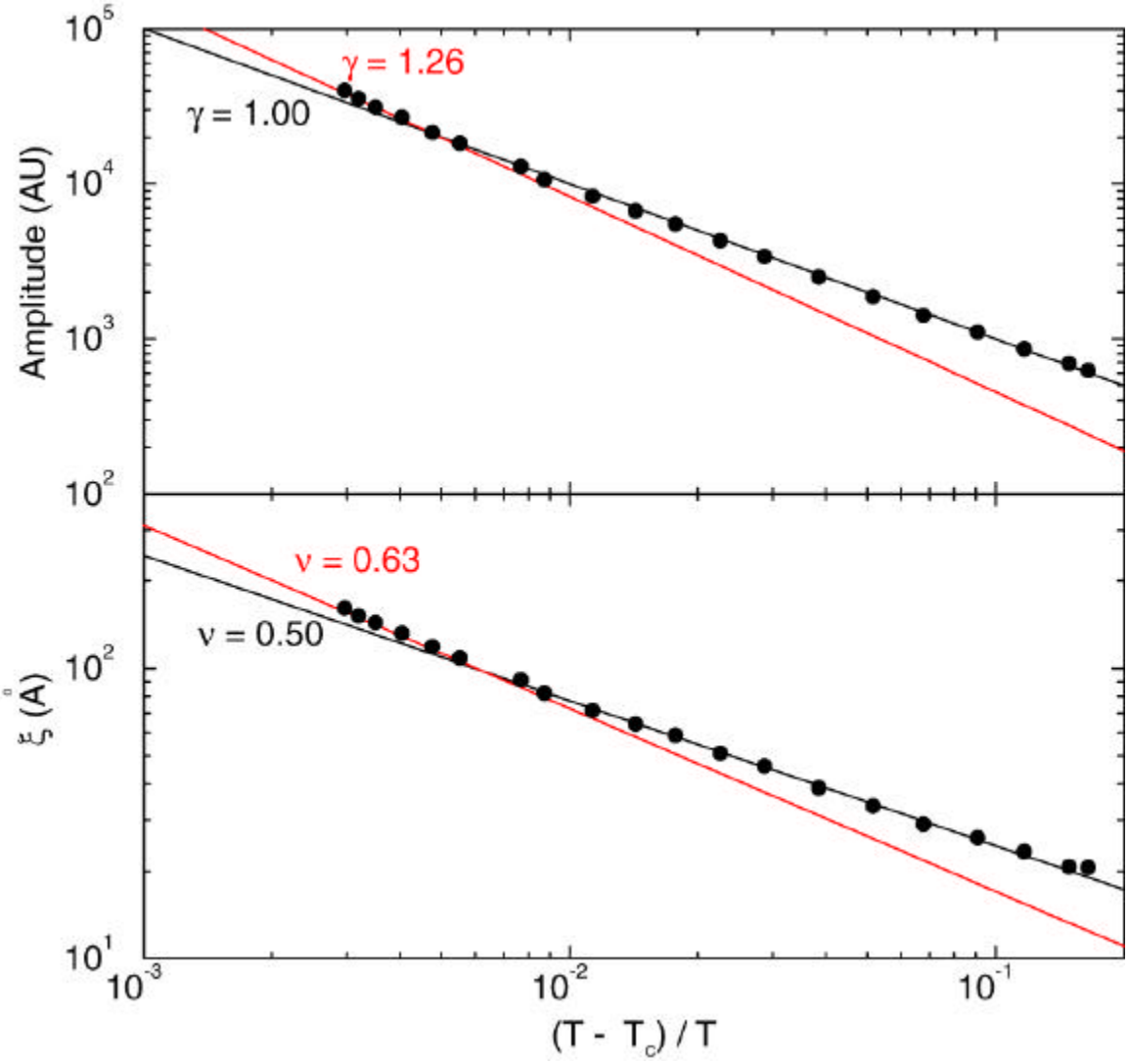

Figure 7.6. Scaling of the amplitude and correlation length as a function of reduced temperature for a f_{PS} = 0.65 PS/PB mixture. T_c = 33.60° C.

larger than the background for temperatures very close to T_c. This is because the background includes contributions such as the dark current and readout noise of the CCD which do not scale with incident x-ray flux. In addition, the signal was only above background for a narrow range of sufficiently low q such that the scattering was strong but not so low as to be dominated by the increased parasitic background at low q. As a

result, we were only able to obtain reasonable dynamic correlation functions for several wave vectors at a few temperatures near T_c on the f_{PS} = 0.557 sample.

The dynamic data were collected in a sequence of 6000 exposures of the CCD. The exposure time for each frame was 0.15 seconds and the frame-to-frame time was 0.33 seconds. The latter is longer than the exposure time due to the finite readout rate of the CCD. Thus, the sample time was 0.33 seconds. The total measurement time for each sequence was thus 33 minutes, of which the sample was exposed to x-rays for a total of 15 minutes, i.e., around 900 seconds. During this time the sample was exposed to a radation level of about 2000 kGy, which was the threshold above which the sample was determined to sustain x-ray radiation damage, as reported in Chapter 6.

The x-ray scattering was collected over a CCD area of 180 x 180 pixels. At the detector-to-sample distance of 0.70 m, the pixel resolution was $q = 5.839 \times 10^{-5}$ Å^{-1}/pixel. The CCD was offset from the q = 0 position so that the q-range covered was from ~3.5×10^{-3} Å^{-1} to ~1.8×10^{-2} Å^{-1}.

The data were collected and then analyzed offline using the procedure described in Appendix. In brief, a multitau correlation technique, utilizing 8 quasi-logarithmic software correlators with 16 channels per correlator, was used to determine the correlation functions.

Figures 7.7, 7.8, and 7.9 show the so-calculated correlation functions together with fits of single exponential relaxation functions for temperatures of 36.54^o C, 36.39^o C, and 36.33^o C, respectively. These temperatures are quite close to T_c, which was determined to be 36.05^o C for this composition. For each temperature, we obtained reasonable correlation functions for wave vectors, q, of 4.3 x 10^{-3} Å^{-1}, 4.7 x 10^{-3} Å^{-1}, and

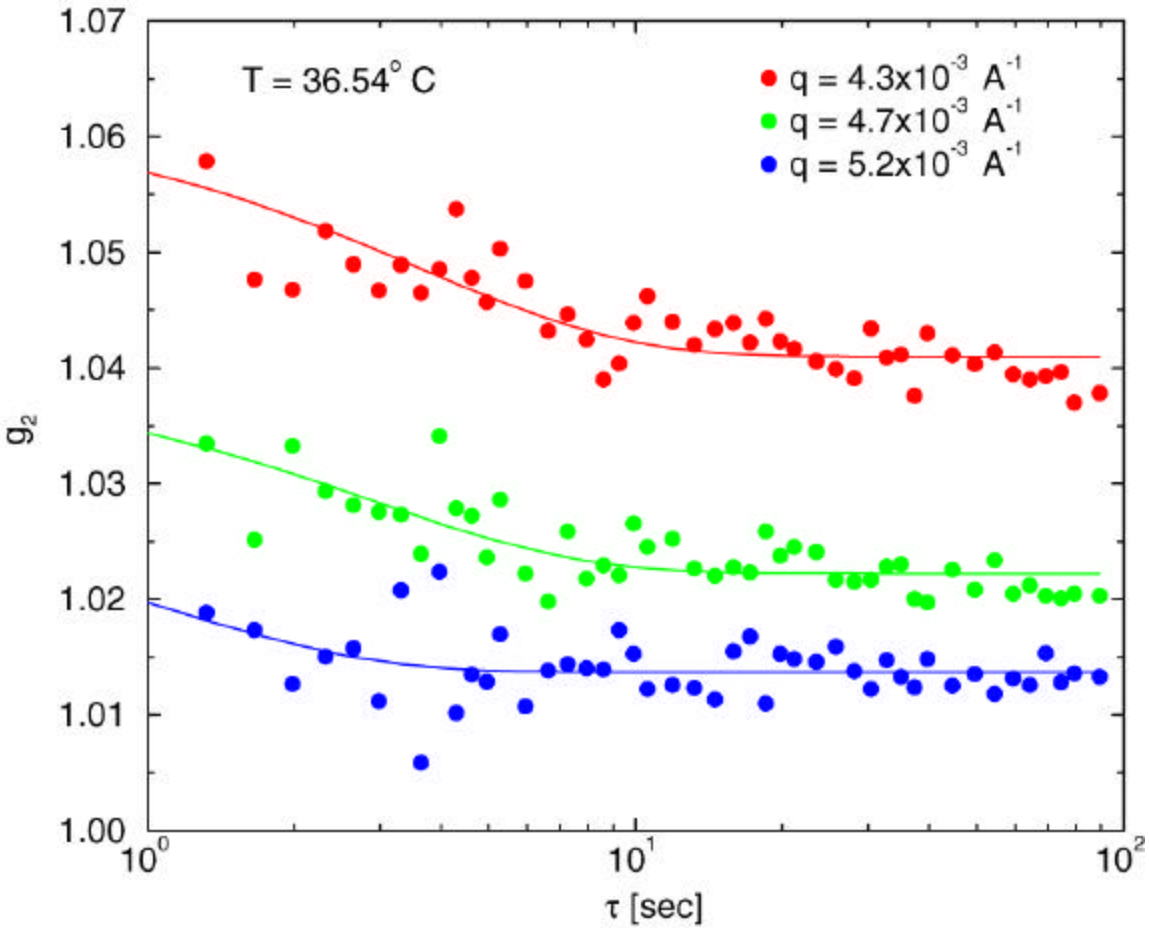

Figure 7.7. Correlation functions for a f_{PS} = 0.557 PS/PB mixture at T = 36.54° C and three different wave vectors, as indicated. Solid lines are fits of a single exponential relaxation.

5.2 x 10^{-3} $Å^{-1}$, as shown in the Figures. The contrast of the correlation functions, β, was between 1 and 3 %, similar to the values we found for the measurements on the hexane/nitrobenzene mixtures made using a single channel detector and a hardware correlator.

The fit values of the relaxation rates are plotted versus *q* for all three temperatures in Figure 7.10. The manner in which the relaxation rate scales with wave vector depends on the conditions of the sample and the manner in which we probe it. As discussed in

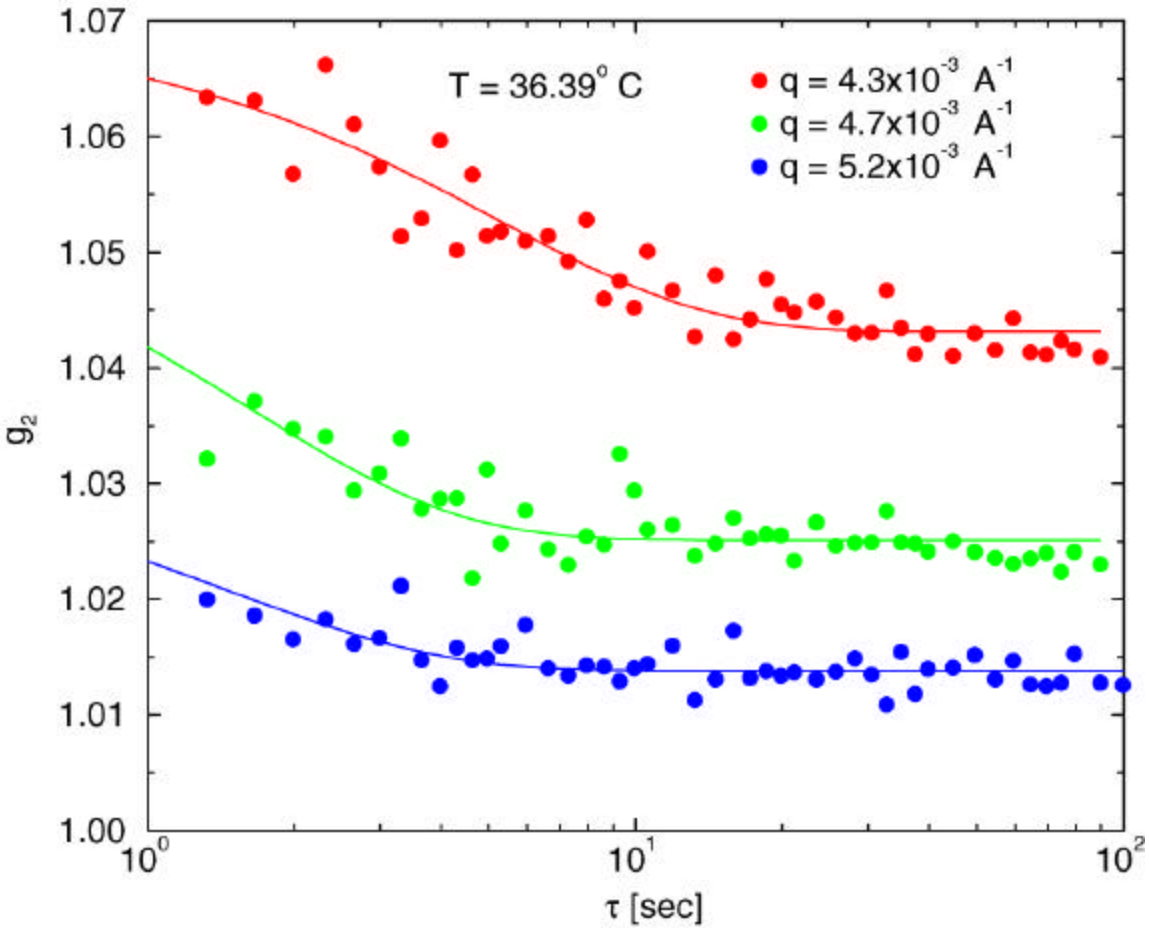

Figure 7.8. Correlation functions for a f_{PS} = 0.557 PS/PB mixture at T = 36.39° C and three different wave vectors, as indicated. Solid lines are fits of a single exponential relaxation.

Chapter 3, these conditions can be characterized by the values of q, ξ, and R_g, in terms of the values of $1/qR_g$, $q\xi$, and q/R_g. For the results shown in Figures 7.7 through 7.10, the wave vector ranges from about 4 to 6 x 10^{-3} Å^{-1}, for which we can take an average value of 5 x 10^{-3} Å^{-1}. The reduced temperatures range from 9.1 x 10^{-4} to 1.6 x 10^{-3}. From the results for ξ shown in Figure 7.5, ξ is about 400 Å for this range of reduced temperature. And, using Equation (3.1) and the properties listed in Table 7.1, we calculate that R_g is 10.2 Å and 8.2 Å, for PS and PB, respectively. An average value for R_g is thus 9.2 Å.

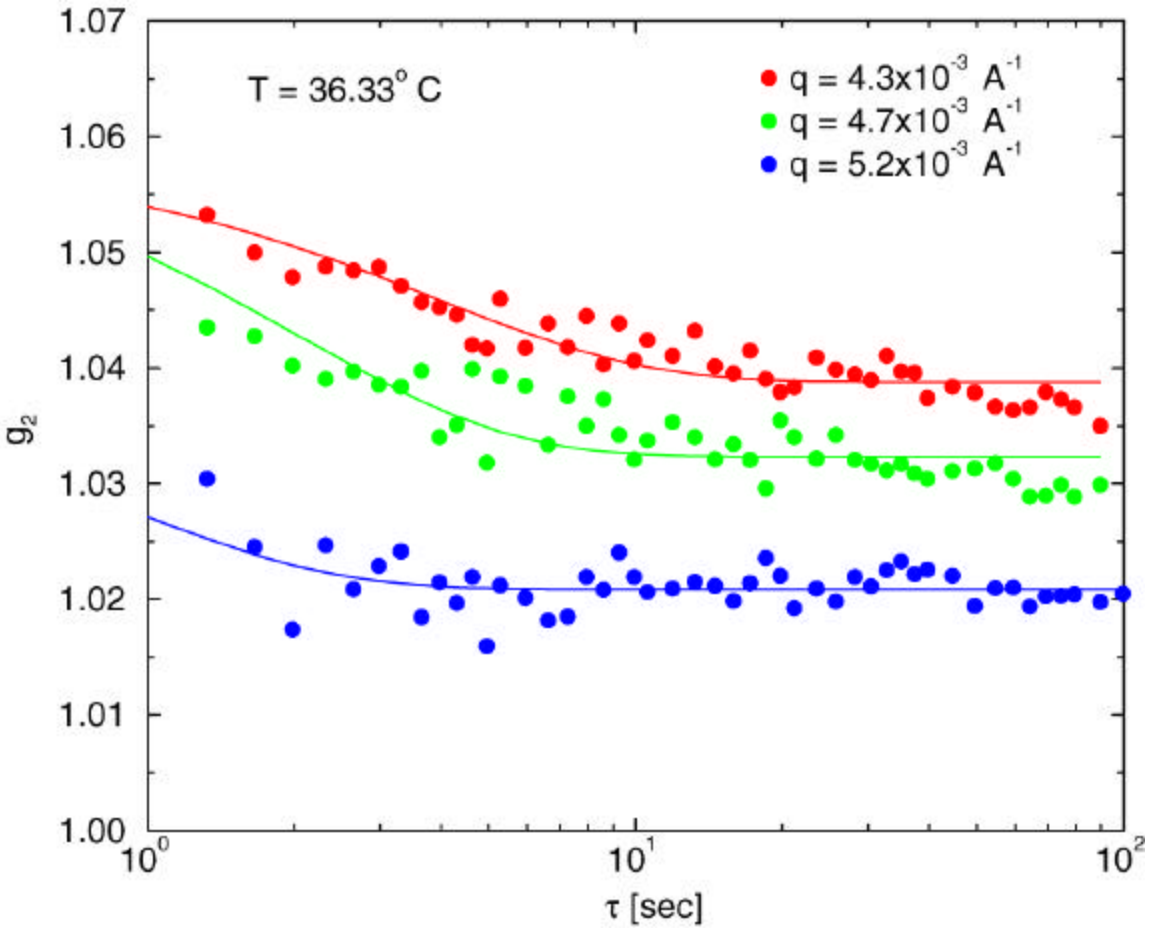

Figure 7.9. Correlation functions for a f_{PS} = 0.557 PS/PB mixture at T = 36.33° C and three different wave vectors, as indicated. Solid lines are fits of a single exponential relaxation.

Finally, $N^{0.5}$ equals 4.4. Hence, the relevant physical regime is determined by the values $1/qR_g = 21.7 > N^{0.5}$, $\xi/R_g = 43.5 > N^{0.5}$, and $q\xi = 2 > 1$. This puts us in the so-called "critical non-diffusive" regime, labeled III in Figure 3.7, where mode coupling corrections dominate and the relaxation rate should scale with wave vector as $\Gamma \sim q^3$ and should be temperature independent, apart from the temperature dependence of the viscosity. A guide to the eye which shows a q^3 dependence of Γ on q is also shown in Figure 7.9. While the measured values of Γ do increase with wave vector, they appear to

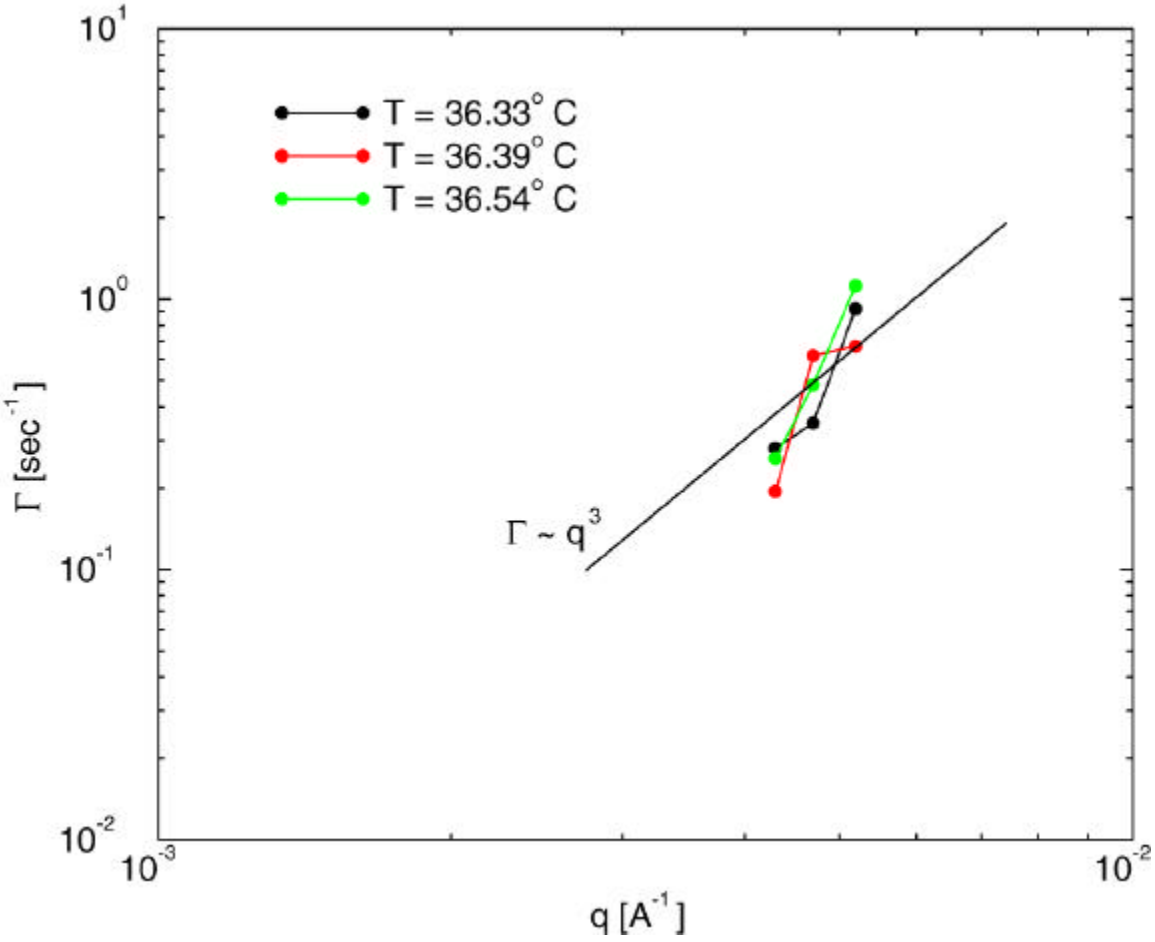

Figure 7.10. Relaxation rate versus q from fits to the data shown in Figures 7.6-7.8 and three different temperatures, as indicated. A guide to the eye showing a q^3 scaling of Γ is also shown.

increase much more quickly than q^3. Within the evident large scatter, the results for Γ are also approximately temperature independent.

Unfortunately the dynamic data we have been able to collect so far are not extensive enough nor of sufficient quality to warrant drawing broader conclusions at this time. Nevertheless, we have demonstrated the ability to use XPCS to measure the relaxation rate from this polymer mixture and our work has identified a number of opportunities for enhancing the signal quality. For example, removal of the multiple

windows in the current 7ID beamline should increase the coherent flux by as much as a factor of 10. A deep depletion CCD detector would increase the detection efficiency by up to a factor of 4. Instead of using a monochromatic beam, a pink beam which has been attenuated by a factor of 10 would provide an increase in coherent flux by a factor of 10. Of course, the exposure time would have to be limited to ~ 100 seconds rather than 1000 seconds in order to stay below the damage threshold. However, from the results of Figure 7.7 through 7.9, that would be sufficient when ensemble analysis techniques are employed. The total collection time could be extended beyond 100 seconds by "batching" together the results of multiple 100 second experiments, each on a fresh spot on the sample. With this technique, essentially an unlimited collection time could be attained. Hence, by these and other optimizations, there is good reason to expect that much better quality data, covering a more extensive range of reduced temperatures and wave vectors, can be obtained in the near future and the tantalizing results shown in Figure 7.10 further pursued.

CHAPTER 8

CONCLUSIONS

A significant amount of work has been accomplished to design, build, and utilize a Small Angle X-Ray Scattering Setup at the MHATT-CAT insertion device beamline 7ID. This setup was successfully tested in many experiments described in this Thesis and in some others that were not in the scope of my research.

The SAXS setup was used to study the static and dynamic critical behavior of a binary fluid mixture of hexane and nitrobenzene. Although it was a challenging experiment, it showed that it is possible to obtain reliable data with XPCS even with low density and low viscosity mixtures that are governed by fast dynamics. The results of this experiment were consistent with literature results obtained with laser light scattering and visible PCS. We also measured the absolute cross section for x-ray scattering from concentration fluctuations in this mixture and found it to be in reasonable agreement with the predictions of a simple theory.

Although the hexane/nitrobenzene samples did not show any signs of damge due to exposure to the x-ray beam, the polymer samples proved to be quite sensitive to radiation damage effects. We conducted a detailed study of the effects of x-ray radiation damage on the polystyrene/polybutadiene binary mixtures. We found that experimental and theoretical predictions derived from studies using high-energy radiation (1 MeV and higher) are in general valid for the x-ray energy range of our experiments (a few to a few

10 keV). Polystyrene, containing aromatic groups, was more robust against damage, as was predicted from high-energy radiation studies. Polybutadiene was more susceptible to radiation damage, with radiation inducing cross-linking, or polymerization, of the sample. Our experiments indicated that there is a threshold x-ray dose, below which the effects of x-ray radiation on the polymer samples was negligible. This value measured to be ~2000 kGy for the polystyrene/polybutadiene mixtures.

In our x-ray studies of polystyrene/polybutadiene mixtures, we measured the static critical scattering and observed a crossover from mean field to Ising critical behavior as the phase separation transition temperature was approached. The crossover temperature was found to be in good agreement with predictions based on the Ginzburg criterion. Measurements of the dynamics of the polymer mixtures using XPCS were successful in demonstrating that such measurements are feasible. We obtained limited results for the relaxation rate in the critical non-diffusive regime and observed indications that the relaxation rate scales with wave vector faster than the q^3 scaling predicted by theory. We have identified a number of improvements in the technique with which it should be possible to obtain much more extensive and higher quality XPCS data on these and other polymer mixtures in the future.

APPENDIX

Multitau multispeckle correlator software

XPCS data collected with a CCD detector consists of “movies” of fluctuating speckles, with each movie frame consisting of thousands of pixels which correspond to

functions from these movies is briefly described in this Appendix. To access a wide range of delay

power, we adopted the multitau correlator scheme, first proposed by Schätzel[48], and

144

tistics even for short

-

pixels within the same band of are averaged. We set the width of -

percentage of , usually 10 %. Since the dynamical relax

square of the magnitude of , this is a good comprose between having a large number of

n of the correlation function

-

delay times with a greatly reduced number of channels

The software implements a set of linear correlators (typically 8), each with a small

each consecutive correlator. To increase statisti

from one correlator to the next. For all correlators after the first it is only necessary to

calculate the correlation function for the second half of the channels, since the previous correlator covers the first half. The desired correlation function is obtained by merging the outputs of all linear correlators.

The input of the first correlator is the raw data from the CCD camera, whose sampling time is usually set to the shortest possible but still with a reasonable duty cycle (usually 50 %) between readout time and exposure time. Thus, the minimum delay time is limited by the readout speed of the CCD camera. The CCD used in these experiments could readout a 180 x 180 pixel subarray in 0.18 s and with an exposure time of 0.15 s the corresponding sample time was 0.33 s. Each consecutive correlator was fed with the sum of two consecutive samples from previous correlator.

The unnormalized intensity correlation function is calculated by averaging over the appropriate set of pixels:

$$G_I(q,t) = \left\langle \left\langle I_p(t) I_p(t+t \right\rangle_f \right\rangle_t , \qquad \textbf{(A.1)}$$

where $I_p(t)$ is the pth pixel intensity at time t, and $\langle\ \rangle_f$ and $\langle\ \rangle_t$ indicate azimuthal averaging over all pixels within the same q-band and time averaging, respectively. The normalized intensity correlation function, $g_I(q,t)$, is computed by applying a fully symmetric normalization scheme:

$$g_I(q,t) = \frac{G_I(q,t)}{\left[\left\langle \left\langle I_p(t) \right\rangle_f \right\rangle_{0 \le t \le t_{\text{run}} - t} \left\langle \left\langle I_p(t) \right\rangle_f \right\rangle_{t \le t \le t_{\text{run}}} \right]}, \qquad \textbf{(A.1)}$$

where t_{run} is the duration of the experiment, and $\langle\ \rangle_{t_1 \le t \le t_2}$ indicates the time average from time t_1 to time t_2, with the experiment starting time at $t = 0$.

The fully symmetric normalization utilized in Equation (A.2) reduces the sensitivity to drifts in the incident beam intensity. This is an essential feature for long experiment durations where the incident beam intensity can significantly change due to, for example, the natural storage ring current decay. This reduced sensitivity is obtained

the same periods of time that are used to calculate $G(q,)$.

correlation function for non-

over all pixels first and is only then normalized. This directly yields the ensemble averaged correlation function. For an ergodic sample one could equivalently average the normalized, time averaged correlation function calculated for each individual pixel. However, this would be

large number of correlation functions

of q

-bit data e

minutes. So, it is suitable for on-

here the CCD data was stored and analyzed off- -line analysis

e very useful in future experiments.

BIBLIOGRAPHY

BIBLIOGRAPHY

[1] B. Chu, Laser Light Scattering, (Academic Press, New York, 1974)

[2] K. Exner. Wiedemanns. Ann. Phys., 9:239, 1880

[3] K. Exner. Sitzungsber. Kaiserliche Acad. Wiss. (Wien), 76:522, 1877.

[4] M. von Laue. Sitzungsber. Akad. Wiss. (Berlin), 44:1144, 1914

[5] E. M. Rowe and J. H. Weaver, *The Uses of Synchrotron Radiation*, Scientific American **236** (6), 32-41 (1977)

[6] E. M. Rowe, *Synchrotron Radiation Facilities in the United States*, Physics Today **34** (5), 28-37 (1981)

[7] C. J. Sparks, Jr., *Synchrotron Radiation Research with X-Rays*, Physics Today **34** (5), 40-49 (1981)

[8] A. Bienenstock and H. Winick, *Synchrotron Radiation Research*, Physics Today **36** (6), 48-58 (1983)

[9] M. Blume and D. E. Moncton, *Large Facilities for Condensed Matter Science*, Physics Today **38** (3), 68-76 (1985)

[10] D. E. Moncton, *The Advanced Photon Source: Performance and Results from Early Operation*, J. Synchrotron Rad. **5**, 155-157 (1998).

[11] H. Winick, G. Brown, K. Halbach, and J. Harris, *Wiggler and Undulator Magnets*, Physics Today **34** (5), 50-63 (1981)

[12] E. Gluskin, *APS Insertion Devices: Recent Developments and Results*, J. Synchrotron Rad. **5**, 189-195 (1998).

[13] H. Winick, *Synchrotron Radiation Sources – Present Capabilities and Future Directions*, J. Synchrotron Rad. **5**, 168-175 (1998).

[14] K. Kim, *Advanced Capabilities for Future Light Sources*, J. Synchrotron Rad. **5**, 202-207 (1998).

[15] The LCLS Design Study Group, *Linac Coherent Light Source (LCLS) Design Study Report*, SLAC-R-521, December (1998)

B. Stephenson, S. Mochrie, M. Sutton, S. Dierker, K. Nelson, S. Sinha, F. Sette, and G. Ruocco. *sed Matter at LCLS* (private

[17] *X-*
Photon Correlation Spectroscopy Study of Brownian Motion of Gold Colloids in Glycerol **75** (3), 449 452 (1995)

T. Thurn Albrecht, W. Steffen, A. Patcowski, G. Meier, E. W. Fischer, G. Grubel, and D. L. Abernathy,
a Coherent X- , Phys. Rev. Lett. **77**

[19] - -Buschbaum, A. Partkowski, W. Steffen, G. Grübel, D. Abernathy, O. Diat, M. Winter, M. Koch, and M. Reetz. *Structure and dynamics of surfactant-stabilized aggregates of palladium nanoparticles under dilute and semidilute conditions: Static and dynamic x-ray scattering*. Phys. Rev. E **59** (1), 642-649 (1999)

[20] O. K. C. Tsui and S. G. J. Mochrie, *Dynamics of Concentrated Colloidal Suspensions Probed by X-Ray Correlation Spectroscopy*, Phys. Rev. E, **57**, 2030-2034 (1997).

[21] L. B. Lurio, D. Lumma, A. R. Sandy, M. A. Borthwick, P. Falus, S. G. J. Mochrie, J. F. Pelletier, M. Sutton, L. Regan, A. Malik, and G. B. Stephenson, *Absence of Scaling for the Intermediate Scattering Function of a Hard-Sphere Suspension: Static and Dynamic X-Ray Scattering from Concentrated Polystyrene Latex Spheres*, Phys. Rev. Lett. **84**, 785-788 (2000)

[22] S. Mochrie, A. Mayes, A. Sandy, M. Sutton, S. Brauer, G. Stephenson, D. Abernathy, and G. Grübel. *Dynamics of Block Copolymer Micelles Revealed by X Ray Intensity Fluctuation Spectroscopy* . Rev. Lett. **78** -1278 (1997)

[23] S. Brauer, G. B. Stephenson, M. Sutton, R. Bruning, E. Dufresne, S. G. J. Mochrie, G. -Nielsen, and D. L. Abernathy, *-Ray Intensity Fluctuation* $_3$*Al* Phys. Rev. Lett. **74** 2010 (1995)

J. Mainville, F. Bley, F. Livet, E. Geissler, J. F. Legrand, D. Abernathy, G. Grübel, S. Mochrie and M. Sutton. *Speckle Structure in Small Angle Coherent X-Scattering*. J. Appl. Crystallogr. Volume 30, Part 5 Number 2.

[25] *Ph.D. thesis*, McGill University, 1995

[26] A. Malik, A. R. Sandy, L. B. Lurio, G. B. Stephenson, S. G. J. Mochrie, I. McNulty, *Coherent X-*
Coarsening, Phys. Rev. Lett. , 5832 (1998)

[27] G. N. Ramachandran, Proc. Indian Acad. Sci. A **18**, 190 (1943).

[28] P. N. Pusey, *Statistical properties of scattered radiation*. In *Photon correlation spectroscopy and velocimetry*. Ed. H. Z. Cummins and E. R. Pike. Plenum Press, New York (1977)

[29] C. V. Raman, *Lectures in Physical Optics, Part 1*. p160. Bangalore: Indian Academy of Sciences (1959)

[30] P. Hariharah, Optica Acta. 19, 791 (1972)

[31] H. Z. Cummins and H. L. Swinney, *Light Beating Spectroscopy*, in Progress in Optics, **8**, 133-200, Ed. E. Wolf. Amsterdam (1970).

[32] H. Z. Cummins, N. Knable, and Y. Yeh, *Observation of Diffusion Broadening of Rayleigh Scattered Light*, Phys. Rev. Lett. **12**, 150-153 (1964).

[33] S. S. Alpert, Y. Yeh, and E. Lipworth, *Observation of Time-Dependent Concentration Fluctuations in a Binary Mixture Near the Critical Temperature Using a He-Ne Laser*, Phys. Rev. Lett. **14**, 486-488 (1965).

[34] N. C. Ford, Jr. and G. B. Benedek, *Observation of the Spectrum of Light Scattered From a Pure Fluid Near Its Critical Point*, Phys. Rev. Lett. **15**, 649-653 (1965).

[35] J. B. Lastovka and G. B. Benedek, *Spectrum of Light Scattered Quasielastically From a Normal Liquid*, Phys. Rev. Lett. **17**, 1039-1042 (1966).

[36] A. T. Forrester, *J. Opt. Soc. Am*. **51**, 253 (1961)

[37] D. J. Pine, D. A. Weitz, P. M. Chaikin, and E. Herbolzheimer, *Diffusing-wave Spectroscopy*, Phys. Rev. Lett. **60**, 1134-1137 (1988).

[38] J. D. Brock, R. J. Birgeneau, J. D. Litster, and A. Aharony, *Liquids, Crystals, and Liquid Crystals*, Physics Today **42** (7), 52-9 (1989).

[39] S. B. Dierker and R. Pindak, *Dynamics of Thin Tilted Hexatic Liquid Crystal Films*, Phys. Rev. Lett. **59**, 1002-5 (1987).

[40] J. V. Selinger and D. R. Nelson, *Theory of Transitions among Tilted Hexatic Phases in Liquid Crystals*, Phys. Rev. A **39**, 3135-47 (1989).

[41] J. V. Selinger, *Dynamics of Tilted Hexatic Phases in Liquid Crystal Films*, Journal de Phys. II **1**, 363-73 (1991).

[42] *Density Fluctuation Dynamics in a Screened Coulomb Colloid: Comparison of the Liquid and BCC Crystal Phases* Physics **86** -21

[43] *Effects of Partial Coherence on the Scattering of X Rays by Matter*, Phys. Rev. B , 2740-

[44] *Statistical optics*. Wiley, New York (1985)

[45] B. Saleh, . Springer, Berlin (1978)

[46] B. R. Frieden, . Springer, Berlin (1982)

N. G. Van Kampen, *Stochastic processes in physics and chemistry* Amsterdam (1981)

K. Schätzel, *Dynamic light scattering. The method and some applications* Press, Oxford (1993)

R. J. Glauber, *Phys. Rev* **131**, 2766 (1963)

[50] K. A. O'Donnel, J. Opt. Soc. Am., **A3**, 193 (1986)

[51] W. Feller, *An introduction to probability theory and its applications*, Vol. II, 2nd ed., pp. 244ff. Wiley, New York (1966)

[52] J. D. Jackson, *Classical Electrodynamics*, 2nd Edition, John Wiley & Sons, New York (1975).

[53] W. H. Zachariasen, *Theory of X-Ray Diffraction in Crystals*, John Wiley & Sons, New York (1945).

[54] B. E. Warren, *X-Ray Diffraction*, Addison-Wesley Publishing Co., Reading (1969).

[55] B. D. Cullity, *Elements of X-Ray Diffraction*, 2nd Edition, Addison-Wesley Publishing Co., Reading (1978).

[56] J. W. Goodman, *Introduction to Fourier optics*. McGraw-Hill, New York (1968)

[57] H. Z. Cummins and E. R. Pike, *Photon Correlation and Light Beating Spectroscopy*, Plenum, New York (1974).

[58] K. Schätzel, *Optica Acta*, **30**, 155 (1983)

[59] B. E. Saleh and M. F. Cardoso. *J. Phys. A*, **6**, 1897 (1973)

[60] C. Oliver. *J. Phys. A*, **12**, 591 (1979)

[61] K. Schätzel, M. Drewel, and S. Stimac. *J. Modern Optics*, **35**, 711 (1988)

[62] K. Schätzel, R. Kalström, B. Stampa, and J. Ahrens. *J. Opt. Soc. Am. B*, **6**, 937 (1989)

[63] K. Schätzel. *Appl. Phys. B*, **41**, 95 (1986)

[64] P. N. Pusey, In *Liquids, freezing and the glass transition* (ed. D. Levesque, J. P. Hansen, and J. Zinn-Justin). Elsevier, Amsterdam (1990)

[65] A. Einstein, *Ann. Phys*., **19**, 371 (1906)

[66] P. J. Carrol, and G. D. Patterson, *J. Chem. Phys*., **82**, 9 (1985)

[67] S. B. Dierker, *X-Ray photon correlation spectroscopy*. Proceedings of NATO Advanced research workshop, E. R. Pike, Ed. (Kluwer Academic, Dordrecht, The Netherlands, 1997)

[68] D. Forster, *Hydrodynamic Fluctuations, Broken Symmetries, and Correlation Functions*, W. A. Benjamin, Reading (1975).

[69] P. G. de Gennes. *Scaling concepts in polymer physics*, Cornell University Press, Ithaca, NY (1979).

[70] P. Flory, *Principles of Polymer Chemistry*, Ch. V, Cornell University Press, Ithaka, NY (1971)

[71] P. E. Rouse, *J. Chem. Phys*. **21**, 1273 (1953)

[72] P. J. Flory, J. Chem. Phys. **10**, 51 (1942).

[73] M. Huggins, J. Phys. Chem. **46**, 151 (1942); J. Am. Chem. Soc. **64**, 1712 (1942).

[74] E. A. Guggenheim, *Thermodynamics*. Elsevier, New York (1985).

[75] F. F. Abraham, *Homogeneous Nucleation Theory*, Academic, New York (1974).

[76] J. W. Cahn, J. Chem. Phys. 42, 93 (1965).

[77] K. Binder, *J. Chem. Phys*. **79**, 6387 (1983).

[78] K. Binder, *Phys. Rev. A* **29**, 341 (1984)

[79] H. E. Stanley, *Phase transitions and critical phenomena*. Claredon Press, Oxford (1971)

[80] S. K. Ma. *Modern theory of critical phenomena*. Benjamin, Reading, MA (1976)

[81] A. Sariban and K. Binder, *Critical Properties of the Flory-Huggins Lattice Model of Polymer Mixtures*, J. Chem. Phys. **86**, 5859-5873 (1987).

[82] D. Schwahn, K. Mortensen, and H. Yee-Madeira, *Mean-Field and Ising Critical Behavior of a Polymer Blend*, Phys. Rev. Lett. **58**, 1544-1546 (1987).

[83] C. Domb, and M. S. Green (editors). *Phase transitions and critical phenomena*. V 5,6. Academic Press, London (1976)

[84] V. L. Ginzburg. *Sov. Phys. – Solid State*, **2**, 1824 (1960)

[85] P. F. Green and B. L. Doyle. *Macromolecules*, **20**, 2471 (1987)

[86] P. G. de Gennes, *J. Phys. Lett.*(Paris) **38**, L-441 (1977)

[87] J. F. Joanny, *J. Phys. A* **11**, L117 (1978)

[88] F. S. Bates, J. H. Rosedale, P. Stepanek, T. P. Lodge, P. Wiltzius, G. H. Fredrickson, and R P. Hjelm, Jr., *Static and dynamic crossover in a critical polymer mixture*. Phys. Rev. Lett. **65**, 1893 (1990)

[89] D. Schwahn, K. Mortensen, and H. Yee-Madeira. *Mean-field and Ising Critical Behavior of a polymer blend*, Phys. Rev. Lett. **58** (15), 1544 (1987)

[90] S. Janssen, D, Schwahn, and T. Springer. *Mean-field Ising crossover and the critical exponents g, n, and h for a polymer blend: d-PB/PS studied by SANS*, Phys. Rev. Lett. 68 (21), 3180 (1992)

[91] D. W. Hair, E. K. Hobbie, A. I. Nakatani, and C. C. Han. *Deviation from mean-field behavior in a low molecular weight critical polymer blend*, J. Chem. Phys. 96 (12), 9133 (1992)

[92] P. C. Hohenberg, and B. I. Halperin. *Rev. Mod. Phys*., **49**, 435 (1977)

[93] D. W. Oxtoby, and W. M. Gelbart. *J. Chem. Phys*., **61**, 2957 (1974)

[94] H. L. Swimnney, and D. L. Henry. *Phys. Rev. A*, **8**, 2586 (1973)

[95] D. B. Jacobson and B. S. Freiser, J. Am. Chem. Soc. **108**, 27 (1986)

[96] K. Kawasaki. *Ann. Phys*., **61**, 1 (1970)

[97] K. Kawasaki, and S. Lo, *Phys. Rev. Lett*., **29**, 48 (1972)

[98] G. H. Fredrickson, and F. S. Bates. *Critical dynamics of binary polymer mixtures*, J. Chem. Phys., **85**, 633 (1986)

[99] G. H. Fredrickson. *Kinetics of near-critical quenches in homogeneous binary polymer mixtures*, J. Chem. Phys., **85**, 3556 (1986)

[100] P. Stepanek, T. P. Lodge, C. Kedrowski, and F. S. Bates, *Critical Dynamics of Polymer Blends*, J. Chem. Phys. **94**, 8289 (1991).

[101] P. F. Green, C. J. Palmstrom, J. W. Mayer, and E. J. Kramer, *Macromolecules* 18, 501 (1985)

[102] B. Lai, A. Khounsary, R. Savoy, L. Moog, and E. Gluskin, "*Undulator A characteristics and specifications*", Tach. Rep. ANL/APS/TB-3, Argonne National Laboratory, 1993.

[103] R. J. Dejus, B. Lai, E. R. Moog, and E. Gluskin, "*Undulator A characteristics and specifications: Enhanced capabilities*", Tech. Rep. ANL/APS/TB-17, Argonne National Laboratory, 1994.

[104] T. Kuzay, "*Functional description of APS beamline front ends*", Tech. Rep. ANL/APS/TB-5, Argonne National Laboratory, 1993.

[105] Yoshio Suzuki, Atsushi Momose and Hiroshi Sugiyama. *Characterization of windows and filters for coherent X-ray beamlines.* J. Synchrotron Rad. (1998). **5**, 596-599

[106] Henderson S. J. *Comparison of Parasitic Scattering from Window Materials used for Small-Angle X-ray Scattering: a Better Beryllium Window*. J. Appl. Cryst. (1995). **28**, 820-826

[107] P. Illinski, R. J. Dejus, E. Gluskin, and T. I. Morrison, "*Some practical aspects of undulator radiation properties*", in Optics for High-Brightness Synchrotron Radiation Beamlines II, L. E. Berman and J. R. Arthur, eds., Proc. SPIE 2856, pp. 16-25, 1996.

[108] Si substrates were purchased from General Optics, 554 Flinn Ave., Moorpark, CA 93021, (805) 529-3324. They are 25 mm wide by 50 mm long by 7 mm thick.

[109] Kutateladze, S. *Fundamentals of Heat Transfer*. New York. Academic Press, **1963**

[110] P. Illinski, R. J. Dejus, E. Gluskin, and T. I. Morrison, in *Optics for High-Brightness Synchrotron Radiation Beamlines II* (SPIE, The International Society for Optical Engineering, P.O. Box 10, Bellingham, Washington 98227-0010 USA, 1996), VOL 2856, pp. 16-25

[111] B. Yang, L. Emery. *Updates to ANL/APS/TB-17*, July 1999.

[112] E. Dufresne, T. Nurushev, R. Clarke, and S. Dierker. *A Study of Concentration Fluctuations in the Binary Mixture of Hexane-Nitrobenzene with X-ray Photon Correlation Spectroscopy*. (Preprint)

[113] S.-H. Chen, C.-C. Lai, J. Rouch, and P. Tartaglia, Phys. Rev. A. **27**, 1086 (1983)

[114] P. Damay, F. Leclercq, and P. Chieux. *Critical scattering function in a binary fluid mixture: A study of sodium-deuteroammonia solution at the critical concentration by small-angle neutron scattering*. Phys. Rev. B **40**, 4696-4708 (1989)

[115] Y. Izumi. X-ray scattering study of the critical correlation scaling function for a binary liquid mixture. Phys. Rev. A **39**, 5826-5831 (1989)

[116] K. Dawes and L. C. Glover. *Effects of Electron Beam and g-Irradiation on Polymeric Materials*. Raychem Corporation, 300 Constitution Dr., Menlo Park, CA 94025

[117] A. Chapiro, *Radiation Chemistry of Polymeric Systems*. Interscience, New York, 1962

[118] A. Charlesby. *Atomic Radiation and Polymers*. Pergamon Press, London, 1960.

[119] *The Radiation Chemistry of Macromolecules, Volume I*, edited by M. Dole. Academic Press, New York, 1972.

[120] *The Radiation Chemistry of Macromolecules, Volume II*, edited by M. Dole. Academic Press, New York, 1973.

[121] *Radiation Processing of Polymers*, edited by A. Singh and J. Silverman. Hanser, Munich, 1992.

[122] Irradiation *of Polymeric Materials*, edited by E. Reichmais, C. W. Frank, and J. H. O'Donnell. American Chemical Society, 1993.

[123] Y. Y. Maruo, S. Sasaki, T. Haga, H. Kinoshita, T. Horiuchi, and T. Tamamura. *Changes in refractive index and in chemical state of synchrotron radiation irradiated fluorinated polyimide films.* J. of Vac. Sci. Technol. A 14 (4), pp. 2470-2474

[124] A. Charlesby, J. Polym. Sci. **11**, 513 and 521 (1953)

[125] J. C. Spiro and C. A. Winkler, J. Appl. Polym. Sci. **8**, 1709 (1964)

[126] G. G. A. Bohm and J. O. Tveekrem. Rubber Chem. Technol. **55**, 575 (1982)

[127] V. T. Kozlov, A. G. Yevseyev, and P. I. Zubov. Vysokomol. Soed. **A11**, 2230 (1969)

[128] A. Von Raven and H. Heusinger. J. Polym. Sci.: Polym. Chem. Ed. **12**. 2255 (1974)

[129] E. Witt. J. Polym. Sci. **41**, 507 (1959)

[130] R.-J. Roe and W.-C. Zin, *Determination of the Polymer-Polymer Interaction Parameter for the Polystyrene-Polybutadiene Pair, Macromolecules* **13**, 1221-1228 (1980).

[131] E. L. Atkin, J. A. Kleintjens, R. Koningsveld, and L. J. Fetters, *Deuterium Isotope Effect in Polymer Compatibility*, Makromol. Chem. **185**, 377-387 (1984).

[132] S. Rostami and D. J. Walsh,. *Simulation of Upper and Lower Critical Phase Diagrams for Polymer Mixtures at Various Pressures*, Macromolecules **18**, 1228-1235 (1985).

[133] G. Ronca and T. P. Russel, *Thermodynamics of Phase Separation in Polymer Mixtures*, Macromolecules **18**, 665-670 (1985).

[134] J.-L. Lin, D. Rigby, and R.-J. Roe, *Deuterium Isotope Effect on the Compatibility between Polystyrene and Polybutadiene*, Macromolecules **18**, 1609-1611 (1985).

[135] H. Frielinghaus, D. Schwahn, K. Mortensen, L. Willner and K. Almdal, *Pressure and Temperature Effects in Homopolymer Blends and Diblock Copolymers*, J. Appl. Cryst. **30**, 696-701 (1997).

[136] D. Schwahn, T. Springer and S. Janssen, *Investigation of Equilibrium and Non-equilibrium States of Polymer Blends by Small Angle Neutron Scattering*, J. Appl. Cryst. **24**, 685-691 (1991).

[137] S. Janssen, D. Schwahn, and T. Springer, *Mean-Field Crossover and the Critical Exponents g, n, and h for a Polymer Blend: d-PB/PS Studied by Small Angle Neutron Scattering*, Phys. Rev. Lett. **68**, 3180-3183 (1992).

[138] D. W. Hair, E. K. Hobbie, A. I. Nakatani, and C. C. Han, *Deviation from Mean-Field Behavior in a Low Molecular Weight Critical Polymer Blend*, J. Chem. Phys. **96**, 9133-9137 (1992).

[139] T. P. Russell, G. Hadziioannou, and W. K. Warburton, *Phase Separation in Low Molecular Weight Polymer Mixtures*, Macromolecules **18**, 78-83 (1985).

[140] G. Ronca and T. P. Russell, *Concentration Fluctuations of Polystyrene-Polybutadiene Blends*, Phys. Rev. B **35**, 8566-8571 (1987).

[141] D. W. Hair, E. K. Hobbie, J. Douglas, and C. C. Han, *Critical Dynamics of an Asymmetric Binary Polymer Mixture*, Phys. Rev. Lett. **68**, 2476-2479 (1992).

[142] H. Yajima, D. W. Hair, A. I. Nakatani, J. F. Douglas, and C. C. Han, *Dynamic Light Scattering Study of a Diluted Polymer Blend Near Its Critical Point*, Phys. Rev. B **47**, 12,268-12,271 (1993).

[143] Polysciences, Inc. 400 Valley Road, Warrington, PA 18976. (800)523-2575

[144] L. Cipelletti, D. A. Weitz. *Ultralow-angle dynamic light scattering with a charge coupled device camera based multispeckle, multitau correlator*. Rev. of Sci. Inst. **70** (8) 3214-3221 (1999)